NSF Grant ATM-9321361

National Science Foundation

INTEGRATION OF WSR-88 AND GOES-8 DATA FOR DETECTING AND FORECASTING STORM INITIATION

by Rita D. Roberts and Steven A. Rutledge

Colorado State University

DEPARTMENT OF ATMOSPHERIC SCIENCE

PAPER NO. 666

INTEGRATION OF WSR-88D AND GOES-8 DATA FOR DETECTING AND FORECASTING STORM INITIATION

by

Rita Dineen Roberts

and

Steven A. Rutledge

Department of Atmospheric Science

Colorado State University

Fort Collins, CO 80523

Research Supported by

National Science Foundation

under Grant ATM-9321361

Summer 1998

Atmospheric Science Paper No. 666

ABSTRACT

INTEGRATION OF WSR-88D AND GOES-8 DATA FOR
DETECTING AND FORECASTING STORM INITIATION

Several studies utilizing research radar have documented the importance of surface convergence boundaries in initiation of convection. Detection and tracking of these boundaries provides valuable information for forecasting thunderstorm occurrence. The presence of cumulus clouds above these boundaries is believed to increase the probability that thunderstorm development could occur. With the advent of the GOES-8 satellite 15 min update rate and higher spatial resolution, it is now possible to detect and track cumulus cloud growth more closely. The focus of this thesis is to show how operational WSR-88D radar and GOES-8 satellite data can be used together to provide information on the growth of cumulus clouds into thunderstorms, based on radar-detected, boundary layer convergence features, cloud-top brightness temperatures, and change in reflectivity echo intensity with time.

The evolution of cumulus clouds over a spectrum of radar-detected, boundary layer features have been examined. While thunderstorms did form above horizontal convective rolls in the absence of any additional surface forcing, the most intense storms initiated above gust fronts, gust front interaction with horizontal rolls, and above stationary convergence zones. In all cases presented, cloud growth was evident in the satellite data in the form of decreasing cloud top temperatures, prior to the first detection of 10-20 dBZ radar echoes aloft. Sub-freezing cloud top temperatures were found to be precursors to the start of precipitation phase in clouds, with cloud

top temperatures below 0° C occurring 15 min prior to the detection of 20 dBZ echoes, and 30 min prior to the detection of 30 dBZ echoes. The rate of cloud top temperature change was found to be important for discriminating between slow and rapid storm growth. Results of this thesis show that both satellite and radar data can be exploited to provide up to 30 min additional lead time in issuing forecasts of thunderstorm initiation, by monitoring the data in an automated way.

ACKNOWLEDGEMENTS

We would like to thank thesis committee members Dr. Thomas McKee and Dr. V. Chandrasekar for their constructive comments on the thesis. Thanks are also in order to Pat Kennedy for providing CHILL radar data on early cloud growth. Special appreciation goes to Jim Wilson for his encouragement and support throughout these graduate research activities.

This research was sponsored by the National Science Foundation, under grant number ATM-9321361.

TABLE OF CONTENTS

1. INTRODUCTION **1**

1.1 Atmospheric instability 2

1.2 Boundary layer features 4

1.3 Environmental Winds 22

1.4 Operational thunderstorm forecasting 23

1.5 Objectives of this study 27

2. DATA PROCESSING / ANALYSIS TECHNIQUES **29**

2.1 Radar data 29

2.2 Satellite data 33

2.3 Soundings 39

2.4 Integration of data 39

3. THEORETICAL CONSIDERATIONS FOR RADAR AND SATELLITE REMOTE SENSING **41**

3.1 Doppler radar 41

3.1.1 Sensing precipitating echoes 41

3.1.2 Sensing cloud features 44

3.1.3 Sensing clear-air, boundary layer features 50

3.2 GOES satellite 53

3.2.1 Radiative transfer 53

3.2.2 Sensing clouds 57

4. CASE STUDIES 61

4.1 23 August 1995 61

4.1.1. Environmental conditions 61

4.1.2. Relationship of clouds to boundary layer features 67

4.1.3. Growth of cumulus clouds 81

4.2 24 August 1995 99

4.2.1 Environmental conditions 99

4.2.2. Relationship of clouds to boundary layer features 107

4.2.3. Growth of cumulus clouds 116

i. Cloud growth associated with gust front passage 122

ii. Cloud growth above horizontal rolls 129

iii. Cloud growth associated with gust front / horizontal roll interactions 134

4.3 21 July 1995 136

4.3.1 Environmental conditions 136

4.3.2. Relationship of clouds to boundary layer features 140

4.3.3. Growth of cumulus clouds 143

i. Cloud growth associated with gust front / horizontal roll interaction 146

ii. Cloud growth above less organized roll convection 146

4.4 24 July 1995 149

4.4.1 Environmental conditions 151

4.4.2 Relationship of clouds to boundary layer features 151

4.4.3. Growth of cumulus clouds 155

5. CONCLUSIONS 164

6. REFERENCES 171

LIST OF FIGURES

1.1: (a) GOES-East VIS image over the Gulf of Mexico on 30 July 1986 at 1300 local time (1900 UTC), showing an arc cloud line AB and an area of convection P; (b) two hours later, the line has merged with the pre-existing convection at C. (from Bader et al. 1995) 5

1.2a: Conceptual model of arc cloud line formation: CZ is a convergence zone and DSL is a density surge line. (from Bader et al. 1995) 6

1.2b: (b) Model of an outflow, with typical numerical values, moving into a region with pre-existing convection: ahead of the boundary there is negative buoyancy only from the Cu tops to the LFC. (from Bader et al. 1995) 7

1.3: S-band reflectivity images over Colorado at (a) 2226, (b) 2252, (c) 2323, and (d) 2340 UTC on 25 July 1984, showing two outflow boundaries AA and BB meeting at X; a new convective line XY forms. Range rings are at 20 km intervals. Values in dBZ. (from Wilson and Roesli, 1985) 9

14: Schematic diagram showing how a buoyant updraft may be influenced by wind shear and/or a cold pool. (a) With no shear and no cold pool, the axis of the updraft produced by the thermally created, symmetric vorticity distribution is vertical. (b) With a cold pool, the distribution is biased by the negative vorticity of the underlying cold pool and causes the updraft to lean upshear. (c) With shear, the distribution is biased toward positive vorticity and this causes the updraft to lean back over the cold pool. (d) With both a cold pool and shear the two effects may negate each other, and allow an erect updraft. (from Rotunno et al. 1998) 12

1.5: East-west vertical projection of TREC-based streamlines for (a) 1500, (b) 1530 (c) 1600, and (d) 1618. Heights (Z) are MSL; the surface elevation is ~1.6 km. The cloud base and top are based on the observed larger clouds as determined by photogrammetry; the cloud widths are intended for schematic representation only. (from Wilson et al. 1992) 13

1.6: Relative location of convergence line (heavy solid line), horizontal rolls (light solid lines), misocyclones (labelled open circles beginning with letter C), clouds (cross hatched features in panels (e) and (f)), and precipitation echo at 6.5 km MSL (panels (f) - (k); contours are 10, 30, 50 dBZ). Times shown are 1600-1730 MDT. (from Wilson et al. 1992) 15

1.7: Interpolated CP3 reflectivity (dBZ; gray line) and time series of aircraft-measured vertical velocity (m/s; thin solid line), potential temperature (K; thick solid line), and mixing ratio (g/kg; dashed line). Data from the (a) NCAR King Air at 0.52zi, (b) UW King Air at 0.15zi on 2 August, (c) UW King Air at 1.15zi, and (d) NCAR King Air at 0.57zi on 10 August are shown. Letters correspond with locations of reflectivity maxima along the flight tracks. Schematic clouds in (c) indicate times of cloud penetrations. (from Weckwerth et al. 1996) 16

1.8: Schematic diagram summarizing results. Gray lines indicate roll circulations. Thick black lines are contours of moisture with the maximaexisting within the roll updraft regions. Actual cloud base and depth are shown by the solid cloud. Dashed clouds represent relative cloud bases and depths expected if stability parameters were estimated from CBL moisture values directly beneath those clouds. (from Weckwerth et al. 1996) 17

1.9: Schematic representation of the low-level circulations across the central Florida penisula on 2 August. The upper panel (a) shows the three major circulations that exist in the early afternoon: the coastline wind surges (equivalent to sea-breeze fronts), the large-scale convergence between the wind surges (substantiated by the cooling aloft), and the convective rolls. Later in the afternoon (b) when the surface heating decreases, the convective rolls decay and the large-scale convergence collapses to produce a single narrow intermediate updraft. (from Fankhauser et al. 1995) 21

2.1: WSR-88D half power beamwidth in degrees as a function of radio frequency in megahertz according to four formulas: (a) Andrew Corporation data in Sirmans (1992); (b) the rule of thumb SQRT (32000/G), where G is from the INCO 1994 gain formula: (c) the INCO 1993 beamwidth formula; (d) the INCO 1994 beamwidth formula. (from Pratt and Ferraro, 1995). 30

2.2: Earth location error of tall clouds in GOES imagery. The inset diagram, lower right, shows how the apparent cloud position can be significantly different from the actual one for tall clouds located toward the edges of GOES images. The curves are lines of equal displacement error for a satellite at 75 deg W and are labelled in nautical miles. The values are for a cloud top of 12 km (40,000 ft); for 6-km tops subtract 50%, for 18 km tops add 50%. To correct a cloud top position for a given height it should be displaced the appropriate distance toward the satellite subpoint in the direction of the small arrows. (from Weiss, 1978) 36

2.3: Parallax-induced cloud displacement from geostationary obit, as a function of the angular distance from nadir. The cloud displacement is expressed in terms of its apparent offset from its true position, normalized by the height of the cloud. (from Johnson et al. 1994) 37

3.1: Size parameter χ as a function of wavelength of the incident radiation and particle radius. (Based on Wallace and Hobbs, 1977. From Kidder and Vonder Haar, 1995). 43

3.2: Trade-offs between refractive index and particulate return. Curves are for equal scatter from C_n^2 and from Rayleigh liquid spheres found by equating Eqs. (3.2) and (3.8). Various cloud types are shown for reference. Figure parametric in C_n^2. (From Gossard, 1990) 48

3.3: Emission and absorption spectra. The upper portion of the diagram shows normalized emission spectra for blackbody radiation at 6000K, the temperature of the Sun, and for a body of 250 K corresponding roughly to the radiation emitted by the Earth and atmosphere. The middle part of the diagram shows the absorption spectrum of the atmosphere. The atmosphere is much more transparent to incoming solar radiation than it is to outgoing (IR) terrestrial radiation. The shaded band is the IR region $(10.5 - 12.5\mu m)$ commonly used for IR cloud imagery. The line at $0.63\mu m$ is centered in the region where VIS measurements are made. (From Anderson, 1990) 55

4.1: Denver NWS 1200 UTC sounding from 23 August 1995. 62

4.2: Upper air 500 mb map from 23 August 1995 at 1200 UTC. 63

4.3: Upper air 700 mb map from 23 August 1995 at 1200 UTC. 64

4.4: Upper air 850 mb map from 23 August 1995 at 1200 UTC. 65

4.5: Surface analysis map from 23 August 1995 at 1800 UTC. 66

4.6: Cartesian (CIDD) KFTG reflectivity plot from 23 August 1995 at 1930 and 2 km MSL (0.5 km AGL) showing the reflectivity thin line features associated with the DCVZ and the horizontal rolls. The yellow box defines the domain of data analyses for this case. The arrow points to the horizontal roll that first intersects and then later merges with the DCVZ. Data is plotted in 1 km grid increments. Range rings are overlaid as an additional reference. 68

4.7: Cartesian (CIDD) display of GOES-8 Visible data (in counts) at 1930 UTC with the KFTG radar location as the center of the plot. Data is in 1 km grid increments. The white arrow points to the cloud line analyzed from this day. 69

4.8: KFTG radar fields and satellite Visible imagery on 23 August 1995 at 19:28 UTC for the domain shown by the yellow box in Fig. 4.6. a) Reflectivity in dBZ at 2.2 MSL (0.5 km AGL), b) radial velocity in m/s, c) GOES-8 Visible imagery (in counts), and d) TREC-derived convergence (yellow shades). Grays and browns are divergence. TREC vectors are overlaid onto all panels. 71

4.9: CEDRIC plot of Visible data from 23 August 1995 at 1930 with reflectivity contours overlaid. Contours are in increments of 12, 14, and 16 dBZ. The Visible gray scale is in counts; values are listed as negative for plotting purposes only. 72

4.10a: Time series of cartesian reflectivity plots at 0.5 km AGL from 23 August 1995 at a) 2000 UTC. 73

4.10b: b) at 2030 UTC. 74

4.10c: c) at 2100 UTC. 75

4.10d: d) at 2130 UTC. 76

4.11a: Time series of GOES-8 Visible data at a) 2000 UTC. 78

4.11b: b) at 2030 UTC. 79

4.11c: c) at 2130 UTC. 80

4.12: CEDRIC plots at 1932 on 23 August 1995 of a) IR brightness temperatures (in deg C) with contours of reflectivity overlaid, b) KFTG reflectivity (in dBZ) at 4.5 km AGL with contours of brightness temperature overlaid, and c) GOES-8 Visible image in counts (negative for plotting purposes only). 82

4.13: Same as Fig. 4.12, except at 1945 UTC. 84

4.14: Same as Fig. 4.12, except at 2002 UTC. 85

4.15: Same as Fig. 4.12, except at 2015 UTC. 88

4.16: Same as Fig. 4.12, except at 2032 UTC. 89

4.17a: Plots of reflectivity (dBZ), radial velocity (m/s) and differential reflectivity (Zdr) collected by the CHILL radar on 13 July 1995. a) 1616 MDT. 91

4.17b: b) at 1620 UTC. 92

4.17c: c) at 1624 UTC. 93

4.17d: d) at 1629 UTC. 94

4.18: Histogram plots of GOES-8 brightness temperature (deg C) and KFTG maximum reflectivity at 4.5 km AGL. Data is from 23 August 1995, at 1932, 2002, 2015, and 2032 UTC. The thin vertical line above the histogram bars is the median value for each plot. 96

4.19: Time series plot of Infrared brightness temperature (deg C) and maximum radar reflectivity (dBZ) associated with growth of the cloud line above the DCVZ. Median (dashed curve) and minimum (black solid curve) temperature values and maximum reflectivity (gray curve), obtained from histogram information, are shown. 97

4.20: Histogram plots of change in brightness temperature with time for time period a) 1932 - 1945 UTC and b) 1945 - 2002 UTC. The thin vertical line above the histogram bars is the median value for each plot. 98

4.21: Denver NWS 1200 UTC sounding from 24 August 1995. 100

4.22: Upper air 500 mb map from 24 August 1995 at 1200 UTC. 102

4.23: Upper air 700 mb map from 24 August 1995 at 1200 UTC. 103

4.24: 850 mb map from 24 August 1995 at 1200 UTC. 104

4.25: Surface analysis map from 24 August 1995 at 1800 UTC. 105

4.26: Low level, 0.5 km AGL plots of a) KFTG reflectivity (dBZ) and b) radial velocity (m/s) at 20:05 UTC on 24 August 1995. 106

4.27: Visible satellite image from 24 August 1995 at 2002 UTC. Units are in radiance counts. The gridded region on the plot represents the 20 x 20 km regions analyzed from this day. The numbered boxes represents those regions discussed in the text. 108

4.28: Plot of Visible data from 24 August 1995 at 2005 with reflectivity contours overlaid. Contours are in increments of 8 and 12 dBZ. The Visible scale is in radiance counts; values are listed as negative for plotting purposes only. 109

4.29a: Sequence of cartesian reflectivity plots at 0.5 km AGL from 24 August 1995 at a) 2028 UTC. 111

4.29b: b) at 2127 UTC. 112

4.29c: c) at 2231 UTC. 113

4.29d: d) at 2330 UTC. 114

4.30: Time sequence of TREC convergence plots with TREC wind vectors overlaid. Brown, green and gray, colors are regions of divergence. Yellow, orange and red are convergence. 115

4.31a: Visible satellite imagery on 24 August 1995 at a) 2132 UTC. 117

4.31b: b) at 2232 UTC. 118

4.32a: Composite image of GOES-8 Infrared brightness temperature field and KFTG radar reflectivity at 4.5 km AGL. In the upper righthand colorscale (in deg C), gray shade are IR temperatures above freezing, white colors are temperatures near 0 deg C, and subfreezing temperatures are shades of blue and purple. The lower righthand colorscale is for the reflectivity field with the more intense storms represented by shades of red and yellow. The overlaid grid is the same as shown in Fig. 4.27. a) At 2132 UTC. 119

4.32b: b) at 2232 UTC. 120

4.32c: c) at 2332 UTC. 121

4.33: Time series plot of Infrared brightness temperature (deg C) and maximum radar reflectivity (dBZ) associated with cloud growth above a gust front. Median (dashed curve) and minimum (black solid curve) temperature values and maximum reflectivity (thin black curve) are shown for a) box 4 and b) box 3. 123

4.34: CEDRIC plots of brightness temperatures and radar reflectivity on 24 August 1995. a) IR temperatures (deg C) at 2002 with contours of reflectvity overlaid. b) Reflectivity at 4.5 km with contours of temperature overlaid. c), d) Same as a), b) except at 2032. 124

4.35: Same as Fig. 4.34, except a), b) at 2115 UTC and c), d) at 2132 UTC. 125

4.36: Same as Fig. 4.34, except a), b) at 2202 UTC and c), d) at 2232 UTC. 127

4.37: Same as Fig. 4.34, except a), b) at 2300 UTC and c), d) at 2330 UTC. 128

4.38: Time series plots of IR temperatures and radar reflectivity associated with cloud growth above horizontal rolls within a) box 15, b) box 12 and c) box 11. 130

4.39: Same as Fig. 4.38, except for pulsating cloud growth above horizontal rolls within a) box 27 and b) box 24. 133

4.40: Same as Fig. 4.38, except for cloud growth above gust front interactions with horizontal rolls within a) box 17 and b) box 22. 135

4.41: CLASS sounding taken at 1700 UTC on 21 July at the Denver NWS. 137

4.42a: Cartesian reflectivity plots at 0.5 km AGL from 21 July 1995. A finer colorscale increment has been used to show the low intensity, horizontal rolls. Black regions within the storms are reflectivities greater than 43 dBZ. a) 2028 UTC. 138

4.42b: b) at 2057 UTC. 139

4.43: GOES-8 Visible imagery from 21 July at 1902 UTC. Units are in radiance counts. The gridded region on the plot represents the 20 x 20 km regions analyzed from this day. The numbered boxes represent those regions discussed in the text. 141

4.44: Visible data at 1902 UTC on 21 July 1995 with reflectivity contours overlaid. Contours are in increments of 4 and 8 dBZ. The Visible data is in radiance counts; values are negative for plotting purposes only. Reflectivity at a) 0.5 km AGL and b) 1.5 km AGL. 142

4.45: CEDRIC plots of brightness temperatures and radar reflectivity on 21 July 1995. a) IR temperatures at 1900 UTC. b) Reflectivity at 4.5 km AGL. c), d) Same as a), b), except at 1930 UTC. 143

4.45: e) Temperatures at 2000 UTC, f) reflectivity at 2000 UTC, g) temperatures at 2030 UTC, and h) reflectivity at 2030 UTC. 144

4.46: Time series plots of IR temperatures and maximum reflectivity associated with cloud growth ahead of a gust front on 21 July 1995. Median (dashed) and minimum temperature (black) curves and reflectivity (gray line) are shown for box 1. 147

4.47: Same as Fig. 4.46, except for cloud growth above weak horizontal rolls within a) box 2, b) box 3, and c) box 4. 148

4.48: CLASS sounding taken at 1700 UTC on 24 July 1995 at the Denver NWS. 150

4.49: Cartesian reflectivity plot at 0.5 km AGL from 24 July 1995 at 1957 UTC. A finer colorscale increment has been used to show the low intensity, horizontal rolls. 152

4.50a: GOES-8 Visible data from 24 July 1995. Units are in radiance counts. a) Image at 1815 UTC. 153

4.50b: b) Image at 1932 UTC. The gridded region on the image represents the 20 x 20 km regions analyzed from this day. The numbered boxes represent those regions discussed in the text. 154

4.51: Visible data at 1902 UTC on 24 July 1995 with reflectivity contours overlaid. Contours are in increments of 2 and 6 dBZ. The Visible data is in radiance counts; values are negative for plotting purposes only. Reflectivity at a) 0.5 km AGL and b) 1.5 km AGL. 156

4.52: CEDRIC plots of brightness temperatures and radar reflectivity on 24 July 1995. a) Temperature at 1902 UTC with contours of reflectivity overlaid. b) Reflectivity at 4.5 km AGL. c), d), Same as a), b), except at 1932 UTC. 157

4.53: CEDRIC plots of brightness temperatures and radar reflectivity on 24 July 1995. a) Temperature at 2002 UTC with contours of reflectivity overlaid. b) Reflectivity at 4.5 km AGL. c), d), Same as a), b), except at 2032 UTC. 158

4.54: CEDRIC plots of brightness temperatures and radar reflectivity on 24 July 1995. a) Temperature at 2115 UTC with contours of reflectivity overlaid. b) Reflectivity at 4.5 km AGL. c), d), Same as a), b), except at 2202 UTC. 159

4.55: CEDRIC plots of brightness temperatures and radar reflectivity on 24 July 1995. a) Temperature at 2232 UTC with contours of reflectivity overlaid. b) Reflectivity at 4.5 km AGL. 160

4.56: Time series plots of IR temperatures and maximum reflectivity associated with cloud growth capped by temperature inversions on 24 July 1995. Median (dashed) and minimum (black) temperature curves and reflectivity (gray curve) are shown for the regions defined by a) box 4 and b) box 5. 162

5.1: Visible satellite, radar, and derived satellite products that forecasters can use as guidance in issuing short term, thunderstorm forecasts. See text for discussion. 169

LIST OF TABLES

Table 1: WSR-88D Technical Parameters, as updated from FMH-11 (NOAA) 31

Table 2: GOES-7 and GOES-I imager characteristics. IGFOV at nadir and SSR are presented in kilometers, and noise equivalent temperatures for the thermal bands are specified for nominal scene temperatures (300 K for the window bands and 230 K for the water vapor band). 34

Chapter 1

INTRODUCTION

Understanding the process of thunderstorm formation and evolution has been the focus of years of study and observations. Modelling and observational studies have shown that storm initiation and growth are intimately related to boundary layer characteristics, atmospheric stability and the dynamics associated with interactions between the environment and storm-generated circulations. In recent years, the advent of more sensitive instrumentation and increased computing capabilities have facilitated more detailed examination of storms and the environments in which they form. Using GOES-8 satellite, WSR-88D radar, and radiosonde data, the relationship of cumulus clouds to boundary layer features and the growth of cumulus clouds into thunderstorms are the subject of this thesis.

Cumulus cloud formation typically occurs in unstable or conditionally unstable environments where buoyant or mechanically forced parcels rise until they reach their Convective Condensation Levels (CCL) or their Lifted Condensation Levels (LCL). Cumulus clouds form at the top of the Mixed Layer (ML), with cloud bases at the LCL. Forced and active clouds are triggered by thermals eminating from the ML. Thermals that are able to penetrate beyond the negative buoyancy above the capping inversion of the ML eventually reach the Level of Free Convection (LFC), resulting in active cloud growth which may under some conditions extend to the tropopause.

1.1 Atmospheric instability

Using radiosonde data, an assessment can be made of the potential instability of the atmosphere based on stability indices, such as the Lifted Index. Fankhauser and Wade (1982) compared temperature profiles for the mean NHRE (National Hail Research Experiment) hail day sounding with the Denver 20-yr mean (of June and July soundings) and found the profiles to be nearly identical above 650 mb (which was close to mean cloud base altitude). This suggested to them that the major distinction between the static stability on convective and non-convective days was largely determined by conditions in the boundary layer. Mueller et al. (1993) made use of a dense network of Colorado mesonet data and specially-collected soundings (from the CINDE Project) for the purpose of nowcasting thunderstorm development over the High Plains. A modified lifted index (MLI) was calculated using the potential temperature at 400 mb and the mean potential temperature and mixing ratio in the lowest 50 mb of the sounding. Soundings were collected in the proximity of boundary-layer convergence lines and the frequencies of storms with reflectivities exceeding 30 dBZ in the area were compared to the calculated lifted index values. They found that the soundings were useful for delineating regions that would not produce storms when the MLI > -1. However, in potentially unstable atmospheres (MLI < -1) thunderstorms did not always form, nor was thunderstorm intensity correlated to the MLI value.

They attributed the temporal and spatial variability observed in the static stability to variations of temperature and moisture in the boundary layer, in agreement with Fankhauser and Wade (1982). For the Colorado Front Range mixing ratio values ranged from 1-3 g/kg in air masses and potential temperature varied from 1-2 deg C typically. Potential temperature variations were as

much as 10 deg C within thunderstorm outflows. Using a 2-D numerical cloud model initialized with CINDE soundings, Mueller et al. (1993) concluded that variabilities of 3 deg C in temperature, 1 g/kg in low level (50 mb) moisture, and the depth of the moisture in the boundary layer have significant influences on the formation of deep convection over the High Plains. Features such as stationary boundaries, horizontal rolls, and mesoscale air masses were cited as contributing to boundary layer temperature and moisture variability.

Crook (1996) looked at the sensitivity of moist convection to various low-level thermodynamic parameters using a high-resolution, non-hydrostatic numerical model. The control runs he used for comparison with model sensitivity studies were based on observations from CINDE and NCAR/RAPS case studies. He found that convection initiation was most sensitive to the magnitude of the decrease in temperature and in moisture as measured both at the surface and in the well-mixed boundary layer. Convection initiation was least sensitive to the shape of the moisture profile or to the depth of the moisture. Specifically, for the situation in which convection was well-developed, changes in the strength of convection was quite sensitive to a change of only 1 g/kg of moisture in the boundary layer and less sensitive to surface temperature dropoff. That is, a change of one standard deviation in moisture variability equates to 2.5 times the effect on the Convective Available Potential Energy (CAPE) as compared to one standard deviation in temperature variability. However, the magnitude of CAPE does not dictate whether convection will occur. In the simulations examining whether convection or no convection will occur, the strength of convection produced was most sensitive to changes in temperature between the surface and in the well-mixed boundary layer. This is because convection initiation is dependent on the magnitude of the convective inhibition (CIN) which Crook shows to be more sensitive to temperature

variations than to moisture variations when applying the same moist static energy change. Thus, changes of only 1 deg C in the boundary layer temperature profile could affect whether convection will occur or not. Unfortunately this small change in temperature is within the measurement error of current observing systems and likely will be difficult to detect for purposes of predicting storms.

1.2 Boundary layer features

The convective ML is composed of an unstable surface layer, a convective boundary layer (CBL) and an entrainment zone at the top (Stull, 1988). In the surface layer and extending up into the CBL, surface convergence boundaries give rise to vertical motions and thermals ultimately associated with penetrative convection in unstable atmospheres. These surface convergence boundaries may represent the leading edge of mesoscale air masses, thunderstorm outflows, wind-shift lines, colliding outflows, horizontal boundary layer rolls, sea breeze, or other terrain-induced, convergence zones. Numerous studies using satellite, radar and mesonet data have documented the role of surface convergence boundaries in the initiation of new convection or enhancement of existing convection (Byers and Braham, 1949; Pielke, 1974; Purdom, 1976; Holle and Maier, 1980; Wade and Foote, 1982; Purdom and Marcus, 1982; Wilson and Schrieber, 1986; Wilson et al. 1992; Wilson and Mueller, 1993; Fankhauser et al. 1995, among others). One of the earliest detections of a sea breeze front and thunderstorm outflow was made using a WSR-57 radar (Boyd, 1965). The radar fine lines associated with these two features were observed to collide as revealed by the radar data. Several building cumuli were subsequently observed visually in the direction of the colliding boundaries.

A decade later, Purdom (1976) demonstrated that GOES satellite imagery provided valuable information on the initiation and maintenance of convective activity. Using time lapse imagery of VIS and IR data, he documented the propagation of sea breezes inland and the enhancement of convective cloudiness along the front prior to thunderstorm development. He was able to show with the increased spatial resolution (8 km for the IR channel and 1 km for the Visible channel) of the GOES-1 and GOES-2 satellites that new thunderstorm formation as well as enhancement of exisiting thunderstorms often occurred when one convective line intersected with another convective line, or when a line merged with an area of enhanced cumulus activity. An example of such an merger is shown in Fig. 1.1 (Bader et al, 1995). A schematic representation of arc cloud line formation (from Bader et al. 1995) is shown in Fig. 1.2a along with a conceptual model and repre-

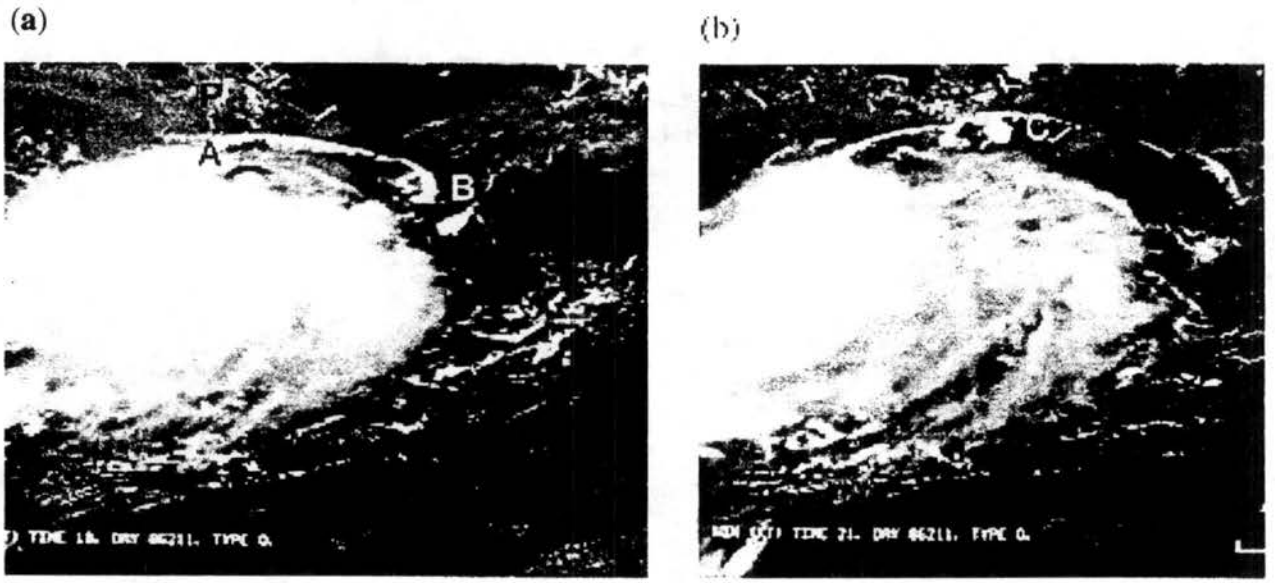

Fig. 1.1. (a) GOES-East VIS image over the Gulf of Mexico on 30 July 1986 at 1300 local time (1900 UTC), showing an arc cloud line AB and an area of convection P; (b) two hours later, the line has merged with the pre-existing convection a C. (from Bader et al 1995)

sentative magnitudes of an outflow boundary moving in a region of pre-existing convection (Fig. 1.2b). The ability of the satellite to precisely locate these arc cloud boundaries and their interactions with other boundaries was viewed as a significant tool for short range forecasting of intense convection.

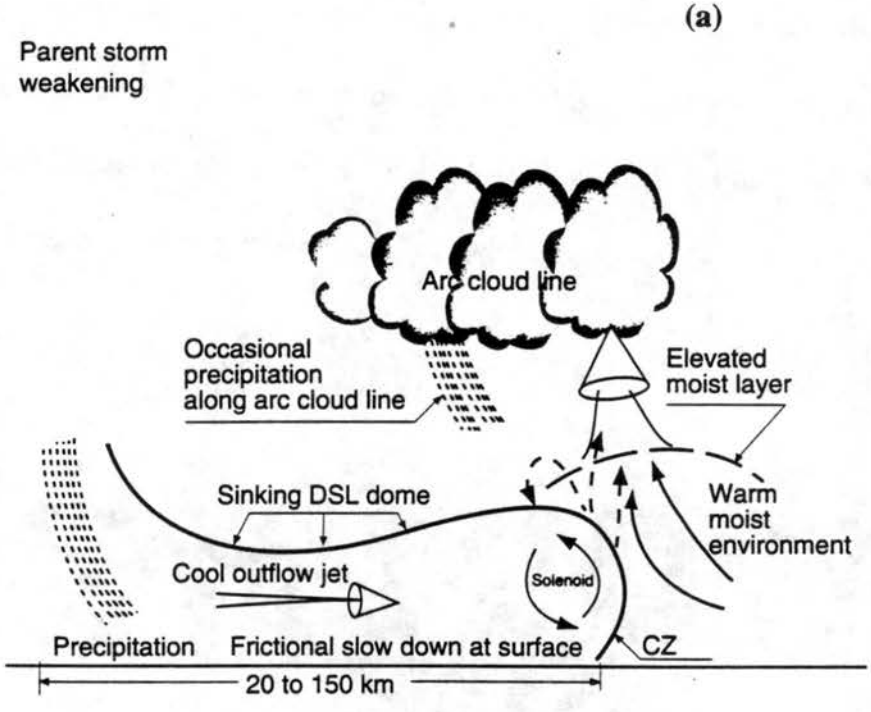

Fig. 1.2a. Conceptual model of arc cloud line formation: CZ is a convergence zone and DSL is a density surge line. (from Bader et al. 1995)

(b)

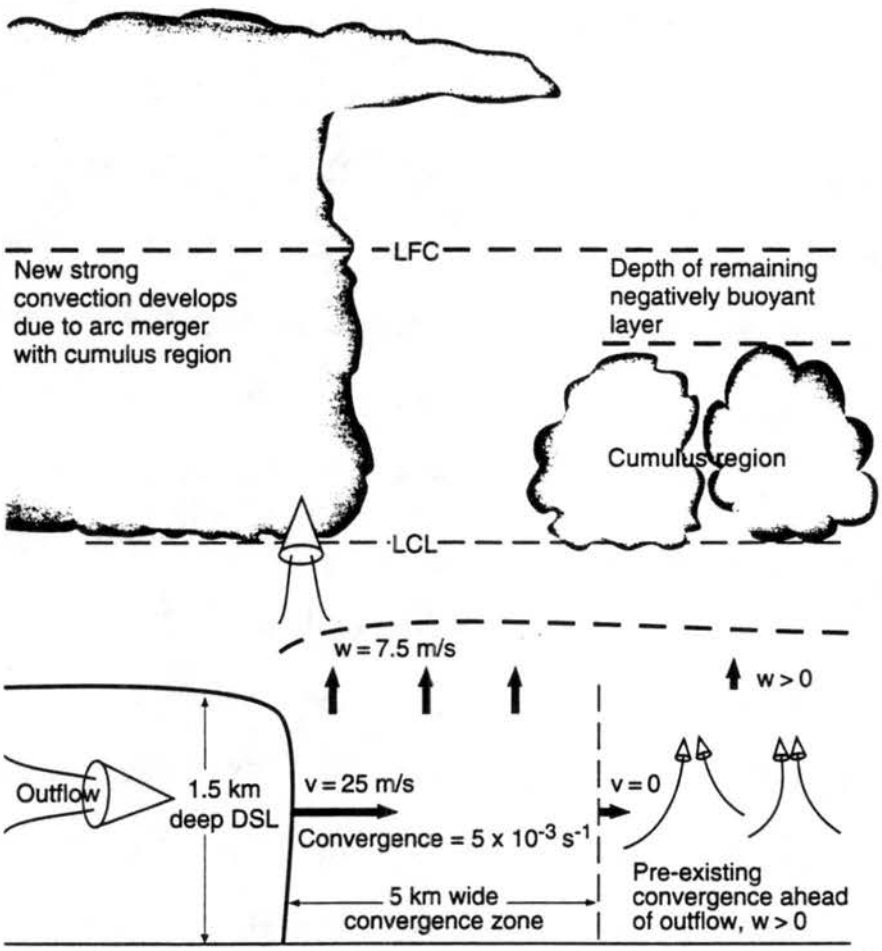

Fig. 1.2b. Model of an outflow, with typical numerical values, moving into a region with pre-existing convection: ahead of the boundary there is negative buoyancy only from the Cu tops to the LFC. (from Bader et al. 1995)

Purdom and Marcus (1982) examined nearly 10,000 storms during a 92 day period in southeast U.S. and found that early in the day, local forcing by thunderstorm outflows was the primary forcing mechnism for convection. Later in the day, they found that the most intense convection occurred when the dominant trigger mechanism was from arc cloud merger and intersection, the latter occurring over hundreds of kilometers in scale (as shown in Fig. 1.1). A subsequent study by Wilson and Schreiber (1986) examined the origin of 418 storms in the area east of the Coloradao Rocky Mountains using Doppler radar and mesonet data. In contrast to Purdom and Marcus (1982) assertion that arc cloud lines are almost never detected by radar, Wilson and Shreiber found that 79% of the storms initiated in close proximity to radar-observed boundary layer convergence lines. Moreover, 95% of the most intense storms (>60 dBZ) were located within 10-20 km of convergence lines. Indeed, earlier studies by Foote and Fankhauser (1973), Wilson and Carbone (1984), Szoke et al. (1985) and Schreiber (1986) along with Boyd (1965) and others, have illustrated the role of radar-observed convergence lines in initiating deep convection. In general agreement with Purdom (1976) and Purdom and Marcus (1982), Wilson and Schreiber found that colliding convergence lines initiated or enhanced existing convection in 71% of their cases. Many of these convergence lines were observed in radar clear-air return, in the absence of clouds. The origin of many of the boundaries in their study were from convectively-generated storm outflows. Other boundaries formed due to topography and differential heating. Fig. 1.3 shows a time series of radar reflectivity images illustrating the collision of locally-generated boundaries (reflectivity thin lines) and the subsequent precipitation echoes associated with the storms that were initiated by the collision (see Wilson and Roesli, 1985).

Convergence lines can persist for considerable time in the boundary layer with no detectable

clouds located above them. This often occurs with stationary boundaries caused by topography variations, stalled mesoscale air masses or boundaries arising from differential heating. The Denver Convergence and Vorticity Zone (DCVZ), a terrain-induced flow regime in Colorado, has been observed to persist for several hours before cumulus development and intense convection is observed (Szoke et al. 1984; Roberts and Wilson, 1995). Studies have shown that these stationary

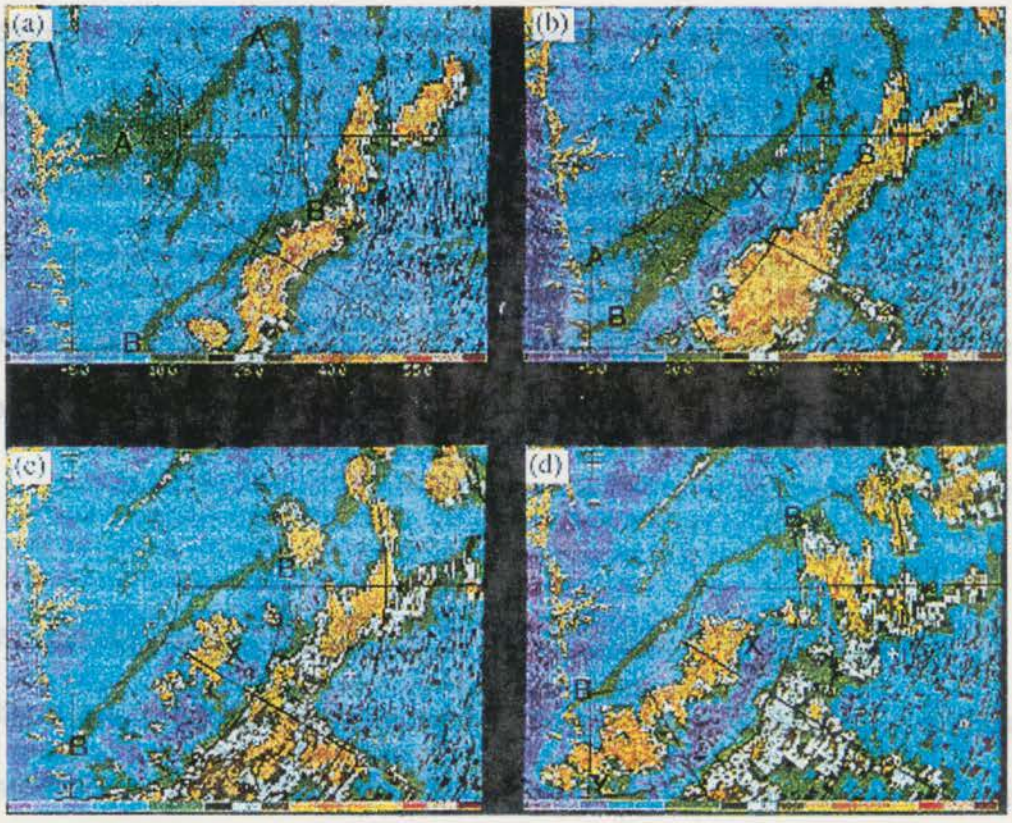

Fig. 1.3. S-band reflectivity images over Colorado at (a) 2226, (b) 2252, (c) 2323, and (d) 2340 UTC on 25 July 1984, showing two outflow boundaries AA and BB meeting at X; a new convective line XY forms. Range rings are at 20 km intervals. Values in dBZ. (from Wilson and Roesli, 1985)

boundaries act to create zones of deep moisture.

A stationary convergence line that persisted in eastern Colorado on 17 July 1987 for seven hours was examined through the use of the Clark numerical cloud model (Lee et al. 1991). Cumulus clouds developed slowly above the convergence region, eventually producing an intense line of 65 dBZ storms. A series of sensitivity studies were performed to examine the reaction of simulated convection to variations in boundary layer moisture, boundary layer convergence and vertical wind shear above the boundary. Lee et al. found that a 1 g/kg increase in surface moisture (added over the domain of the convergence line) acted to increase the intensity of convection and allowed easier penetration of the dry layer between 2 and 4 km AGL resulting in convection starting several minutes earlier. Adding more moisture to either the east side of the convergence line or the west side did not change the intensity of convection but affected the timing of the rapid storm development stage.

By decreasing the model winds by 2 m/s on both sides of the convergence zone, and thereby decreasing the strength of the convergence zone, (Lee et al. 1991) found that the initiation of convection was delayed in the model, but the intensity of the convection was much stronger. They attributed this to weaker convergence that slowed the dynamic forcing of the updraft but allowed more moisture to accumulate along the boundary, so that once the ML capping inversion was penetrated, there was more moisture available to produce more intense convection. Finally, changing the vertical wind shear in the boundary layer by reducing the magnitude of the horizontal vorticity on one side of the boundary, resulted in changes in both the intensity of convection, location/tilt of convection and vertical depth of the storms. This latter result is consistent with the study by

Rotunno et al. (1988) that is discussed in the following paragraph.

As shown first by Thorpe et al. (1982) in their 2-D model and then by Rotunno et al. (1988) in their 3-D model simulations and their review of selected squall line case studies, different types of convection can result depending upon the low-level shear profile and the strength of a rain-produced cold pool. The main results of the Rotunno et al. 3-D simulations were shown schematically in their Fig. 18 (here Fig. 1.4), illustrating that a cold pool in the absence of low-level shear (Fig. 1.4b), will produce an updraft and convection that is directed rearward over the cold pool. Depending on the initial intensity of convection and mesoscale processes involved, hours of stratiform type precipitation may persist over the cold pool. Under condition of low-level shear, but no initial cold pool, the updrafts and initial convection will lean downshear. If a rotating thunderstorm (e.g. a supercell) is initiated by the shear, the storm will be long-lived. Otherwise, the typical thunderstorm produced is more representative of cumulus convection (Fig. 1.4c) which after its initial pulse, will dissipate due to rain falling into the updraft flow or as a consequence of the shear itself. In the optimal situation for long-lived, self-sustaining convection, as is typically observed with squall lines, the presence of a cold outflow pool balanced by favorably oriented, low-level shear will lead to a more vertically upright updraft and deeper convection (Fig. 1.4d). That is, if the negative horizontal vorticity associated with the cold pool approximately balances the positive horizontal vorticity associated with the low-level shear, then sustained, deep lifting will be produced. When the convective cells produce precipitation, the resulting cold pool will trigger new convection where it encounters the strongest low-level shear (downshear of existing convection).

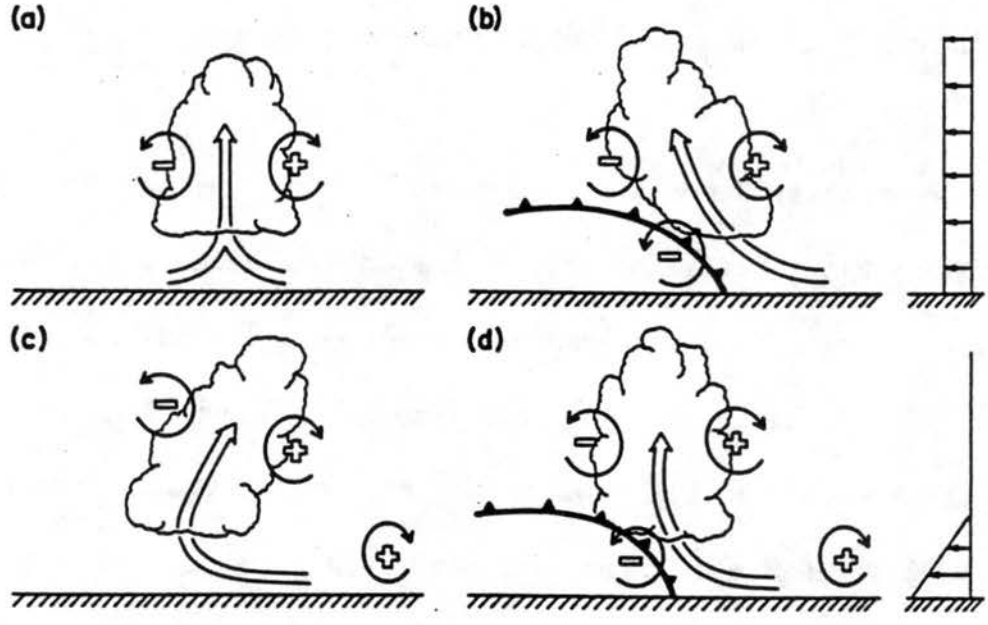

Fig. 1.4. Schematic diagram showing how a buoyant updraft may be influenced by wind shear and/or a cold pool. (a) With no shear and no cold pool, the axis of the updraft produced by the thermally created, symmetric vorticity distribution is vertical. (b) With a cold pool, the distribution is biased by the negative vorticity of the underlying cold pool and causes the updraft to lean upshear. (c) With shear, the distribution is biased toward positive vorticity and this causes the updraft to lean back over the cold pool. (d) With both a cold pool and shear, the two effects may negate each other, and allow an erect updraft. (from Rotunno et al., 1988)

Wilson et al. (1992) used both multi-sensor observations and 3-D simulations using the Clark numerical cloud model to address the initiation of thunderstorms along the 17 July, quasi-stationary boundary. They found that the primary effect of the long-lived convergence zone was in concentrating and deepening the moisture in the mixed layer, rather than directly causing the vertical motions associated with convective initiation. The timing of convection was found to be quite dependent on the tilt of the updrafts along the convergence zone and also sensitive to the depth of the convergence line circulation. As the shear profiles on both sides of the convergence zone became more balanced, the updraft was observed to become more erect (as shown in Fig. 1.5) and

the convergence deeper. This is complementary to the theoretical results of Rotunno et al. (1988) except that baroclinic production of horizontal vorticity was not considered a factor in this case. A key factor influencing the location of storm development was the presence of boundary layer horizontal rolls. Storms were triggered where the horizontal rolls intersected the stationary convergence zone (as can be seen in the the time series plots in Fig 1.6). Model simulations indicated

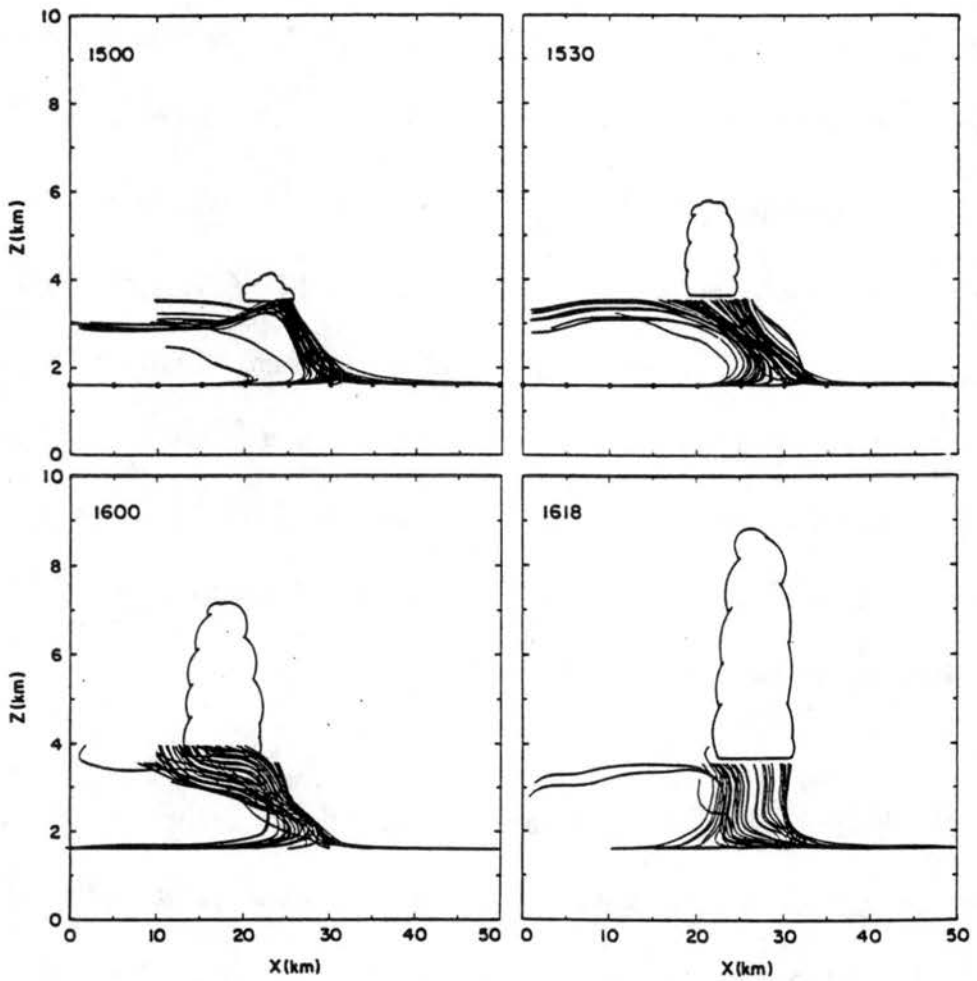

Fig. 1.5. East-west vertical projection of TREC-based streamlines for (a) 1500, (b) 1530, (c) 1600, and (d) 1618. Heights (Z) are MSL; the surface elevation is ~1.6 km. The cloud base and top are based on the observed larger clouds as determined by photogrammetry; the cloud widths are intended for schematic representation only. (from Wilson et al. 1992)

that the horizontal rolls acted to increase the convergence at the intersection points and thereby the strength of the existing updraft, rather than cause the formation of new updrafts (i.e., through vertical tilting of horizontal vorticity). Similar interactions between pre-existing convergence lines and horizontal roll vortices have been modelled by Crook et al. (1991).

Horizontal rolls have been observed to set up in the CBL under conditions of weak wind, modest vertical wind shear and surface heating. Rolls tend to align with the mean wind (LeMone, 1973), require very little shear (2×10^{-3} s^{-1}) within the CBL (Weckwerth et al. 1997) and can often be detected by Doppler radar (Kropfli and Kohn, 1978; Christian and Wakimoto, 1989; Weckwerth et al. 1997). Provided there is sufficient moisture, clouds can form above these rolls (Kelly, 1982; Christian and Wakimoto, 1989; Fankhauser et al. 1995). Extensive streets of cumulus clouds observed from aircraft (Plank, 1960; LeMone, 1973; LeMone and Pennell, 1976), ground-based observations (Malkus and Riehl, 1964) and by satellite are believed to be associated with horizontal boundary layer rolls.

Christian and Wakimoto (1989) found that radar thin line echoes associated with horizontal rolls were aligned directly beneath cloud streets whose locations were determined photogrammetrically. Aircraft data collected on three specific days during the CaPE experiment in Florida provided further evidence that the updrafts encountered by the aircraft corresponded to the reflectivity thin lines associated with horizontal rolls in the boundary layer (Weckwerth et al. 1996). In addition, Weckwerth et al. (1996) showed that the location of the updrafts and enhanced reflectivity lines agreed well with the maximum mixing ratio values at all levels of the CBL. Figure 1.7 (their Fig. 6) illustrates the agreement. A comparison of two nearly simultaneous sound-

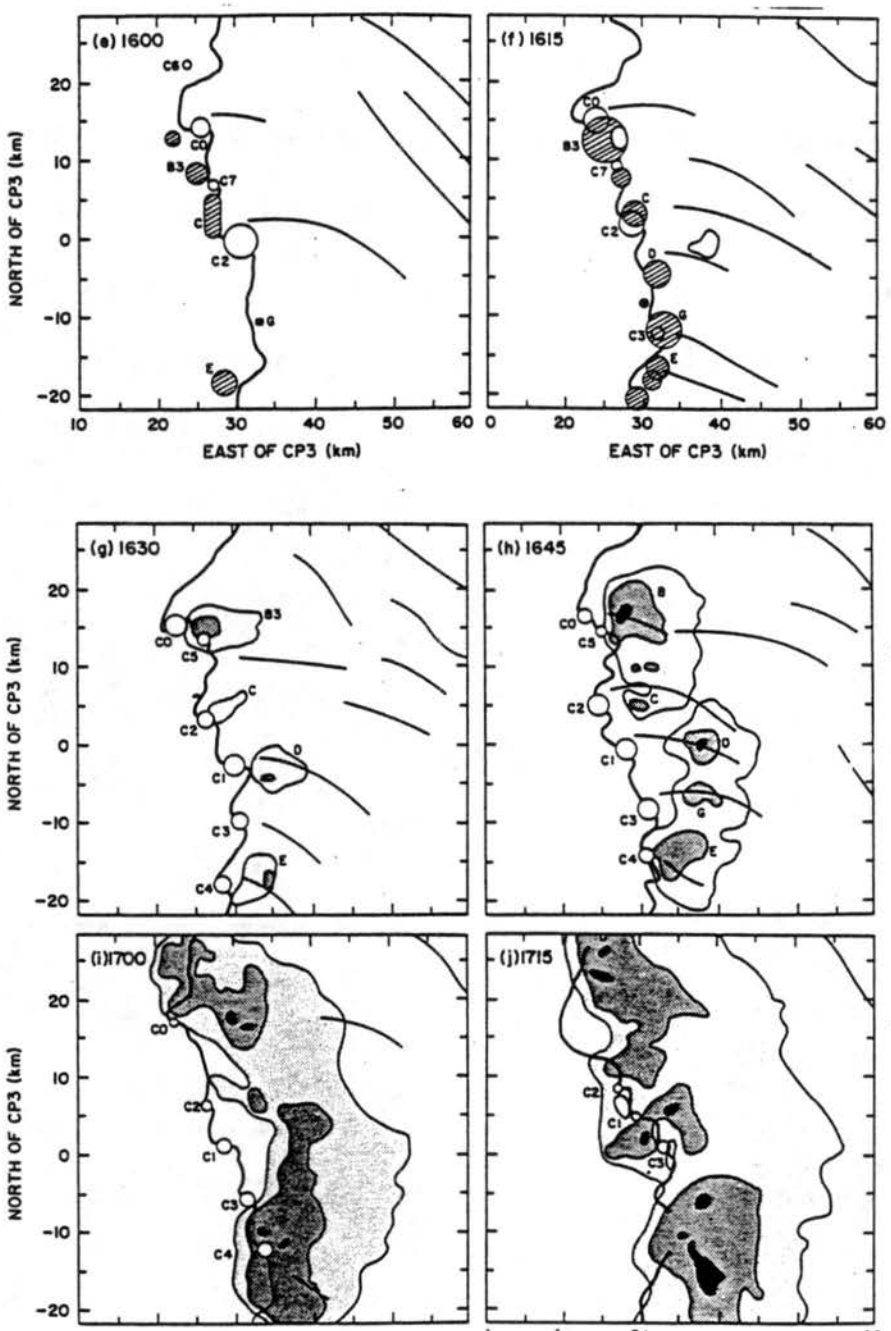

Fig. 1.6. Relative location of convergence line (heavy solid line), horizontal rolls (light solid lines), misocyclones (labeled open circles beginning with letter C), clouds (cross-hatched features in panels (e) and (f)), and precipitation echo at 6.5 km MSL (panels (f) - (k); contours are 10, 30, 50 dBZ). Times shown are 1600 - 1730 MDT. (from Wilson et al. 1992)

ings, one collected within the updraft axes between two rolls and the other within a roll showed the sounding within the updraft branch contained 1. 5 g/kg more moisture throughout the CBL. A comparison of the aircraft and radar data with analyses of cloud base and height determined from both soundings and photogrammetric analyses of clouds was also performed. Weckwerth et al. found that the clouds at the observed heights could only have formed from the air parcels containing the relatively high mixing ratio values that were observed within the roll updraft regions. Specifically, the mixing ratio values necessary to produce the observed cloud bases were close to

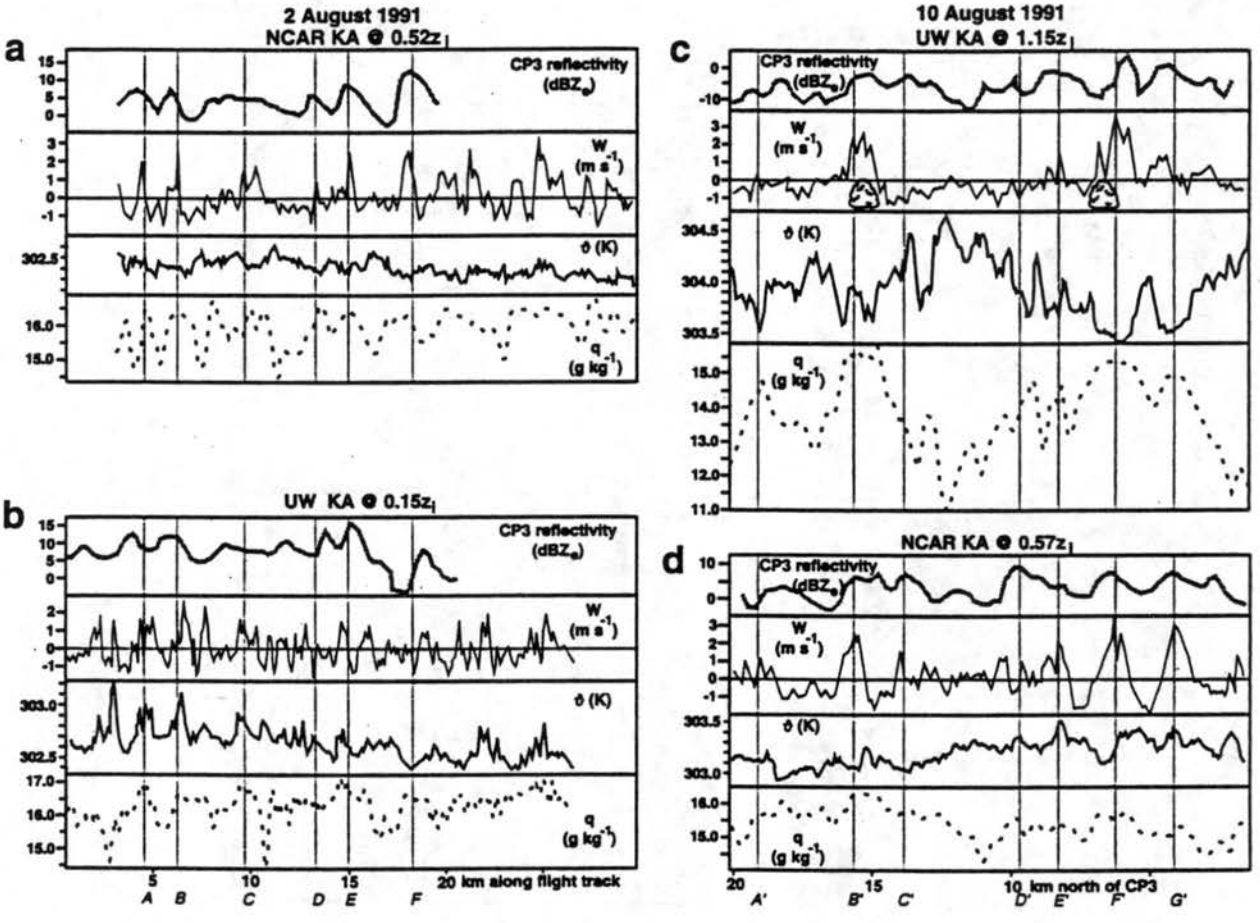

Fig. 1.7. Interpolated CP3 reflectivity (dBZ; gray line) and time series of aircraft-measured vertical velocity (m/s; thin solid line), potential temperature (K; thick solid line), and mixing ratio (g/kg; dashed line). Data from the (a) NCAR King Air at 0.52zi, (b) UW King Air at 0.15zi on 2 August, (c) UW King Air at 1.15zi, and (d) NCAR King Air at 0.57zi on 10 August are shown. Letters correspond with locations of reflectivity maxima along the flight tracks. Schematic clouds in (c) indicate times of cloud penetrations. (from Weckwerth et al. 1996)

the surface mixing ratio values within the updraft branches of the rolls. The results of Weckwerth et al. are complementary to an earlier study by Fankhauser and Wade (1982) who determined from aircraft measurements of the northeastern Colorado CBL that the average value of moisture in the lowest 50-mb layer was usually a good estimate of the moisture content to be found in updrafts at cloud base.

A summary of the results in Weckwerth et al. (1996) in schematic form, shown in Fig. 1.8, depicts the various cloud bases and heights that would result above specific locations of the roll

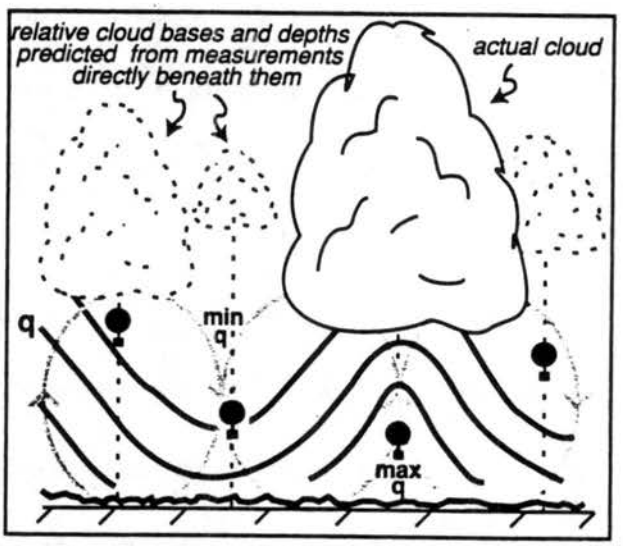

Fig. 1.8. Schematic diagram summarizing results. Gray lines indicate roll circulations. Thick black lines are contours of moisture with the maxima existing within the roll updraft regions. Actual cloud base and depth are shown by the solid cloud. Dashed clouds represent relative cloud bases and depths expected if stability parameters were estimated from CBL moisture values directly beneath those clouds. (from Weckwerth et al. 1996)

vortex circulations, given the moisture profiles observed at those locations. The implication for forecasters is to recognize that the moisture profiles within the CBL can be quite variable due to the thermally-induced, horizontal roll circulations and that sounding moisture profiles may not be

representative of the convection that is actually produced, if the sounding is not released in the updraft branch of a roll. Additionally, the moisture that feeds the clouds is associated with the maximum moisture concentration observed in the lowest levels of the boundary layer along the convergence between roll circulations. Forecasters could use these near surface maxima to adjust the sounding mixing ratio values as necessary to assess convective potential.

Applying 2-D wavelet transformations to both the reflectivity and radial velocity convergence fields, Fankhauser et al. (1995) were able to confirm that enhanced reflectivity bands coincided with the convergence zones between axes of roll vortex pairs. However, in the Florida case they examined, using both radar, aircraft and mesonet information, they did not always see a one-to-one correspondence between updraft maxima and radar thin line structures, as was reported by Weckwerth et al. (1996). In addition, they found little evidence of high correlation between updrafts and temperature and moisture parameters. They postulated that convective plumes of much larger aspect ratios, evolving from an afternoon of convective heating, may have begun to dominate over the horizontal roll structures. It should be noted that their aircraft data was collected at a height of 900 m, close to the stable layer. In the Weckwerth et al. (1996) study, two aircraft were used to collect data at four different heights in the CBL.

Initiation of convection can also result from what is sometimes referred to as "dry" atmospheric mesoscale circulations. These circulations set up under conditions of differential heating over land, as in regions of irrigated land adjacent to dry land or in areas with variable soil moisture caused by heavy, sporadic precipitation from a previous day (Pielke and Segal, 1986; Segal et al, 1989). However, Segal et al. (1989) found that while significant changes in moisture, temperature

and wind can be observed from dry to irrigated regions, synoptic flow and flow associated with gradients in terrain often mask the mesoscale circulations that set up. Thus they were unable to assess whether the mesoscale circulation alone was of sufficient intensity or large enough in horizontal scale to initiate convection.

The sea breeze and drylines are also manifestations of mesoscale circulations caused by horizontal temperature gradients. Numerous studies have documented the onset, structure and evolution of sea breezes and the convection observed with them (Plank, 1960; Estoque, 1962; Simpson, 1967; Pielke, 1974; Purdom, 1976; Simpson et al. 1980; Zhong and Takle, 1992 among others). Of interest here are some recent studies examining the interaction of the sea breeze front with horizontal rolls (Wakimoto and Atkins, 1994; Fankhauser et al. 1995; Atkins et al. 1995) and horizontal roll interaction with a dryline over the Texas Panhandle (Atkins et al. 1997). These studies showed that the thermodynamic variability observed along the leading edge of a sea breeze front or dryline were caused by horizontal roll vortices out ahead of the front intersecting or merging with the front. Atkins et al. (1995) examined dual-Doppler data to show that at these intersection points, the helical pairs of clockwise and counter-clockwise roll vortices were tilted upward by the sea breeze front. The portion of the roll pair that was rotating clockwise, when tilted upward, gave rise to positive vertical vorticity that in turn, resulted in deeper updrafts and were the preferred locations for clouds to form. The counter-clockwise portion of the helical pair, when tilted, produced negative vertical vorticity and was less likely to produce clouds. The periodicity of cloud development along the sea breeze front was attributed in part to the contribution to vertical motions created by these alternating sequence of lifted vortex pairs. Similar results were observed by Atkins et al. (1997) in examination of the dryline using WSR-88D radar and aircraft

data. Maxima in reflectivity and vertical velocity were observed at the intersection of the horizontal rolls and the dryline. Clouds were initiated at these intersection points. The dryline circulation was believed to be similar to a sea breeze circulation, exhibiting similar kinematic and thermodynamic characteristics.

The case studied by Fankhauser et al. (1995) examined how deep convection occurred over the Florida peninsula as east and west coast sea breezes approached each other, interacted with intervening horizontal roll circulations, and eventually collided. In contrast to the Atkins et al. (1995) results, they found that as the westward-moving, east coast sea breeze front encountered horizontal rolls, no significant convection occurred above the sea breeze front, even given enhanced vertical motions and relative moisture maxima at the intersection points. Closer inspection of the data showed that the sea breeze air lifted from the surface had to overcome negatively buoyant air to reach the LFC. Also, the vertical wind profiles on both sides of the sea breeze front were not favorable for producing vertically erect updrafts and deep convection as discussed by Thorpe et al. (1982) and Rotunno et al. (1998). The west coast sea breeze, as it propagated to the east, was modified by the outflows from several waves of convection that formed above it, and behaved as a large gust front. Its interaction with the horizontal rolls was different fromt that observed with the east-coast sea breeze. Clouds were observed ahead of the gust front along the convergence axes between the horizontal roll pairs. As the gust front encountered these rolls (oriented essentially parallel to the gust front) and passed beneath the convection, storms were observed to reach their maximum intensity produced by the enhanced convergence and updraft. A similar scenario of convection and intensification was observed by Kingsmill (1993) in association with the west coast density current, and by Kessinger and Mueller (1991) as moving

boundaries intersected horizontal rolls. Major storms resulted when the two coastal fronts collided. However, prior to this collision, storms erupted along an intermediate convergence line between the two fronts. Figure 1.9 shows a schematic of how this intermediate convergence line evolved following an afternoon of heating characterized by horizontal convective rolls. As the afternoon heating decreased, the 1-2 deg K of cooling at the top of the boundary layer disappeared and the large scale ascent observed over the peninsula collapsed to produce one narrow, stationary convergence zone and updraft.

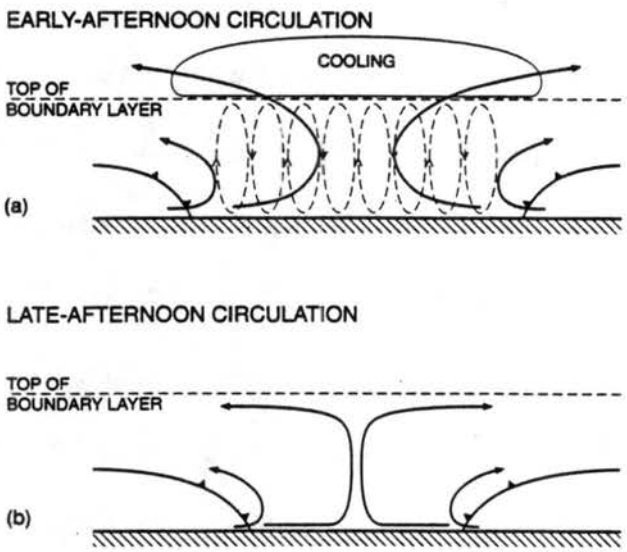

Fig. 1.9. Schematic representation of the low-level circulations across the central Florida penisula on 2 August. The upper panel (a) shows the three major circulations that exist in the early afternoon: the coastline wind surges (equivalent to sea-breeze fronts), the large-scale convergence between the wind surges (substantiated by the cooling aloft), and the convective rolls. Later in the afternoon (b) when the surface heating decreases, the convective rolls decay and the large-scale convergence collapses to produce a single narrow intermediate updraft. (from Fankhauser et al. 1995)

1.3 Environmental winds

Although the presence of a stationary or moving boundary increases the likelihood that convection will occur, it does not guarantee it. The variability of boundary layer moisture and temperature has been shown to play a significant role in the occurrence, timing and intensity of convection, as discussed above. If boundary layer moisture is confined to a very shallow layer close to the ground, it can be very difficult for a gust front to provide enough lift for the moist air parcels to reach the LFC and trigger cumulus cloud development (Foote, 1984). The strength of the environmental winds at the top of the ML can also be a factor in inhibiting cumulus development. Crook et al. (1996) have shown numerically that as parcels rise above a convergence line, environmental winds at the top of the boundary layer are forced to rise over the upward protuding air, setting off gravity waves in the stratified layer at the top of the ML. The bulge of protuding air gets displaced downwind, with the net effect of decreasing the depth of lifting in the boundary layer. As the environmental winds at the top of the ML get stronger, the depth of lifting is further decreased, ultimately affecting plume penetration above the negatively buoyant, stable layer.

Numerous studies have shown how the environmental wind shear and buoyancy contribute to the formation and persistence of storms (Rotunno et al. 1988) and influence the structure and evolution of storm systems that range from multicellular to squall lines (Moncrieff and Miller, 1976; Houze, 1977; Bluestein and Jain, 1985; Smull and Houze, 1985; Rotunno et al. 1988; Braun and Houze, 1997) to supercellular (Browning, 1964; Wilhelmson and Klemp, 1983; Weisman and Klemp, 1984). In Florida, thunderstorm development was found to be most favorable when the low level wind was oriented in a direction opposite to the inland movement of the sea breeze (Pur-

dom, 1976; Wakimoto and Atkins, 1994). Wilson and Megenhardt (1997) showed that the environmental winds were generally westerly near the top of the east coast sea breeze and at the storm steering level, opposite in direction to the sea breeze movement. This wind profile had two effects on storm formation and evolution. One effect was that the low-level wind shear normal to the sea breeze was small and was unable to balance the intensity of the convergence produced by the sea breeze outflow. Thus, weak, tilted updrafts resulted and produced generally shallow convection. Secondly, because of the westerly steering winds, storms that formed above the east coast sea breeze moved quickly away from the sea breeze convergence boundary and dissipated. This contrasted with a more favorable scenario over the west coast sea breeze when storms moved in the same direction as the sea breeze front. A self-sustaining mechanism for continually generating new convection resulted. Storms moving with the front produced outflows that modified and strengthened the baroclinicity and convergence along the front which in turn enhanced new storm initiation, evolution, mergers, and outflows.

1.4 Operational thunderstorm forecasting

Purdom (1976, 1982) has shown in his landmark studies that a forecaster can monitor satellite-observed, mesoscale arc cloud lines and forecast intense thunderstorms when the arc lines collide. Wilson and Carbone (1984) and Wilson and Schrieber (1986) demonstrated that a forecaster could track and monitor convergence boundaries using single Doppler radar for the purpose of forecasting thunderstorm initiation, even when clouds were absent above the boundaries. However, monitoring surface convergence boundaries alone does not provide information on the timing and location of convection (Wilson and Mueller, 1993). As mentioned above, other factors

such as boundary layer moisture, temperature, vertical wind shear, and atmospheric instability in the form of large CAPE and low CIN govern when and where convection will occur.

To issue the best possible forecast of thunderstorm initiation, a forecaster needs access to the highest resolution datasets available. Most NWS WFO offices have access to some but not all of the sensors used in research experiments, and data sampling of sounding and mesonet information in particular, is operationally much less frequent and not representative for all forecast zones. In addition, for a forecaster to monitor and analyze several different datasets for the purpose of making very short-range, time and place specific forecasts of thunderstorms can be very labor intensive and really requires the aid of computer processing (Browning and Collier, 1982; Wilson and Carbone, 1984; Wilson and Mueller, 1993; Wilson et al. 1997).

Browning and Collier (1982) discussed the process of making very short range forecasts using an integrated radar-satellite nowcasting system. Their system, called FRONTIERS and later NIMROD (Collier, 1991), is a man-computer mix tailored for forecasting surface precipitation intensity. This system makes use of satellite IR radiance values for determining cloud heights and VIS brightness values as a measure of cloud thickness in conjunction with radar reflectivity (Lovejoy and Austin, 1979) to forecast precipitation areas spanning the synoptic scale. Others (Scofield and Oliver, 1977; Griffith et al. 1978; Scofield, 1987) use cloud history information in addition to the above satellite-derived information, to improve rainfall estimation. Radar and satellite IR imagery have also been used together to assess a thunderstorm's intensity and severity (e.g., Negri and Adler, 1981; Reynolds and Smith, 1979; Green and Parker, 1983) by comparing satellite-derived information on cloud top mean vertical growth rates, cloud top temperature, and

anvil expansion rates with radar reflectivity information and change in radar echo volumetric properties with time (Scofield and Purdom, 1986). All of the afore-mentioned techniques have been applied to pre-existing storms, not to the initiation of thunderstorms.

Providing nowcasts (< 60 min forecasts) of thunderstorm initiation, movement, evolution and dissipation is indeed a labor- intensive task for a forecaster. To counter this, two systems are being developed and tested that provide site-specific, automated nowcasts of thunderstorms. A procedure known as GANDOLF (Generating Advanced Nowcasts for Deployment in Operational Land surface Flood forecasting), developed by the UK Met. Office, is run in parallel with NIMROD. The purpose of GANDOLF is to provide nowcasts of heavy rain events by tracking the initiation and development of thunderstorms. The system is based on extrapolation techniques and object-oriented code that uses radar and satellite imagery to identify the stage of development of convective cells (Collier and Lilley, 1994; Hand, 1996). Specifically, satellite IR temperatures are used to determine cloud top height and combined with radar reflectivity information to characterize storm type (Hand, 1996). In addition, Collier and Lilley (1994) state that changes in cloud top temperatures can be good indicators of convective development and cited examples that showed that the start of decrease in IR cloud top temperatures preceded the increase in maximum rainfall rate by 1-2 hrs. Detection of boundary layer convergence lines are not a component of this system.

A second automated thunderstorm nowcasting system, developed by NCAR, uses a set of rules developed by Wilson and Mueller (1993) for different forecasting scenarios (e.g., rules that govern thunderstorm initiation by a boundary, cell intensification by a boundary, cell extrapolation, initiation by boundary collision and storm growth under favorable boundary-relative, steer-

ing flow). Radar, soundings, satellite, mesonet and numerical cloud model simulations are the data sources for this system. Based on two years of nowcasting exercises using predominantly radar data and visual observations of clouds, Wilson and Mueller (1993) found that the likelihood for a surface convergence boundary to initiate new storms was increased if cumulus clouds were observed above or ahead of the boundary. In the absence of high frequency mesonet and sounding information, observation of cumulus clouds was often the only indicator of a locally well-mixed, moist boundary layer. However, it is not practical for a forecaster to constantly make visual sightings of clouds. Wilson and Mueller did not consider satellites a feasible tool for cloud detection since the GOES-7 satellite had update rates of 30 min (too long a period for monitoring cumulus cloud development) and frequent registration errors. Instead, they proposed using a very sensitive 10 cm radar to map cumulus cloud locations.

Radars can detect precipitation clouds (cumulus congestus) in the early stages of echo development when reflectivities are as low as 10 dBZ (Henry and Wilson, 1993). Using 10, 5 and 3 cm wavelength research radars, Knight and Miller (1993a,b, also conf. on cloud physics) have shown that research radars (with gate spacings of 150 m) are capable of detecting the first radar echo (< 10 dBZ) return arising from the index-of-refraction variations (Bragg scattering) along the edges and tops of cumulus clouds. However, it is not clear that an operational WSR-88D radar will be able to routinely detect Bragg-scatter echo and ultimately, individual cumulus clouds due to the 1 km gate spacing of the reflectivity field.

1.5 Objectives of this study

The focus of this thesis is to show how operational WSR-88D radar and GOES-8 satellite data can be used together to provide information on the growth of cumulus clouds into thunderstorms, by monitoring cloud-top brightness temperatures, radar-detected, boundary layer convergence features, and changes in reflectivity echo intensity with time. When available, sounding and meso-net data are also examined to characterize the environment. The presence of cumulus clouds above radar-detected, surface convergence boundaries increases the likelihood that thunderstorms could develop, given an unstable or conditionally unstable environment. Thus, being able to detect and monitor cumulus cloud growth is an important component in providing automated forecasts of convection initiation. This study will also examine the ability of the WSR-88D radar to detect echo caused by Bragg scattering. Several hours of radar and satellite data from Denver, Colorado are analyzed from four different days during the summer of 1995. The pattern of cumulus cloud growth above both moving and stationary boundaries, above horizontal boundary layer rolls and in regions where there were no well-organized, boundary layer convergence lines detectable by radar are documented to examine their roles in convective initiation.

This study is unique in a few respects. With the improved data resolution, sharper imagery, and more frequent (15 min) update rates of the GOES-8/9 satellites, it is now possible to examine the evolution of cumulus cloud development more closely than was possible prior to this study. The studies cited above used combined radar and satellite information to forecast precipitation and intensity and severe weather potential, but did not address monitoring these datasets for thunderstorm initiation. Hence, this is the first study where satellite and radar data have been com-

bined specifically for the purpose of studying cumulus cloud growth. While several of the above studies had examined the location of cumulus clouds relative to radar-detected horizontal rolls using photogrammetry and aircraft data, this is the first time that satellite and radar have been used together to document the location of cumulus clouds relative to surface boundary layer features. This is possible because of minimal errors (<4 km) in registration of the GOES-8/9 satellites.

The goals of this thesis are threefold.

1. To determine the boundary layer convergence features that are associated with the more intense cloud growth and thunderstorm development.
2. To determine the contribution of the 15 min satellite IR data in increasing our knowledge of when and where thunderstorms will form.
3. To evaluate how WSR-88D radar and GOES-8 satellite information can best be utilized to extend the lead time in issuing time and space-specific forecasts of thunderstorms.

Chapter 2

DATA PROCESSING AND ANALYSIS TECHNIQUES

2.1 Radar data

The radar data used in this study is the Archive Level II data collected by the Denver WSR-88D S-band (10 cm wavelength) radar located approximately 20 km to the southeast of the Denver International Airport (DIA) and 60 km to the east of the Colorado Front Range. While the radar actually transmits and receives pulse volumes having gate spacing of 250 m, level II data is only archived at 1 km reflectivity and 250 m radial velocity gate spacing. For the cases shown here, the radar scanned in precipitation mode (VCP-21) which is a 6 min scan composed of eleven 360 deg surveillance sweeps ranging from 0.5 to 19.5 deg in elevation. At 30 km range from the radar, the vertical distance between beams varies from 0.5 to 0.7 km in the lowest scans, to vertical distances of 1.9 to 2.7 km between the higher scans. The radar has a 0.95 deg half-power beamwidth (Crum et al. 1993) which translates to an azimuthal resolution of 500 m at a range of 30 km from the radar. Updated estimates of half-power beamwidth using an INCO 1994 beamwidth formula, show the beamwidth to be closer to 0.91 for a 2.8 GHz NEXRAD radar (Pratt and Ferraro, 1995) as can be seen in Fig. 2.1. An azimuthal resolution of 480 m at 30 km range is computed when using this beamwidth. Table 1 is an updated list of the WSR-88D technical parameters (Pratt and Ferraro, 1995) published originally in the Federal Meteorological Handbook (FMH-11, 199).

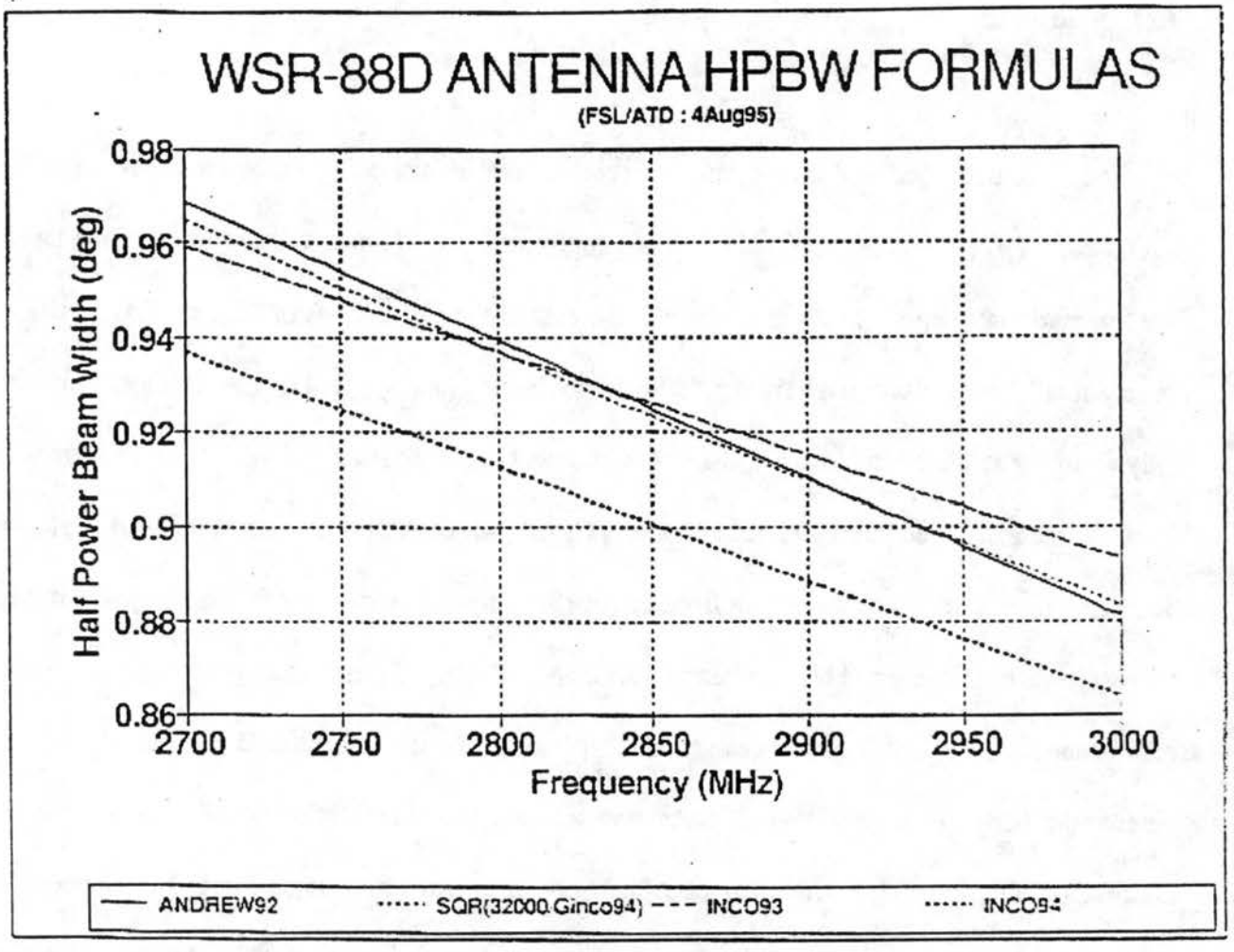

Figure 2.1. WSR-88D half power beamwidth in degrees as a function of radio frequency in megahertz according to four formulas: (a) Andrew Corporation data in Sirmans (1992); (b) the rule of thumb SQRT (32000/G), where G is from the INCO 1994 gain formula; (c) the INCO 1993 beamwidth formula; (d) the INCO 1994 beamwidth formula. (from Pratt and Ferraro, 1995)

Table 1. WSR-88D Technical Parameters, as updated from FMH-11 (NOAA)

Antenna Subsystem	
Radome	Rigid fiber glass
Diameter	39 ft (12 meters)
RF loss - two way	0.3 dB
Pedestal	Elevation over azimuth
Azimuth rates fast scan	18.7 to 25.7°/s (VcP 11)
Azimuth rates medium scan	11.3 to 14.4°/s (VcP 21)
Azimuth rates slow scan	5.0 to 5.1°/s (VcP 31)
Acceleration - maximum	15°/s/s
Mechanical limits	-1° to +60° elevation
Antenna	Paraboloid of revolution
Polarization	Linear horizontal
Reflector diameter	28 ft (8.5 meters)
Gain (at 2800 MHz)	45.6 dB
Beam width (at 2800 MHz)	0.91°
First sidelobe level	-29 dB
Transmitter and Receiver Subsystem	
Transmitter	
Frequency range	2700 MHz to 3000 MHz
Peak power	750 kW
Pulse widths, 6dB	1.57μs and 4.71μs
RF duty cycle	0.002 maximum
PRFs short pulse	318 Hz to 1304 Hz
PRFs long pulse	318 Hz to 452 Hz
Receiver	
Linear dynamic range	>96 dB
Noise temperature	>400° K
Intermediate frequency	57.6 MHz
Band width, 3 dB	630 kHz
System phase noise	-54 dBc

Signal Processor Subsystem	
Clutter canceller	5-pole infinite impulse response
Suppression	30 dB to 50 dB
Notch half widths	0 to 4 m/s (0 to 8 knots)
Intensity bias	0 to 10 dB
Minimum usable velocity	0 to 4 m/s (0 to 8 knots)
Range increment (Doppler)	0.25 km (0.13 n mi)
Velocity calculation	Pulse - pair
Velocity estimate fluctuations (nominal)	1 m/s (2 knots)
Number of pulses (Doppler)	40 to 230
Spectrum width calculation	Pulse-pair logarithm
Azimuth increment (Doppler)	1°
Intensity calculation	Linear return power average
Intensity fluctuation estimate (nominal)	1 dB
Number of pulses (surveillance)	16 to 65
Range increment (surveillance)	1 km (0.54 n mi)
Azimuth increment surveillance	1°
Elevation increment	1° to 5°
Ze (0dBSNR, 50 km)	<-11 dBZ
System noise (kTB)	-115 dBm
Base data	Z, V, W threshold on SNR
Communications	ADCCP/T1
Archiving medium	8mm tape SCSI
Time series data	I, Q, encoder angles

Ground clutter contamination was not obtrusive over most of the domain used in this study. NEXRAD radars use by-pass filter maps for removal of ground clutter (FMH-11, 1990). One by-pass filter map is generated for the 0.5 and 1.5 deg scans. A separate by-pass map is generated for the scans above 1.5 deg. During operations, received signals are compared to ground clutter maps. Predefined gates of clutter are removed unless the velocity power spectrum has values larger than zero, indicating signals associated with weather or insects. Ground clutter may still show up in a radar scan in regions of the by-pass filter maps that were defined as no-clutter regions. Clutter appears due to changes in the refractive index profile of the atmosphere during the current operational data collection compared with the atmospheric profile for when the clutter maps were generated. For example, an atmospheric temperature inversion may cause super refraction, with the radar detecting more ground returns in a region than was previously observed when the clutter map was developed. Thus clutter shows up in previously defined, no-clutter gates. Clutter may also show up due to seasonal influences if the by-pass filter maps have not been updated within the past year. The by-pass filter maps remove most of the clutter typically observed close in to the Denver radar and clutter due to the Front Range. There is usually very little clutter contamination at the higher elevation scans, with the exception of ground contamination picked up by the vertical sidelobes. The sidelobe return was minimized by the clutter filter maps. For these reasons, no editing for clutter removal was done on the WSR-88D data.

Thresholding is also done on NEXRAD data prior to level II archival in regions where the SNR is < 5 dB (usually about 3 dB; FMH-11, 1990). System noise for the WSR-88D radars has been determined to be approximately -115 dBm (see Table 1). Using a radar constant of 70, the minimum effective reflectivity for 0 dB SNR is -21.5 dBZ at 15 km range from the radar, -17.0

dBZ at 25 km range, increasing to -11 dBZ at 50 km range, and to -5 dBZ at 100 km range. Thus, at ranges of 10-15 km from the radar, signals lower than about -15 dBZ get removed because their intensity is not 3 dB above the noise level. The sensitivity of the radar to pick up these weak signals is important, especially for detecting Bragg scatter echo along the perimeter of cumulus clouds and detecting clear air return due to insects (Wilson et al. 1994).

2.2 Satellite data

The GOES-8 Visible (0.62 μm; channel 1) and Infrared (10.7 μm; channel 4) imager data at 15 min intervals were used in this study. This geostationary satellite is located 35,800 km above the equator at 75 deg W longitude. This satellite has improved (10 bit) imager resolution in the visible channel and improved signal to noise in the IR channels making it capable of resolving finer detail than its predecessors (Menzel and Purdom, 1994). The satellite oversamples in the E-W direction. At highest resolution (i.e., at satellite subpoint), a VIS pixel (element) is 0.5 km in the E-W direction and 1.0 km in the N-S direction. The corresponding resolution for an IR pixel is 2 km and 4 km. However, the data is usually processed at lower resolution: 1.0 km for the VIS and 4.0 km for the IR, to save on disk space. This is the quoted resolution by Menzel and Purdom (1994) and is listed in Table 2. Moreover, the satellite can now resolve features along the edges of the FOV (Field of View), i.e., beyond 60 deg slant angle (Weiss, 1977) to a greater degree than previously possible (Menzel and Purdom, 1994; Purdom and Menzel, 1995) .

Parallax is still a significant problem when viewing clouds at locations of increasing satellite nadir angles. Weiss (1978) and Rao et al. (1990) illustrate how the apparent cloud location can be

TABLE 2. *GOES*-7 and GOES-I imager characteristics. IGFOV at nadir and SSR are presented in kilometers, and noise-equivalent temperatures for the thermal bands are specified for nominal scene temperatures (300 K for the window bands and 230 K for the water vapor band).

Wavelength (μm)	IGFOV (km) E/W × N/S	SSR (km) E/W × N/S	Noise
GOES-7			
0.55–0.75	0.75 × 0.86	0.75 × 0.86	6-bit data ± 2 counts 3 σ
3.84–4.06	13.8 × 13.8	3.0 × 13.8	0.25 K @ 300 K, 6.00 K @ 230 K
6.40–7.08	13.8 × 13.8	3.0 × 13.8	1.00 K @ 230 K
10.4–12.1	6.9 × 6.9	3.0 × 6.9	0.10 K @ 300 K, 0.20 K @ 230 K
12.5–12.8	13.8 × 13.8	3.0 × 13.8	0.40 K @ 300 K, 0.80 K @ 230 K
GOES-I			
0.52–0.72	1.0 × 1.0	0.57 × 1.0	10-bit data ± 8 counts 3 σ
3.78–4.03	4.0 × 4.0	2.3 × 4.0	0.15 K @ 300 K, 3.50 K @ 230 K
6.47–7.02	8.0 × 8.0	2.3 × 8.0	0.30 K @ 230 K
10.2–11.2	4.0 × 4.0	2.3 × 4.0	0.20 K @ 300 K, 0.40 K @ 230 K
11.5–12.5	4.0 × 4.0	2.3 × 4.0	0.20 K @ 300 K, 0.40 K @ 230 K

significantly displaced from the actual cloud location. Figure 2.2 shows a schematic illustration of this displacement, along with curves representing the magnitude of cloud displacement errors at different locations in the U.S. In eastern Colorado, at a nadir angle of 40 deg, there is approximately a 1 to 1 correspondence in magnitude between the height of a cloud and its horizontal displacement on an image due to the parallax view. This is shown graphically by Johnson et al. (1994) in Fig. 2.3 which shows that for a cloud at any given height, the offset is just the height of the cloud, expressed in any desired units, multiplied by the normalized offset value from the graph. Thus, in Colorado, a cumulonimbus cloud that has a cloud top of 12 km, will have approximately a 12 km horizontal displacement in its location, in a direction away from the satellite. In this study, the focus is primarily on observation of cumulus and cumulus congestus clouds. Cumulus clouds have lifetimes on the order of tens of minutes and lateral and vertical dimensions that are approximately equivalent. Spacing of cumulus clouds depends on the climate and topography of the area. A "typical" cumulus cloud extends from 1-3 km in length (height), depending on the region (midlatitude, subtropical, etc) (Stull, 1984). For cumulus clouds in particular, the horizontal displacement then may vary between 1-3 km. For cumulus congestus clouds, the displacement will be greater.

Estimation of the magnitude of the registration error was determined by using the Visible images and correcting for the offset by comparing *observed* geographical features on the satellite image with their correct latitude and longitude locations as depicted by contour overlays. Of greater concern for this study is the offset in registration between the Visible and Infrared imagery. Examination of highest resolution GOES-8 and GOES-9 data show a shift of approximately 1 pixel (or element) between the VIS and IR images in the E-W direction. Given the slightly

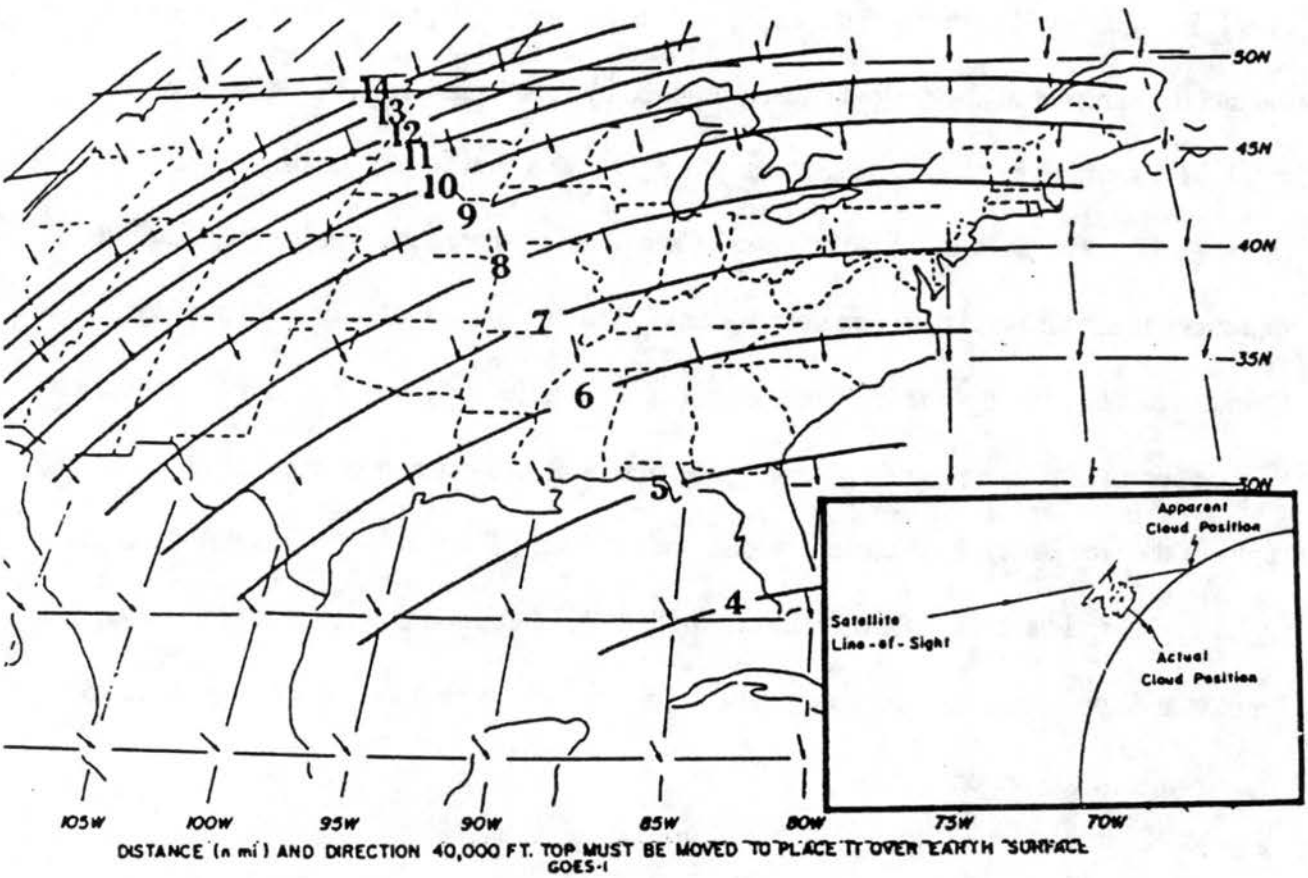

Figure 2.2. Earth location error of tall clouds in GOES imagery. The inset diagram, lower right shows how the apparent cloud position can be significantly different from the actual one for tall clouds located toward the edges of GOES images. The curves are lines of equal displacement error for a satellite at 75 deg W and are labeled in nautical miles. The values are for a cloud top of 12 km (40,000 ft); for 6-km tops subtract 50%, for 18-km tops add 50%. To correct a cloud top position for a given height it should be displaced the appropriate distance toward the satellite subpoint in the direction of the small arrows. (from Weiss, 1978)

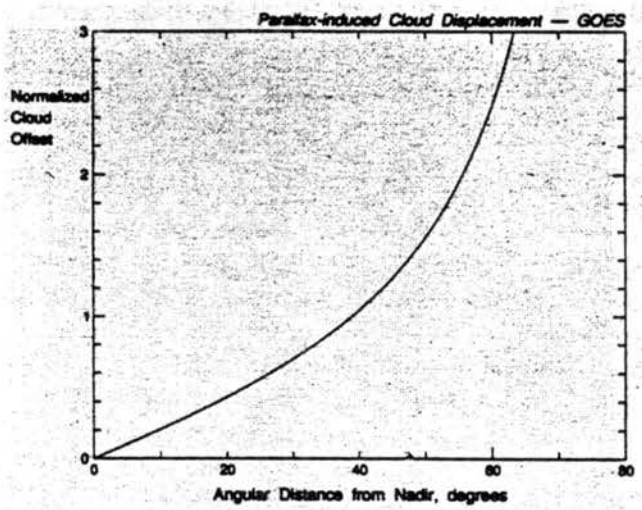

Figure 2.3. Parallax-induced cloud displacement from geostationary orbit, as a function of the angular distance from nadir. The cloud displacement is expressed in terms of its apparent offset from its true position, normalized by the height of the cloud. (from Johnson et al., 1994)

degraded resolution of the data in this study, this shift is a bit greater (1-2 km in the E-W). The cause of this shift, which exists in all GOES-8, 9 datasets, is believed to be related to how the initial upper left starting point of the CONUS scan is defined for all imager channels in terms of line/element and latitude/longitude specifications, given the difference in horizontal resolution between channels (J. Weaver and P. Dills, personal communication). For one 4 x 4 km IR element there exists a set of four 1 x 1 km VIS elements that correspond to the same region. The shift occurs because the upper left point of the first IR line/element is aligned between two VIS elements for the same region. While this shift may not be critical when examining large scale features, such as synoptic scale cyclones, it does cause problems when examining cloud features that have spatial dimensions on the order of the element offset, e.g., cumulus clouds, and when attempting to compare cloud features with radar-detected boundary layer features. Adjustments for this shift have been made using the CEDRIC software package prior to intercomparison of the radar and satellite datasets (section d).

At lower sun angles characteristic of the late afternoon, cloud shadows become more evident, especially associated with towering cumulus and cumulonimbus clouds. The clear sky regions within the shadow of the clouds radiate at cooler temperatures compared to clear sky regions to the east that are still receiving full solar radiation. However, even these shadowed regions radiate at warmer temperatures compared to the cloud emissions. Examination of only an IR image in a shadow region would lead one to interpret that a cloudy region extends further east, composed of lower altitude clouds. Thus the VIS images were used to delineate actual cloud locations in this study and regions for obtaining brightness temperatures.

2.3 Soundings

In addition to the 1200 and 0000 UTC soundings obtained from the Denver NWS during the summer of 1995, CLASS (Cross-Chain Loran Atmospheric Sounding System; Lauritsen et al. 1987) soundings were also released daily at 1700 UTC at the NWS site. The sounding system was housed in a mobile van. Because of its mobility, the van was deployed to various locations east of the Front Range during the summer afternoons, and supplemental soundings were released. Four days of data have been analyzed in this study. The soundings and pertinent information derived from each of the soundings are presented and discussed in section 4.

2.4 Integration of data

The Denver KFTG radar location was used as the center of a 160 x 160 km domain that defined the region of analysis for this study. Radar volumes were examined using a gridded, cartesianized display system called CIDD (Cartesian Integrated Data Display). The CIDD display has the ability to overlay cartesian, color-filled radar imagery directly onto satellite imagery. Use of this display enabled qualitative comparison of cumulus cloud locations with radar-detected convergence lines and Bragg-scatter echoes. To compare these fields quantitatively, the CEDRIC (Custom Editing and Display of Reduced Information in Cartesian space) software package (Mohr et al. 1986) was used.

Prior to running CEDRIC, the radar and satellite data had to be modified for ingest into the CEDRIC code. The NCAR REORDER program was used to interpolate the radar data to a carte-

sian grid using a Cressman weighting technique. The MCIDAS satellite data were written to arrays in ASCI format then converted into MUDRAS format, compatible with CEDRIC, using ingest scripts modified with satellite header information. The large reflectivity gate spacing of 1.0 km dictated that the cartesian grid have a spacing of no less than 1.0 km, which fortuitously corresponded to the spacing of the VIS data. Thus, a horizontal and vertical grid spacing of 1.0 was used for the case studies. Brightness temperature fields were calculated from the channel 4 IR data (in counts) using the following equations:

$$emr = (C - B)/G \tag{1}$$

$$ebbt = c2 \times \upsilon / [\ln(1 + c1 \times \upsilon^3/(emr))] \tag{2}$$

$$tebbt = a + b \times ebbt \tag{3}$$

where *emr* is the effective monochromatic radiance, *ebbt* is the effective blackbody brightness temperature, *tebbt* is the true blackbody brightness temperature, *C* is the satellite counts, *B* and *G* are the bias and gain factors in counts, *c1* and *c2* are Planck function constants, υ is the satellite channel wavenumber, and *a* and *b* are integration-related constants. Because of the 4 km resolution of this channel, the brightness temperature and count fields were data-filled to match the 1.0 km VIS and KFTG reflectivity data. The satellite fields were reproduced at each vertical grid, for ease in comparing this 2-D data with the reflectivity fields at various heights.

Chapter 3

THEORETICAL CONSIDERATIONS FOR RADAR AND SATELLITE REMOTE SENSING

Clouds are composed of numerous transitory cloud drops, ice crystals and precipitation-sized water and ice hydrometeors. Cloud drops typically have radii on the order of 10-50 μm and small terminal velocities compared to precipitation-sized particles; the latter having typical radii on the order of 10-2000 μm and terminal fallspeeds of 1-10 m/s. When scanned by Doppler radar and passively sensed by satellite, different but complementary information about the clouds are obtained as a result of how the hydrometeors absorb, emit and scatter energy back to the sensors. In this chapter, some backround theory is provided on the ability of these sensors to detect cloud and boundary layer features.

3.1 Doppler radar

3.1.1 Sensing precipitating echoes

Weather radars, having wavelengths on the order of 3-10 cm, readily detect precipitation-sized hydrometeors within clouds, but not cloud-sized particles. The weather radars are able to detect the precipitation within the clouds because the raindrops, ice crystals and graupel have particle sizes that allow them to scatter and absorb electromagnetic energy at these wavelengths. The hydrometeors absorb the radiant energy, electric and magnetic dipoles are excited in the dielectric

and as a result, energy is scattered forward, backward, and at various other angles relative to the radiation source. From Mie scattering theory (Mie, 1908; Battan, 1973; Wallace and Hobbs, 1977; Liou, 1980) for spherical particles, scattered electromagnetic energy is a function of the viewing angle, index of refraction (which in turn is dependent on dielectric properties of the material) and the size parameter, χ, defined as $\chi = (2\pi r)/(\lambda)$, where r is the radius of the particle and λ is wavelength. Figure 3.1 illustrates the different types of scattering regimes that are a function of both particle size and wavelength of incident electromagnetic energy. Particles with sizes comparable to the wavelength of radiation, such as hailstones at microwave wavelengths, fall under the Mie regime ($\chi = 0.1$ to 50) and the full Mie equations must be used to determine the full angular-dependent, scattering efficiency. Scatterers, such as raindrops, snow, and ice crystals, with values of $\chi << 1.0$ fall into the Rayleigh regime (see Fig. 3.1). For small χ, the particle is small compared to the wavelength, scattering is insensitive to particle shape, and the Mie scattering equation reduces to a single term for scattering efficiency associated with scattering from the electric dipole term only. This simplified form of scattering is referred to as Rayleigh scattering, which is determined by χ to a first order. A Rayleigh approximation for the backscattering cross section of a single particle is given by Battan (1973) as follows:

$$\sigma_i = \frac{\lambda^2}{\pi}\chi^6\left|\frac{m^2-1}{m^2+2}\right|^2 \tag{3.1}$$

$$= \frac{\pi^5}{\lambda^4}|K|^2 D_i^6 \tag{3.2}$$

where m is the complex index of refraction (m = n - ik), K is the dielectric constant representing

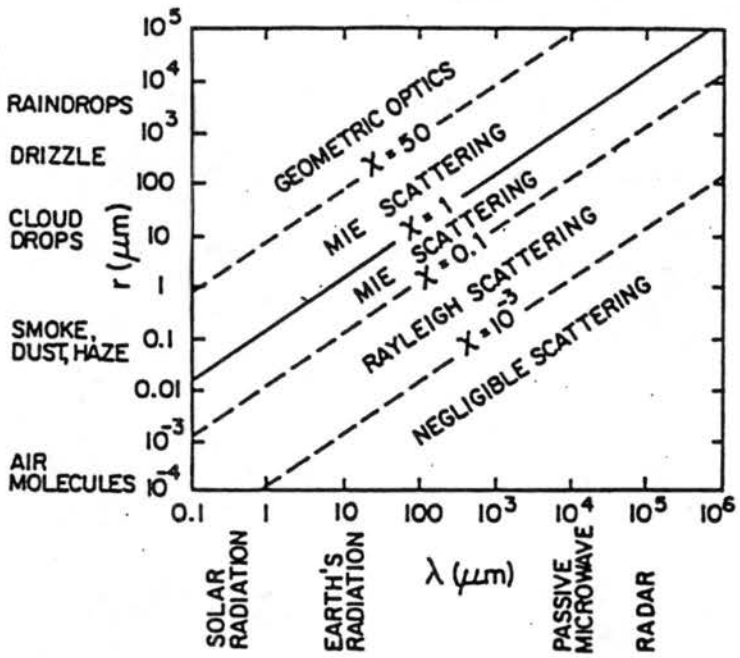

Fig. 3.1. Size parameter χ as a function of wavelength of the incident radiation and particle radius. (Based on Wallace and Hobbs, 1977. From Kidder and Vonder Haar, 1995).

the real part of the relation $(m^2-1)/(m^2+2)$, and D_i is the diameter of the particle. When summed over a volume of space, $\sum_{vol}\sigma_i$ is called the reflectivity, η. Thus,

$$\eta = \sum_{vol}\sigma_i = \frac{\pi^5}{\lambda^4}|K|^2\sum_{vol}D_i^6 \tag{3.3}$$

where $\sum_{vol}D_i^6$ is called the reflectivity factor, Z, to distinguish it from η. Reflectivity factor, Z, provides a measure of the size and concentration of Rayleigh precipitation particles within a resolution volume. It can be computed if the following radar parameters and observables are available. The radar equation for Rayleigh scatterers over a volume of space (i.e., within a pulse volume) is

$$\bar{P}_r = \left(\frac{\pi^3 P_t G^2 \theta\phi h}{16\times 64\lambda^2 \ln 2}\right)\frac{|K|^2}{r^2}\sum_{vol}D_i^6 \tag{3.4}$$

where $\bar{P}_r$ is the received backscattered power, P_t is the transmitted power, G is the antenna gain, θ and ϕ are the horizontal and vertical widths of the beam, *h* is the pulse length and *r*, here, is the range to the target. Some assumption must be made about the hydrometeor types in a storm in order to specify whether to use the dielectric constant for ice or for water. As can be seen, the intensity of Z (in decibels) is directly related to the size and concentration of drops. Values of reflectivity as low as 5-10 dBZ (Knight and Miller, 1993) indicate the presence of precipitation.

3.1.2 Sensing cloud features

Radars are sometimes able to detect backscatter off of very large cloud drops, as implied in Fig.

3.1. However, in general, clouds produce negligible amounts of radar backscatter. Clouds are much better absorbers of microwave radiation. This can be seen by comparing the terms of the Rayleigh absorption cross-section equation below, with the same variables in (3.2). Here, N(r) is

$$\sigma_a = \int_0^\infty \pi r^2 \left(4\chi I_m \left(\frac{m^2 - 1}{m^2 + 1} \right) \right) N(r) dr \qquad (3.5)$$

the number of scatters per unit volume and I_m is the imaginary term. Because σ_a varies with χ while σ_i varies with χ^6 (and more importantly, with λ^{-4}), absorption can quickly dominate over scattering for particles in the Rayleigh regime (Kidder and Vonder Haar, 1995).

It is well known, however, that radars can detect refractive index inhomogeneities in the atmosphere. One of the first studies on the scattering of radiation in inhomogeneous atmospheres was a study by Pekeris (1947). This study described the scattering process in a much broader context than a later study by Bragg who considered only X-ray scattering by crystals (Gossard and Strauch, 1983). It has become the convention over the years, however, to classify all types of backscatter from clear-air refractive index variabilities in the atmosphere as Bragg scattering. Thus, Bragg scattering as it is referred to today, arises when incident radiant energy is scattered as it encounters gradients in temperature and humidity caused by incomplete turbulent mixing of two different types of air. Variability in the composition of clear air can be found along the edges of clouds as drier air mixes with cloudy air, or in the vicinity of stable layers in atmosphere, where moist, boundary layer air mixes with the drier, warmer air from above. In the past, backscatter echoes associated with the latter condition were referred to as lateral angel echoes (Battan, 1973).

For radio or microwave wavelengths, Bean and Dutton (1968) determined the relationship for the refractive index, N as

$$N = \frac{77.6}{T}\left(P + \frac{4810e}{T}\right) \tag{3.6}$$

where T is temperature (°K), P is pressure (mb), and e is vapor pressure (mb). This equation illustrates that at low altitudes, N is more sensitive to water vapor fluctuations, and at higher altitudes in the atmosphere where water vapor concentrations are less, N is more dependent on fluctuations in temperature.

Tatarski (1961), Atlas et al. (1966), Battan (1973), Gossard and Strauch (1983), and Gossard (1990) all present derivations for obtaining the radar reflectivity return due to refractive index variations. These derivations use the following assumptions: 1) that the important scale in the (turbulent) medium for backscattering is $\lambda/2$, which Gossard (1990) terms the Bragg scale, 2) that the refractive index power spectrum can be simplied to one-dimension by assuming it resides in the inertial-convective subrange, and that the turbulence is isotropic and homogeneous, and 3) that the refractive index structure parameter, C_n^2 follows the same wave number power law $\left(\kappa^{\frac{-5}{3}}\right)$ that governs the inertial-convective subrange temperature and humidity structure constants. Based on these assumptions the resulting radar reflectivity (η) equation for refractive index backscatter is

$$\eta = 0.38 C_n^2 \lambda^{\frac{-1}{3}} \tag{3.7}$$

or

$$C_n^2 = \frac{(\lambda^{1/3})\eta}{0.38} \tag{3.8}$$

Equations (3.7) and (3.8) illustrate the relationship between the measured radar reflectivity and computed refractive index structure constant, C_n^2. Comparisons of computed C_n^2 using ground-based radar with in-situ measurements using a refractometer show good agreement (Kropfli et al., 1968), giving confidence that (3.7) and (3.8) provide reasonable estimations of C_n^2. Several studies have used 10 cm wavelength radars to sample refractive index variations in the clear air. Values of C_n^2 range from as low as $10^{-17}\, m^{\frac{-2}{3}}$ to as high as $10^{-11} m^{\frac{-2}{3}}$.

Of particular interest to this study is whether microwave radars can be used to detect clouds or cloud-related features. Combining (3.3) and (3.8), the following relationship is obtained that relates C_n^2 to the reflectivity factor for Rayleigh scatterers

$$C_n^2 = \frac{\lambda^{1/3}\pi^5}{0.38\lambda^4}|K|^2 Z = \frac{\pi^5}{0.38\lambda^{11/3}}|K|^2 Z \tag{3.9}$$

Figure 3.2 illustrates the relationship of C_n^2 backscatter to the size of the Rayleigh scatterers and to wavelength. Gossard and Strauch (1983) note that in order to determine if Bragg scatter is present, two or more radars of different wavelengths should be used to simultaneously observe the same cloud. Recently, Knight and Miller (1993) have addressed the scattering from cumulus clouds using simultaneous, dual-wavelength measurements from the NCAR CP2 radar. They

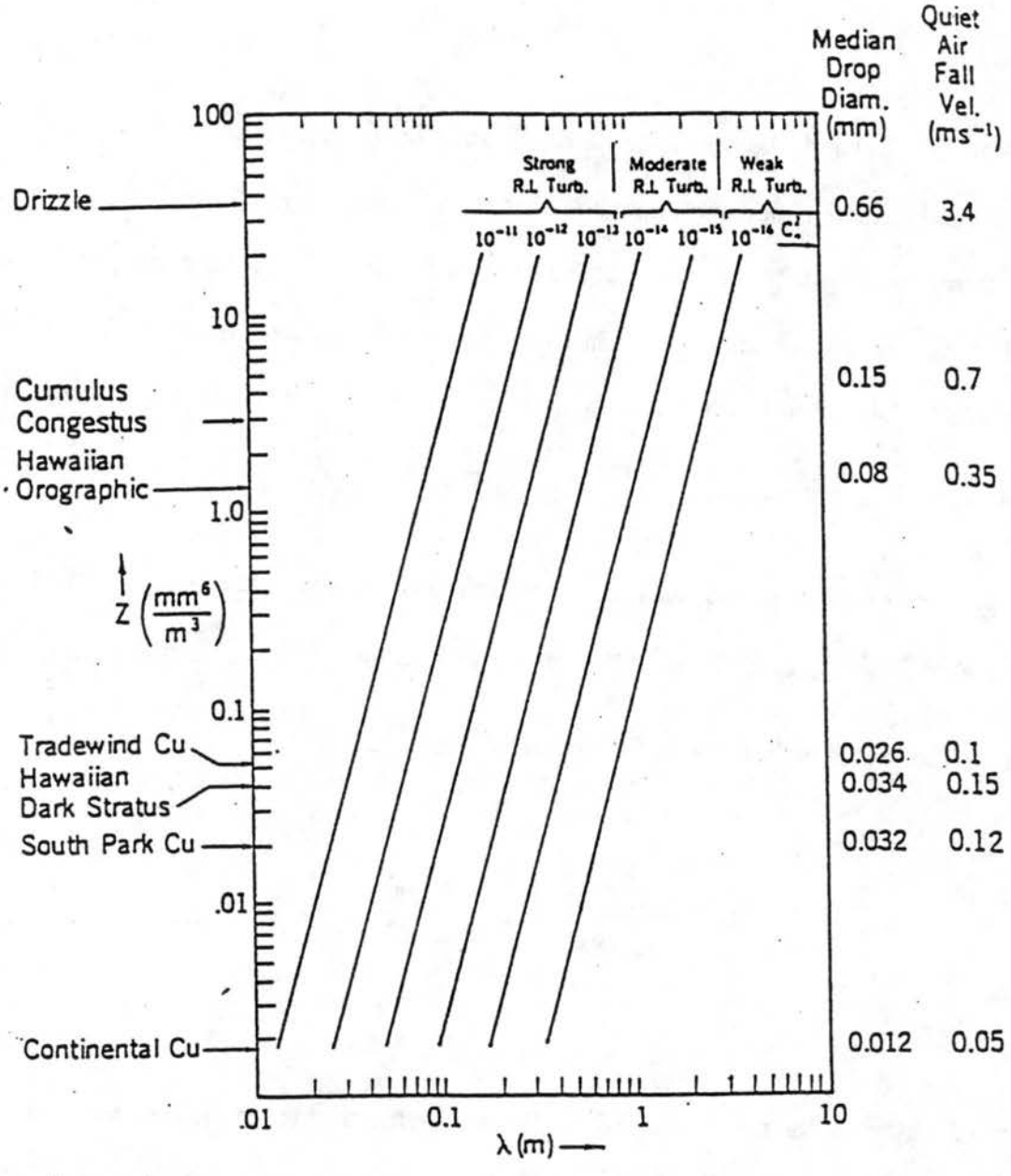

Figure 3.2 Trade-offs between refractive index and particulate return. Curves are for equal scatter from C_n^2 and from Rayleigh liquid spheres found by equating Eqs. (3.2) and (3.8). Various cloud types are shown for reference. Figure parametric in C_n^2. (From Gossard, 1990)

found that all clouds visible to the eye produce detectable radar backscatter when at close range (i.e., < 10 km from the radar). These early or first echoes observed with the cumulus clouds were observed to have a cloud-edge echo pattern (or cloud mantle echo, as it was termed by earlier researchers) that was 500 m thick along the tops and sides of the cloud. This was much larger than the 150 m pulse length and thus represented scattering that is not just confined to the edges of the clouds but extending well into the 1 km depth of the cloud. These mantle echoes were believed to be due to Bragg scattering. Mantle echo reflectivity values from the 10 cm radar ranged from -25 to 5 dBZ.

According to Knight and Miller, differences in reflectivity returns observed between the two different wavelengths would suggest the presence of Bragg scattering. Examination of their data from Florida showed that there was a large difference in the radar reflectivity return at the two wavelengths. They found that by using the Bragg scattering relationship in (3.9) for 10 and 3 cm wavelengths and taking the ratio of Z values for two radar wavelengths, they could define a reflectivity factor ratio value that could be used to discriminate (quantitatively) regions of Bragg scattering from regions of Rayleigh scattering. This ratio was determined to be approximately 19 dB, with ratio values less (greater) than this arising from Rayleigh (Bragg) scattering. The regions of greatest difference in reflectivity echo intensity and > 19 dB reflectivity factor ratio was found within the mantle echo in the 10 cm data. The corresponding region in the 3 cm data showed very little reflectivity return indicating a large portion of the 10 cm echo was not due to Rayleigh scattering.

While the purpose of the Knight and Miller study was to address the onset of precipitation in

clouds by discriminating between regions of Rayleigh and Bragg backscatter, it was clear that the Bragg echo pattern detected by the 10 cm radar was also useful for depicting of the cumulus cloud outline in three dimensions. Thus, while a WSR-88D cannot, for all practical purposes, detect backscatter from cloud drops, it could detect the outer boundaries of the clouds. The main limitation in seeing these Bragg scatter echoes operationally is the 1 km reflectivity gate spacing in the Archive Level II data provided to users.

3.1.3 Sensing clear-air, boundary layer features

Radar's ability to detect clear air features is believed by many to be due to backscattering from primarily insects, and index of refraction variations associated with convective thermals. Backscattering off insects, on the order of several millimeters in size, fall under the Rayleigh regime of scattering at microwave wavelengths (Fig. 3.1). Determining the specific type of scattering that produces the different types of clear air features in the boundary layer has spawned several studies over the last 50 years. A dramatic example of scattering off clear air thermals was shown by Hardy and Ottersten (1969) in which the radar detected refractive index variations along the boundaries between the thermal updraft and subsiding, drier, entraining air. The backscatter at the boundaries of the convective cells produced reflectivity echoes in the shape of doughnuts. They believed that while the upward moving air within the thermals were likely composed of insects, the doughnut echoes resulted from the drier, downward moving air, devoid of insects, being entrained into the thermals.

Numerous authors have also shown the capability of microwave radars to detect horizontal,

convective rolls under clear sky conditions (Konrad, 1968; Hardy and Ottersten, 1969; Kelly, 1982; Wilson and Schreiber, 1986; Christian and Wakimoto, 1989; among others). Christian and Wakimoto (1989) used two different wavelengths (5 and 10 cm), not co-located, to compare the radar reflectivity from horizontal convective rolls. For the reflectivity return to be due to refractive index gradients, they expected to see differences in the reflectivities from the two radars on the order of 11 dBZ (Bragg scattering). The maximum difference they observed was 1-3 dBZ, causing them to conclude that the radar echoes associated with the horizontal rolls was not caused by Bragg scattering, but rather due to insects (Rayleigh scattering). Because the source of the insects is likely from the surface, the linear reflectivity features associated with the rolls was attributed to the insects getting caught up into the updraft portions of the convective rolls. No echoes are observed in association with the downdraft portions of the rolls, since the source of the air from upper part of the boundary layer is essentially devoid of insects. Similarly, gust fronts observed on radar (thin line echoes) are also believed to be detectable by radar due to Rayleigh scattering by insects getting caught up in the outflow (Wilson and Schreiber, 1986).

The curves and reference numbers contained in Figure 3.2 provide guidance on what type of scattering mechanism is likely, for a given range of dBZ ($10 \log_{10} Z$) and drop diameter values. The curves, derived using Eq. (3.9), represent points at which the Bragg scattering is equivalent to particulate backscattering, for the spectrum of wavelengths shown. Thus, for a WSR-88D 10 cm radar $\lambda = 0.1\,\mathrm{m}$, values of 0 dBZ could be a result of either particulate or Bragg scattering, but corresponding values of C_n^2 at this wavelength and dBZ values is very high and typically not observed in clear air, except in the vicinity of frontal zones. For echoes > 10 dBZ, at 10 cm wavelength, Fig. 3.2 shows that it is highly unlikely that backscattering could occur from refrac-

tive index turbulence, since in this region of dBZ values, C_n^2 values are much larger, > 10^{-11}, than values observed by radar. Gossard (1990) states that these 10-20 dBZ echoes are clearly due to particulate scattering, i.e., insects. As seen in the Knight and Miller (1993) study, reflectivity values associated with Bragg scattering along cloud boundaries ranged from -25 to 5 dBZ, with values of >10 dBZ (for a 10 cm radar) representing Rayleigh scattering from hydrometeors.

Recently, Wilson et al. (1994) made use of both multiparameter and dual-wavelength radar data to examine the source of boundary layer, clear air radar echoes using data collected from four different regions of the country and during different seasons. They compared radar reflectivities measured in the CBL at 3 different wavelengths with estimates of the type, size, and shape of the targets computed using a theoretical backscattering model. They also compared the measured differential reflectivity values (Z_{dr}) in the clear air to Vaughn's (1985) width-to-length ratios for birds and insects. For the case in which they examined the clear air return along a Florida sea breeze (thin line echo), 10 cm reflectivities ranged from 0 to 30 dBZ along the sea breeze with values of -5 to 5 dBZ in general backround clear air region. The corresponding 3 cm reflectivites along the sea breeze ranged from -6 to 20 dBZ. The dual-wavelength (10 - 3 cm) reflectivity differences yielded only values of 7 dB, not values of > 19 dB, at specific portions of the thin line indicating scattering was by particulates and not by refractive index variations. For the same thin line echo, Z_{dr} values averaged 7 dB which was equivalent to a width-to-length ratio of 1:3 and a diameter of 10 mm. Results from Vaughn's (1985) review of birds and insects detected by radar indicate that this particle size is more consistent with insects being the dominant scatterer rather than birds. They concluded, based on their broader set of results (not discussed here) that insects

are the primary cause of clear air echoes in a well mixed boundary layer which include sea breeze fronts and horizontal convective rolls. Scattering off cold frontal boundaries and thin lines over the ocean could possibly have been due to refractive index variations, but dual-wavelength information was not available on these features to know for sure.

3.2 GOES satellite

3.2.1 Radiative Transfer

The rate of energy transfer by electromagnetic radiation is call the radiant flux. The radiant flux through an area or incident on an area is termed irradiance. If there is no change in constituency in the atmosphere, than the radiance from the earth's surface to a satellite receiver is independent of the distance (Kidder and Vonder Haar, 1995). However, this is typically not the case on any given day of convective weather processes when radiant energy reaching the satellite will vary due to the amount of absorption and scattering of radiation that occurs in the atmosphere and within clouds. The amount of radiant energy that reaches the satellite is also dependent upon the amount of radiation emitted by the earth's surface, emitted and transmitted by the atmosphere, and emitted and reflected by clouds.

The primary satellite instrument for measuring irradiance is the radiometer which is a passive sensor. That is, it does not transmit radiant energy, but measures only the electromagnetic energy incident on the sensor. The radiometer can measure radiation received at selected wavelengths by applying high quality, optical filters. The GOES imager channels represent data collected at the 5 wavelengths listed in Table 2.

All materials emit radiation. Through the use of Planck's function for a hypothetical black-body, the amount of irradiance from a material depends upon the temperature of the material (Wallace and Hobbs, 1977; Kidder and Vonder Haar, 1995). The monochromatic irradiance, $B_\lambda(T)$, is computed as follows

$$B_\lambda(T) = \frac{c_1 \lambda^{-5}}{\exp\left(\frac{c_2}{\lambda T}\right) - 1} \tag{3.10}$$

where c_1 and c_2 are radiation constants (see Chap. 2). Blackbody radiation represents the upper limit to the amount of radiation that a substance may emit at a given temperature. The relationship between irradiance, temperature and wavelength are graphically illustrated in Fig. 3.3. The higher the temperature of a substance, the greater the radiation. At visible $(0.4 - 1.1\mu m)$ wavelengths, temperatures are extremely high and irradiance or radiance (irradiance per unit solid angle) reaching the satellite is due to solar radiation reflected by clouds, land and bodies of water. The intensity of the reflected radiation reaching the satellite and displayed on the GOES channel 1 image depends upon the albedo of the earth's surface and the albedo of the clouds. The wavelengths of the five GOES-8 channels are listed under GOES-I in Table 2, Chap. 2, in numerical order.

Because of their temperatures, the atmosphere and earth (terrestrial radiation) emit in the infrared portion of the electromagnetic spectrum. The GOES-8 imager channels 4 and 5 detect radiation between $(10 - 12.5\mu m)$ wavelengths (see the shaded region in Fig. 3.3). In general,

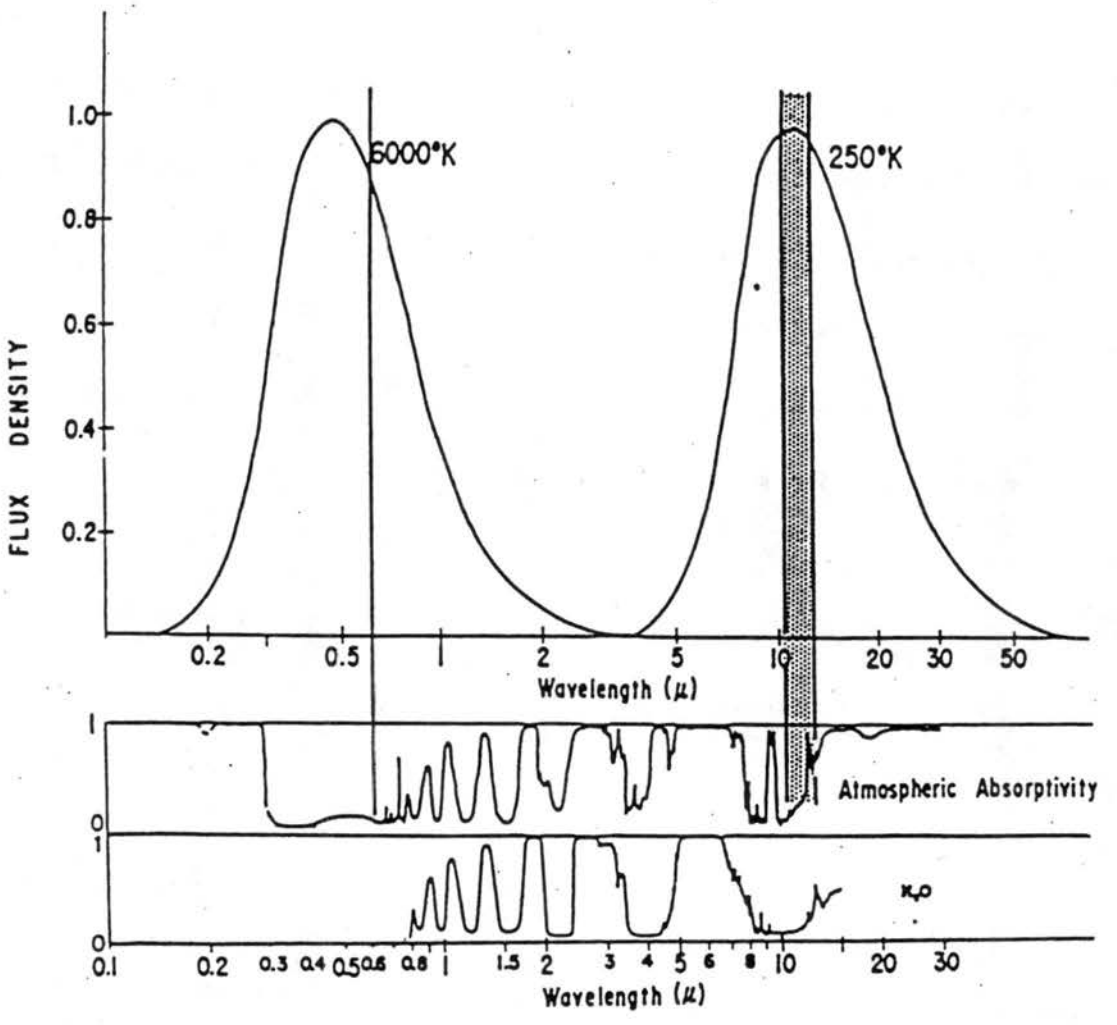

Figure 3.3. Emission and absorption spectra. The upper portion of the diagram shows normalized emission spectra for blackbody radiation at 6000K, the temperature of the Sun, and for a body of 250 K corresponding roughly to the radiation emitted by the Earth and atmosphere. The middle part of the diagram shows the absorption spectrum of the atmosphere. The atmosphere is much more transparent to incoming solar radiation than it is to outgoing (IR) terrestrial radiation. The shaded band is the IR region (10.5 – 12.5μm) *commonly used for IR cloud imagery. The line at* 0.63μm *is centered in the region where VIS measurements are made. (From Anderson, 1990)*

radiation that is emitted from the earth's surface is absorbed, modified, and re-emitted by the atmosphere and clouds. The actual amount of radiation reaching the satellite can be computed using the radiative transfer equation. This equation accounts for the radiation emitted by the surface and the transmittance of this radiation through layers of absorbing medium in the atmosphere, to the top of the atmosphere. Fleagle and Businger (1963), Wallace and Hobbs (1977), Liou (1980), Stephens (1994) and Kidder and Vonder Haar (1995) provide detailed derivations of this equation. Only a few key formulations are presented here.

The relative absorption, emittance and reflectivity of a material is given by the following conservation of energy relationship

$$a_\lambda + r_\lambda + \tau_\lambda = 1 \tag{3.11}$$

where a_λ is the absorptivity (ratio of absorbed to incident radiation) of the material, r_λ is the reflectivity (ratio of reflected to incident radiation) and τ_λ is the transmissivity (ratio of transmitted to incident radiation) of the material. Transmittance through an absorbing medium at a given wavelength depends upon the density of the absorbing molecules over a path length [u(p)] and the magnitude of the absorption (k_λ), or depletion, of radiation occurring over that path length. Because Beer's law states that transmittance decays exponentially with increasing path length, the formula for transmittance is

$$\tau_\lambda(p-0) = e^{-k_\lambda u(p)} \tag{3.12}$$

For a cloudless atmosphere the radiation received by the satellite can be given by

$$I_\lambda = B_\lambda(T(p_s))\tau_\lambda(p_s) + \sum_p \varepsilon_\lambda(\Delta p)B_\lambda(T(p))\tau_\lambda(p) \tag{3.13}$$

where p_s is the pressure at the surface and p is the pressure at some atmospheric layer. From Kirchhoff's Law ε_λ, the emissivity at some layer p, is equal to the absorptivity in the layer or one minus the transmittance of the layer. Using this information, substituting for $\varepsilon_\lambda(\Delta p)$ in (3.13) and writing the equation in the integral form gives

$$I_\lambda = B_\lambda(T(p_s))\tau_\lambda(p_s) - \int_0^{p_s} B_\lambda(T(p))\left[\frac{d}{dp}\tau_\lambda(p)\right]dp \tag{3.14}$$

The first term in (3.14) is the radiance emitted by the surface and attenuated by the atmosphere. The second term is the radiance emitted to space (or to the satellite radiometer) by the atmosphere. The term $\left[\frac{d}{dp}\tau_\lambda(p)\right]$, the weighting function, gives an indication of where in the atmosphere the majority of the radiation comes from, for a given wavelength.

3.2.2 Sensing Clouds

The atmosphere is generally transparent to solar radiation, i.e., it absorbs very little of the solar

radiation passing through it. However, in the visible ($\lambda = 0.5\mu m$) portion of the wavelength spectrum, cloud drops are geometric scatters (see Fig. 3.1) and scatter the solar radiation. Solar radiation is scattered equally well for most visible wavelengths and thus clouds appear white. Welch et al. (1980) and Cox (1981) found that the reflectance of clouds was highly dependent on the cloud droplet concentration. Most clouds have higher concentrations of small droplets with smaller concentrations of larger drop sizes and higher reflectance was found to be associated with clouds of this type. Liquid water in clouds absorbs very little visible radiation (Kidder and Vonder Haar, 1995). However, slightly more absorption of solar radiation was found to occur when clouds were composed of large drops and raindrops (Cox, 1981).

For the GOES-8 satellite, the infrared channels 4 and 5 were purposely selected because absorption and modification of the radiation by various gases in the atmosphere is actually fairly small at these wavelengths (Menzel and Purdom, 1994). This can be seen in the portion of the atmospheric absorptivity spectra in Fig. 3.3 that corresponds to these wavelengths ($10.0 - 12.5\mu m$). These wavelengths are commonly referred to as atmospheric windows (Liou, 1980). Because the atmospheric gases absorb very little of the IR radiation at these wavelengths, the IR radiation received by the satellite is emitted primarily by the earth's surface or clouds. This means that useful information about the properties of the clouds themselves can be obtained since clouds act as blackbodies to infrared radiation. They absorb (and emit) nearly all the infrared radiation they receive.

While satellite radiometer measurements are recorded in radiation count values, it is more infor-

mative for meteorological purposes to represent the radiation values for the IR channels in units of temperature. This is done by inverting the Planck function (3.10) to obtain the equivalent blackbody temperature, which is more commonly referred to as brightness temperature. Brightness temperature is the temperature required to match the satellite measured radiance to the Planck blackbody function at a given wavelength (Stephens, 1994). The relation for brightness temperature, T_b, is

$$T_b = \frac{hc\tilde{\upsilon}}{k_b}\left[\ln\left(\frac{2hc^2\tilde{\upsilon}^3}{I_m} + 1\right)\right]^{-1} \tag{3.15}$$

where I_m is the intensity measured at the characteristic wavenumber $\tilde{\upsilon}$ of the radiometer, c is the speed of light, h is Planck's constant and k_b is Boltzmann's constant. The brightness temperature provides some indication of the temperature and the altitude in the atmosphere at which the radiation is being emitted. Brightness temperatures associated with clouds represent the radiation emitted out of the top of the cloud. The source of this radiation is from the upper 200-500 m of the cloud (Vivekanandan, 1997). Thus, cloud temperatures discussed in this study represent temperatures at the very top of the clouds. Operationally, this information can be used to monitor vertical growth of clouds and estimation of cloud top heights with the aid of NWS sounding data. In this study, emphasis is placed on monitoring when cloud top temperatures drop to sub-freezing temperatures. The implication is that in the immediate layers below cloud top, freezing temperatures are responsible for the production of cold cloud (coalescence) precipitation processes and

increased growth of clouds into thunderstorms via a dynamic response to latent heat of fusion.

Chapter 4

CASE STUDIES

In this chapter, we present data collected in the vicinity of Denver, Colorado on 21 and 24 July, and 23 and 24 August 1995. These cases illustrate the evolution of cumulus clouds over a spectrum of radar-detected, boundary layer features. Cases with more vigorous thunderstorm development are presented first.

4.1 23 August 1995

4.1.1 Environmental conditions

The DEN NWS sounding (Fig. 4.1) taken at 1200 UTC indicated a conditionally unstable atmosphere with plenty of moisture available at all levels, a modified LI (as defined by Mueller et al., see chap. 1) of -2.37 forecasted for the afternoon, surface mixing ratio of 9.5 g/kg, a CAPE of 621 J/kg, and surface winds from the south-southeast. The forecasted CIN was -17 J/kg, which is a rather small amount of negative area to overcome before free convection could ensue. The Mid-west and High Plains were under the influence of a high pressure system as evidenced in the 500 and 700 mb maps in Figs. 4.2 and 4.3. A weak, short wave disturbance that was passing mostly to

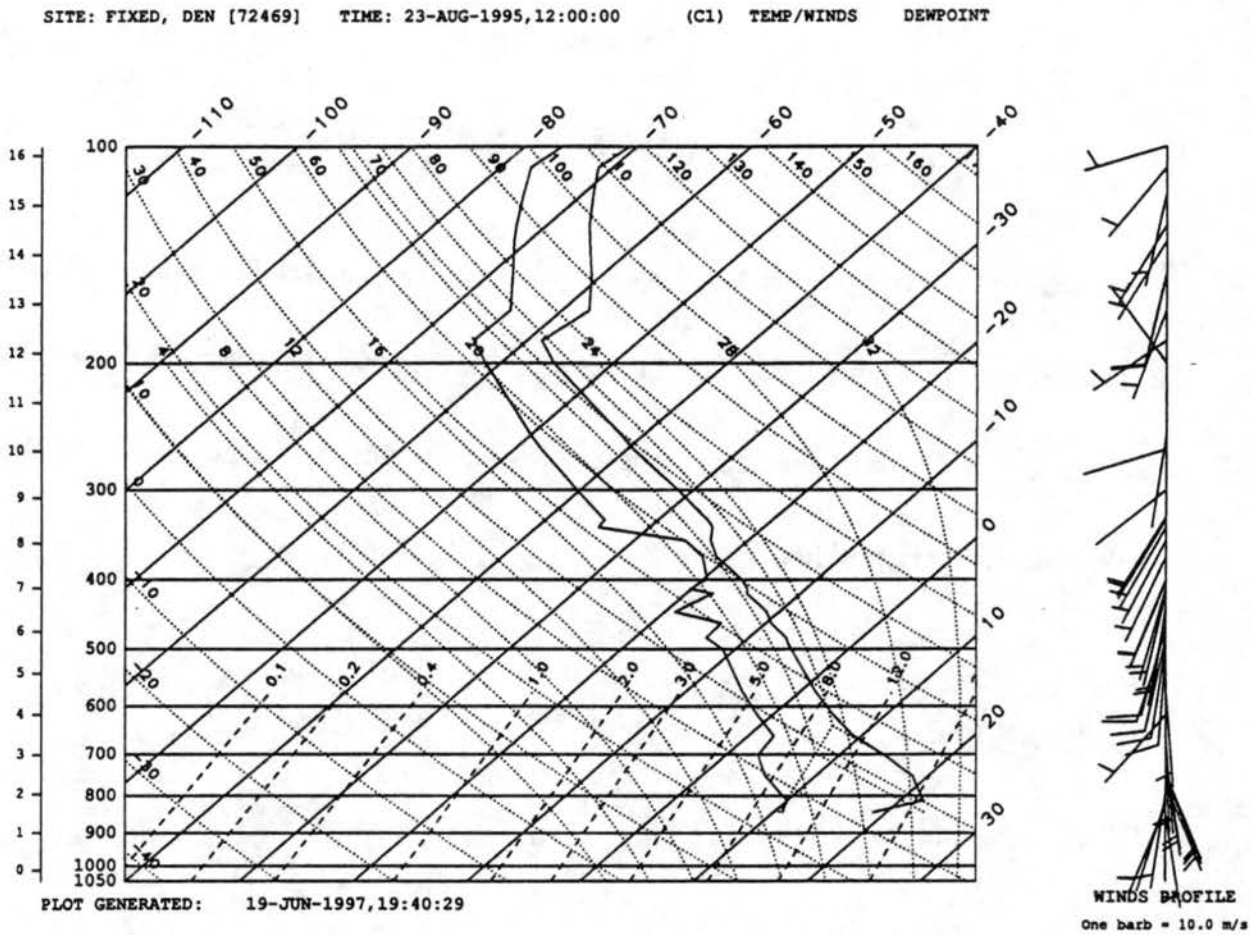

Figure 4.1. Denver NWS 1200 UTC sounding from 23 August 1995.

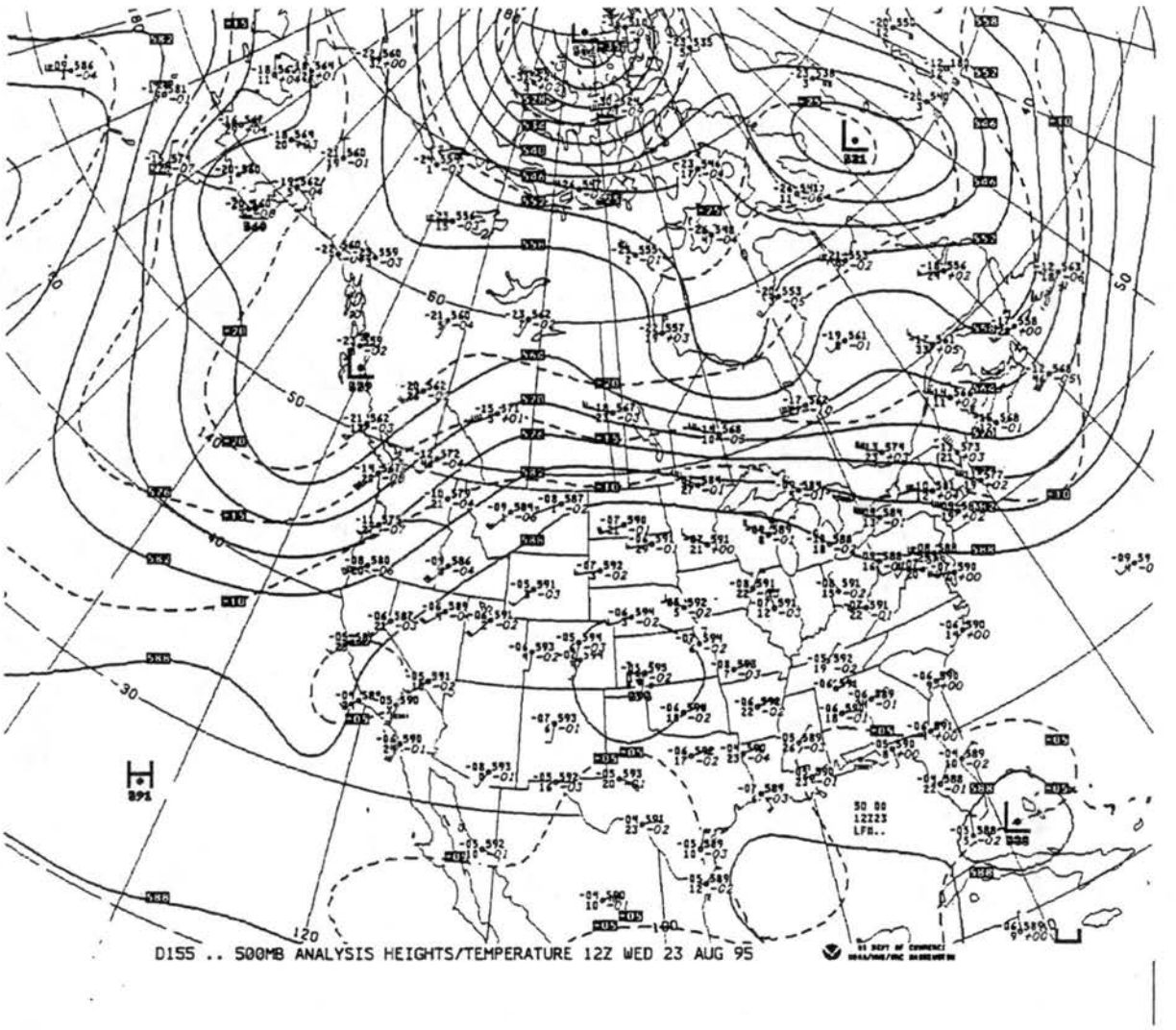

Figure 4.2. Upper air 500 mb map from 23 August 1995 at 1200 UTC.

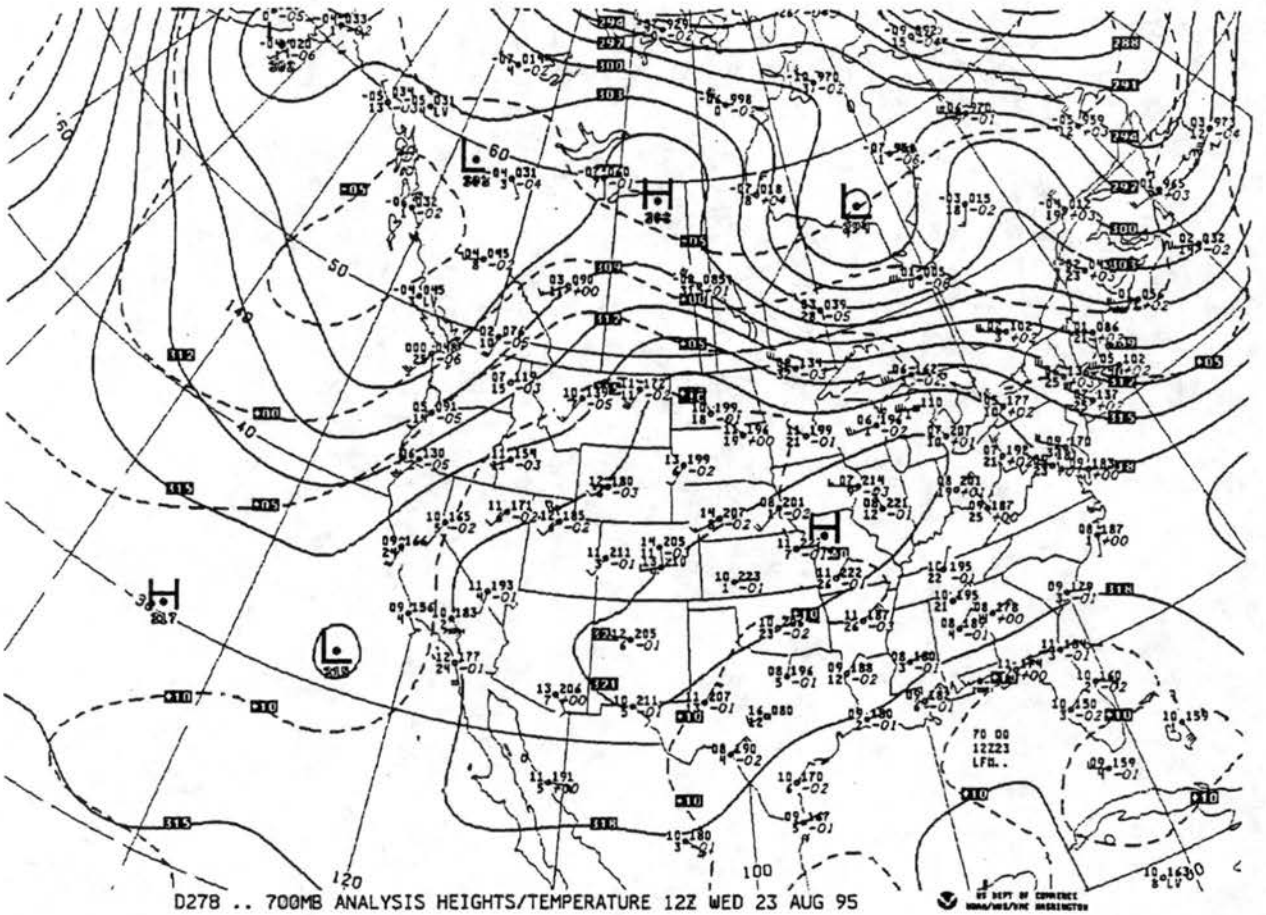

Figure 4.3. Upper air 700 mb map from 23 August 1995 at 1200 UTC.

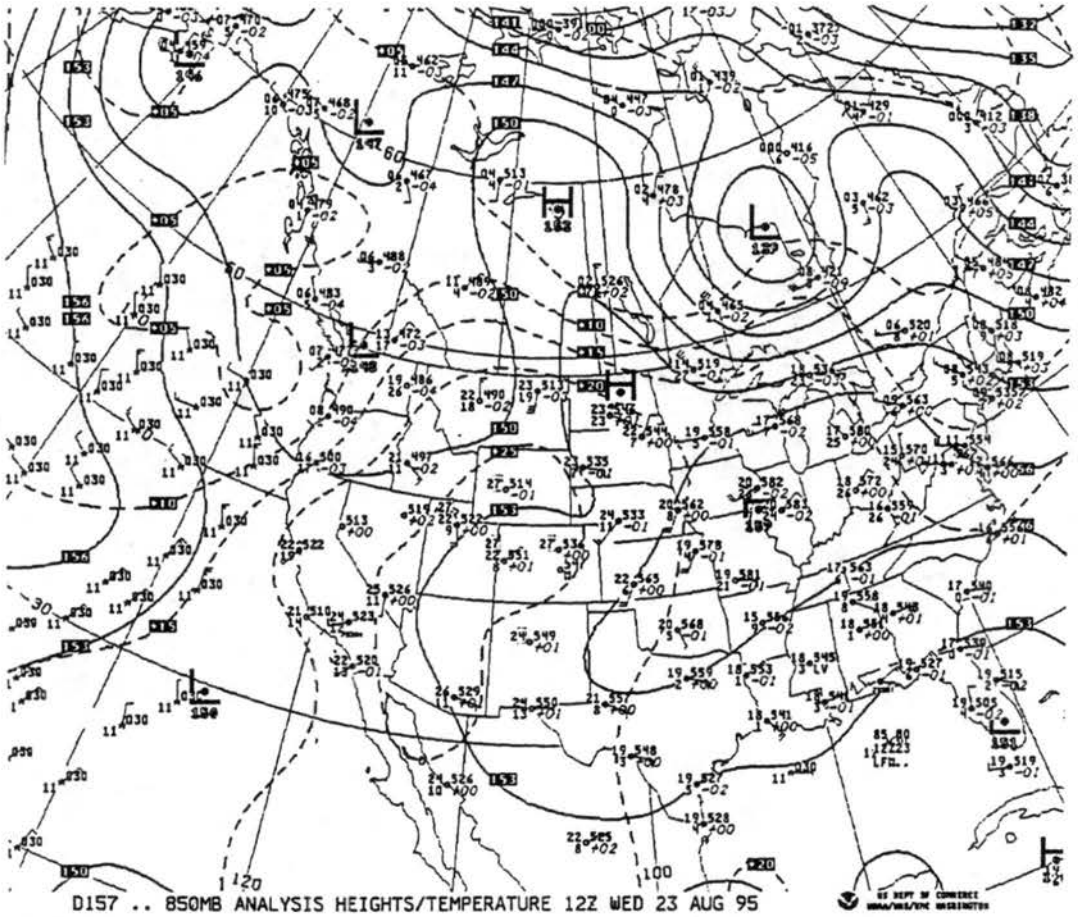

Figure 4.4. Upper air 850 mb map from 23 August 1995 at 1200 UTC.

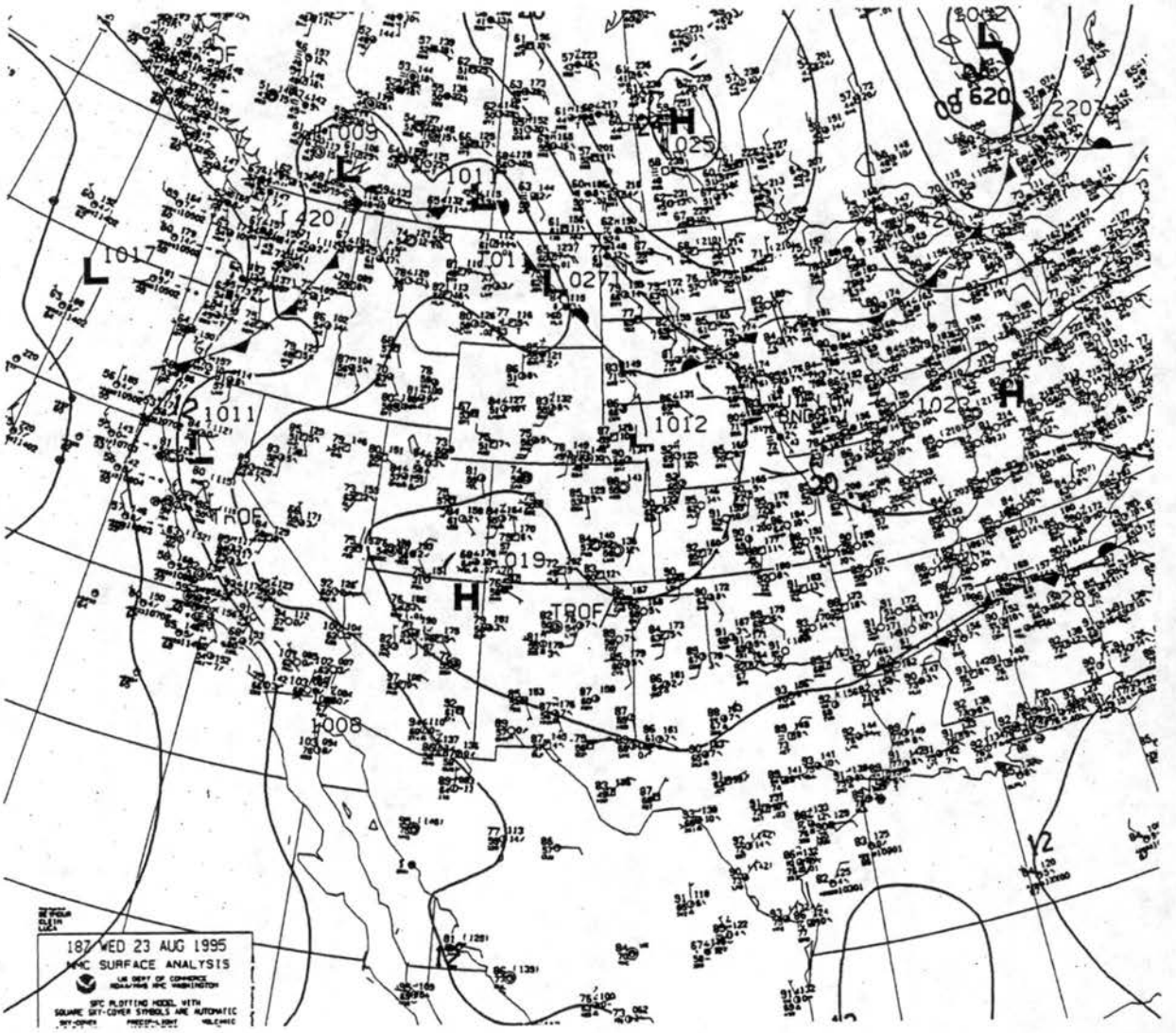

Figure 4.5. Surface analysis map from 23 August 1995 at 1800 UTC.

the north of Colorado was also apparent in the 850 mb map (Fig. 4.4) as indicated by the trough extending down into northeastern Colorado in the surface map (Fig. 4.5) at 1800 UTC (hereafter, all times in UTC). By 1800, the convective temperature of 86 had already been reached in Denver, with a maximum temperature of 90 reached at 2000. Following trough passage, weak high pressure built into northeastern Colorado, bringing moist (dewpoints in the mid-50's), southeasterly flow into the Denver area.

4.1.2 Relationship of clouds to boundary-layer features

As the afternoon progressed, a topographically-induced, stationary convergence zone known as the DCVZ (Szoke et al., 1984; Wilczak and Glendening, 1988) set up, oriented in a line southwest to northeast of KFTG. This DCVZ represents the area in which the moist, southeasterly flow converges with the relatively dry, west-northwesterly downslope flow off the Rocky Mountains. The DCVZ can be seen in Fig. 4.6 at 1932 as the boundary between the horizontal convective rolls to the south and east of the radar, and the less organized, clear air return to the north of the radar. The convective horizontal rolls, oriented in a roughly N-S direction parallel with the low level, southerly, boundary layer flow and with relatively large spatial separation of approximately 8-10 km, intersected the DCVZ at points east and northeast of the radar. These boundary layer features can be seen in Fig. 4.6 located within the area defined by the white box. The domain of

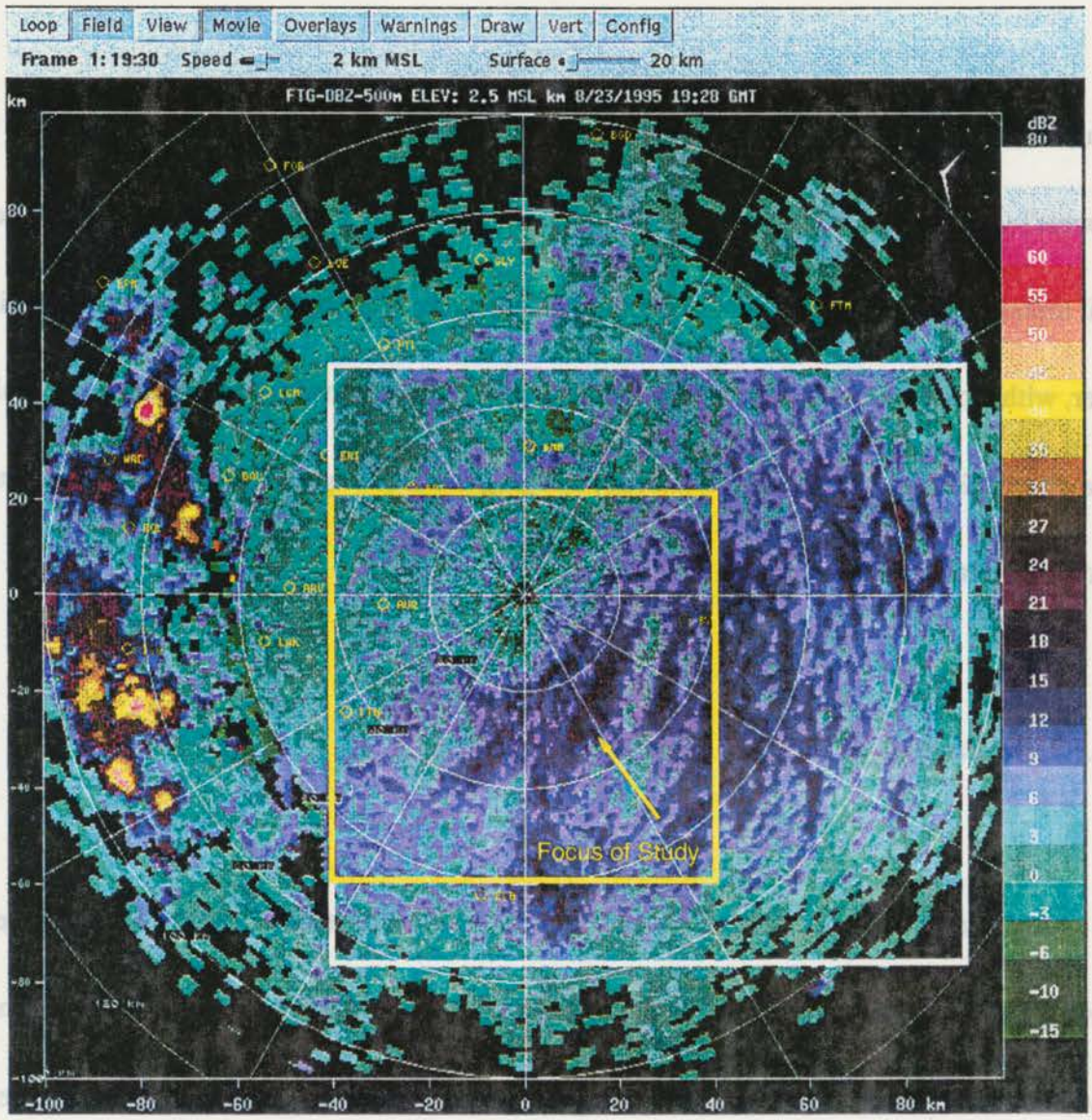

Figure 4.6. Cartesian (CIDD) KFTG reflectivity plot from 23 August 1995 at 1930 and 2 km MSL (0.5 km AGL) showing the reflectivity thin line features associated with the DCVZ and the horizontal rolls. The yellow box defines the domain of data analyses for this case. The arrow points to the horizontal roll that first intersects and then later merges with the DCVZ. Data is plotted in 1 km grid increments. Range rings are overlaid as an additional reference.

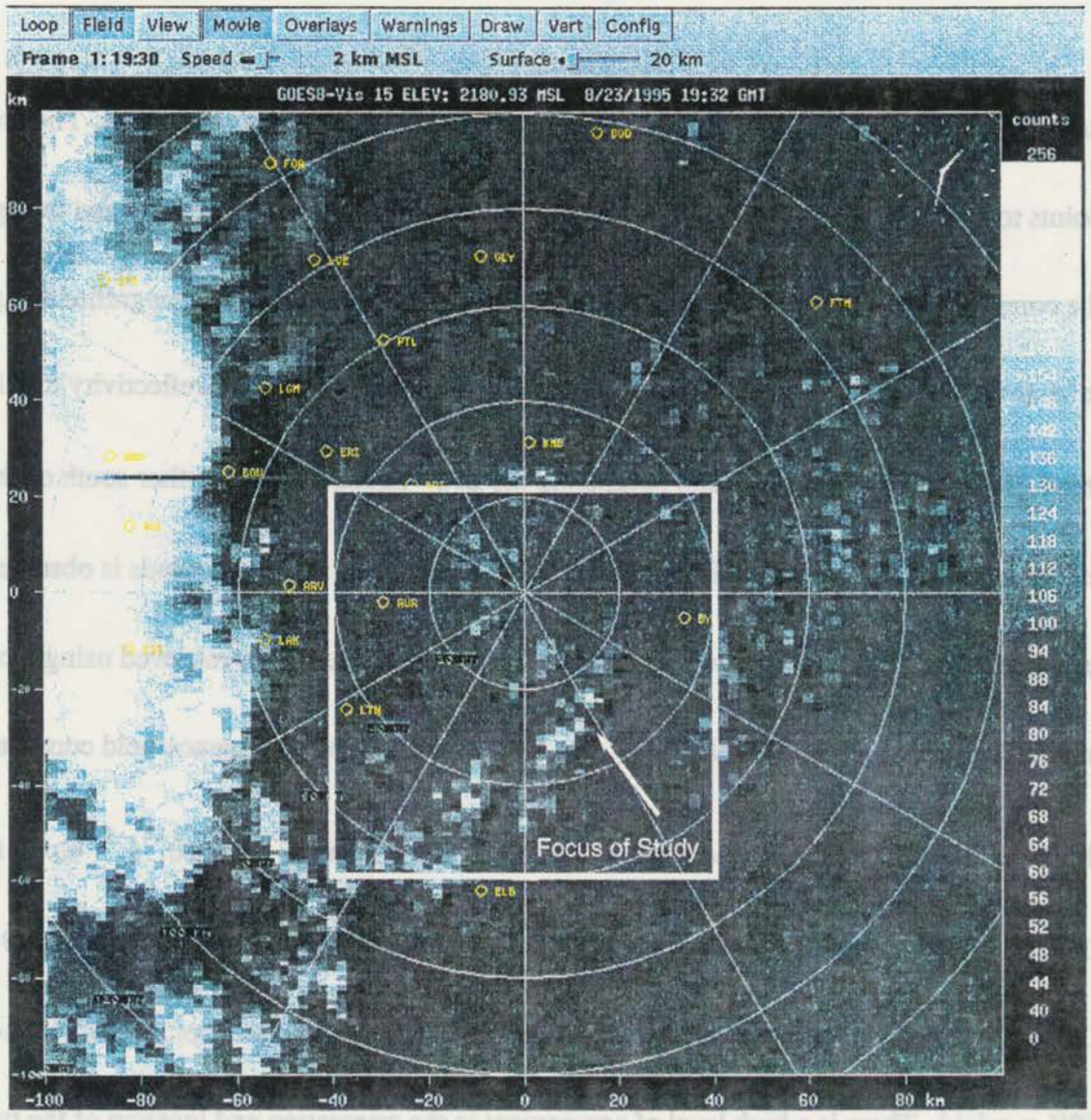

Figure 4.7. Cartesian (CIDD) display of GOES-8 Visible data (in counts) at 1930 UTC with the KFTG radar location as the center of the plot. Data is in 1 km grid increments. The white arrow points to the cloud line analyzed from this day.

data analyzed using the CEDRIC software package is outlined by the yellow box. The arrow points to one of the horizontal rolls intersecting the DCVZ reflectivity thin line and in Fig. 4.7, to the corresponding cloud line of interest in this case study. Figure 4.8a is a magnified image of the reflectivity field within the yellow box in Fig. 4.6. The NE-SW, 15 dBZ reflectivity thin line, centered 25 km south of the radar and paralleling the 210° azimuthal line further south of the radar marks the location of the DCVZ. A change in the direction of the radial winds is observed in this area (Fig. 4.8b). The TREC southerly winds (Tuttle and Foote, 1990) retrieved using a cross-correlation technique on the Doppler radar data are overlaid. The convergence field computed from the TREC winds (yellow shaded areas in Fig. 4.8d) has values of $1.5 \times 10^{-4} s^{-1}$ along the DCVZ and cloud lines. The brown shaded regions indicate weak divergent flow. Fig. 4.9 shows a CEDRIC plot of VIS imagery at 1932 with the 0.5 km AGL reflectivity contours of 12, 14 and 16 dBZ overlaid. There is a high level of agreeement in the orientation and location of the two cumulus cloud lines with the lower-level, reflectivity features. Several studies using aircraft or satellite observations of cloud streets have assumed the cloud streets were associated with boundary layer features. However, our study is one of the few that has directly compared satellite cloud observations with boundary layer features identified by radar. The DCVZ actually extends out to the SW edge of Fig. 4.9 but the lower reflectivity values associated with this portion of the line are not shown. The evolution of the boundary layer features and subsequent production of precipitating storms is shown in the reflectivity plots in Fig. 4.10. It is evident in Fig. 4.10b that the first storms

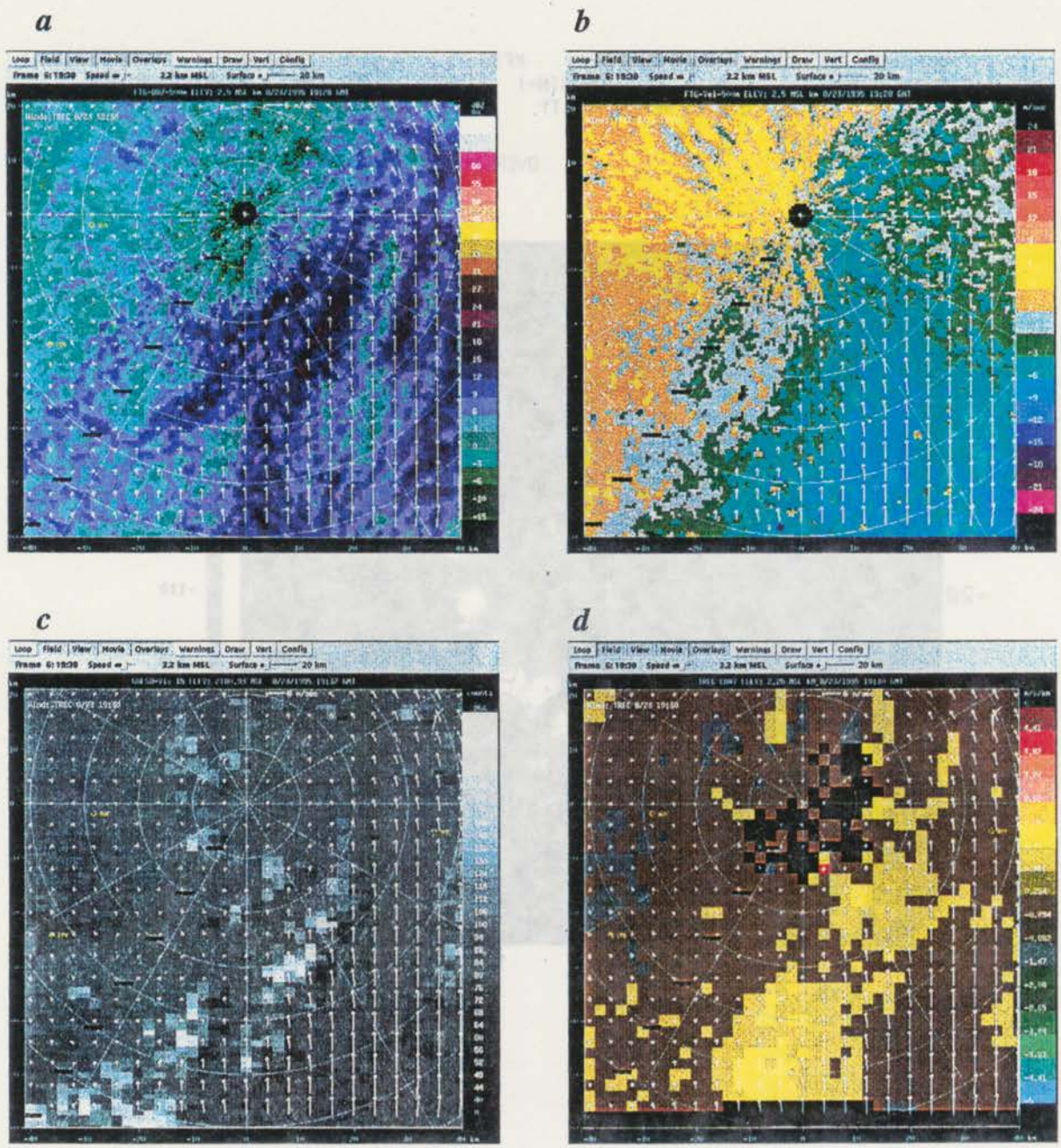

Figure 4.8. KFTG radar fields and satellite Visible imagery on 23 August 1995 at 19:28 UTC for the domain shown by the yellow box in Fig. 4.6. a) Reflectivity in dBZ at 2.2 MSL (0.5 km AGL), b) radial velocity in m/s, c) GOES-8 Visible imagery (in counts), and d) TREC-derived convergence (yellow shades). Grays and browns are divergence. TREC vectors are overlaid onto all panels.

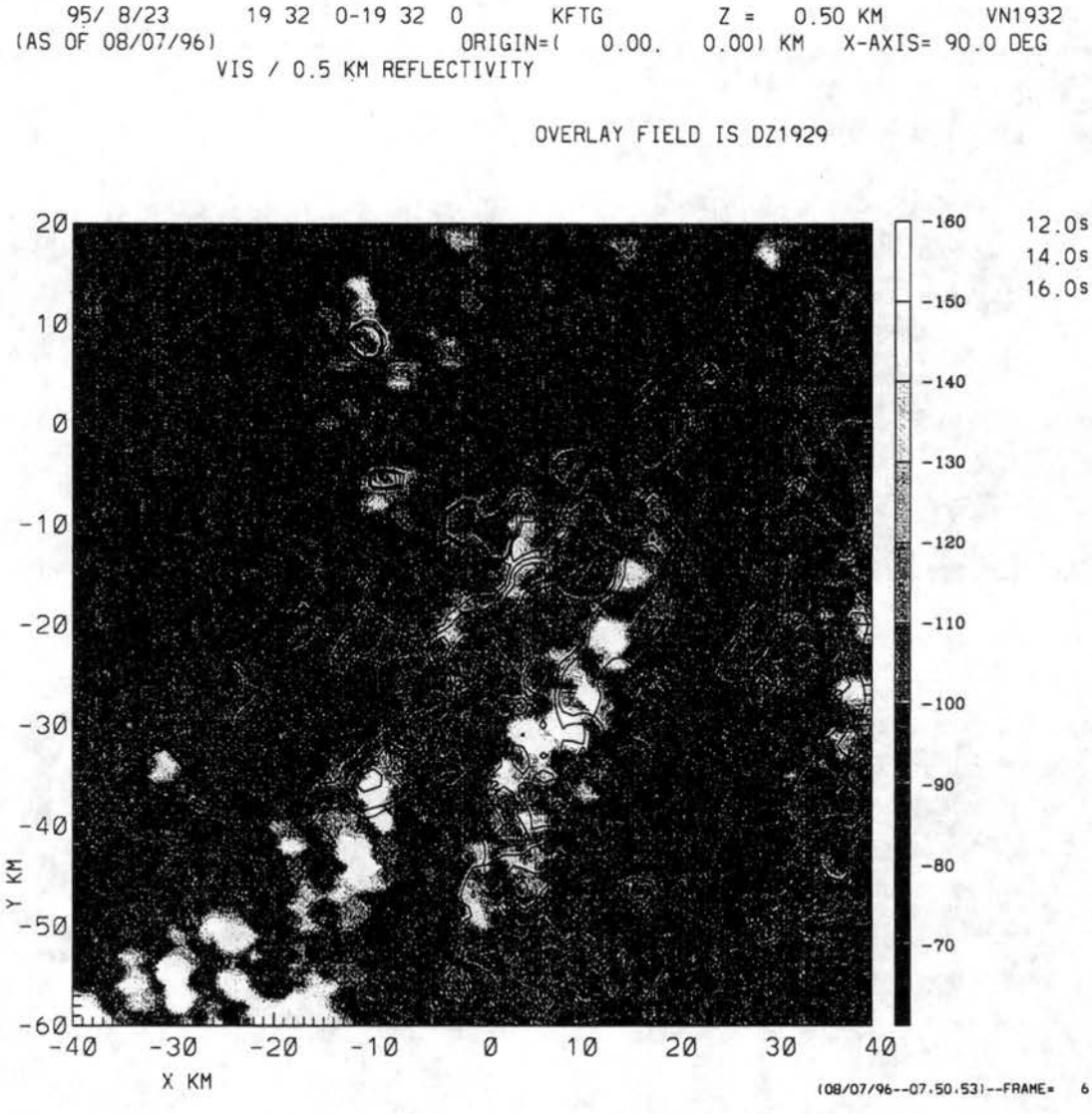

Figure 4.9 CEDRIC plot of Visible data from 23 August 1995 at 1930 with reflectivity contours overlaid. Contours are in increments of 12, 14, and 16 dBZ. The Visible gray scale is in counts; values are listed as negative for plotting purposes only.

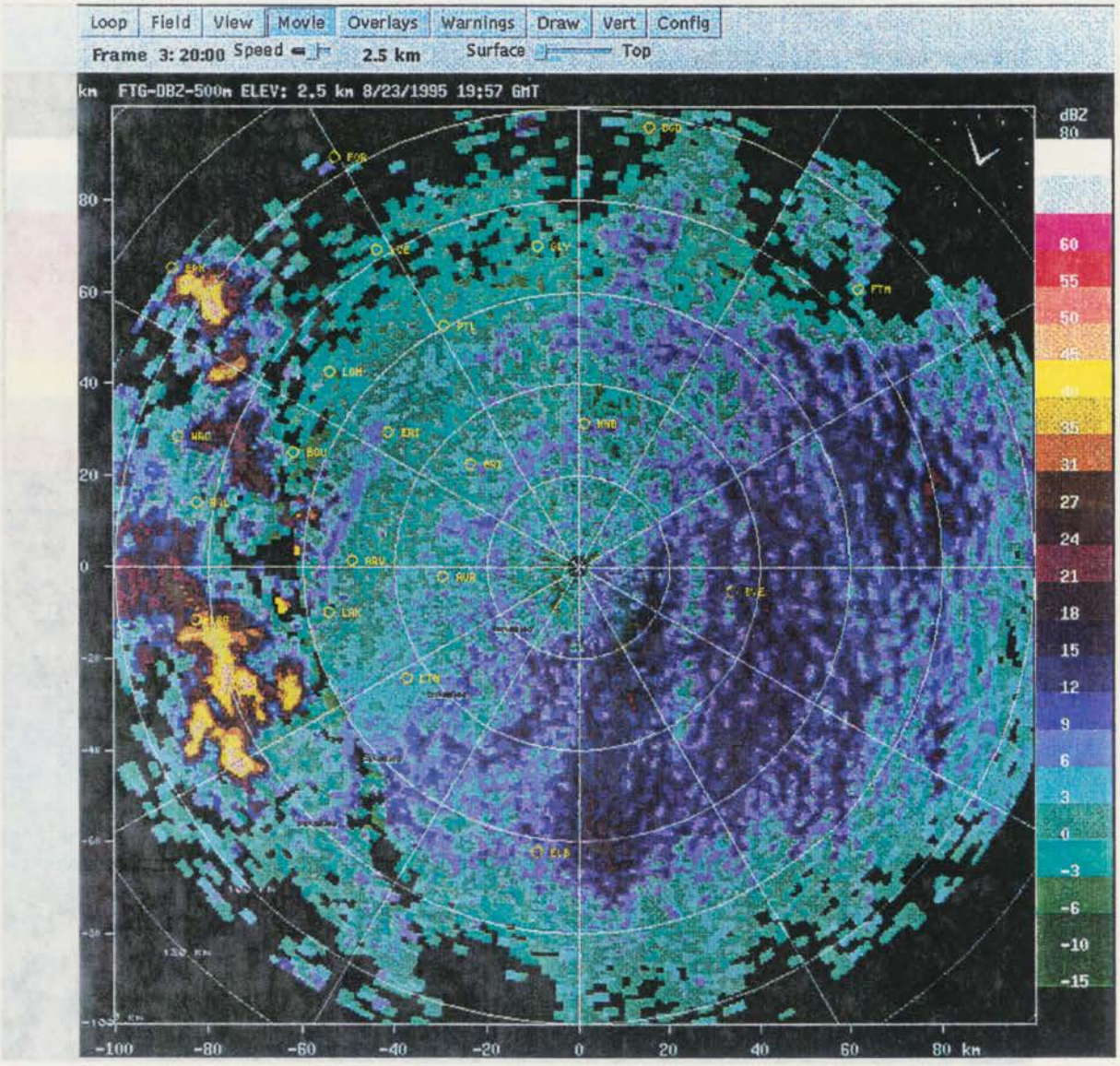

Figure 4.10. Time series of cartesian reflectivity plots at 0.5 km AGL from 23 August 1995 at a) 2000 UTC.

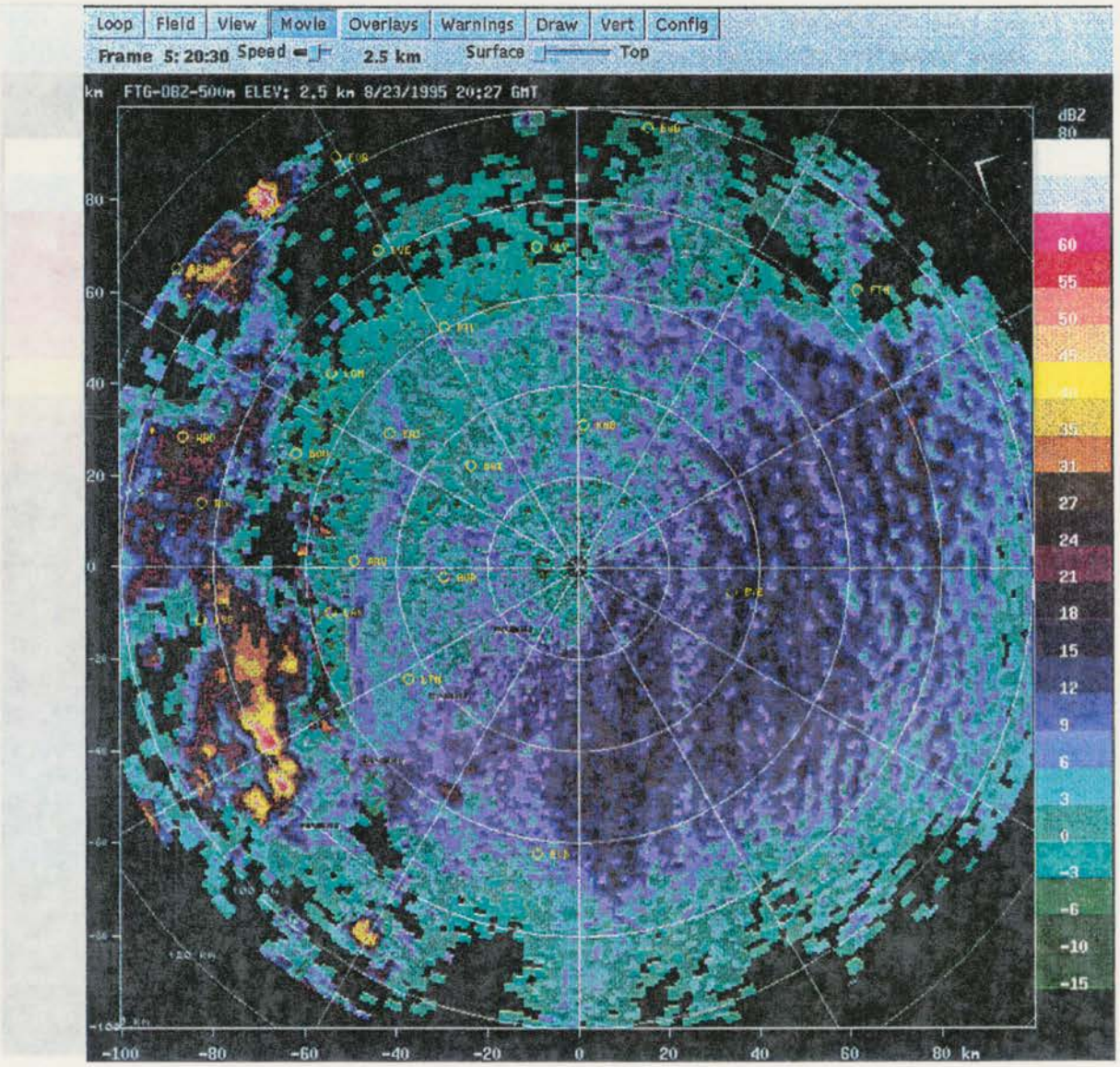

Figure 4.10. b) at 2030 UTC.

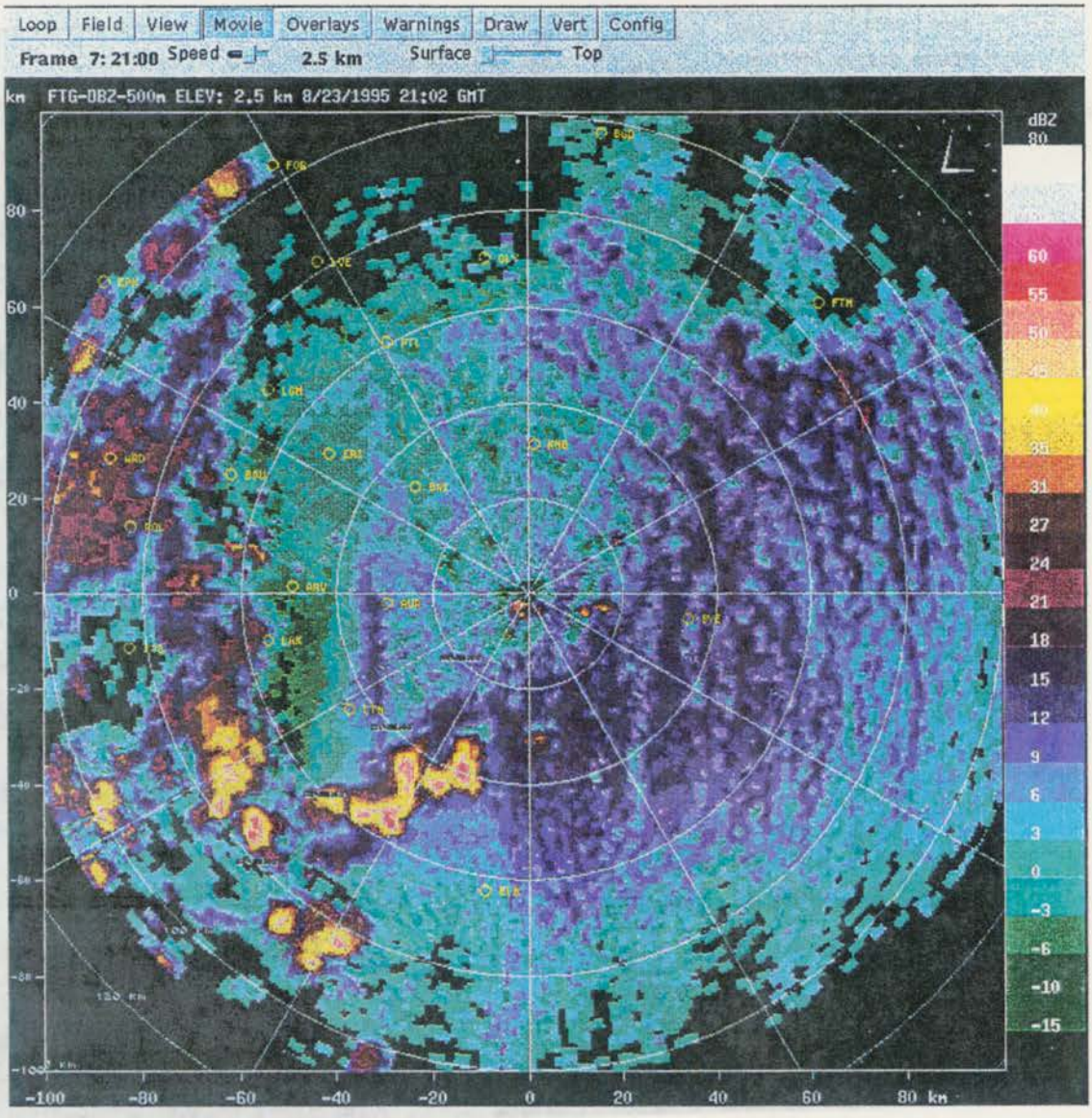

Figure 4.10. c) At 2100 UTC.

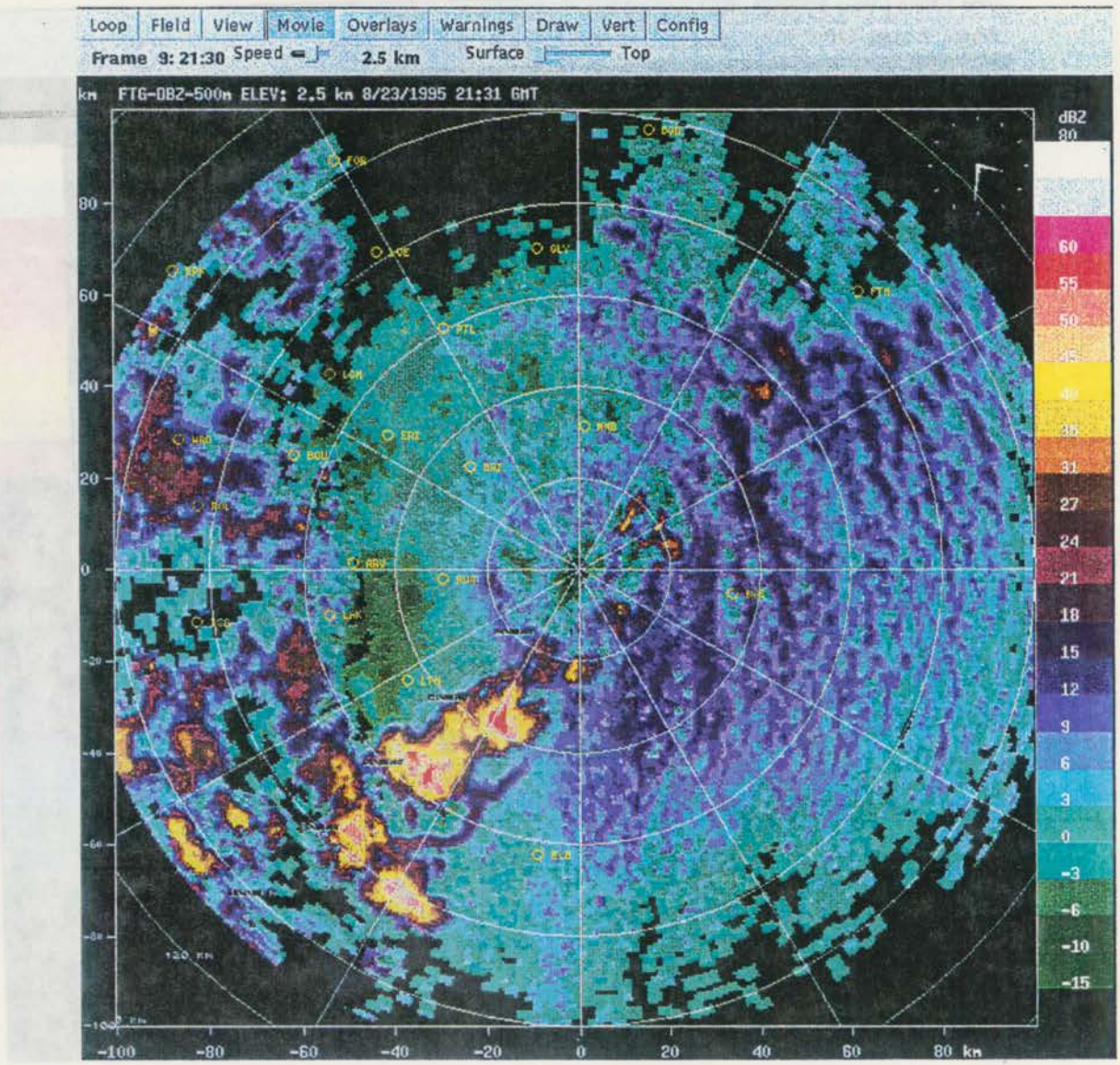

Figure 4.10. d) At 2130 UTC.

(at 210° , 50-60 km in range) developed along the SW portion of the DCVZ. Outflows from these storms initiated new storms immediately northeast of the existing storm locations, along the DCVZ. However, as can be seen at 2130 (Fig. 4.10d), other storms developed where horizontal rolls intersected the DCVZ (e.g., at 75° azimuth and 22 km in range). In their study, Wilson et al. (1992) found these points of intersection to be the most favorable for storm development due to the increased horizontal convergence in these areas. This case focusses on the cloud growth in the vicinty of just such an intersection, as mentioned above.

The Visible satellite images that correspond to the time periods shown in Fig. 4.10 are shown in Fig. 4.11. Note that for all the cases presented in this thesis, there is no satellite data available at 2100, since near this time the GOES-8 satellite performs a hemispheric scan that begins after the 2045 CONUS scan and is not completed until after 2100. From the plots in Fig. 4.11 it is apparent that the vigorous cloud growth south-southwest of the radar is occurring between 2000 and 2100. By 2130, the lines of cumulus clouds above the rolls to the northeast of the radar have undergone growth coincident with change in the structure of the boundary layer features. As the convective processes in the boundary layer became more prevalent, as indicated by the increased horizontal and vertical development of the clouds, the number of horizontal rolls present decreased with only a few prominent rolls remaining (see Figs. 4.10c,d). A similar trend was observed by Fankhauser et al. (1995) with vigorous convection occurring above the remaining

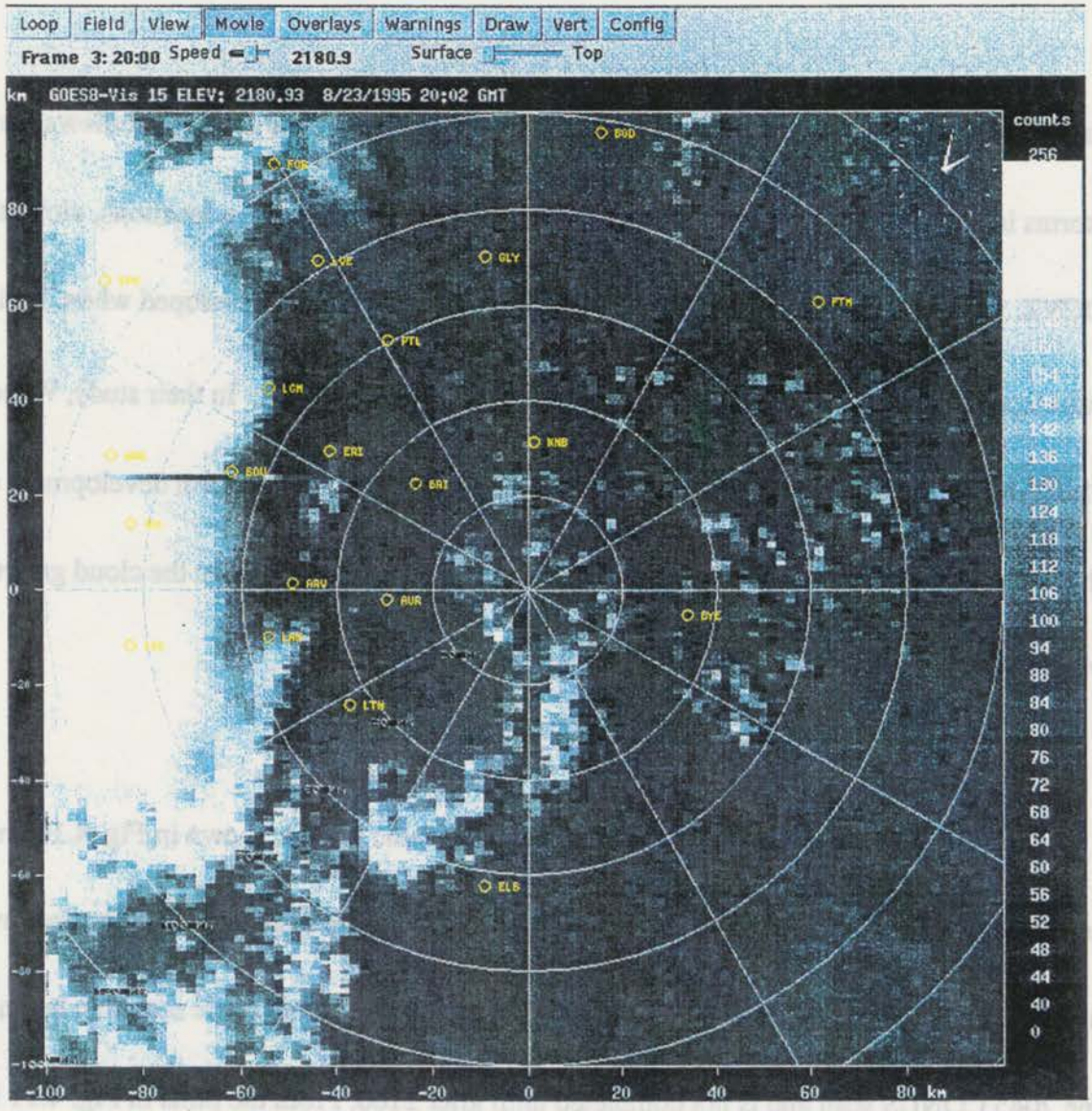

Figure 4.11. Time series of GOES-8 Visible data at a) 2000 UTC.

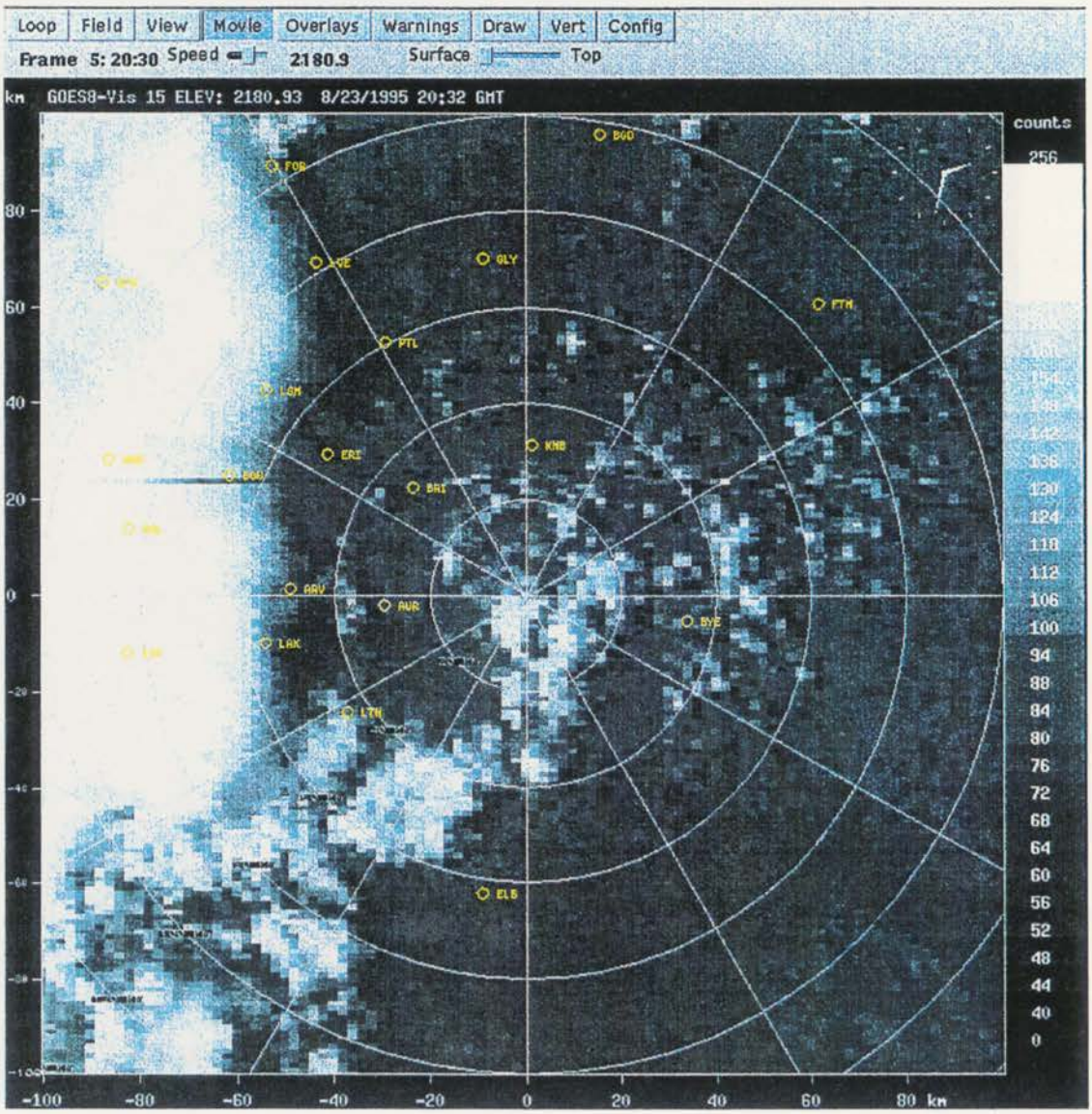

Figure 4.11. b) At 2030 UTC.

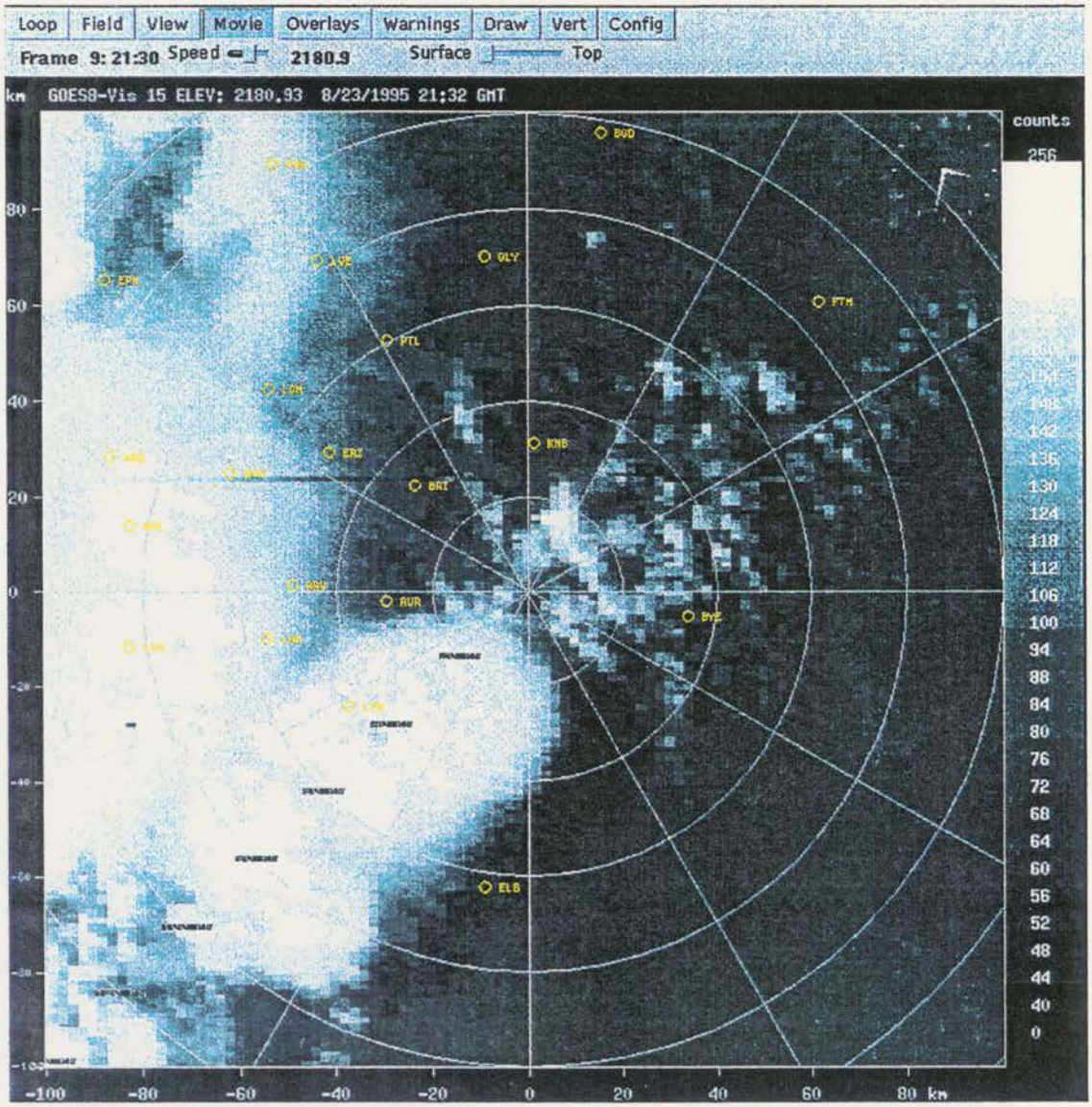

Figure 4.11. c) At 2130 UTC.

convective rolls. As can be seen in Fig. 4.11c, the cloud lines to northeast of the radar are associated with the more intense reflectivity thin lines (see Fig. 4.10d) and stronger surface convergence (not shown).

One other feature of interest in Fig. 4.10 is the reflectivity thin line associated with a thunderstorm outflow from the mountains. This thin line was initially centered at 285° azimuth and 53 km in range from the radar (Fig. 4.10a) and moved eastward with time. In Fig. 4.10c, this feature is centered at 255° azimuth and 35 km in range. Examination of the VIS images (Fig. 4.11) and the reflectivity data at 4.5 km indicate that this convergence boundary was not able to initiate vigorous convection on its own, but likely enhanced some of the initial convection along the DCVZ by enhancing the low level convergence of flow in that area.

4.1.3 Growth of cumulus clouds

To examine the pattern of cloud growth along the cloud line shown in Fig. 4.7, IR brightness temperatures, Visible imagery and radar reflectivities at 4.5 km AGL are compared at 15 min intervals from 1932 to 2030 (Figs. 4.12 - 4.16). The plots shown were generated using the CEDRIC software package; data processing procedures were discussed in Chapter 2. A cursory glance at the brightness temperatures (panel a, Fig. 4.12) illustrates the slightly cooler cloud line

19:32 UTC

(a) BRIGHTNESS TEMPERATURE (° C)

(b) WSR88-D RADAR REFLECTIVITY

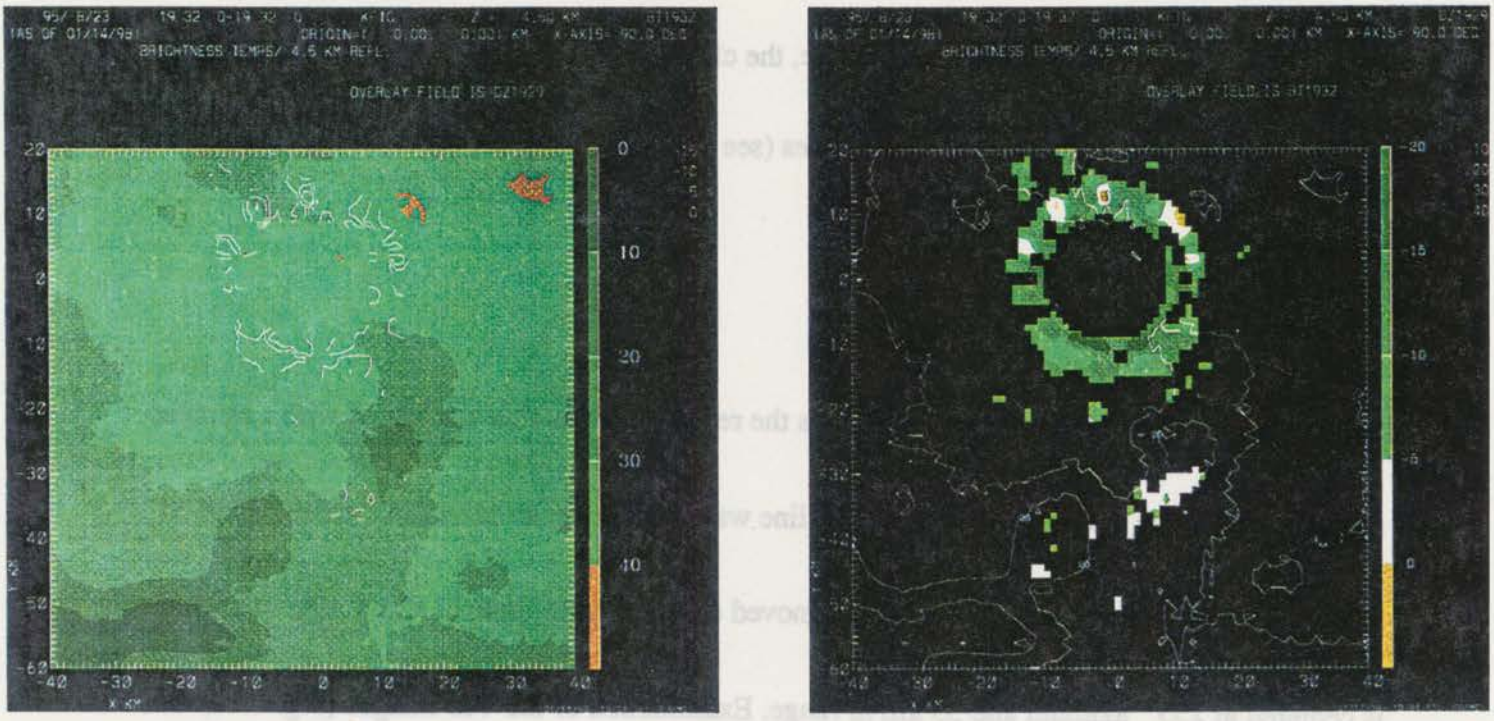

(c) GOES-8 VISIBLE CHANNEL (counts)

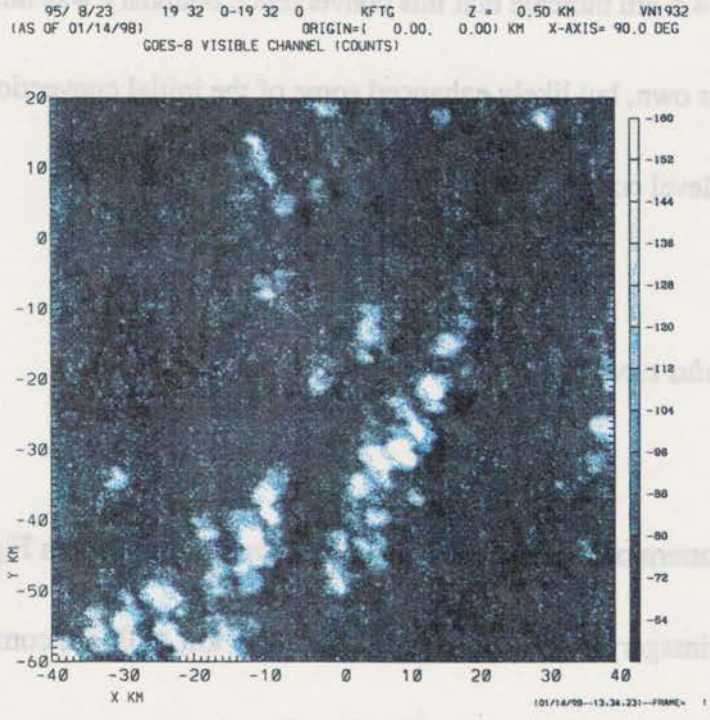

Figure 4.12. CEDRIC plots at 1932 on 23 August 1995 of a) IR brightness temperatures (in deg C) with contours of reflectivity overlaid, b) KFTG reflectivity (in dBZ) at 4.5 km AGL with contours of brightness temperature overlaid, and c) GOES-8 Visible image in counts (negative for plotting purposes only).

(centered at x = 10, y = -30) temperatures (15-20 deg C) compared to the clear sky background temperatures of 30-40 deg C (light green to orange colors). Cumulus clouds associated with the DCVZ are located to the W-SW of this stationary cloud line (in panel c). Over the next 30 min, there is noticeable growth in the cloud lines as evidenced by the brighter gray shades and increased areal extent of the clouds (panel c, Figs. 4.12 - 4.14). The corresponding brightness temperature fields at 2002 indicate temperatures of 5-10 deg C along the stationary cloud line, representing a 10 deg C drop in cloud top temperatures during the 30 min period. Temperatures of 5 deg C correspond to a height of 2.5 km AGL (4.1 km MSL on the sounding), approximately 500 m above the Level of Free Convection (LFC), as obtained from Fig. 4.1 using the afternoon Convective Temperature. Cloud top temperatures may actually be colder than these values at points along the line where the clouds do not completely fill the pixels of data. That is, the satellite field of view at given grid point may be only partially filled by cloud. Radiation sensed by the satellite will have warmer emissions because the radiometer is receiving radiation both from the cloud and the ground under those conditions.

Examination of the reflectivity aloft (panel b) show the presence of transient -3 to -10 dBZ echoes aligned with the cloud line during the same 30 min period. The cluster of weak return at x = 9, y = -33, in Fig. 12b is the vertical extension of backscattering due to insects caught up in the updrafts of a horizontal convective roll. By 1945 and 2002, most of the echo along this portion of

19:45 UTC

(a) BRIGHTNESS TEMPERATURE (° C)

(b) WSR88-D RADAR REFLECTIVITY

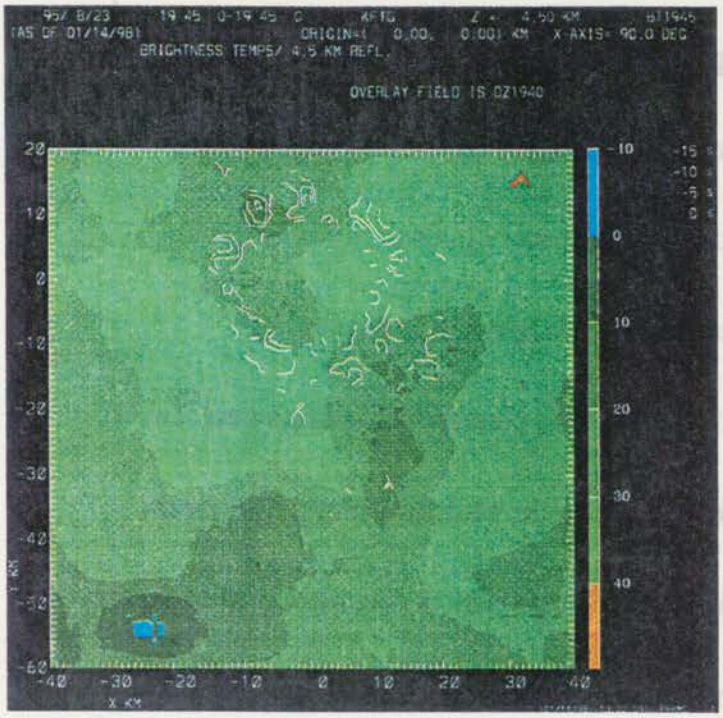

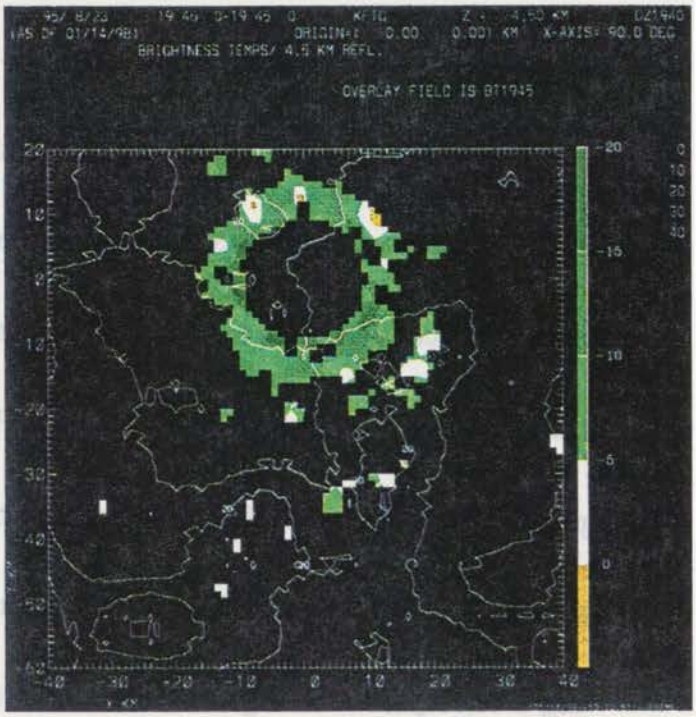

(c) GOES-8 VISIBLE CHANNEL (counts)

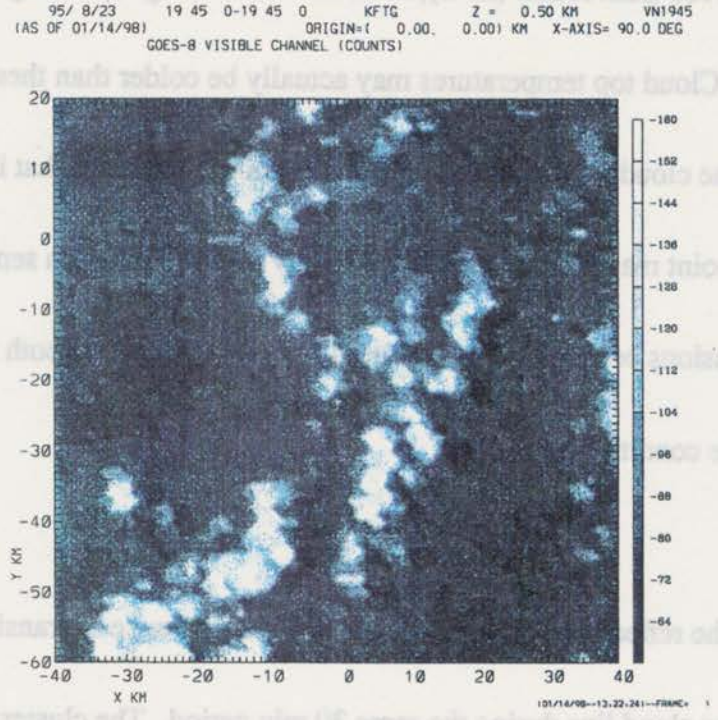

Figure 4.13. Same as Fig. 4.12, exept at 1945 UTC.

20:02 UTC

(a) BRIGHTNESS TEMPERATURE (° C)

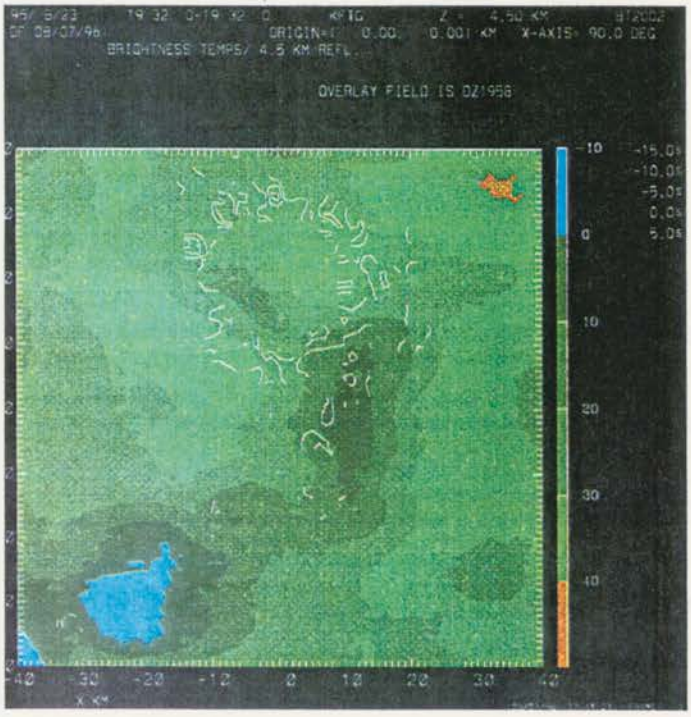

(b) WSR88-D RADAR REFLECTIVITY

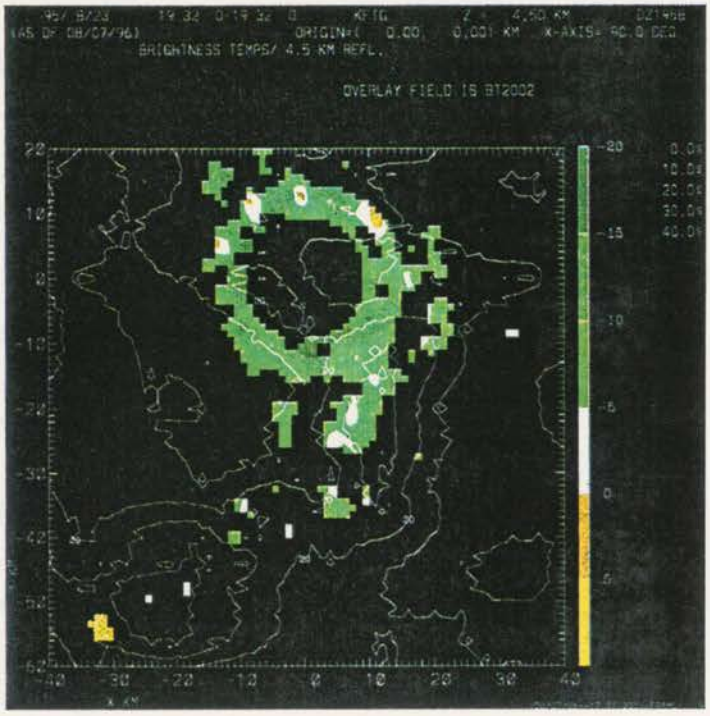

(c) GOES-8 VISIBLE CHANNEL (counts)

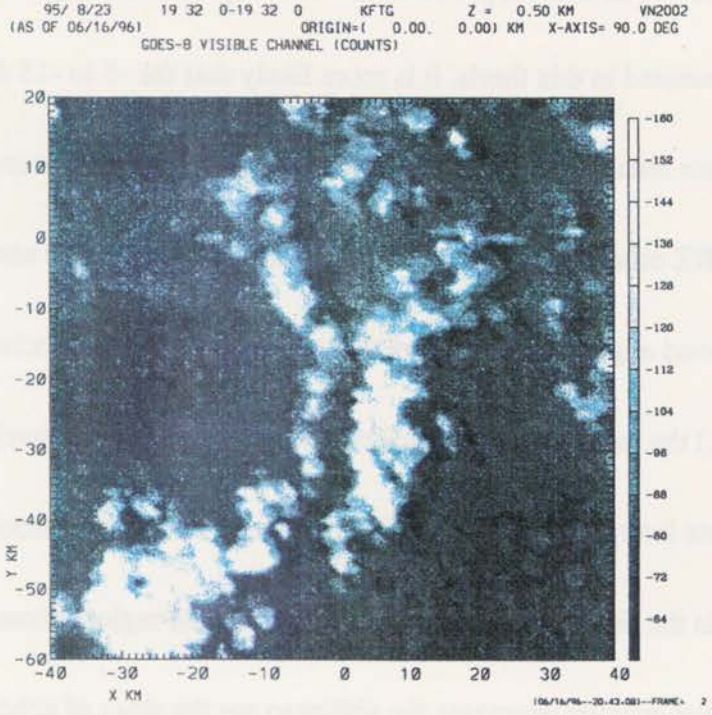

Figure 4.14. Same as Fig. 4.12, except at 2002 UTC.

the line is gone. It is interesting to note that most of the -5 to 0 dBZ echo existed only along the axis of the cloud line.

A curious feature that shows up at all 5 time periods is a ring of -5 to -15 dBZ return within 10 km range of the radar. The Visible imagery shows the presence of cumulus clouds at some locations along this ring of echo. In the Knight and Miller (1993) study, cumulus clouds < 10 km from the radar produced detectable backscatter. However, Gossard and Strauch (1983) found that backscatter echo from cumulus clouds generally had values ranging from -15 to -30 dBZ, which is lower than the values observed in these plots. Since this ring of reflectivity is observed in the data from all four cases presented in this thesis, it is more likely that the -5 to -15 dBZ echo is associated with clear air return interpolated upward from lower altitudes in the boundary layer. It is possible that the -5 to 5 dBZ echo embedded in the lower reflectivities may be associated with Bragg scattering along the cloud edges. Three factors that make it difficult to conclude that Bragg scattering is present are: 1) the lack of an additional radar data at a different wavelength to compare echo returns, 2) the data interpolation scheme likely includes information from particulate scattering at lower altitudes in the higher altitude plots, especially in the regions close to the radar, and 3) the 1 km reflectivity gate spacing decreases the ability to see the rings of echo along the cloud boundaries. Hardy and Ottersten (1969), Christian and Wakimoto (1989) and Henry and Wilson (1993) were able to see the echoes with higher resolution data.

Of particular interest for this thesis is the region of -10 to 0 dBZ echoes (centered at x = 7, y = -23) that appear at 2002 and the 5 dBZ echo located in the SW corner of the plot associated with the large cluster of clouds with subfreezing cloud top temperatures. In the next 15 min (Fig. 4.15) the latter echo had intensified dramatically to > 35 dBZ and the cumulus congestus cloud top temperatures had fallen to < -10 deg C. By 2032 (Fig. 4.16b), this echo was a mature storm with > 45 dBZ precipitation and cloud top temperatures < -30 deg C. In contrast, the -10 to 0 dBZ echoes aligned with the cloud line that intersected the DCVZ, did not intensify as quickly, increasing only to a 5 dBZ, non-precipitating echo over the next 15 min (Fig. 4.15b). But as can be seen in the Visible imagery, the growth of the clouds are evident from the brighter shades of gray and the larger areal extent of the cloud clusters. The corresponding IR cloud top temperatures along the northern portion of the cloud line had fallen below 0 deg C. It is clear that the non-precipitating 5 dBZ echo is associated with Bragg backscattering from a growing cluster of cumulus clouds. With cloud temperatures close to freezing, these echoes are likely not associated with insects within the updrafts of the clouds. It has been shown by Cockbain (1961), Taylor (1963) and Walters and Dixon (1984) that insect flight is rarely observed when temperatures are below 10 deg C. The sequence of plots presented in Figs. 4.12 - 4.15, indicate that the reflectivity echoes associated with this cloud line have evolved from particulate to Bragg scattering and, within the next 15 min, to Rayleigh scattering by precipitation particles (> 25 dBZ echo in Fig. 4.16b). By 2032, cloud top temperatures were -6 deg C, with warmer cloud top temperatures along the

20:15 UTC

(a) BRIGHTNESS TEMPERATURE (° C)

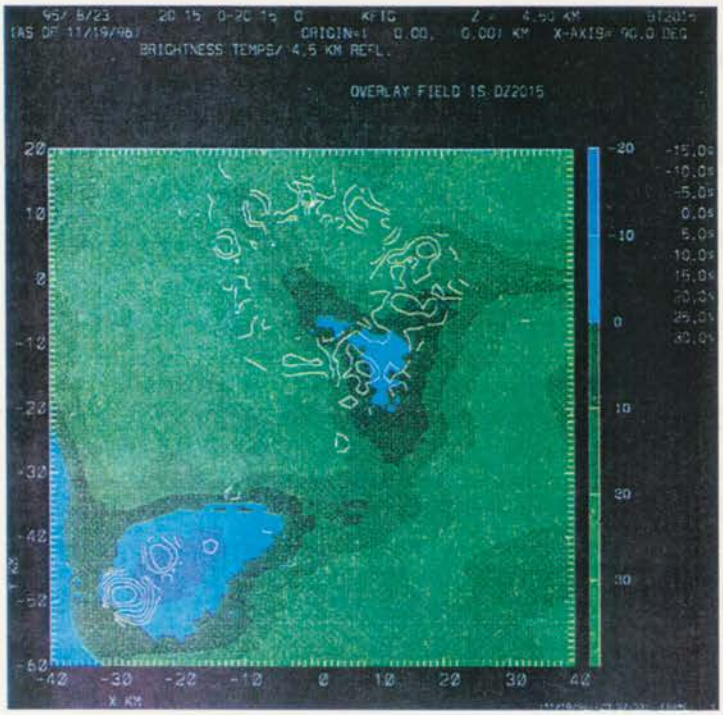

(b) WSR88-D RADAR REFLECTIVITY

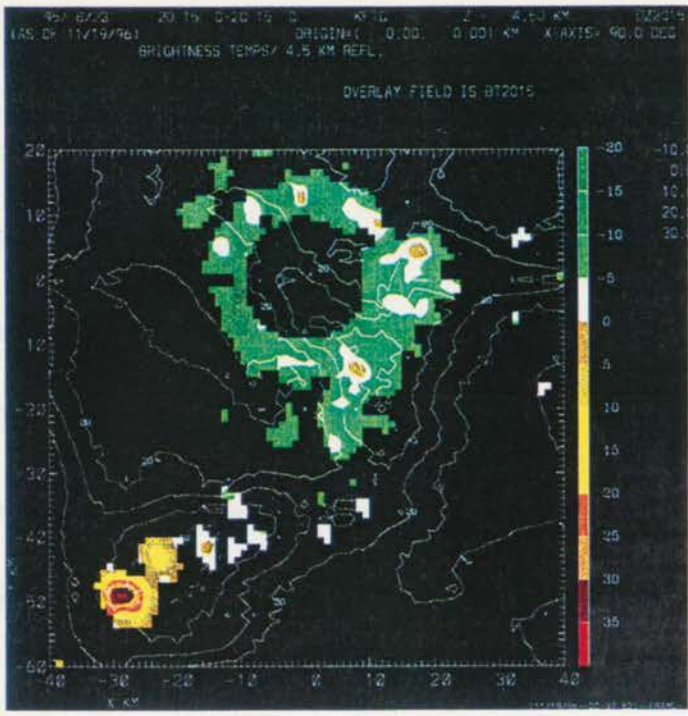

(c) GOES-8 VISIBLE CHANNEL (counts)

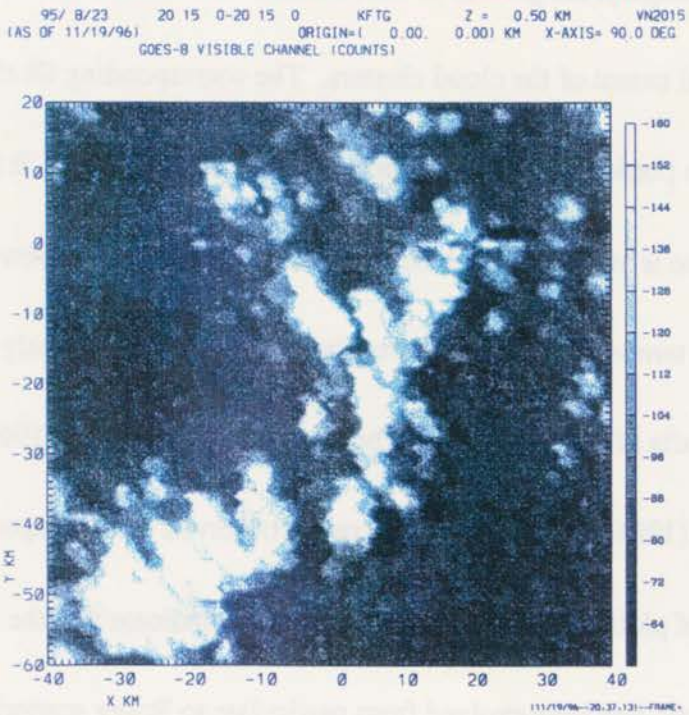

Figure 4.15. Same as Fig. 4.12, except at 2015 UTC.

20:32 UTC

(a) BRIGHTNESS TEMPERATURE (° C)

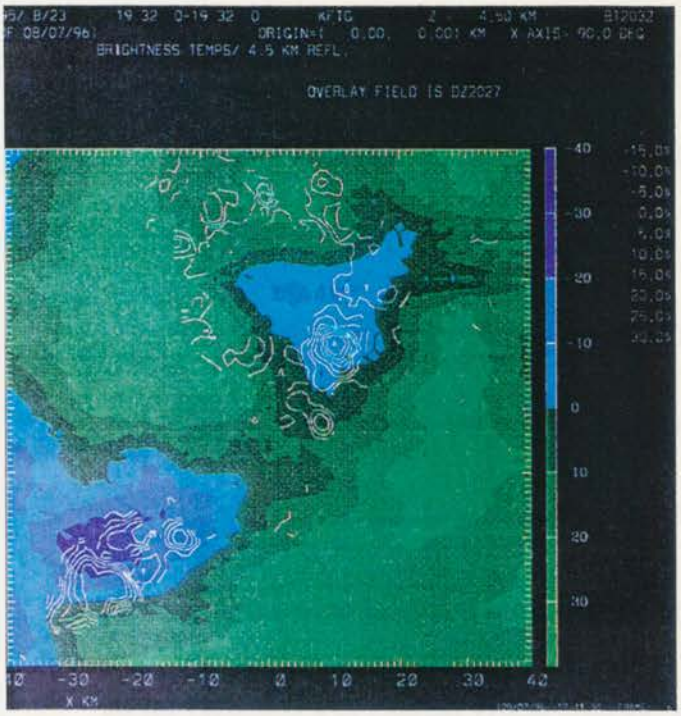

(b) WSR88-D RADAR REFLECITIVITY

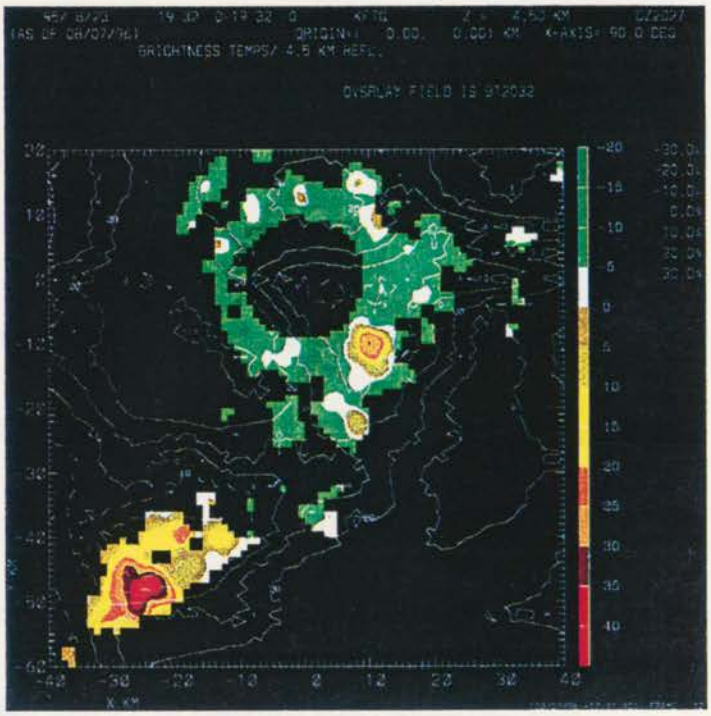

(c) GOES-8 VISIBLE CHANNEL (counts)

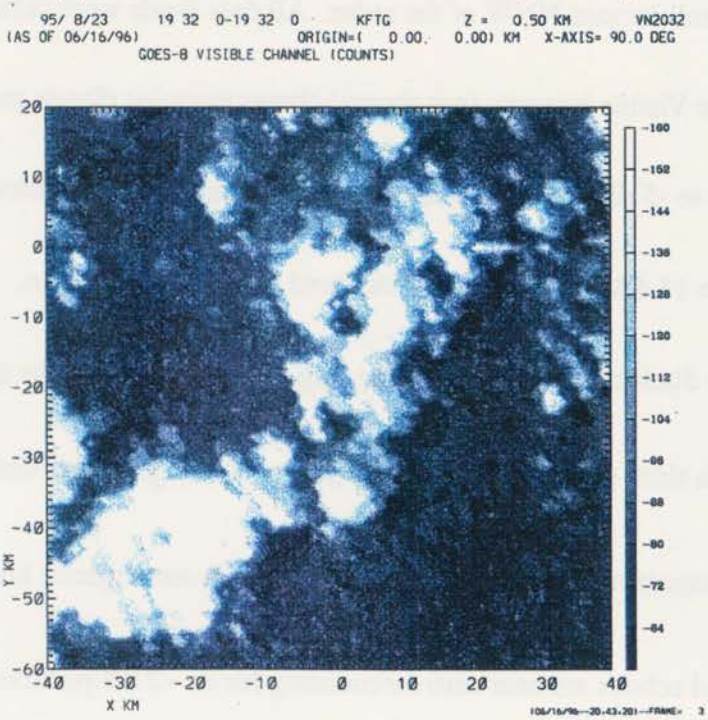

Figure 4.16. Same as Fig. 4.12, except at 2032 UTC.

southern portion of the cloud line (see Fig. 4.16a). The clouds in Fig. 4.16c were no longer small clusters of cumulus, but had grown in area and vertical extent to cumulus congestus clouds.

A visually impressive example of the evolution of radar backscattering off of growing cumulus clouds is shown in the series of RHI images in Fig. 4.17. This data was collected by the 10 cm CHILL radar that is operated by the Colorado State University north of Greeley, Colorado. The RHI cross-sections of reflectivity, radial velocity and Z_{dr} (ratio of horizontal to vertically polarized reflectivity) data collected on 13 July 1995 were oriented nearly parallel to a boundary layer, horizontal convective roll located NNW of the radar. All data fields were collected with 150 m gate spacing. Satellite Visible imagery (not shown) shows cumulus clouds present all along the roll. In Fig. 4.18a, -10 to -5 dBZ Bragg backscatter echoes outlining the cumulus clouds are evident, located above the 15 dBZ horizontal roll centered near 40 km in range. One of the cloud echoes at 39 km had a distinct mantle echo. Receding velocities suggest the presence of upward motion along the north sides of the echoes. The large, positive Z_{dr} values within the roll means the presence of large aspect ratio insects, caught up in the roll convergence and updraft. The Z_{dr} values within the cloud echoes are near zero (accounting for an ~2 dB positive bias in Z_{dr} on this day), which is consistent with the expected targets of small spherical cloud droplets. The rapid growth of the cloud at 44-46 km range is illustrated by its transition from a Bragg scatter mantle echo (Fig. 4.17b) to a 25 dBZ Rayleigh precipitating echo (Fig. 4.17d) and by its transition to

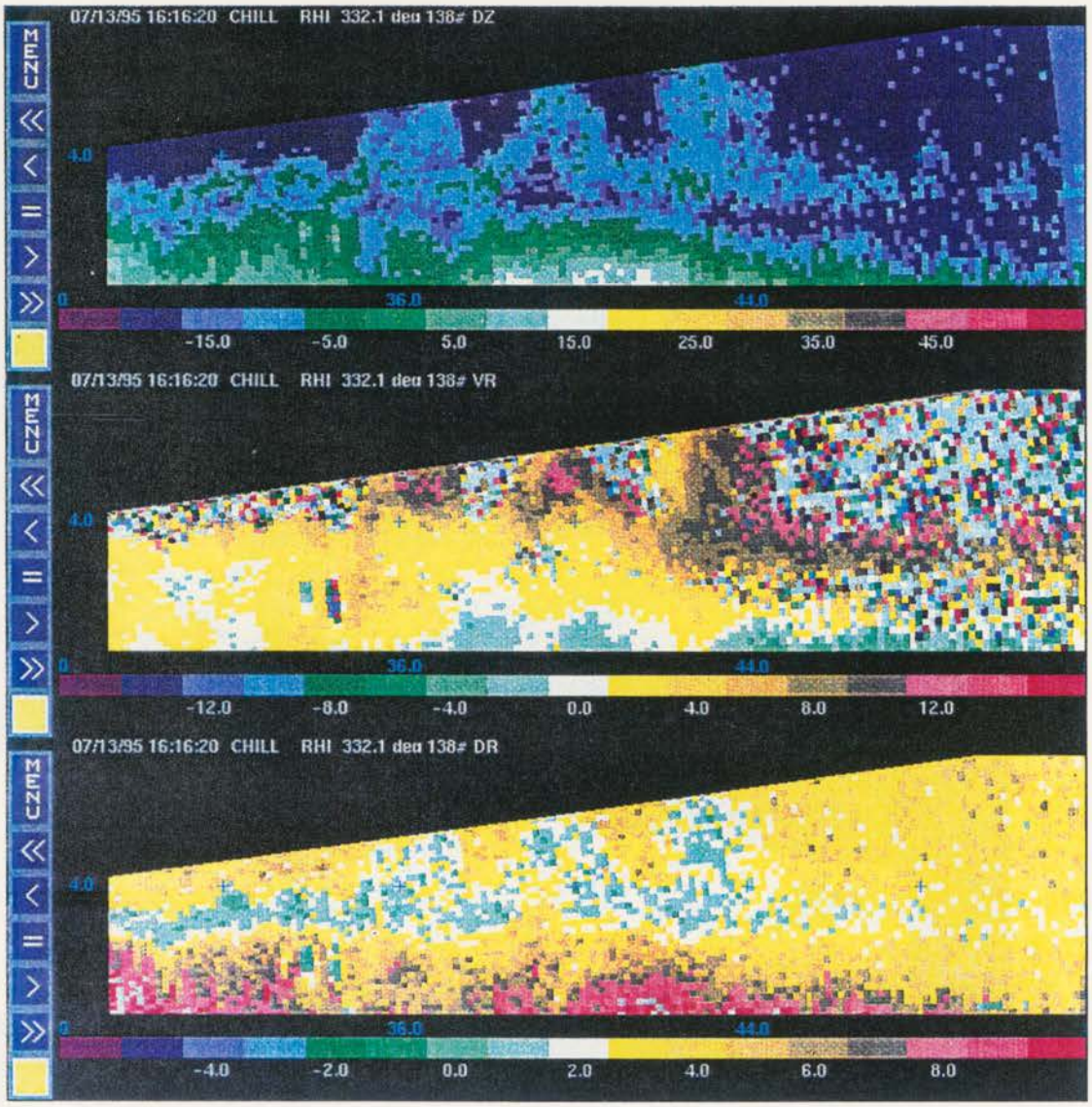

Figure 4.17. Plots of reflectivity (dBZ), radial velocity (m/s) and differential reflectivity (Zdr) collected by the CHILL radar on 13 July 1995. a) 1616 MDT.

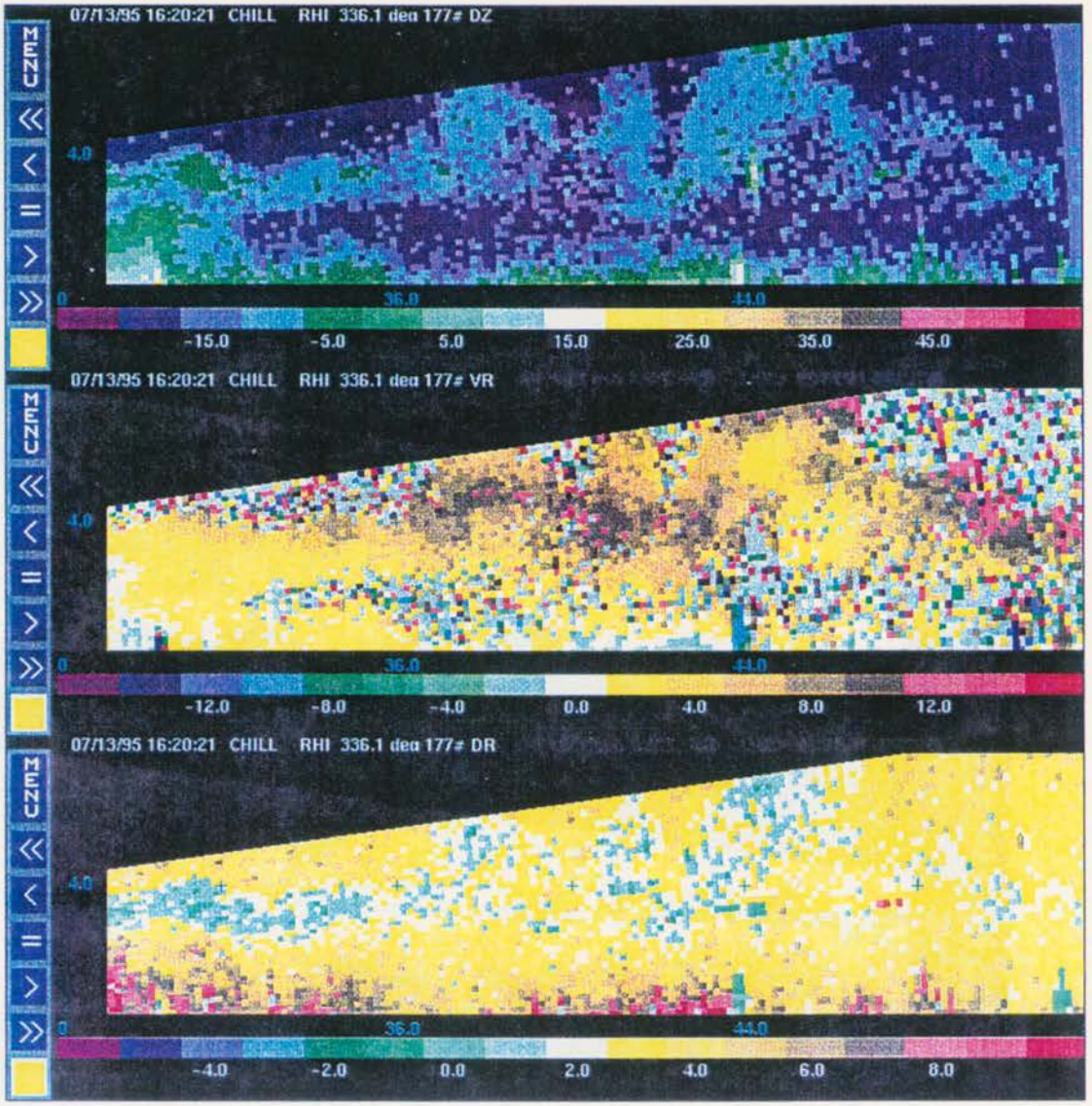

Figure 4.17. b) At 1620 UTC.

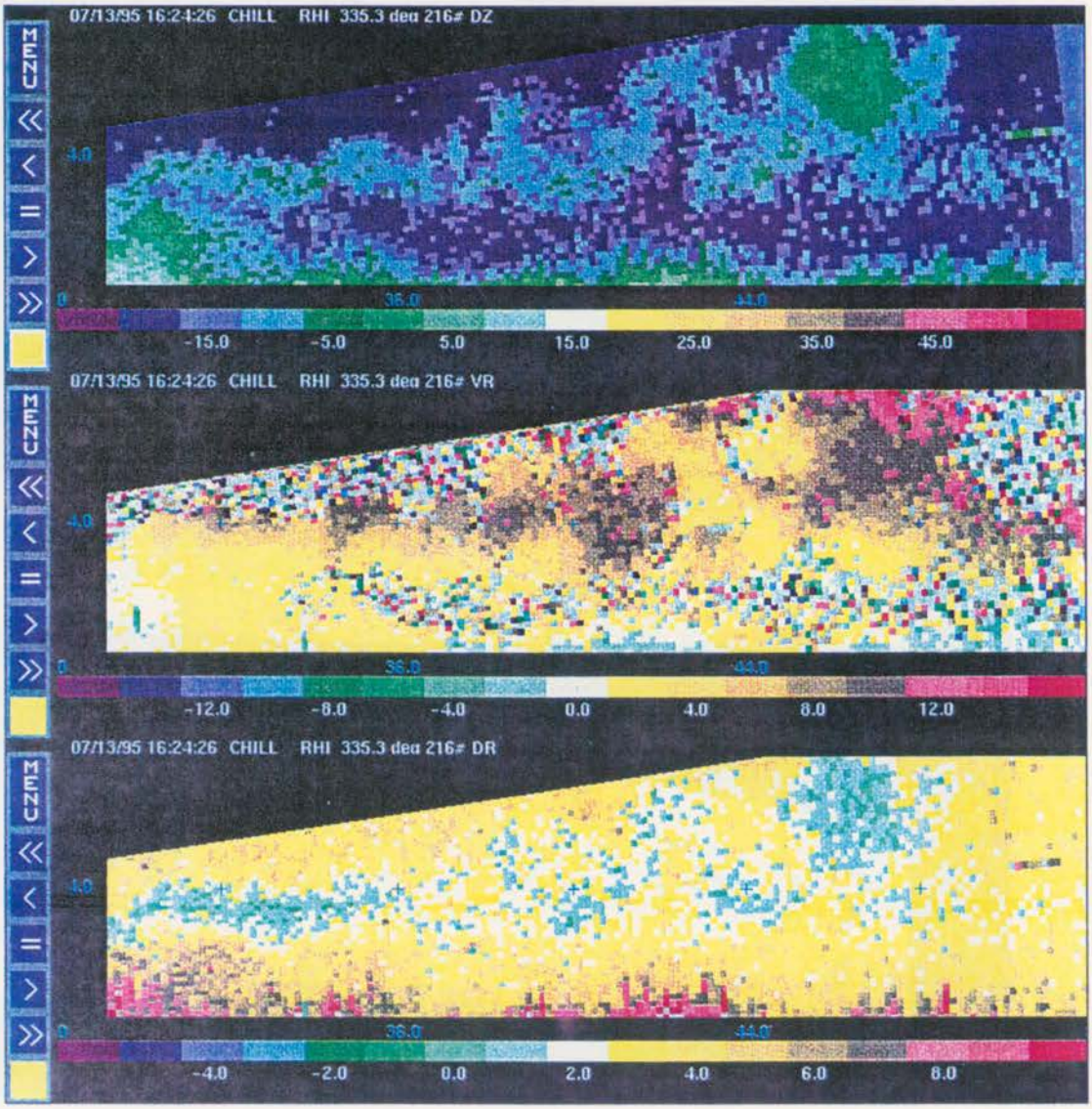

Figure 4.17. c) At 1624 MDT.

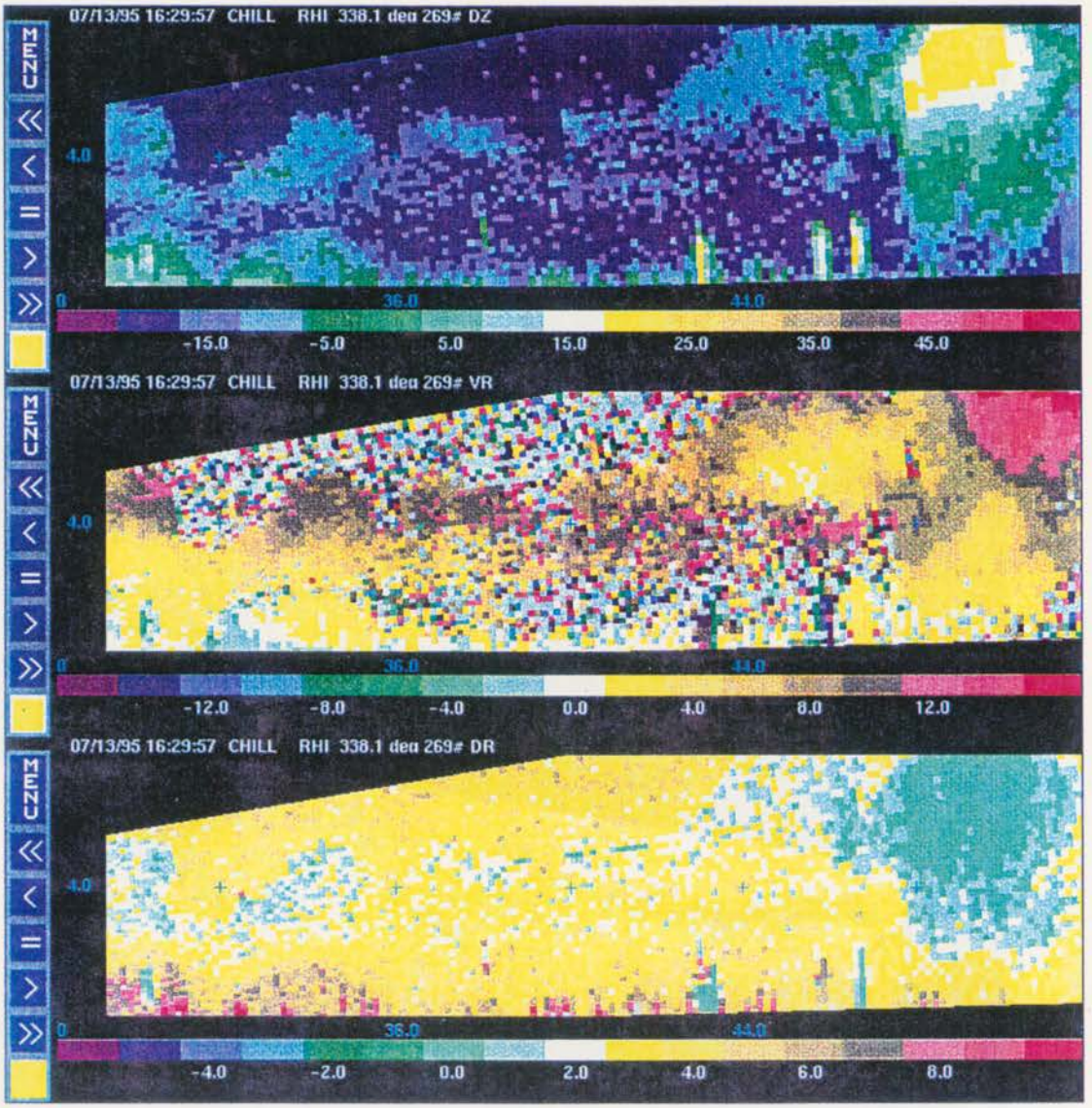

Figure 4.17. d) At 1629 MDT.

0 dB Z_{dr} values, likely caused by graupel. The change over from Bragg to Rayleigh backscattering echo actually starts in Fig. 4.17c. The satellite IR data shows sub-freezing cloud top temperatures at this time suggesting that the early Rayleigh targets are indeed ice particles.

In Fig. 4.18, histograms of brightness temperature and radar reflectivity taken along the 23 August cloud line are plotted with time. The minimum and median value for the brightness temperature plots reflect the trend toward colder cloud tops (and increasing cloud top heights) with time. The minimum and median values at each time period compiled from the histogram data are also plotted in Fig. 4.19, along with the maximum reflectivity along the cloud line. Figs. 4.18 and 4.19 summarize the sequence of events described above. The reflectivity histograms show the persistence of weak, < 0 dBZ echo from 1932 to 2002 due to clear air scattering by insects, while minimum brightness temperatures drop from 15 to -3 deg C. Fifteen minutes later, at 2015, radar echoes due to Bragg scattering are now approaching 10 dBZ intensity as cloud top temperatures cool further to -8 deg C. Growth continues with time, with echoes reaching 35 dBZ by 2032. As can be seen graphically in Fig. 4.19, the reflectivity intensity begins to increase only after the cloud top temperatures drop substantially below freezing, suggesting that the earliest precipitation-sized targets are due to ice. Figure 4.19 shows that satellite data can provide information on cloud growth 15-30 min prior to appreciable radar precipitation echo. This additional lead time to forecast thunderstorm initiation would be quite important to forecasters.

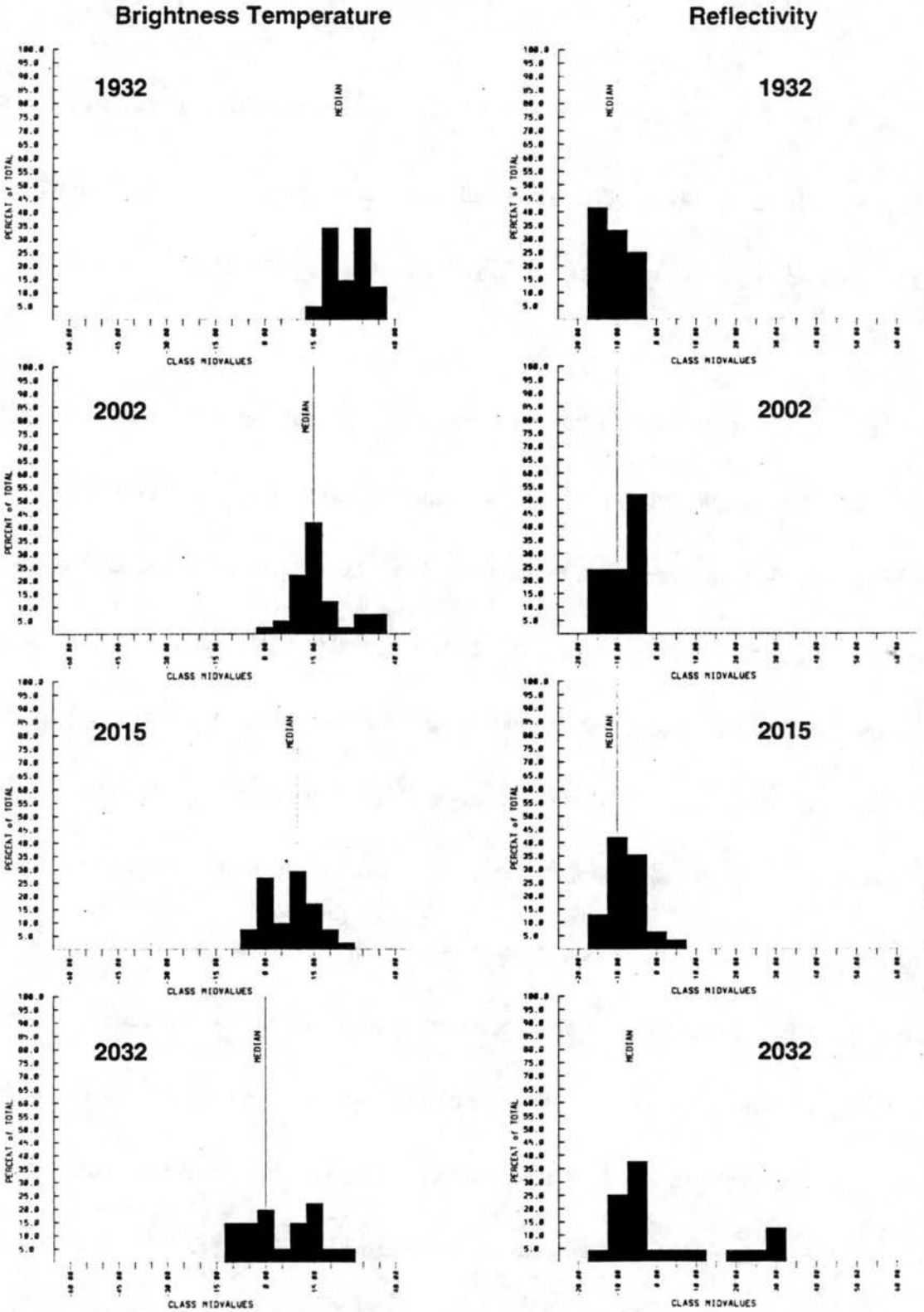

Figure. 4.18. Histogram plots of GOES-8 brightness temperature (deg C) and KFTG maximum reflectivity at 4.5 km AGL. Data is from 23 August 1995, at 1932, 2002, 2015, and 2032 UTC. The thin vertical line above the histogram bars is the median value for each plot.

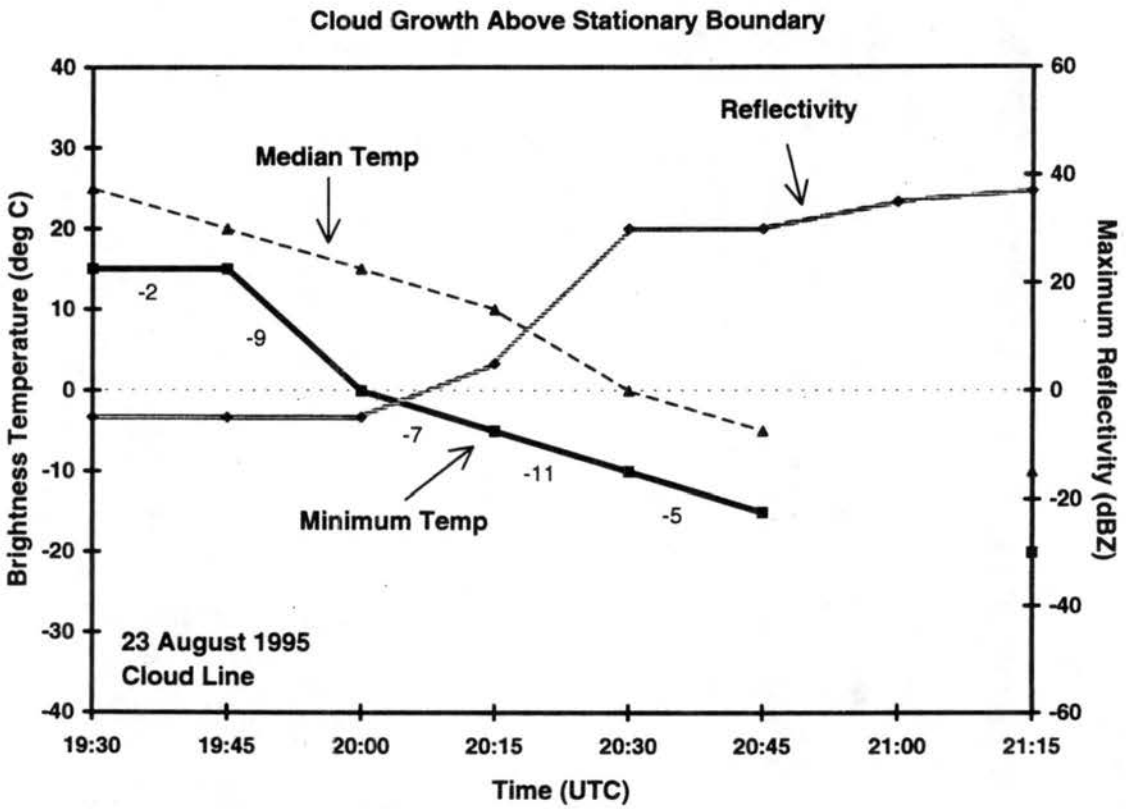

Figure 4.19. Time series plot of Infrared brightness temperature (deg C) and maximum radar reflectivity (dBZ) associated with growth of the cloud line above the DCVZ. Median (dashed curve) and minimum (black solid curve) temperature values and maximum reflectivity (gray curve), obtained from histogram information, are shown.

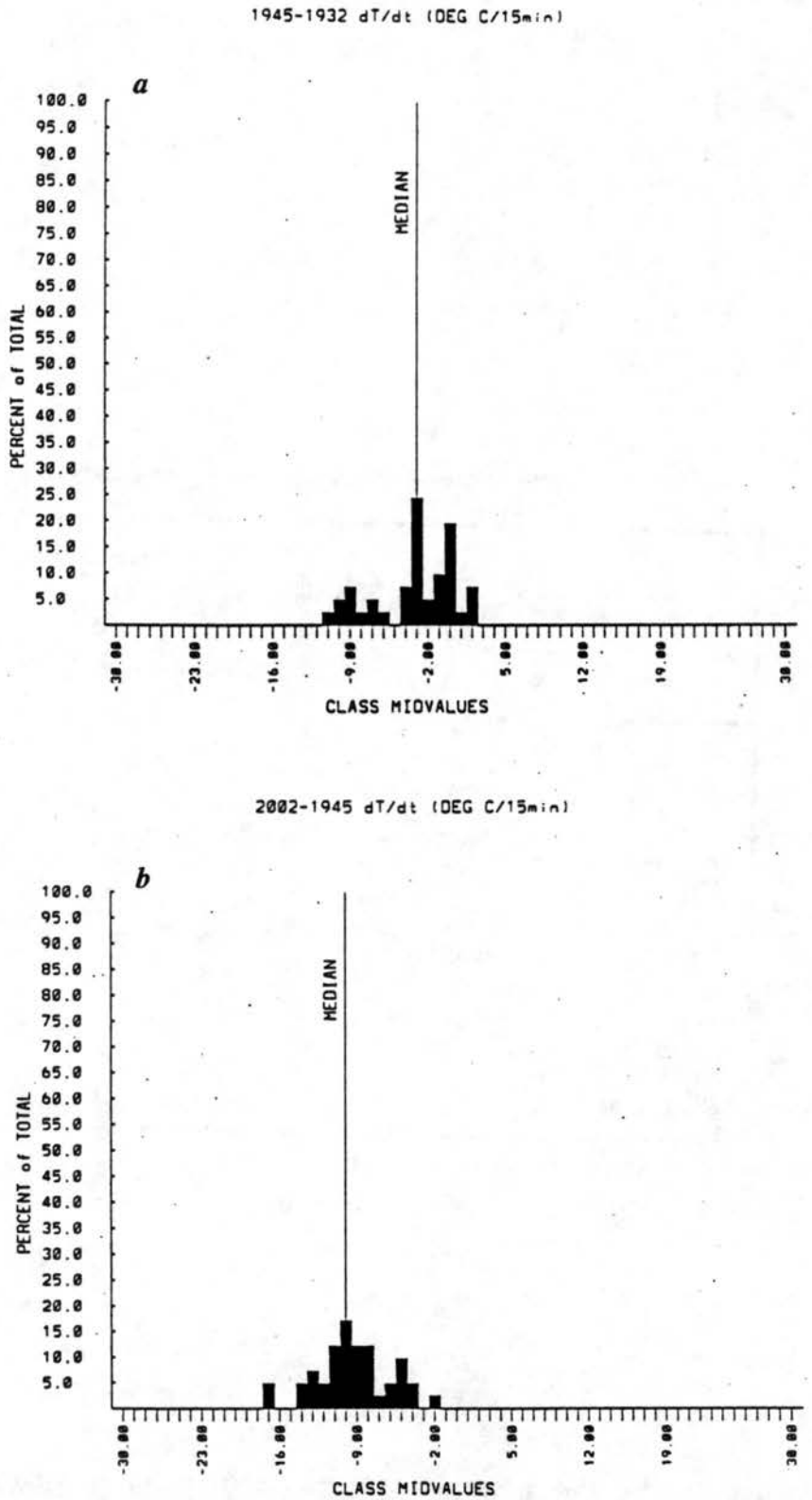

Figure 4.20. Histogram plots of change in brightness temperature with time for time period a) 1932 - 1945 UTC and b) 1945 - 2002 UTC. The thin vertical line above the histogram bars is the median value for each plot.

It will be seen later that for forecasting thunderstorm initiation, it is important to not only monitor cloud top temperatures, but also to monitor the time rate of change of the brightness temperatures. Histograms of the time rate of change of brightness temperatures are shown in Fig. 4.20 for the first two, 15 min time periods. During the early stages of storm growth, between 1932-1945, the time rate of change of temperature varied from +3 to -11° C over a 15 min period. Once storm growth ensued, the time rate of change of temperature over the next 15 min period shifted to values ranging from -2 to -17° C per 15 min period. The median values in Fig. 4.20 also reflect this increased rate of change; that is, -3° C/15 min at 1945 to -10° C/15 min at 2002. The median time rate of change for all 15 min intervals are listed below the minimum temperature curve in Fig. 4.19. In this example, some of the largest values of temperature change occur before the reflectivity echo intensifies. Data from 21 and 24 July will illustrate how this time rate of change information can be helpful in distinguishing between active and suppressed growth in clouds.

4.2 24 August 1995

4.2.1 Environmental conditions

The 1200 UTC DEN NWS sounding in Fig. 4.21 indicates the potential for convective activity that existed on 24 August 1995. The CAPE was 247 J/kg, less than on 23 August, and a CIN

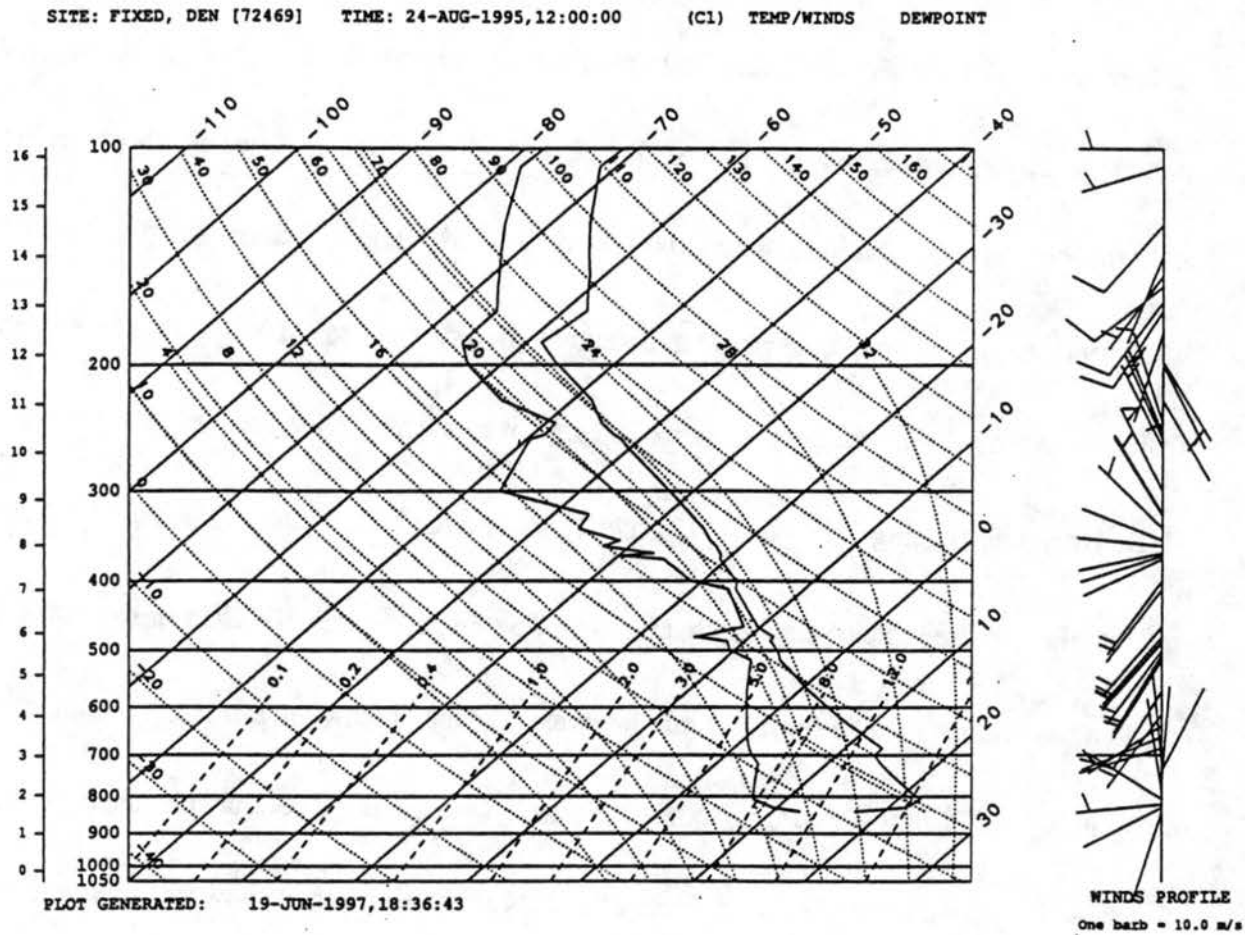

Figure 4. 21. Denver NWS 1200 UTC sounding from 24 August 1995.

of 102 J/kg had to be overcome in order for upward moving parcels to penetrate above the LFC. The mean surface moisture of ~8.5 g/kg observed in the lowest 50 m of the boundary layer did not mix out to lower values during the afternoon, but instead mixed upward to 600 mb by 00 UTC. By 2100 UTC, a convective temperature of 32° C was reached in Denver and at 00 UTC, the temperature profile below 600 mb was dry adiabatic. The forecasted LI for the afternoon was -1.22, just barely in the range of values observed when thunderstorms occur in Colorado near convergence boundaries (Mueller et al., 1993). The wind profile in Fig. 4.21 indicated extremely light, 5 kt winds at all heights and minimal directional shear. Similar magnitudes were observed in the 00 UTC sounding (not shown). These light winds are unusual for eastern Colorado even under the influence of a high pressure ridge that was present on this day at 500 mb (Fig. 4.22). The 700 mb map (Fig. 4.23) showed the presence of a weak disturbance over Colorado, 10 kt SW winds upstream of Denver, and calm over Denver. The low pressure trough associated with this disturbance can be seen on the 850 mb map (Fig. 4.24) and by the dashed line on the surface map (Fig. 4.25) at 1800 UTC. This trough line marks the boundary between the weak environmental flow in Colorado and the stronger 15-30 kt southerly winds, and higher temperatures and dewpoints in eastern Kansas. Given the above synoptic and local environment, it is not surprising that convection occurred first over the mountains and storms propagated slowly. As will be seen in the next section, even though the convective temperature was reached by 2100, convection over the Plains required some boundary layer forcing from storm outflows to initiate new storms.

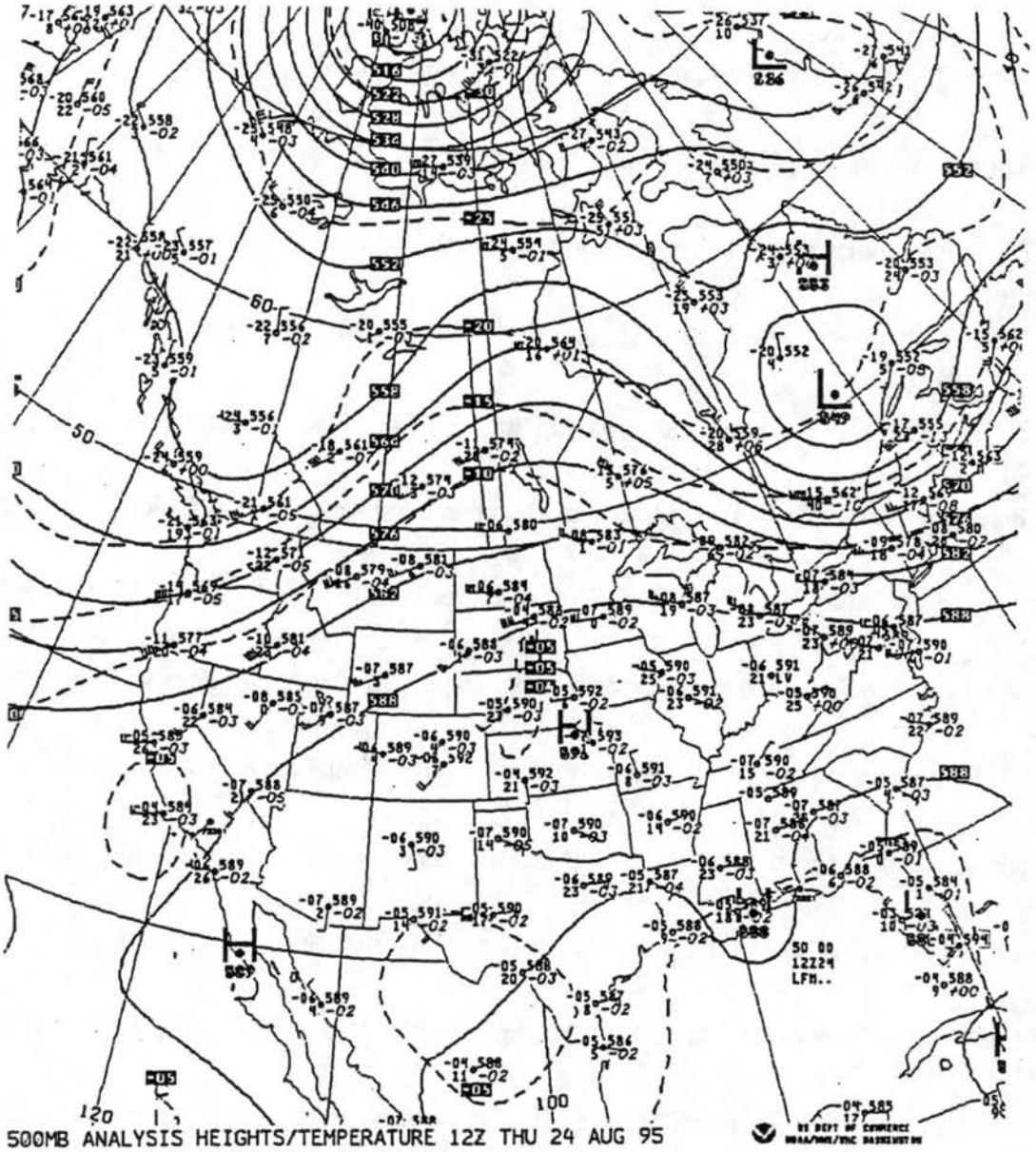

Figure 4.22. Upper air 500 mb map from 24 August 1995 at 1200 UTC.

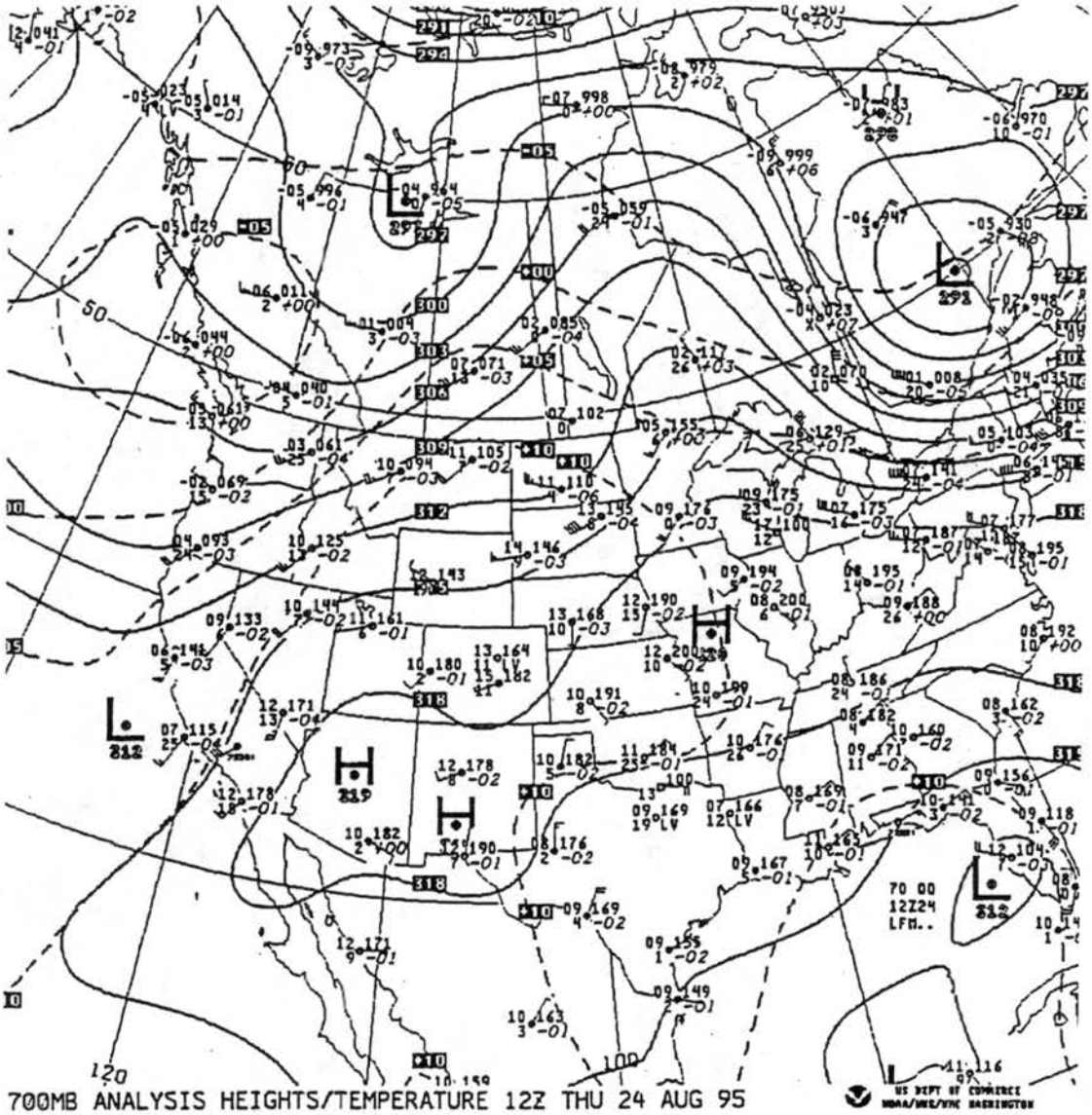

Figure 4. 23. Upper air 700 mb map from 24 August 1995 at 1200 UTC.

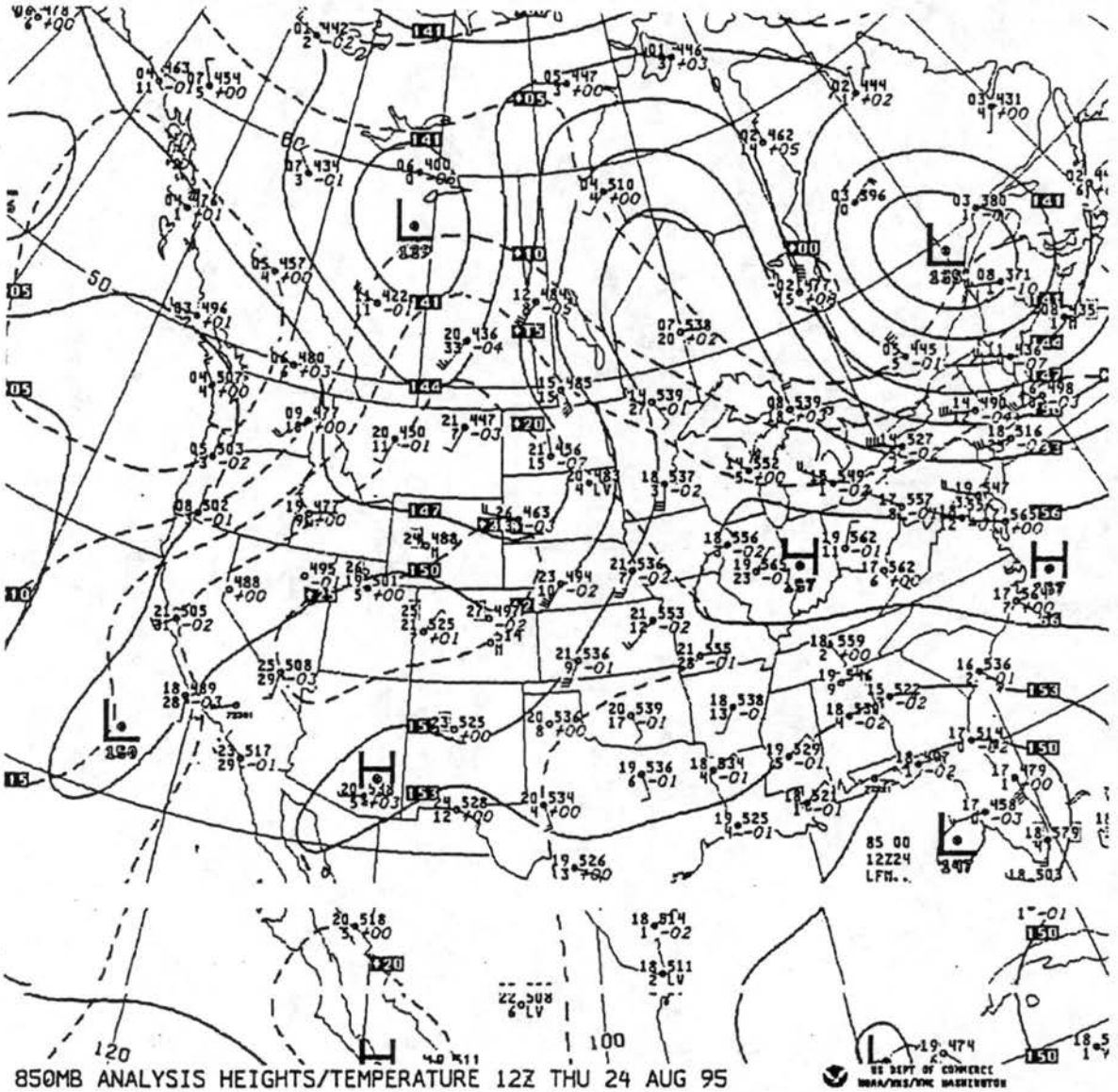

Figure 4.24. 850 mb map from 24 August 1995 at 1200 UTC.

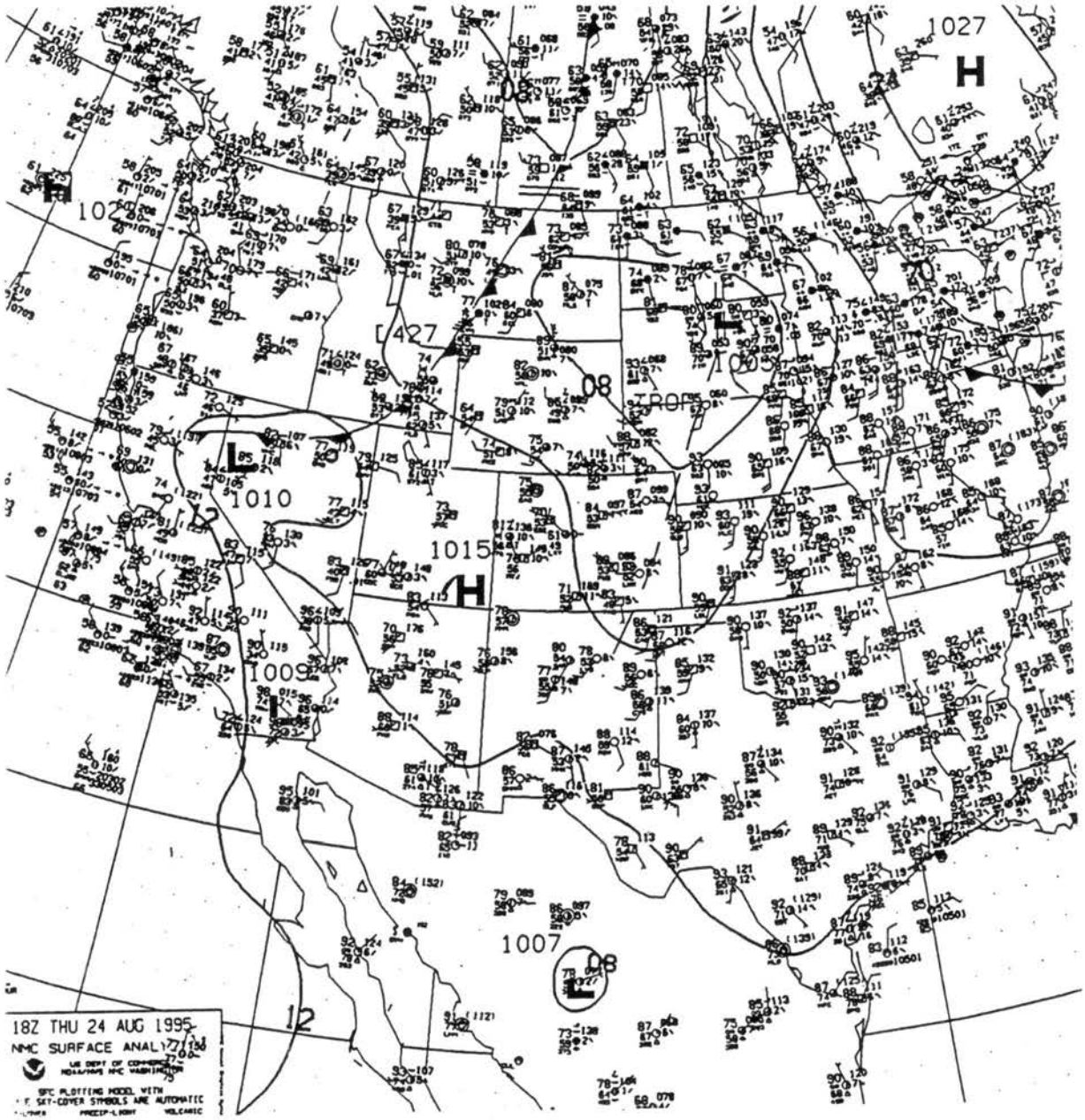

Figure 4.25. Surface analysis map from 24 August 1995 at 1800 UTC

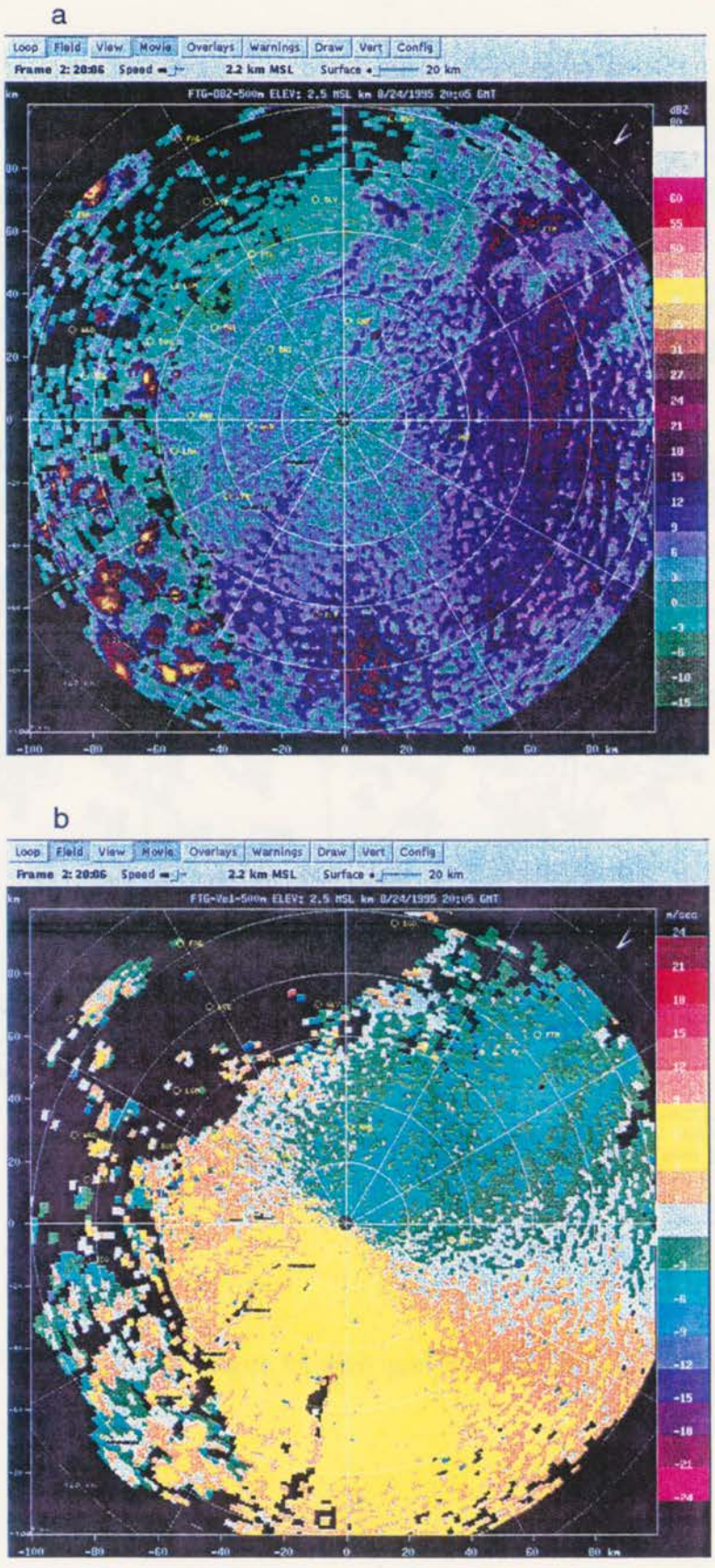

Figure 4.26. Low level, 0.5 km AGL plots of a) KFTG reflectivity (dBZ) and b) radial velocity (m/s) at 20:05 UTC on 24 August 1995.

4.2.2 Relationship of clouds to boundary-layer features

The low altitude plot of reflectivity at 2005 UTC illustrating the boundary layer structure is shown in Fig. 4.26a. Except for the few storms over the mountains (50 km in range west of the radar), horizontal rolls prevailed throughout most of the eastern plains. The more intense rolls (>12 dBZ) had roughly a N-S orientation, in agreement with the orientation of the uni-directional environment winds from the sounding (Fig. 4.21). The companion velocity plot, Fig. 4.26b, shows that the low-level flow was from the N-NE at this time. The alternating green, gray and gold velocities E-SE of the radar are another indication of the presence of horizontal rolls. The mean radial speed was 6 m/s, which is just above the minimum wind speed of 5.5 m/s that has been found to be necessary for the existence of horizontal rolls (Weckwerth et al, 1997). No reflectivity thin lines associated with a gust front were present east of the mountains. Figure 4.27 is the corresponding satellite Visible image at 2002. Cumulus congestus and cumulonimbus clouds associated with the storms over the mountains are evident along the left hand side of the image. East of the radar location (x = 0 km, y = 0 km) clusters of cumulus clouds were present with a suggestion of linear orientation, but nothing as obvious as seen with the 23 August case. A denser cluster of cumulus clouds, mixed with some cumulus congestus clouds can be seen to NE of the radar, beyond 80 km in range. A comparison of the radar boundary layer features at 1.5 km with the cumulus cloud clusters is shown in the CEDRIC plot in Fig. 4.28. This plot is a magnification of the upper righthand portion of Fig. 4.27. Overlaying only the 8 and 12 dBZ contours onto the Visible imagery to simplify comparison of features, shows that there is a high correlation between the reflectivity thin lines and the cloud lines centered at x = 45, y = 30, and x = 60, y = 66. Even the cloud lines with less vertical growth, centered at x = 34, y = 15, and at x = 28, y = 14 are aligned

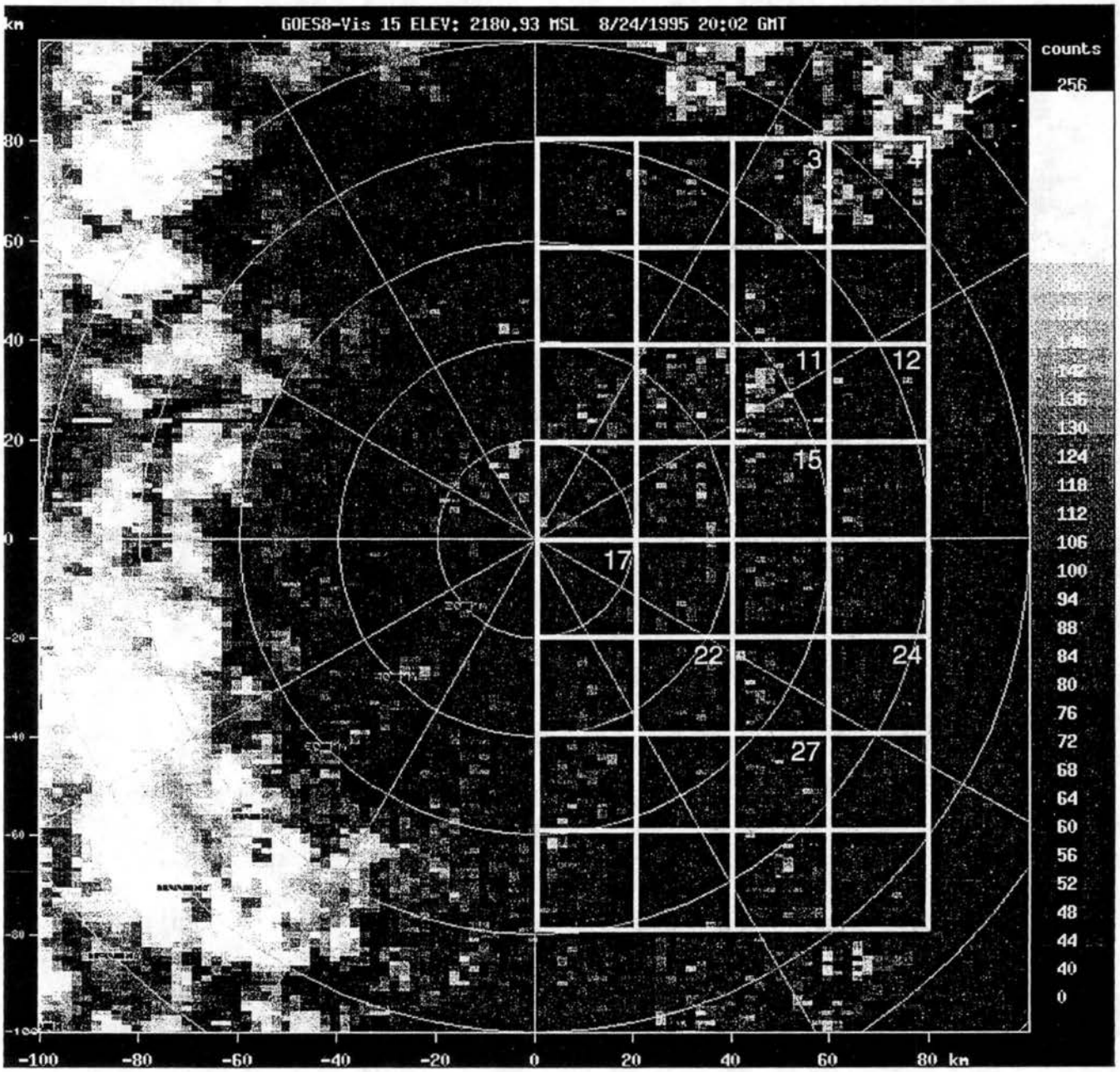

Figure 4.27. Visible satellite image from 24 August 1995 at 2002 UTC. Units are in radiance counts. The gridded region on the plot represents the 20 x 20 km regions analyzed from this day. The numbered boxes represents those regions discussed in the text.

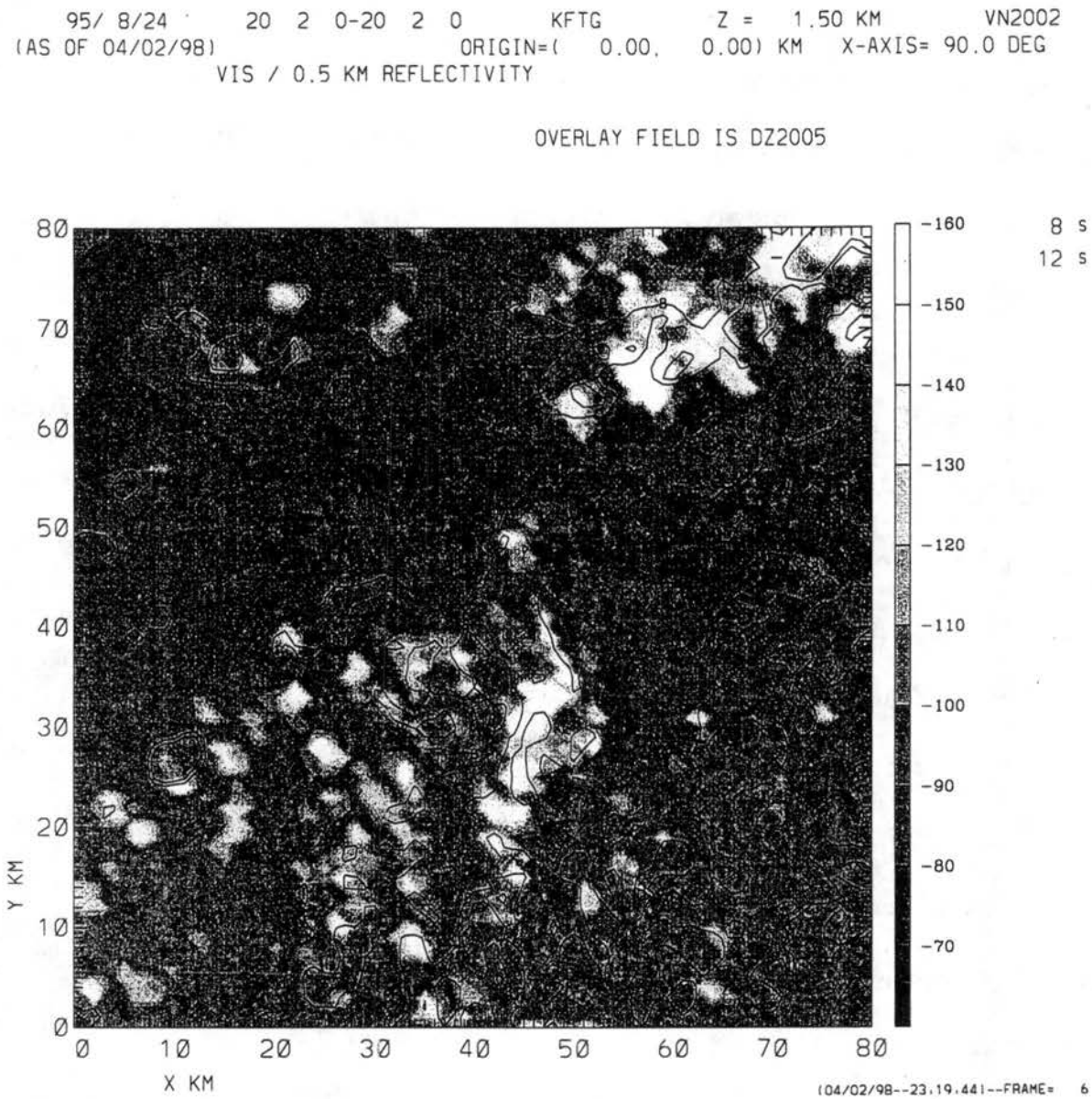

Figure 4.28. Plot of Visible data from 24 August 1995 at 2005 with reflectivity contours overlaid. Contours are in increments of 8 and 12 dBZ. The Visible scale is in radiance counts; values are listed as negative for plotting purposes only.

with the boundary layer rolls beneath them. To the east of these cloud lines in a very broad region with reflectivities <12 dBZ and weaker radial winds (see Fig. 4.26b), is a NNE-SSW cloud line, centered at x = 66, y = 9, with much lower albedoes. The radial convergence of wind is not as strong within this roll and likely accounts for the smaller vertical development of these clouds and lack of a narrow, intense reflectivity thin line in the boundary layer.

The evolution of the boundary layer features can be seen in Fig. 4.29. During the 1.5 hrs following 2000 (Fig. 4.26a) not much change occurred in the boundary layer structure other than the dissipation of some of the less intense, horizontal rolls and the intensification of storms over the mountains. As expected from the synoptic outlook, no storms had formed over the Plains yet. However, by 2231, not only had a few storms made it off the mountains, but a strong ouflow associated with the mountain storms was propagating eastward into the region of horizontal rolls. The thin line associated with this gust front is located to the S-SW of the radar. Another outflow, originating from storms in Wyoming, was moving into the area from the north and can be seen to the northeast of the radar, 75 km in range (Fig. 4.29d). Both of these outflows initiate storms following their passage. In addition, along the rolls that intersect the SW gust front at a perpendicular angle, there was storm growth approximately 10 km ahead of the gust front, a result of enhanced convergence provided by the gust front. Figure 4.30 displays the TREC-derived convergence field associated with the approaching gust front from the SW. Comparison of the convergence region due south of the radar in Fig. 4.30b, with the location of the reflectivity thin line in Fig. 4.29c, indicates that most of the convergence was located ahead of and at the leading edge of the gust front. At 2330, the echoes 20-60 km in range southeast of the radar (Fig. 4.29d) were all located in this convergence region (Fig. 4.30d) ahead of the gust front. Clearly this convergence was

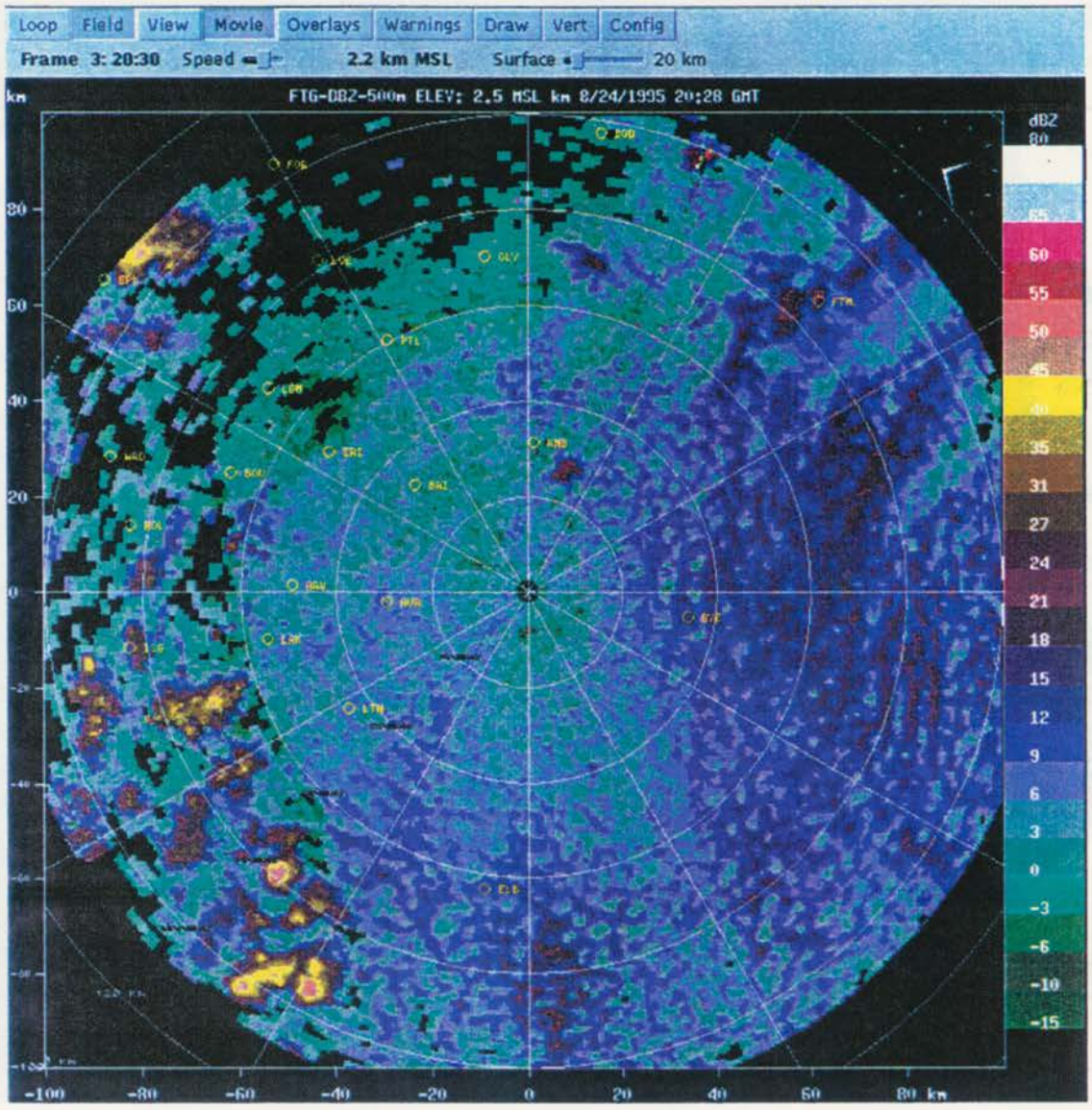

Figure 4.29. Sequence of cartesian, reflectivity plots at 0.5 km AGL from 24 August 1995 at a) 2028 UTC.

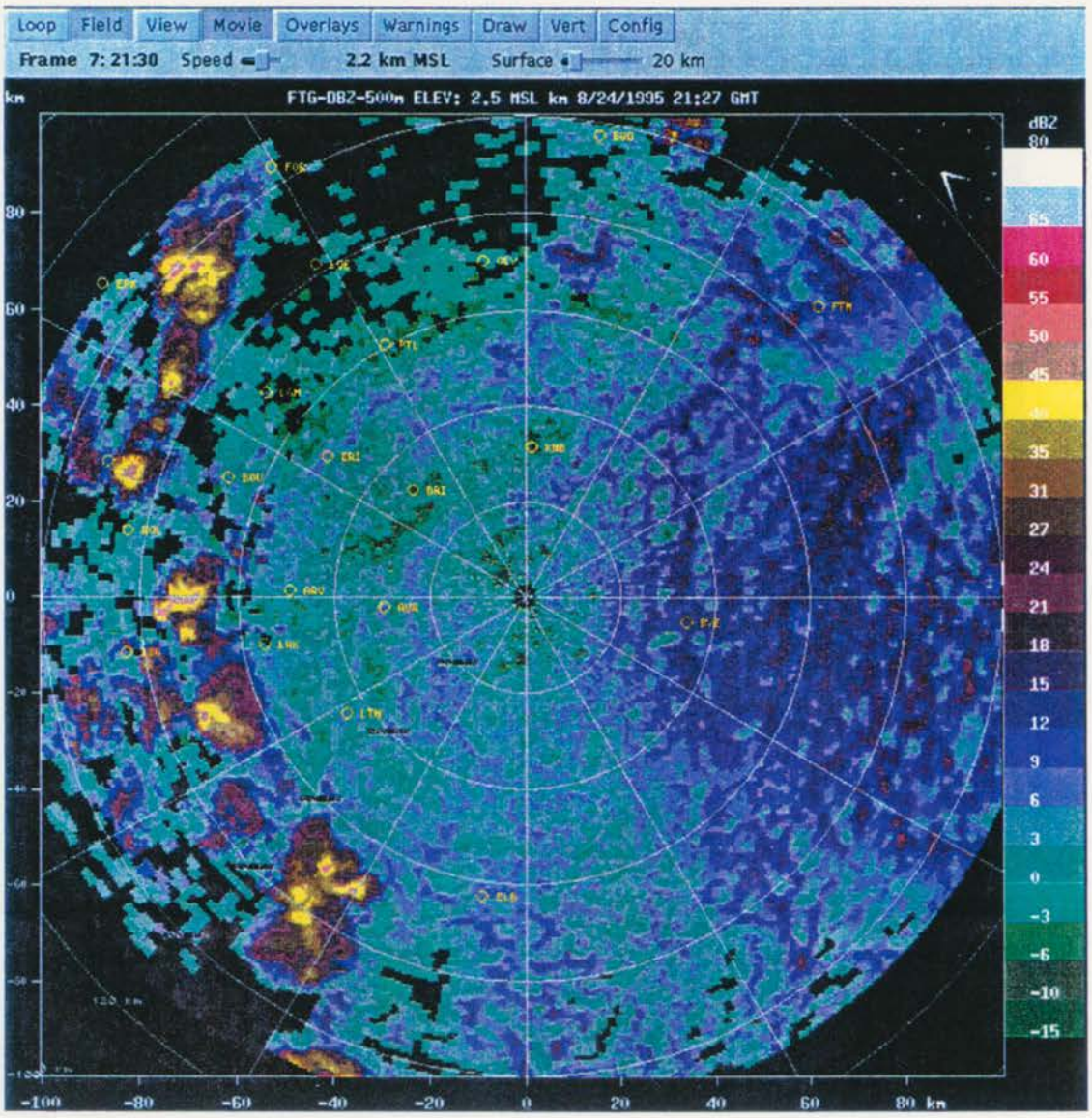

Figure 4.29. b) at 2127 UTC.

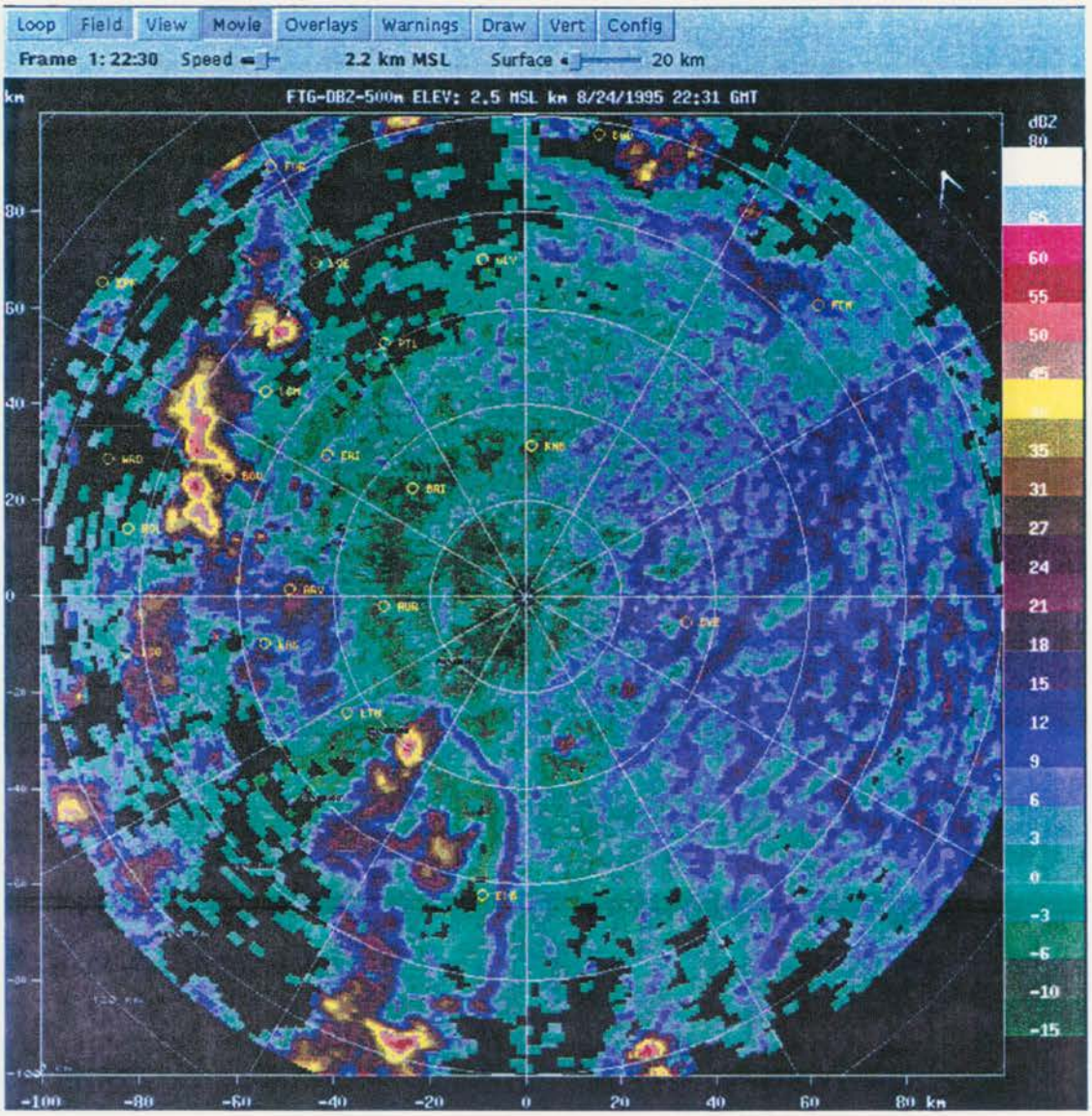

Figure 4.29. c) at 2231 UTC.

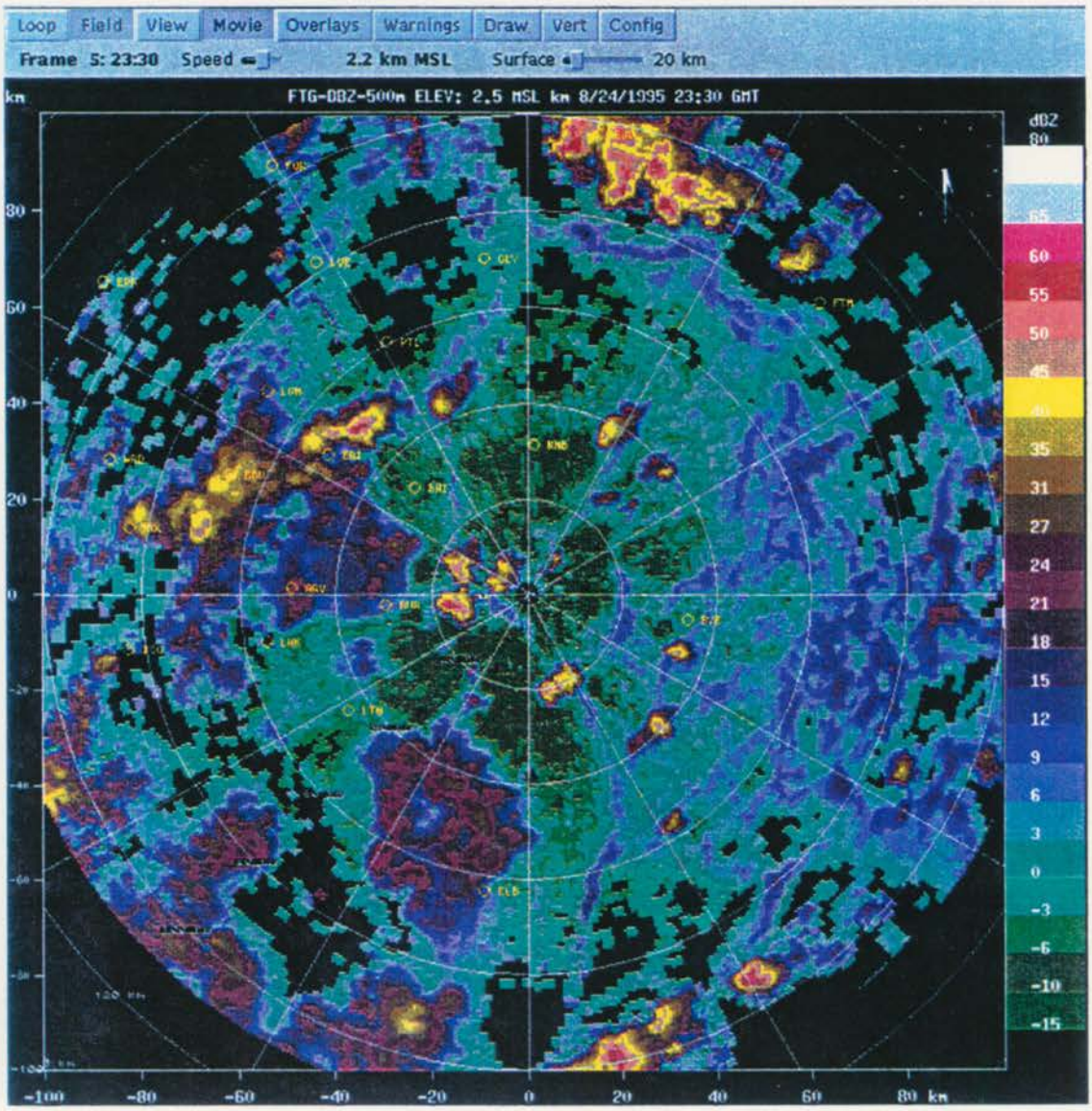

Figure 2.29. d) at 2330 UTC.

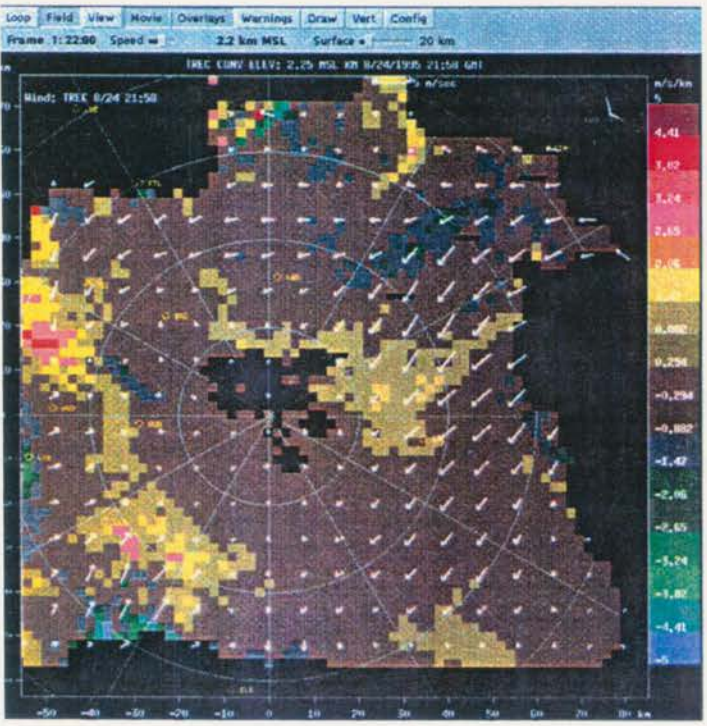

a) 22:00 UTC

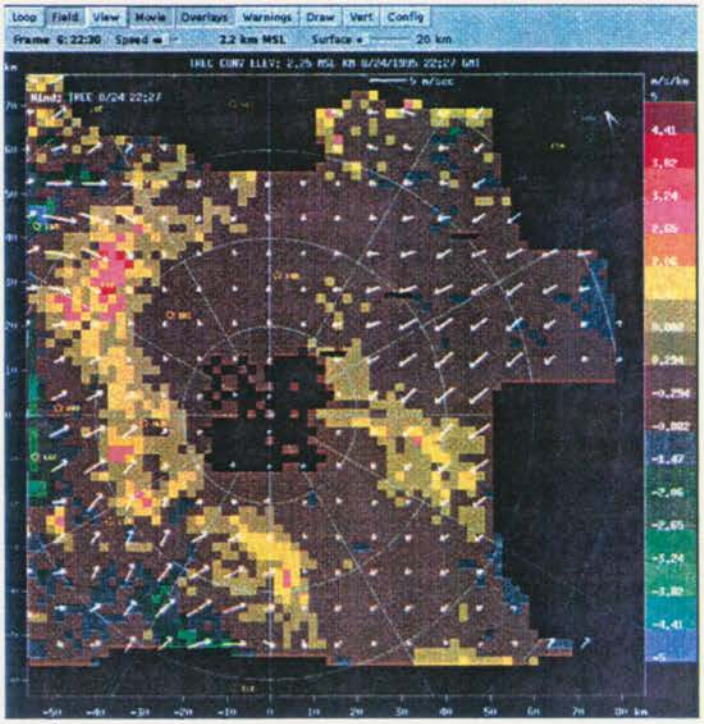

b) 22:30 UTC

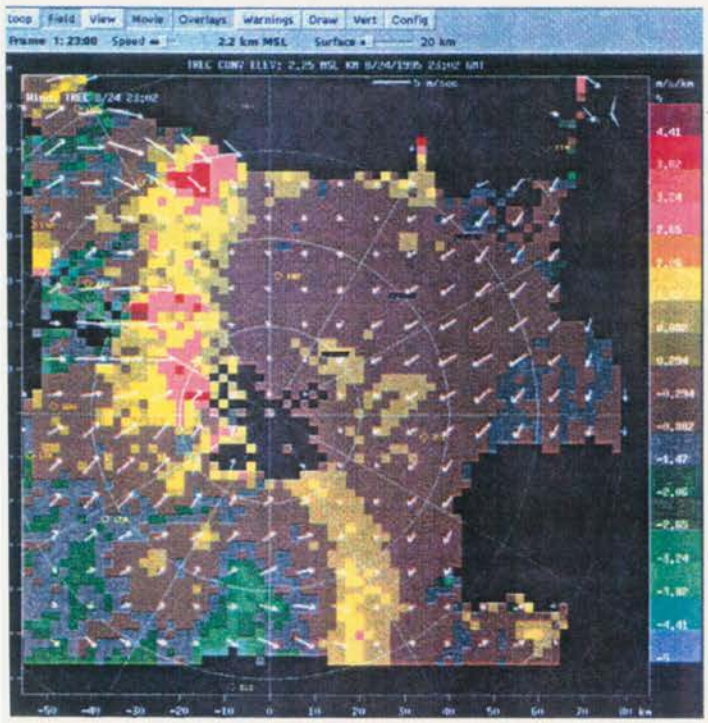

c) 23:00 UTC

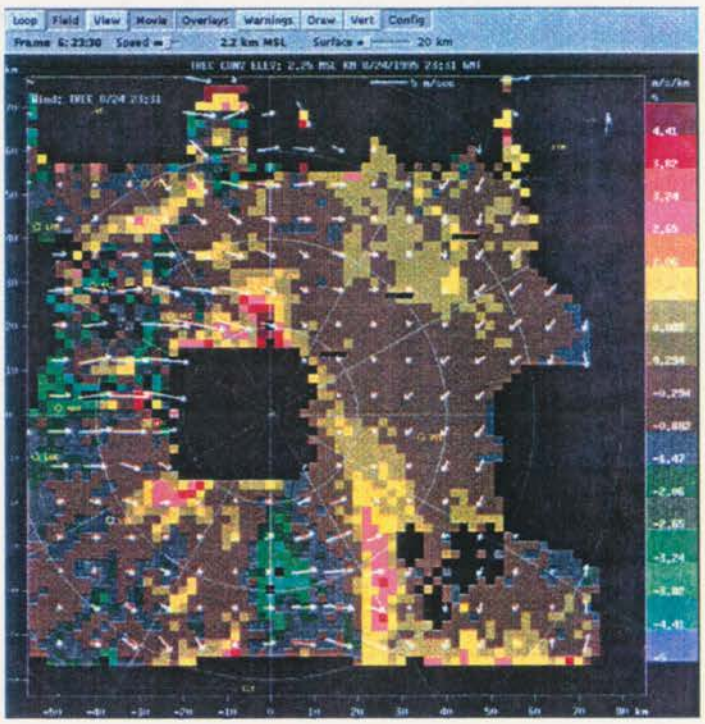

d) 23:30 UTC

Figure 4.30. Time sequence of TREC convergence plots with TREC wind vectors overlaid. Brown, green and gray, colors are regions of divergence. Yellow, orange and red are convergence.

enhancing storm initiation ahead of the gust front. Similar cases of storm initiation ahead of an approaching convergence line interacting with horizontal rolls have been documented by Wilson and Screiber (1986), Atkins et al. (1995), and Atkins et al. (1998).

As mentioned above, the convective temperature was reached by 2100. Following this time, the structure and density of the horizontal rolls changed. Weckwerth et al. (1997) found that roll wavelength was proportional to the CBL depth and that the aspect ratio increased as the instability increased. A similar tendency is evident in this case where the distance between the rolls had increased by 2231 (Fig. 4.29c), and then became less discernible on radar (Fig. 4.29d) as larger scale, deep convective process prevailed (Fankhauser et al., 1995; Weckwerth et al., 1997). The Visible satellite images reflect the increase in convection above the rolls and behind the gust fronts, as clouds grow from the cumulus to cumulus congestus stage (Fig. 31). At 2232 (Fig. 4.31b), convection directly above the gust front located SW of the radar was not obvious, due to anvil obscuration by the cumulonimbus storms located to west of the gust front. However, the evolution of the cumulus clouds lines to more cellular convection ahead of the gust front is apparent by this time.

4.2.3 Growth of cumulus clouds

Figure 4.32 provides an overview of cloud top temperature and storm evolution. Composite plots of cloud top, IR brightness temperatures and radar reflectivity at 4.5 km AGL are shown. A quick perusal of these plots indicate that the only significant echoes (i.e., > 0 dBZ) present at 2132 (Figs. 4.32a) were in association with the convection over the mountains and the gust front north

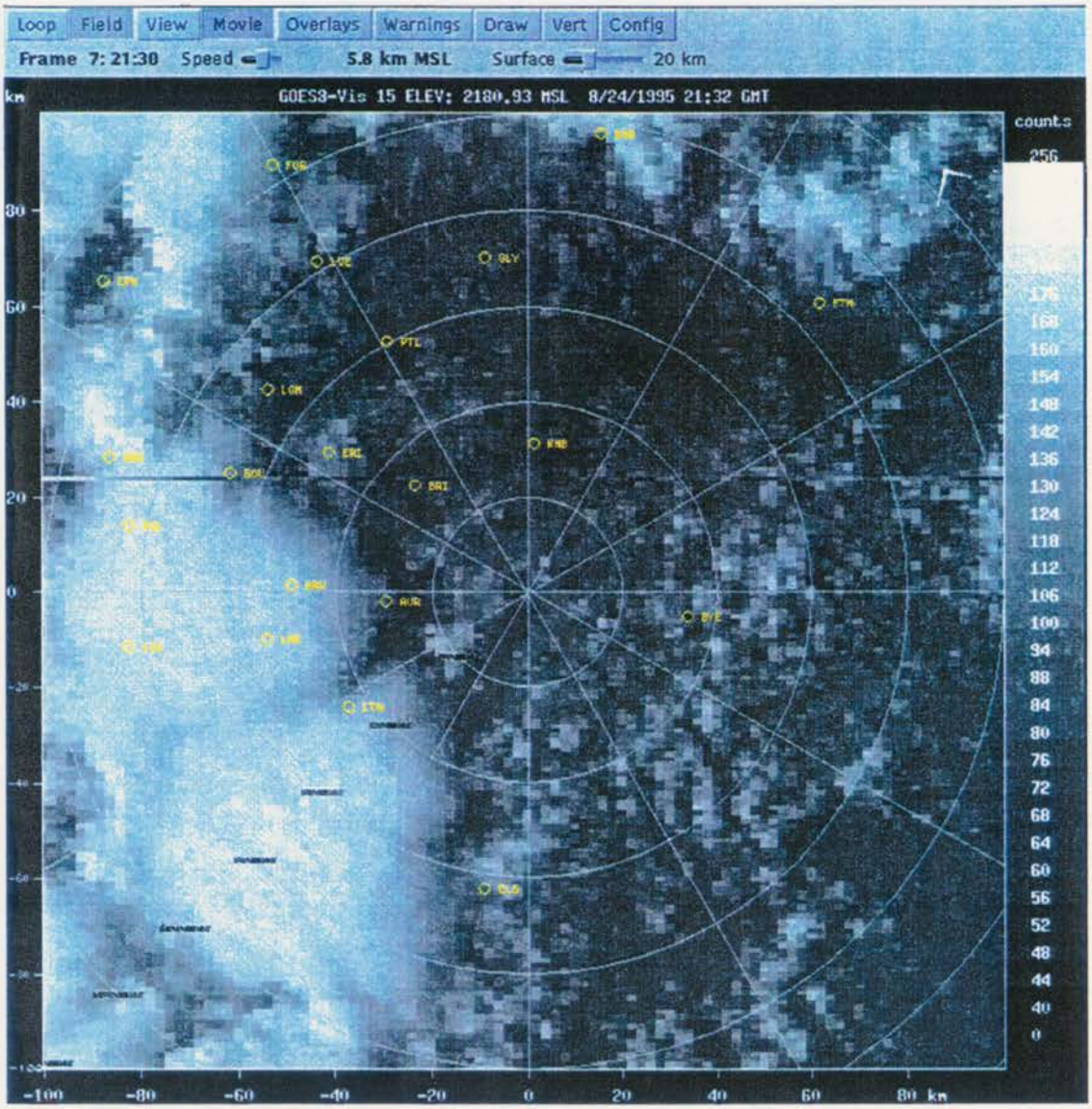

Figure 4.31. Visible satellite imagery on 24 August 1995 at a) 2132 UTC.

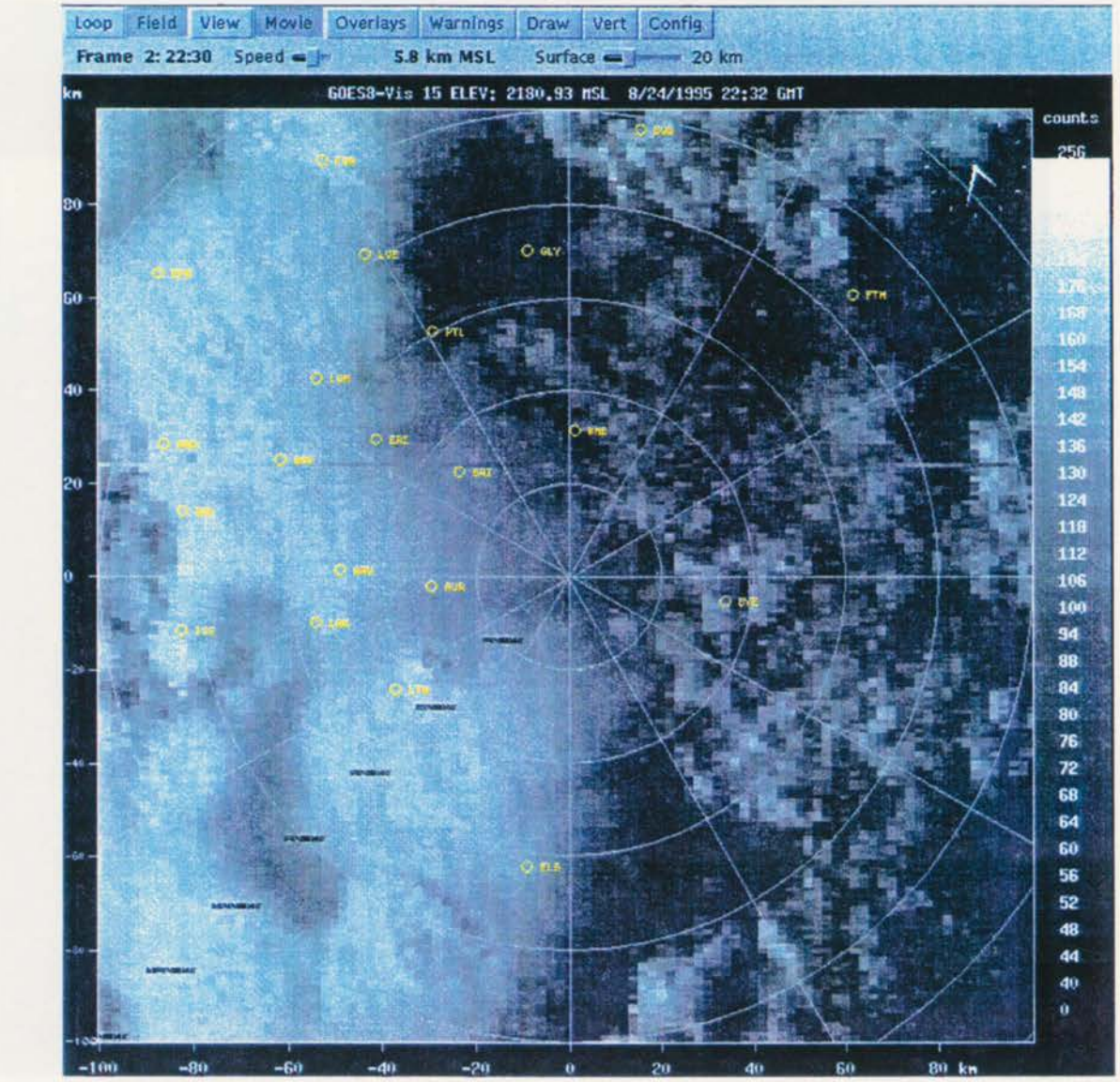

Figure 4.3[illegible]. b) at 2232 UTC.

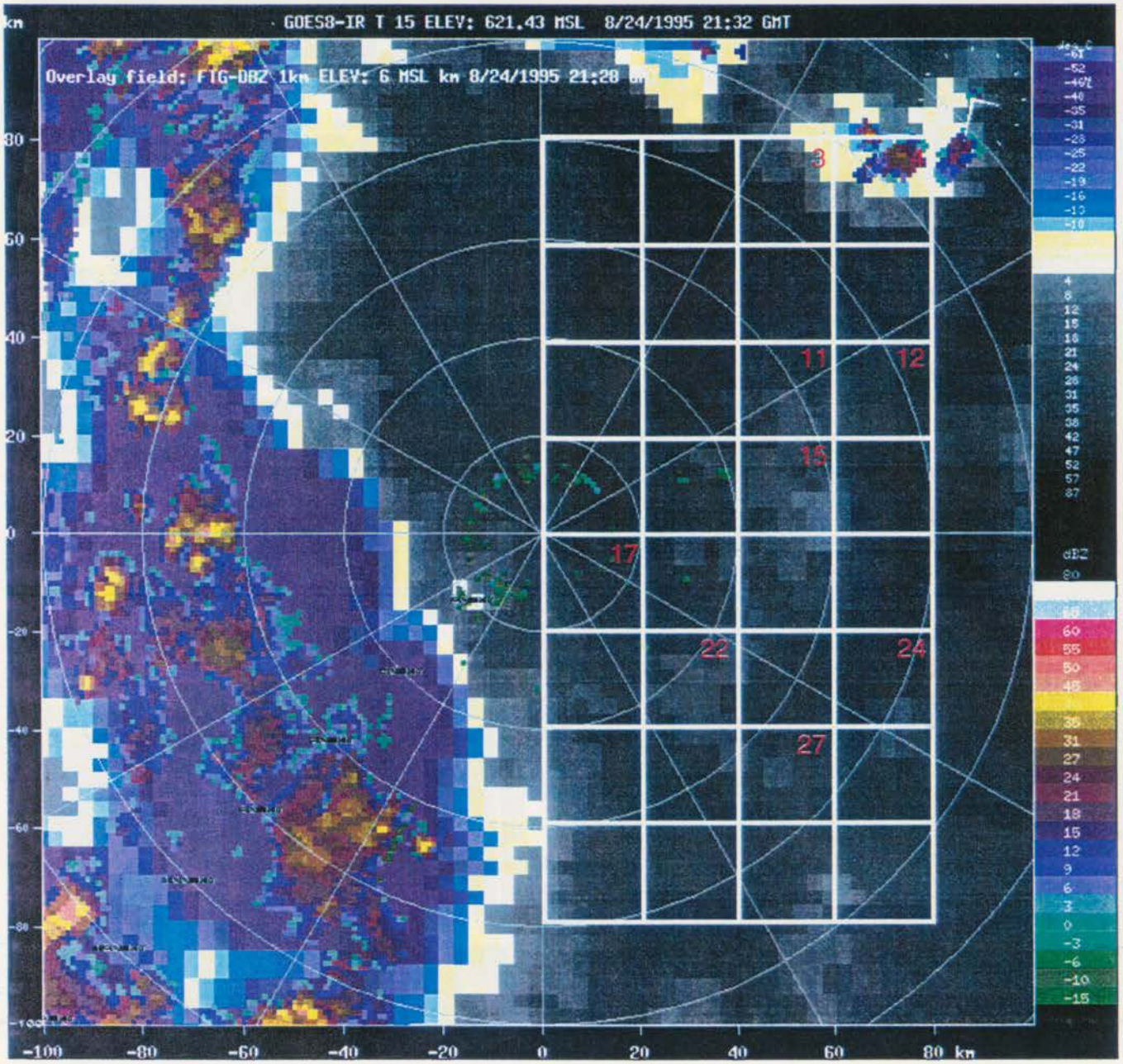

Figure 4.32. Composite image of GOES-8 Infrared brightness temperature field and KFTG radar reflectivity at 4.5 km AGL. In the upper righthand colorscale (in deg C), gray shade are IR temperatures above freezing, white colors are temperatures near 0 deg C, and subfreezing temperatures are shades of blue and purple. The lower righthand colorscale is for the reflectivity field with the more intense storms represented by shades of red and yellow. The overlaid grid is the same as shown in Fig. 4.27. a) At 2132 UTC.

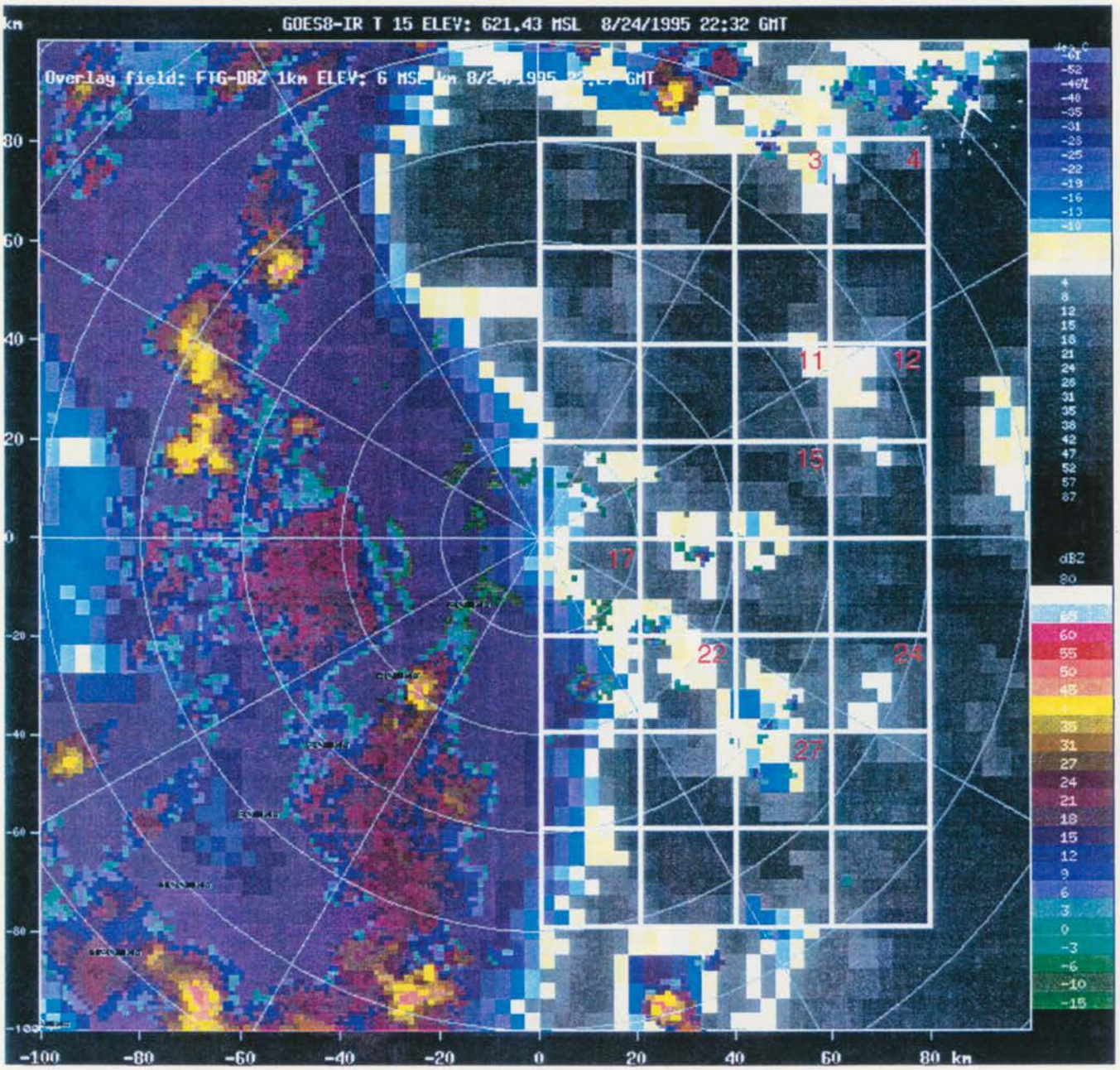

Figure 4.32. b) At 2232 UTC.

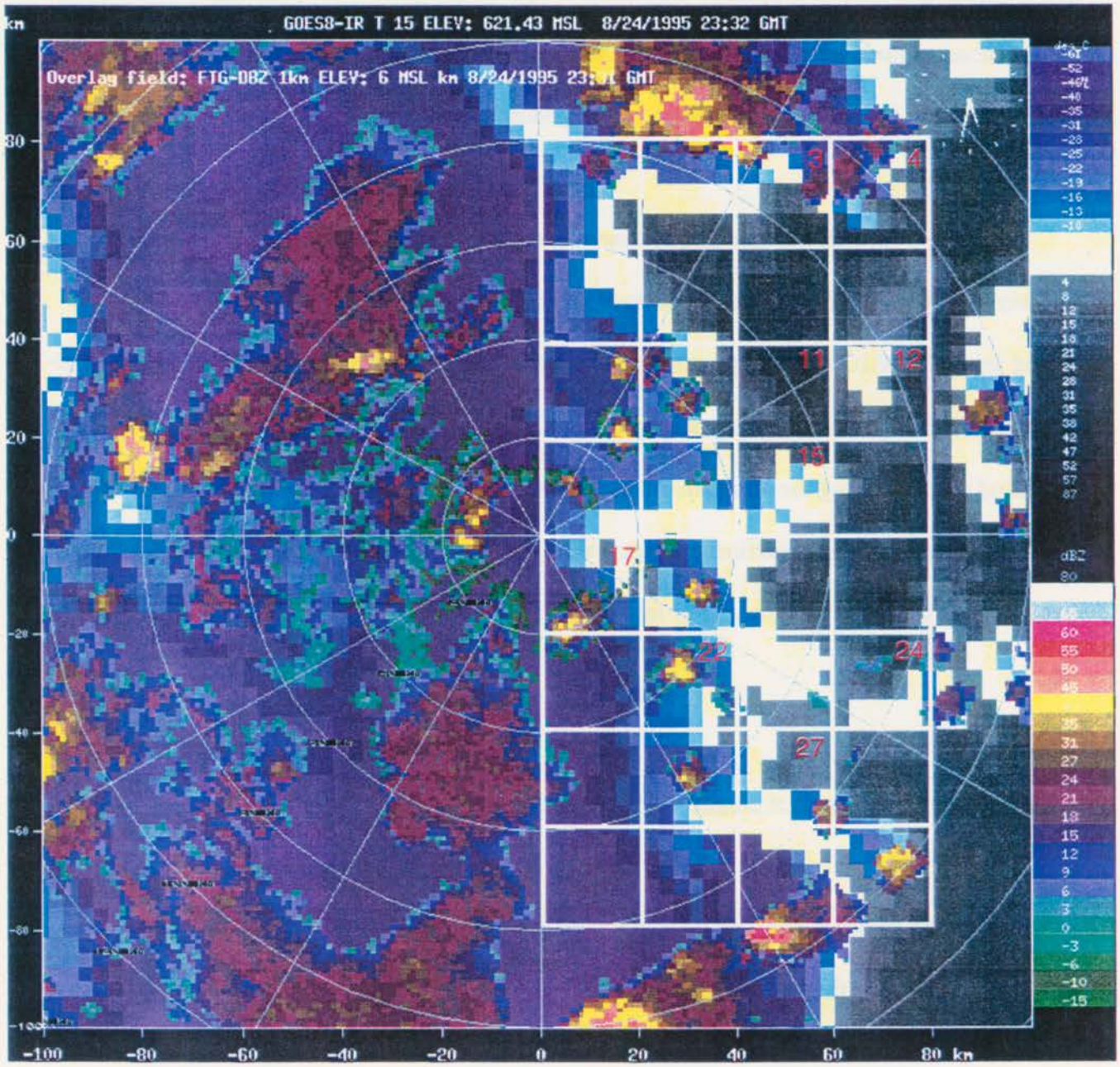

Figure 4.32. c) At 2332 UTC.

east of the radar. Cloud top temperatures for the mountain storms reached values lower than -40 deg C during this time. For most of the Plains, temperatures were above freezing until 2202, and no significant echoes were apparent until 2232 (Fig. 32b). Between 2232 and 2332 (Fig. 32c), deep convection occured in certain areas of the gridded region.

The grid of 20 x 20 km contiguous boxes shown in Figs. 4.27 and 4.32 represent the regions that were analyzed for the characterization of cloud growth. The data within each box was processed using CEDRIC and histograms of IR brightness temperatures, time rate of change of temperature, and maximum reflectivity were produced. Boxes were made large enough to account for any cloud motion during the 4 hr time period of interest. Data from the numbered boxes are presented in this thesis. These particular regions were chosen to illustrate various aspects of cloud growth above different boundary layer features.

i. Cloud growth associated with gust front passage

Figure 4.33 shows time series data on the maximum reflectivity and minimum cloud top temperatures observed within boxes 3 and 4. The median brightness temperature within the boxes at each time period, retrieved from the histogram data, is also plotted. Cloud growth within these boxes were affected by the approach of the gust front from the north. While the gust front was not physically located within the boxes until after 2200, the enhanced lifting ahead of the approaching gust front is apparent already at 2000 as the minimum temperature within these boxes drop from 5-10 deg C to subfreezing temperatures in only 15 min (Fig. 4.33a, b). A color image of the

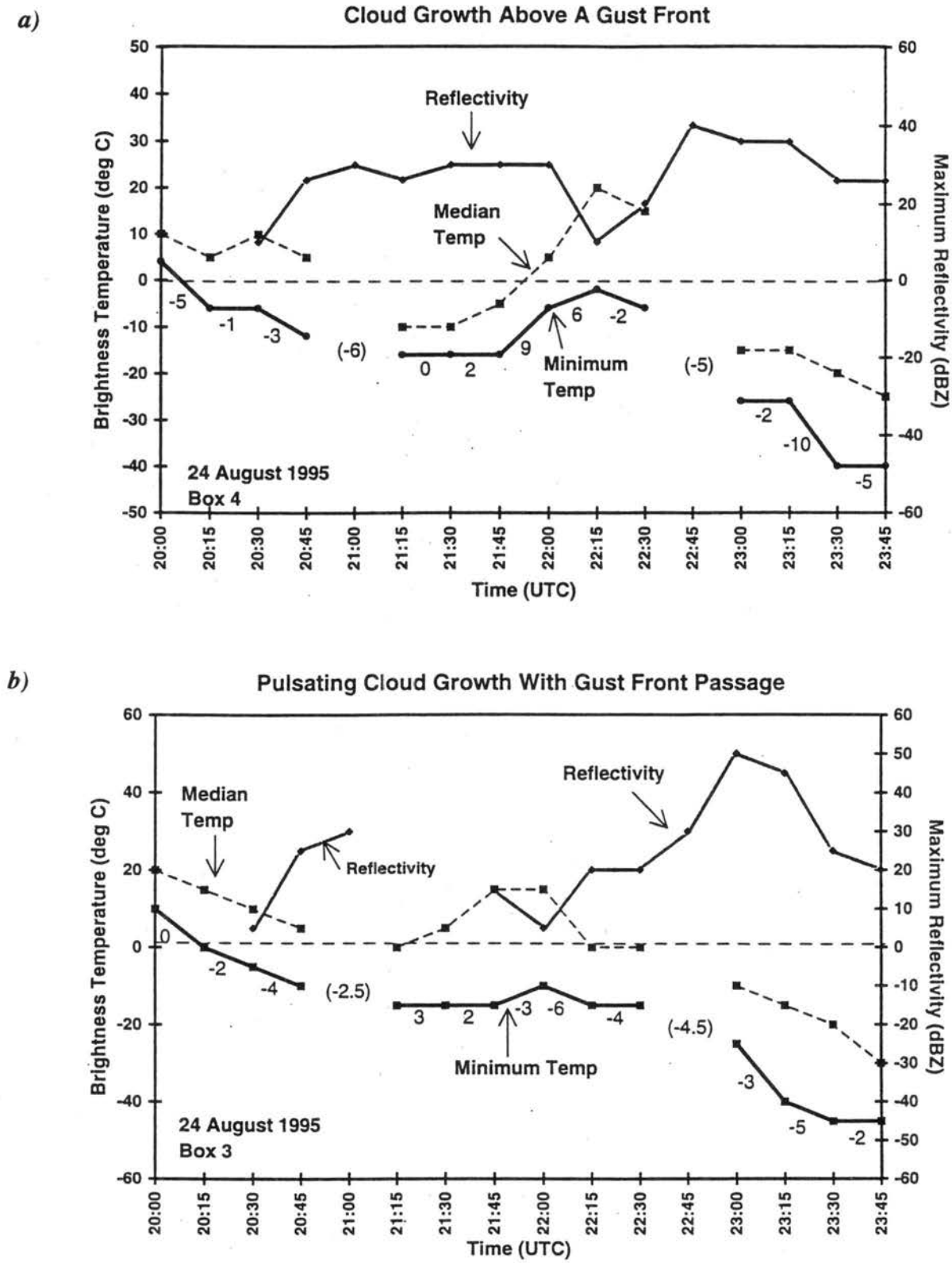

Figure 4.33. Time series plot of Infrared brightness temperature (deg C) and maximum radar reflectivity (dBZ) associated with cloud growth above a gust front. Median (dashed curve) and minimum (black solid curve) temperature values and maximum reflectivity (thin black curve) are shown for a) box 4 and b) box 3.

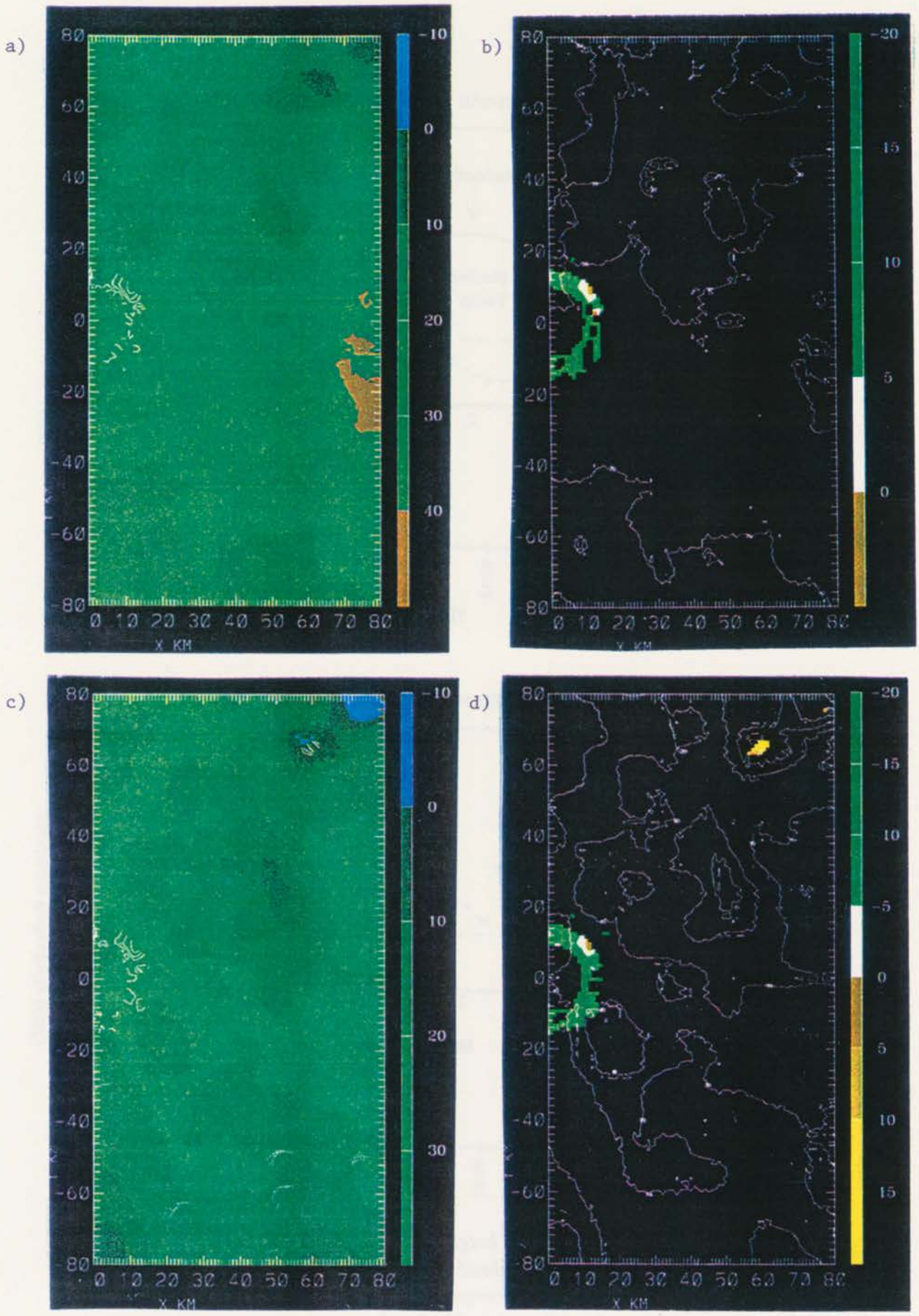

Figure 4.34. CEDRIC plots of brightness temperatures and radar reflectivity on 24 August 1995.a)IR temperatures (in deg C) at 2002 with contours of reflectivity overlaid. b) Reflectivity at 4.5 km AGL with contours of temperature overlaid. c), d) Same as a), b) except at 2032.

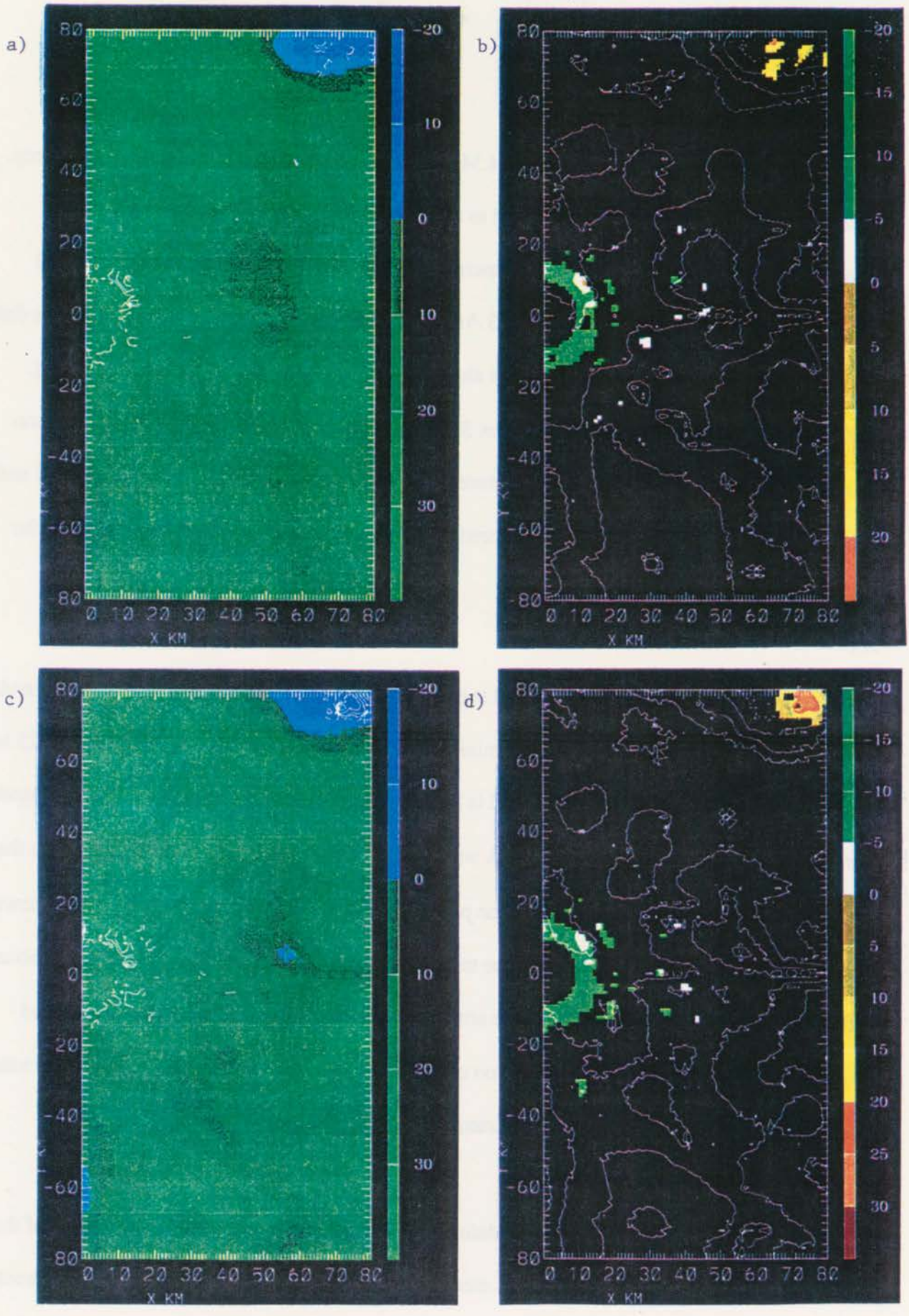

Figure 4.35. Same as Fig. 4.34, except a), b) at 2115 UTC and c), d) at 2132 UTC.

northeast corner of the full domain in Fig. 4.34 (panels a and c) illustrates this temperature drop. Over the next hour, temperatures continued to drop to -15 deg C and the median time rate of change of temperature (Fig. 4.33) was comparable to values observed during the initial cloud growth above the stationary boundary on 23 August (see Fig. 4.19). Small 10-20 dBZ echoes did appear in association with the cloud growth ahead of the gust front. But as can be seen in Fig. 4.33b and Figs. 4.35b,d, the echo within box 3 dissipated rather quickly and cloud top temperatures ceased decreasing. Cloud top temperatures were also observed to stabilize between 2115 and 2145 within box 4 (Fig. 4.33a) and is mirrored by the lack of growth of the echo, once the echo achieved 30 dBZ.

Cloud top temperatures in both boxed regions subsequently indicated a brief warming trend. This is evident in the upward trend of the minimum temperature curve between 2145 and 2215 in Fig. 4.33a. In Fig. 4.33b, the upward trend is less obvious, although the rate of change of temperature between 2115 and 2145 is positive. A warming trend in temperature is more obvious in the median temperature curve for the same time period. All of the median temperature curves shown in this thesis tend to parallel the trend of the minimum temperature curve. When differences occur in the trends of the two curves, this can be attributed to a variability of cloud types (i.e., cloud heights) within the box or due to dissipation of some of the clouds resulting in near ground radiation broadening the spectrum of IR temperatures within the box.

As the gust front entered the region defined by boxes 3 and 4, more vigorous growth of the clouds occured as cloud top temperatures dropped to much colder temperatures and new echoes formed (as seen in Fig. 4.36d) and reach greater intensities (35-50 dBZ) by 2300 (Figs. 4.33,

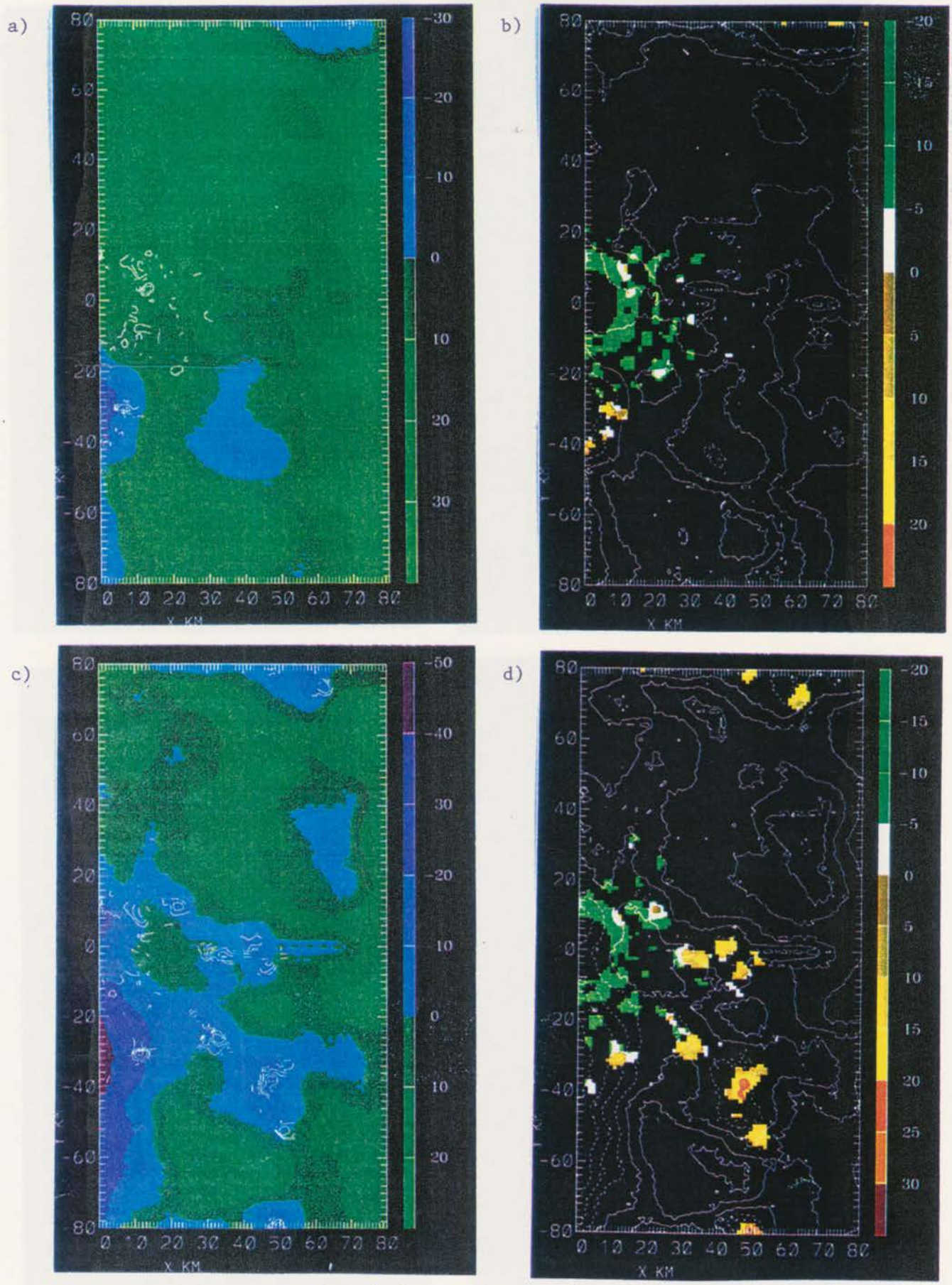

Figure 4.36. Same as Fig. 4.34, except a), b) at 2202 UTC and c), d) at 2232 UTC.

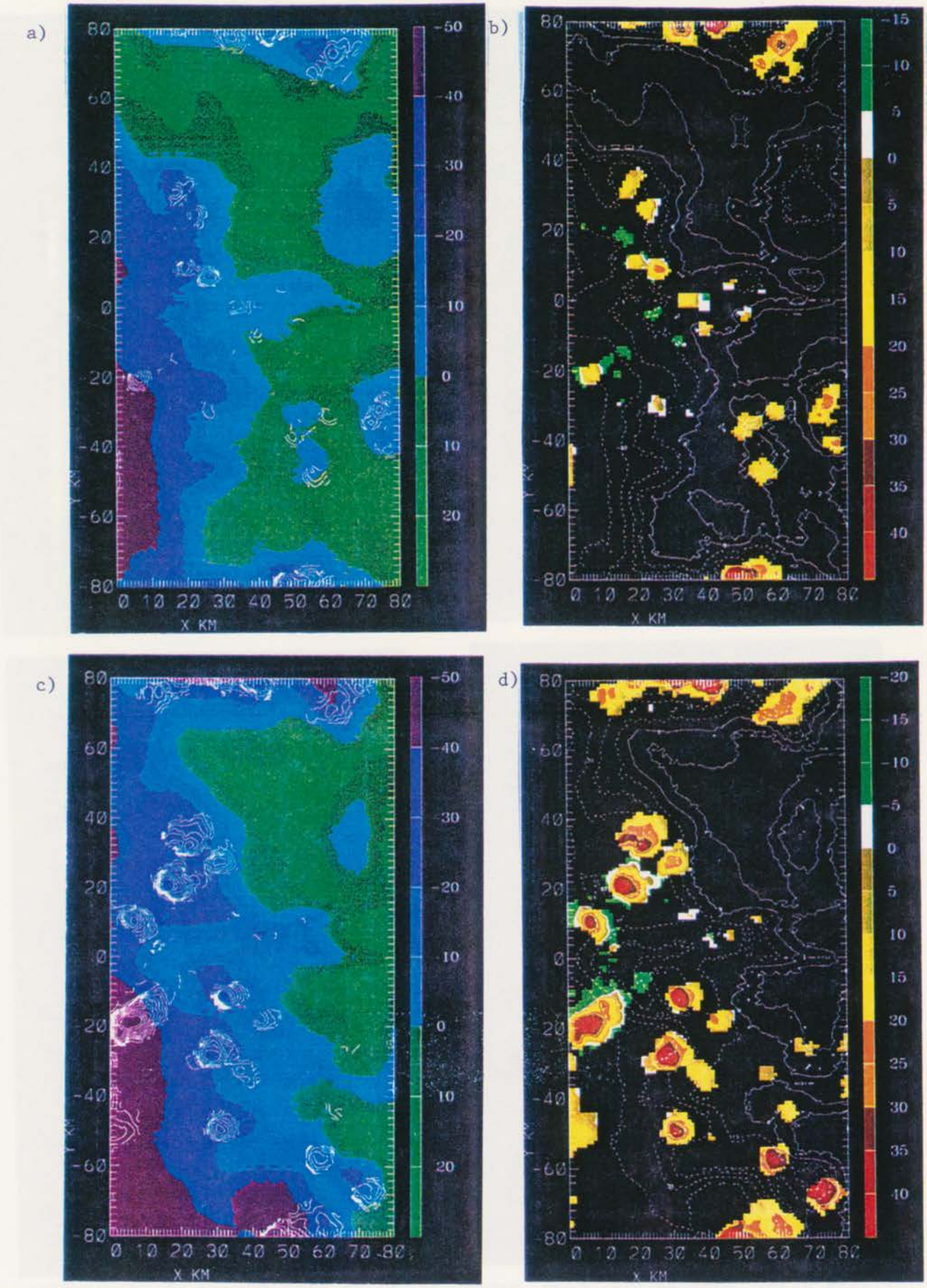

Figure 4.37. Same as Fig. 4.34, except a), b) at 2300 UTC and c), d) at 2330 UTC.

4.37b,d). It is likely that the increased growth rate at colder temperatures is a result of latent heat of fusion associated with the freezing large drops.

While there are some differences in the magnitudes of temperature and reflectivity between box 3 and box 4 during the 4 hour period, the general pattern of pulsating growth is very similar. Prior to gust front passage, an initial surge of growth is observed, marked first by cloud top temperatues dropping below zero and then 30 min later, to the presence of a 20 dBZ echo. This initial surge produces storms of only moderate intensity, that eventually dissipate, and a corresponding warming trend is observed with the cloud top temperatures. With the passage of the gust front, extra lift is provided to the dissipating clouds, producing a second, more intense line of storms. Cloud top temperatures immediately start to drop again following gust front passage, this time coincident with renewed echo growth. Storm duration, from growth to dissipation spans about 60 min.

ii. Cloud growth above horizontal rolls

Looking at the density of cumulus clouds within box 11 in Fig. 4.27 and knowing that a horizontal convective roll was present below these clouds, it would be easy to assume that storms are more likely to occur within this boxed region than in the region defined by box 12 or box 15, where only a small number of cumulus clouds were present. Noting the lack of cumulus clouds and the very warm, near surface IR temperatures (see Fig. 4.34a) within box 24 compared to the more numerous cumulus in box 27, similar inferences might be drawn about the favorable region

a)

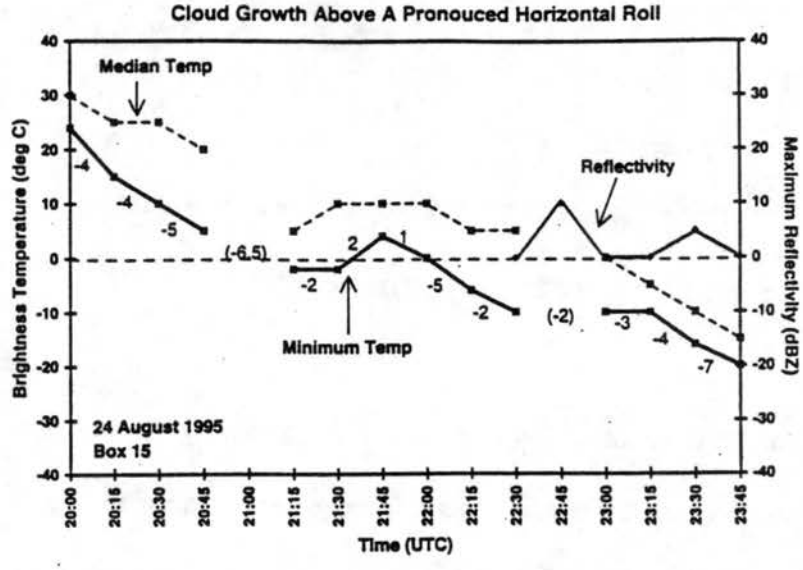

b)

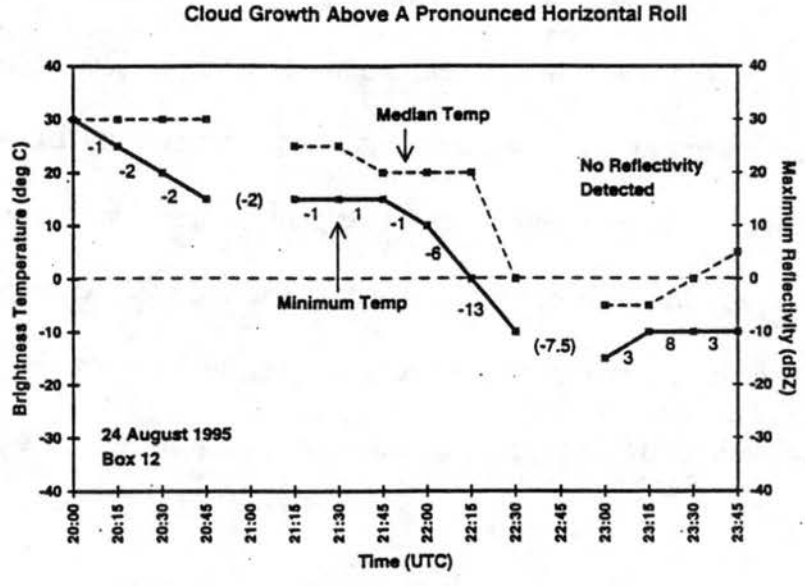

c)

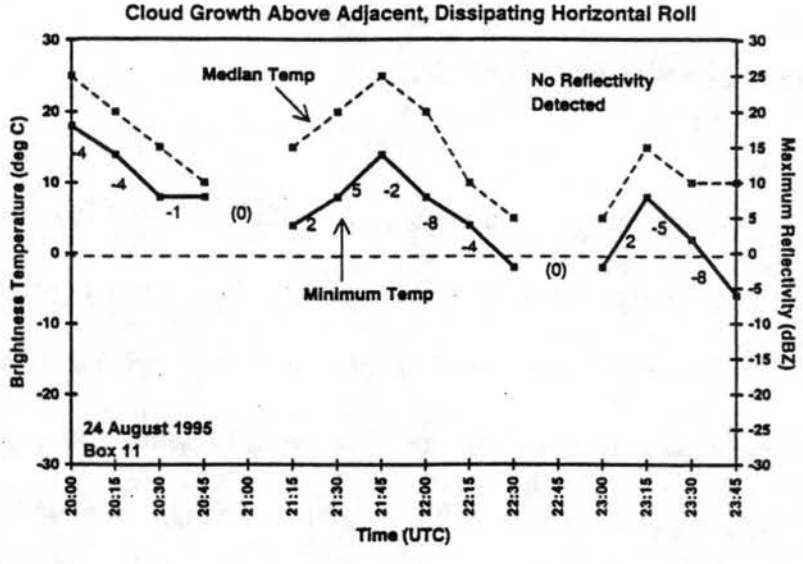

Figure 4.38. Time series plots of IR temperatures and radar reflectivity associated with cloud growth above horizontal rolls within a) box 15, b) box 12 and c) box 11.

for deep convection in this area. While the cloud pattern does vary within these boxes at 2000, the presence of one or more boundary layer, horizontal rolls is common to all boxes.

In Fig. 4.38, time series plots are shown for the adjacent boxes, 11, 12 and 15. A quick inspection of the minimum temperature curves in each plot shows the general trend of decreasing cloud top temperatures with time. This can also be seen in the sequence of brightness temperature plots in Figs. 4.34-4.37 (panels a and c) as the temperatures in the vicinity of these boxes change from warmer values (green shades) to subfreezing values (blue shades). The same horizontal roll runs through boxes 12 and 15 (see Fig. 4.29). Except for the brief appearance of a 10 dBZ echo (at x = 43, y = 1 in Fig. 4.36d) within box 15, no deep convection occurred above the horizontal roll in either of these boxed regions. Furthermore, while both time series graphs showed the cloud top temperatures dropping below 0° C, the median temperature within box 12 generally stayed higher than freezing and showed a warming trend very soon after the temperatures first dropped below zero. The rate of temperature change also indicated a similar warming trend. Given the marginal instability on this day, it is clear that additional boundary layer convergence and vertical lifting of air was needed to trigger deeper convection compared to what the horizontal roll convection was able to provide on its own.

It is surprising that density of cumulus clouds above the roll in box 11 did not result in some limited storm growth. The alternating pattern of warming and cooling temperatures in Fig. 4.38c suggests the growth and suppression of the clouds was due to the presence of a stable layer in the top of the CBL. One would expect to see similar patterns in the time series data in box 15 and box 12, but such is not the case. One possible explanation for the pulsating nature and lack of growth of the clouds in box 11 may be due to the evolution of the boundary layer rolls in this area during

the afternoon. Closer examination of the boundary layer features indicates that while the cumulus clouds seen in Fig. 4.27 were located directly above a horizontal roll in Fig. 4.29a, one hour later that roll was no longer evident in the radar data. Both Weckwerth et al. (1996) and Christian and Wakimoto (1989) have shown that drier, subsiding air prevails in the regions between the reflectivity thin lines associated with horizontal rolls. In these regions between the rolls, convection was generally more suppressed than convection associated with the rolls themselves (see Fig. 1.8). It is possible that the roll dissipated as the CBL depth and instability increased, cutting the cloud off from any surface convergence features. It is also possible that the roll feature was displaced slightly from its original position and the cumulus clouds that had originally formed above the roll, were subsequently subjected to the downward motion component of the roll. Whatever the cause for the disappearance of the roll with time, the lack of sufficient boundary layer convergence clearly affected the intensity of convection. The time rate of change of temperatures highlight the pulsating nature of cloud growth and decay within box 11. The significance of this case for forecasting thunderstorm initiation is to show that one must monitor both cloud top temperatures and change in temperature with time in order to discriminate between active and suppressed growth.

In contrast to the above data, storms do form above horizontal rolls in boxes 27 and 24 (Fig. 4.39). The temperature and reflectivity trends are similar to what was observed with the stationary boundary on 23 Aug (Fig. 4.19). Cloud top temperatures consistently fell during the first 2 hour period shown in the plots. In Fig. 4.39a, temperatures drop below freezing 45 min prior to the appearance of a 20 dBZ echo on radar. In Fig. 4.39b, only 15 min had elapsed between the drop to subfreezing temperatures and the appearance of the first 20 dBZ echo. Subfreezing cloud top

a)

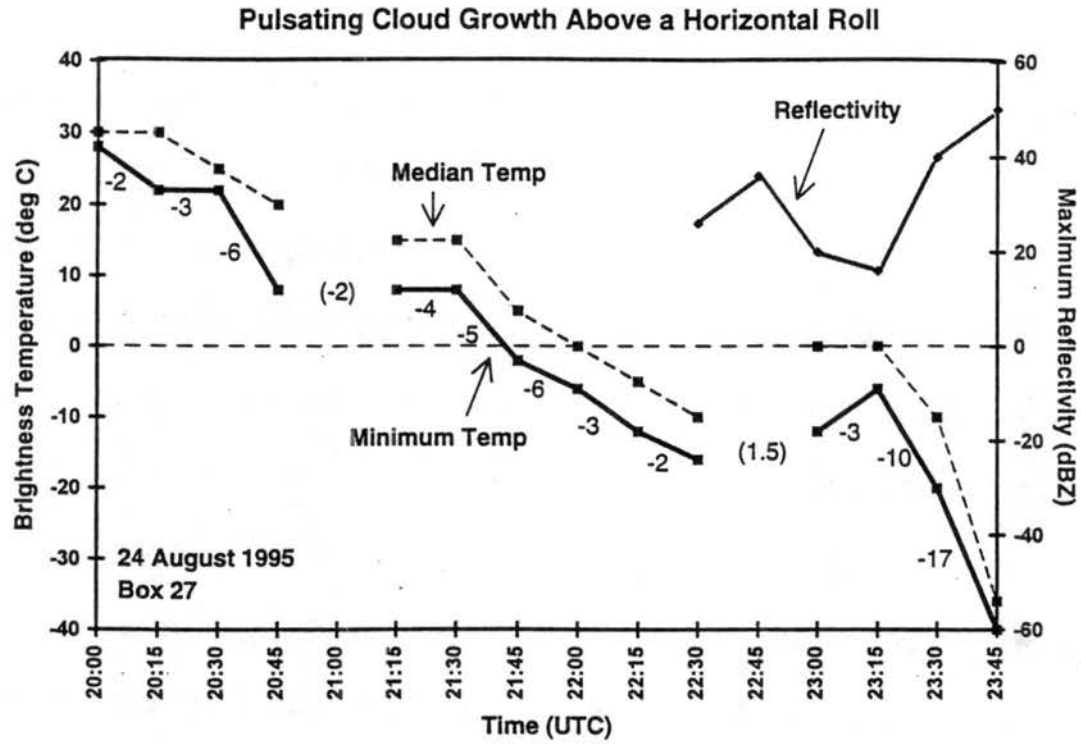

b)

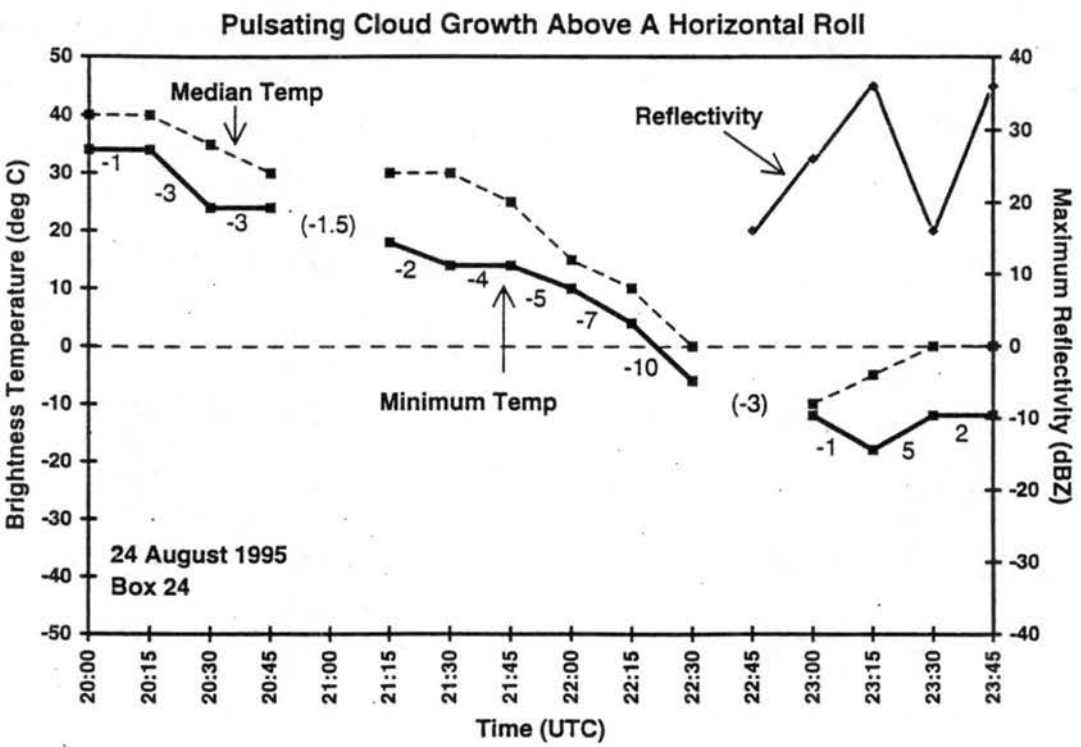

Figure 4.39. Same as Fig. 4.38, except for pulsating cloud growth above horizontal rolls within a) box 27 and b) box 24.

temperatures precede the 35 dBZ echo by 45 min. Given this long period of subfreezing temperatures, the cloud tops during this period may not be directly tied to the convection that results. For both regions presented in Fig. 4.39, storm growth is quick, but also short-lived, followed by new storm growth. The presence of convection within these boxes compared to the lack of vigorous convection above the rolls in the northern boxes may likely be attributed to differences of temperature and/or moisture in the boundary layer. As shown by Crook (1996) in his modelling studies, a change of 1° K had the effect of changing the intensity of the resulting convection. However, a change of 1 g/kg of moisture over the depth of the CBL could make the difference between storm formation and no storms. Dense measurements of CBL moisture and temperature were not available in this study to address the spatial variability of these parameters along the rolls. It can only be conjectured that the deeper convection observed in Fig. 4.39 is due to higher moisture convergence in the area.

iii. Cloud growth associated with gust front / horizontal roll interactions

By far the most vigorous cloud growth on this day occurred at the intersection of the gust front from the SW with the horizontal rolls. Figure 4.40a shows the evolution of the cloud top temperature and reflectivity intensity at the intersection of these features. It is interesting to note that Bragg scatter echo was present for up to an hour before active cloud growth ensued beginning at 2245. In Fig. 4.40b, cloud growth ahead of a gust front intersecting a horizontal roll is almost as rapid as at the intersection point itself. Within both boxes, cloud top temperatures drop below 0° C an hour before 20 dBZ echoes appear. Temperatures continue to fall as the echo associated with storm intensifies. Considering that most storm tracking algorithms generally track storms

a)

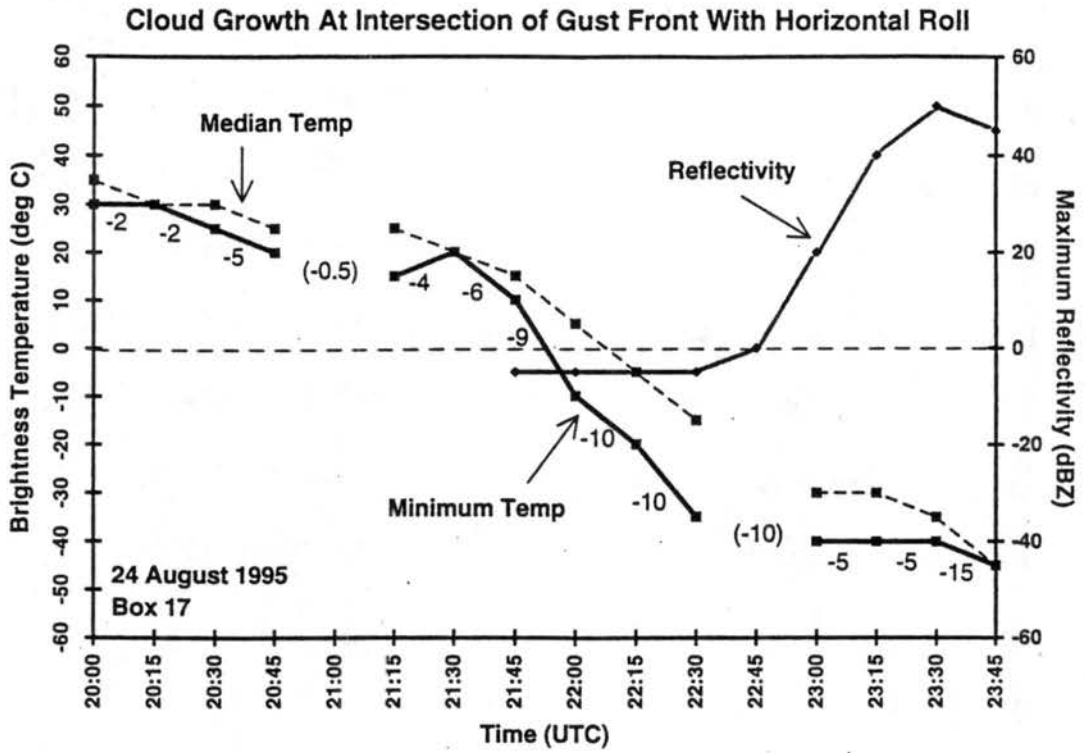

b)

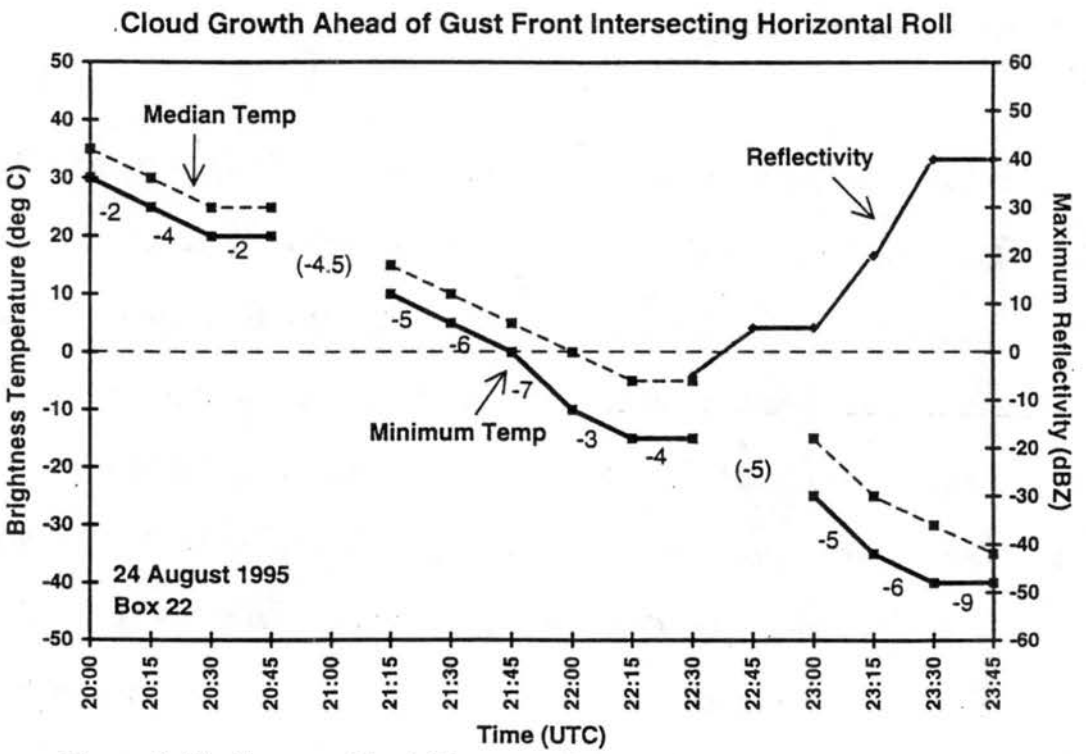

Figure 4.40. Same as Fig. 4.38, except for cloud growth above gust front interactions with horizontal rolls within a) box 17 and b) box 22.

>30 dBZ, it can be seen from these two situations that satellite temperatures provide information on growth over an hour in advance of storms reaching echo intensities of thsi magnitude. Such advance information is not typical though. Rate of temperature change is also quite significant in Fig. 4.40a, and not quite as dramatic in Fig. 4.40b. Data from the 24 August cases suggest that rate of change values less than -5 or -6 indicate a substantial growth stage. While occasionally these rates coincide with radar echo intensification, observation of them and subfreezing cloud top temperatures in the absence of any radar echo is certainly an important precursor of cloud growth.

4.3 21 July 1995

4.3.1 Environmental conditions

The DEN sounding at 1200 UTC was not available from 21 July. A special CLASS (Cross-Chain Loran Sounding System) sounding was launched at 1700 UTC and is shown in Fig. 4.41. The boundary layer was already well mixed at this time, with a dry adiabatic temperature profile and mean available surface moisture of approximately 6 g/kg, less than what was present on the August days. The modified LI was -2.45 with a small amount of CAPE available. The wind profile showed very little directional shear with 5-15 kt winds from the W-SW. The upper level 500 and 700 mb maps indicated that Colorado was under weak, zonal N-NW flow, while the 850 mb and surface maps showed Colorado to be on the back side of a large scale trough running through Kansas and Nebraska, with moderate dewpoints in the mid-40's. With mid-level moisture and drier air aloft, the sounding and weather maps represent a classic environment for microburst-producing storms of moderate (40-45 dBZ) reflectivities.

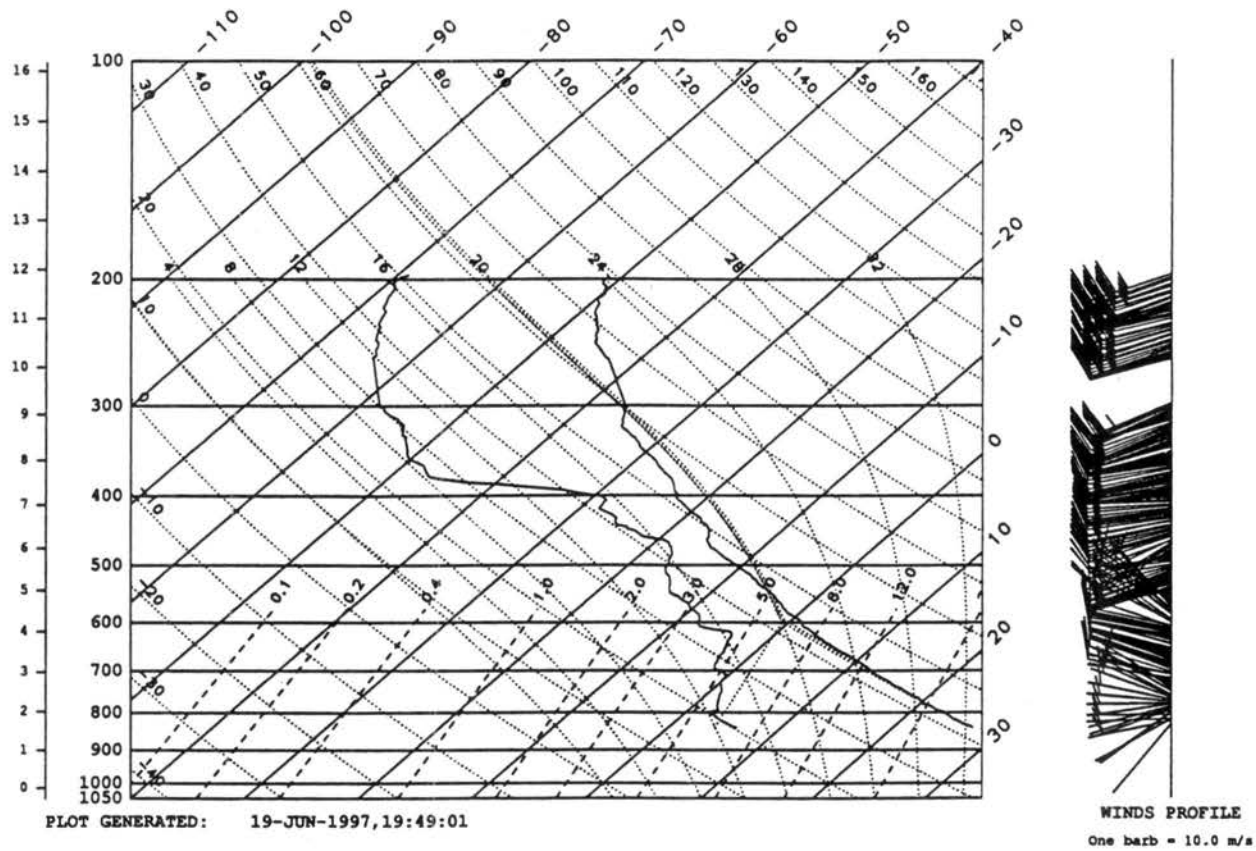

Figure 4.41. CLASS sounding taken at 1700 UTC on 21 July at the Denver NWS.

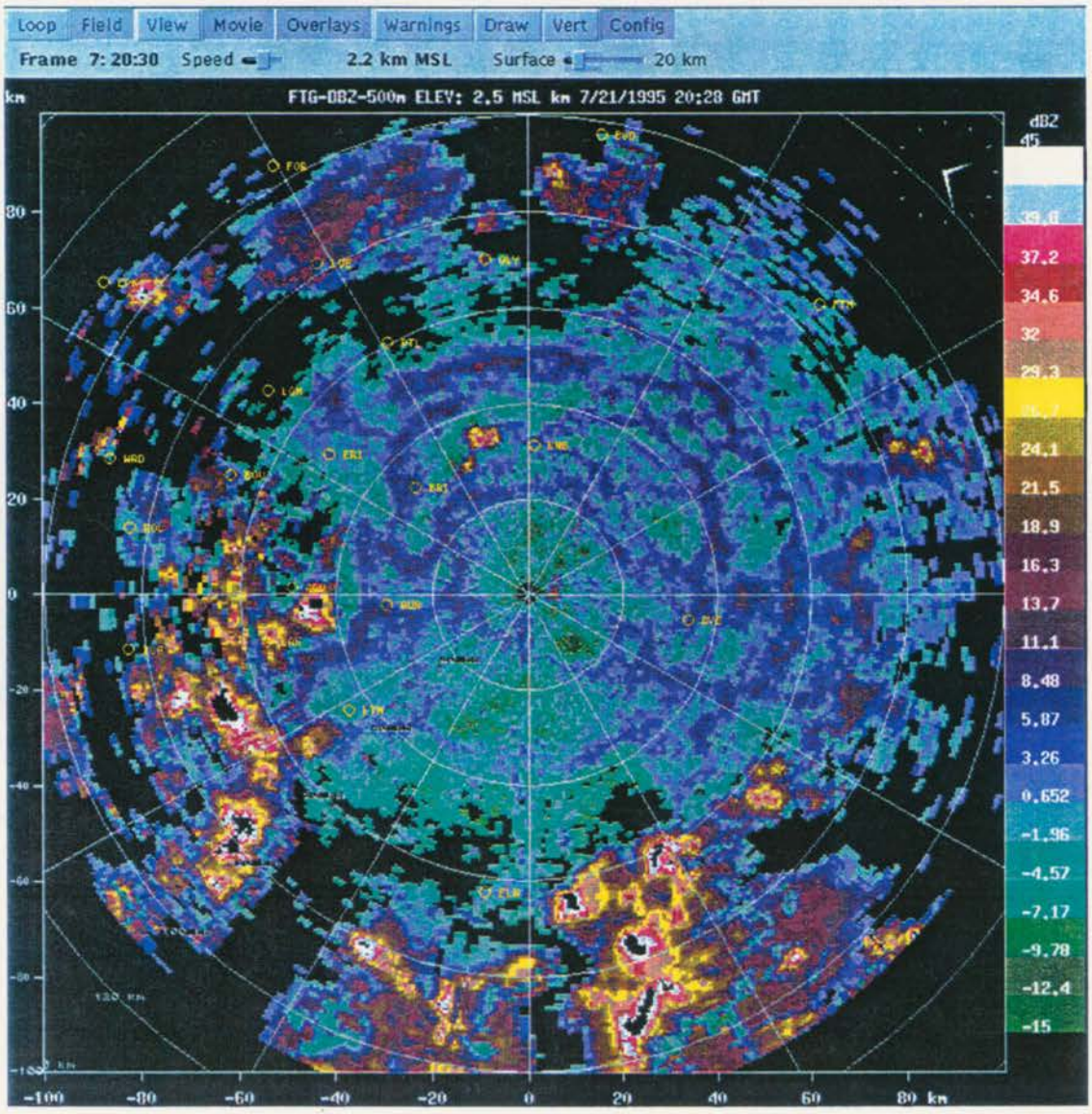

Figure 4.42. Cartesian reflectivity plots at 0.5 km AGL from 21 July 1995. A finer colorscale increment has been used to show the low intensity, horizontal rolls. Black regions within the storms are reflectivities greater than 43 dBZ. a) 2028 UTC.

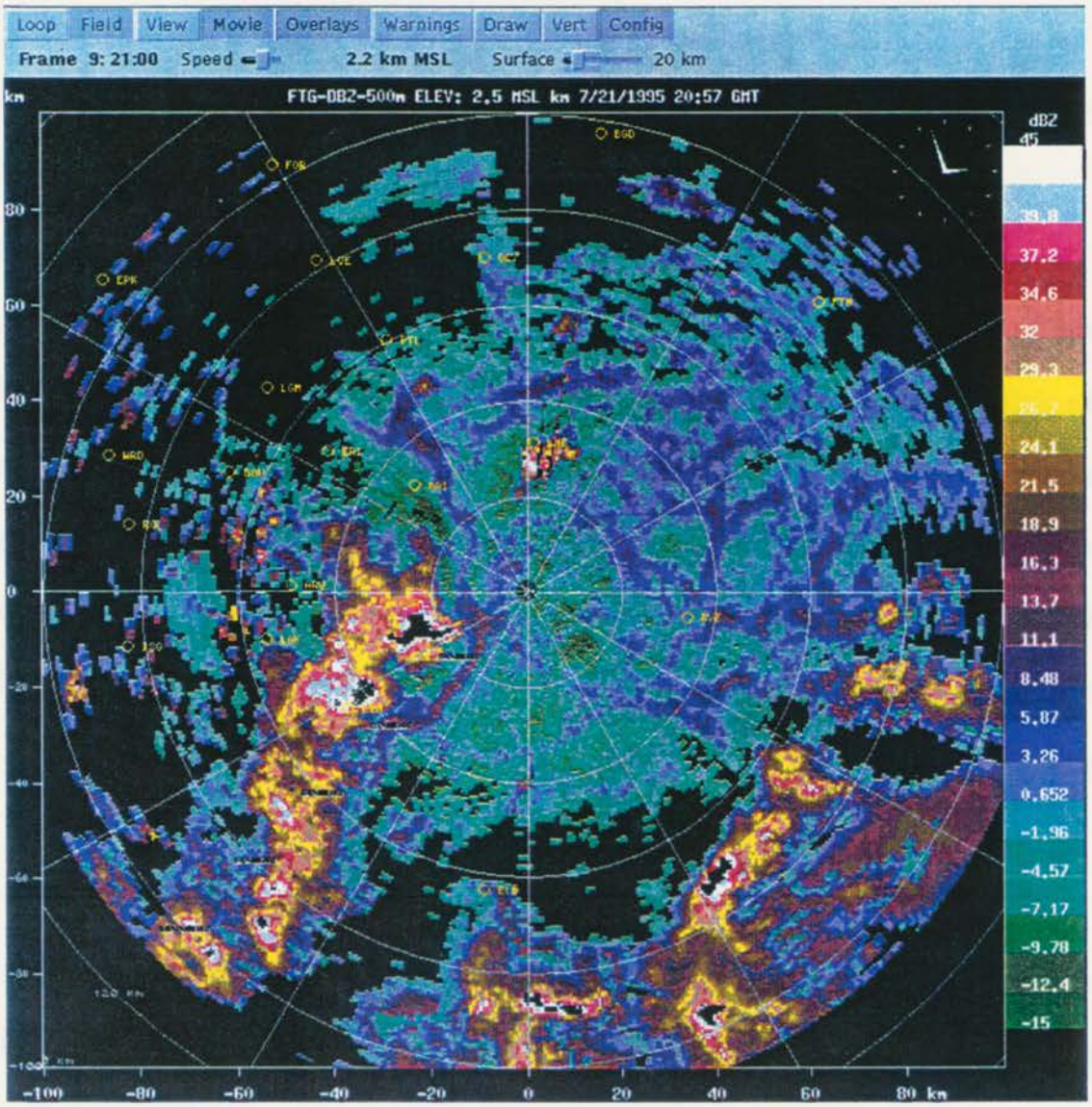

Figure 4.42. b) At 2057 UTC.

4.3.2 Relationship of clouds to boundary layer features

Examining the low level reflectivity data for 21 July, it was difficult to discern any distinct boundary layer features. Reflectivities in the boundary layer were between 0 and 10 dBZ. The reflectivity data shown in Fig. 4.42 are plotted using a colorscale with finer dBZ increments. It is clear that some horizontal roll structures did indeed exist. To the east of the radar, there is some indication that the rolls had a N-S orientation. However, south and north of the radar, they were oriented in an E-W direction, parallel to the environmental winds in the sounding and to the radar radial winds. Some E-W banded structure were embedded within the velocity data also. No precipitating storms existed above these rolls until ~2000 UTC, 70-80 km east of the radar.

The Visible satellite imagery in Fig. 4.43 shows that by 1900, the cloud development was already cellular in nature, making, it difficult to isolate cumulus cloud lines that may have been connected to the roll features in Fig. 4.42. Unfortunately, no satellite data exists prior to 1900 on this day. A comparison of cloud locations with boundary layer reflectivity is shown in Fig. 4.44 at 1900. The reflectivity at 0.5 and 1.5 km AGL is overlaid onto the Visible image. In the 0.5 km plot, there is an obvious lack of organization to the radar features. While one could argue that for every cloud, there is an associated radar echo, the lack of even a 4 dBZ return at 1.5 km AGL is evidence that most of these cloud formations are supported by weak, shallow boundary layer convergence. It is likely that if a spatial autocorrelation technique was applied to this reflectivity data following Weckwerth et al. (1997) the resulting correlation field would fall under their category of "unorganized convection". Under this category, Weckwerth et al. (1997) noted that although the radar reflectivity showed linear convection, they also observed a great deal of variability in the

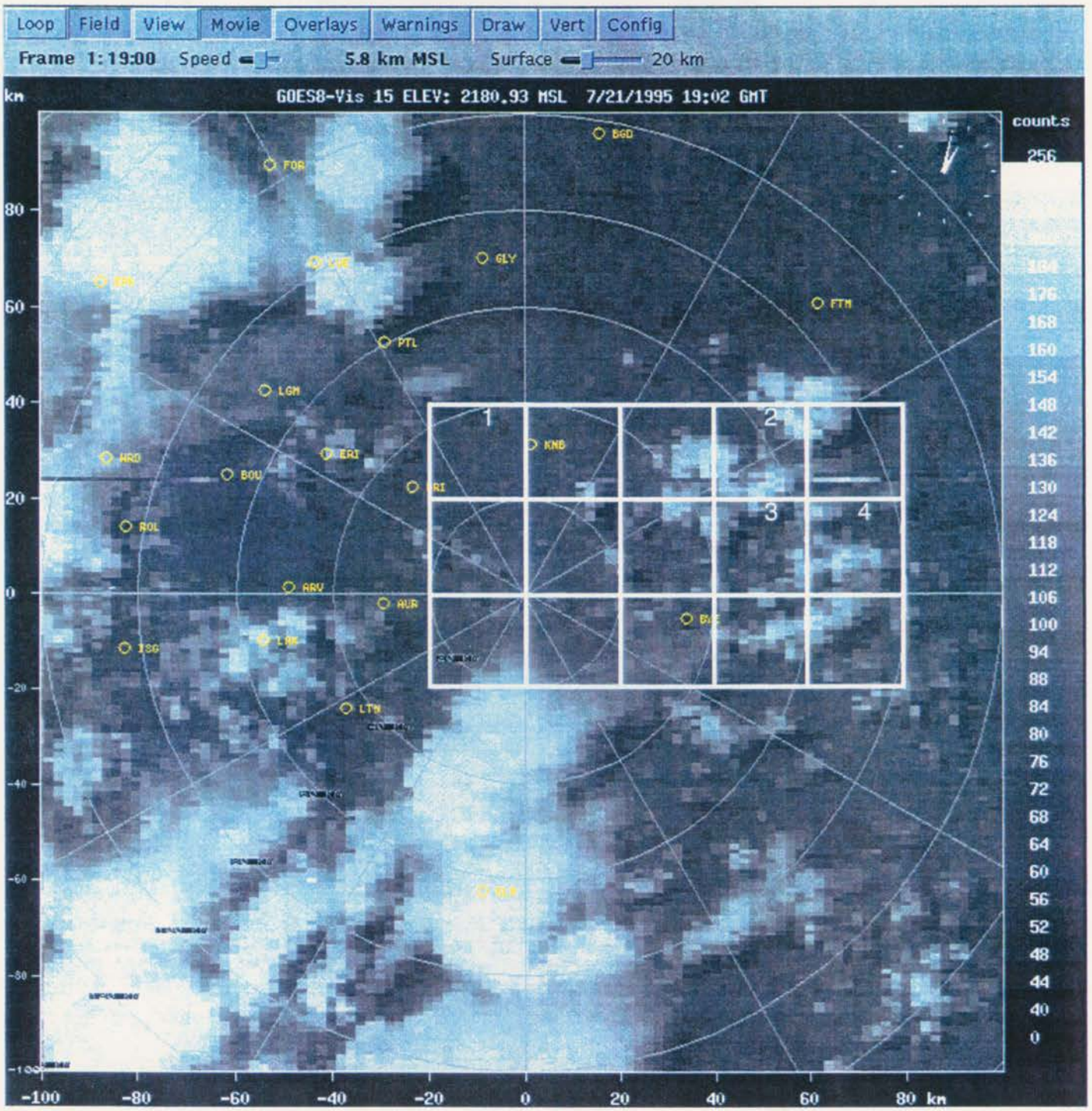

Figure 4.43. GOES-8 Visible imagery from 21 July at 1902 UTC. Units are in radiance counts. The gridded region on the plot represents the 20 x 20 km regions analyzed from this day. The numbered boxes represent those regions discussed in the text.

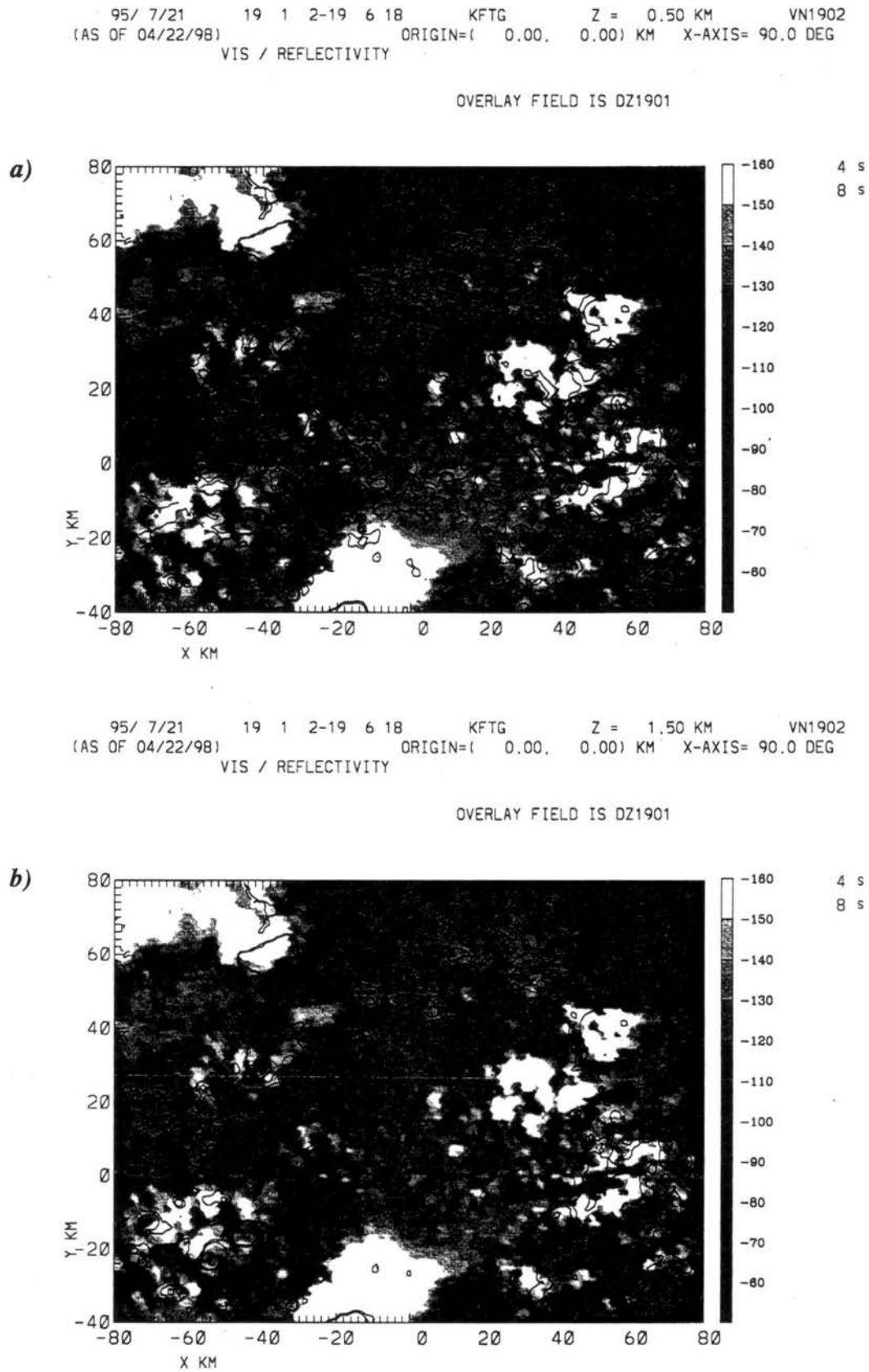

Figure 4.44. Visible data at 1902 UTC on 21 July 1995 with reflectivity contours overlaid. Contours are in increments of 4 and 8 dBZ. The Visible data is in radiance counts; values are negative for plotting purposes only. Reflectivity at a) 0.5 km AGL and b) 1.5 km AGL.

reflectivity field.

One other boundary layer feature of interest on this day was a thunderstorm outflow that moved off the mountains and intersected the E-W lines of reflectivity as it moves eastward. This feature is barely discernible in Fig. 4.42a, but is much more obvious 30 min later at 2057 (Fig. 4.42b) as a scalloped, 15 dBZ reflectivity thin line. This line is centered at x = -15, y = 0 km. Note also, for future reference, the echo along an E-W roll at x = -15, y = 33 at 2028 (Fig. 4.42a) that developed ahead of the gust front. The cloud growth associated with this storm is documented in the following subsection.

4.3.3 Growth of cumulus clouds

The gridded areas in Fig. 4.43 show the regions that have been analyzed. Data from box 1 is presented to show the pattern of cloud growth ahead of the gust front. Data from boxes 2, 3 and 4 are shown to document cloud growth above weak, less organized horizontal roll convection. To facilitate the discussion of cloud growth, the evolution of the brightness temperature and 4.5 km radar reflectivity fields are shown in Fig. 4.45. These plots include a larger region than the domain contained within the gridded region in Fig. 4.43. Inspection of the brightness temperature field shows the very cold, subfreezing temperatures associated with convection initially over the mountains (x = -80 to -60 km) in Figs. 4.45a,c and the eastward encroachment of these cold temperatures associated with convection behind the gust front (Figs. 4.45 e,g). The thunderstorms responsible for these temperatures can be seen initially in the NW corner of Figs. 4.45b,d. The

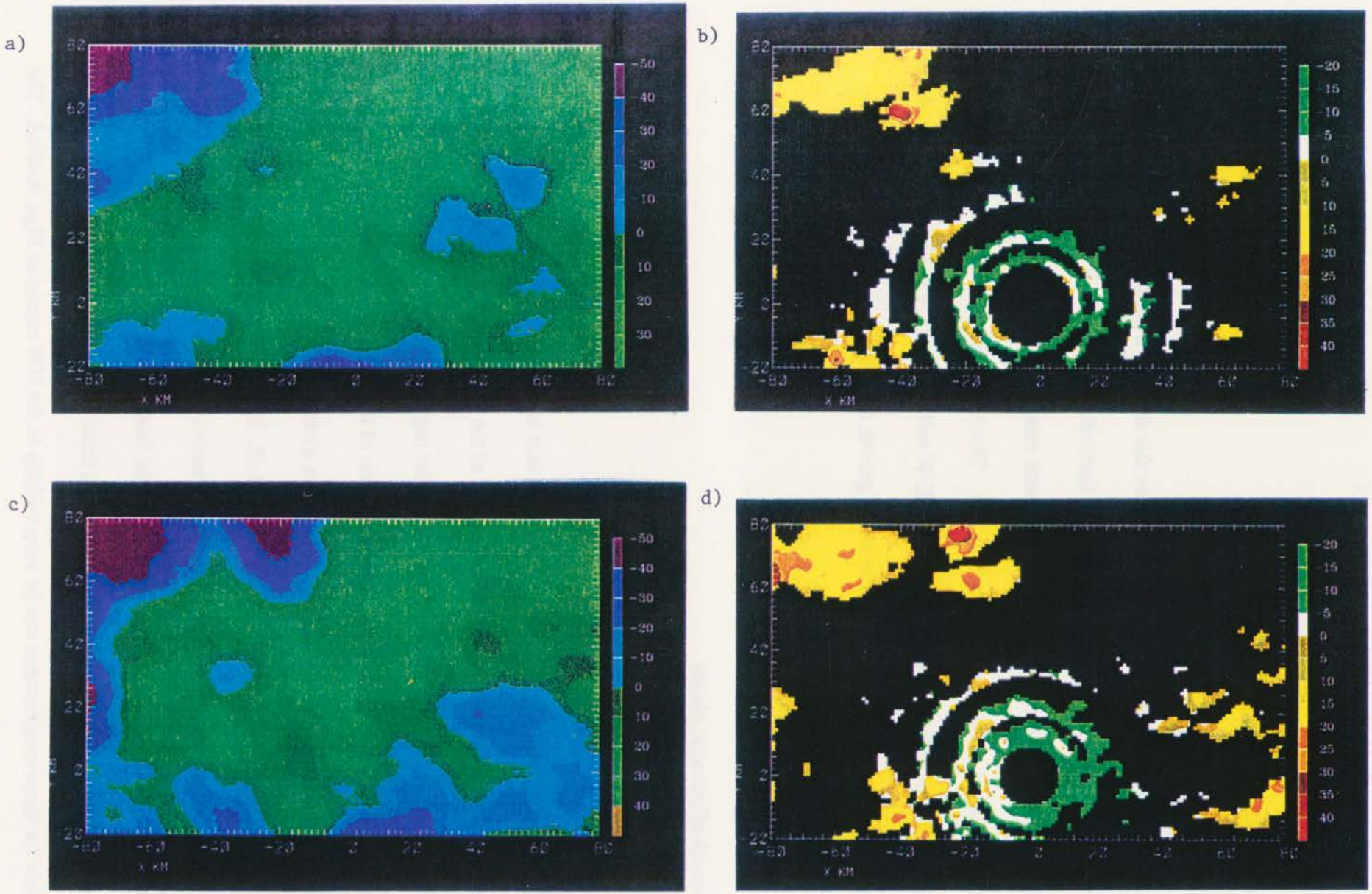

Figure 4.45. CEDRIC plots of brightness temperatures and radar reflectivity on 21 July 1995. a) IR temperatures at 1900 UTC. b) Reflectivity at 4.5 km AGL. c), d) Same as a), b), except at 1930 UTC.

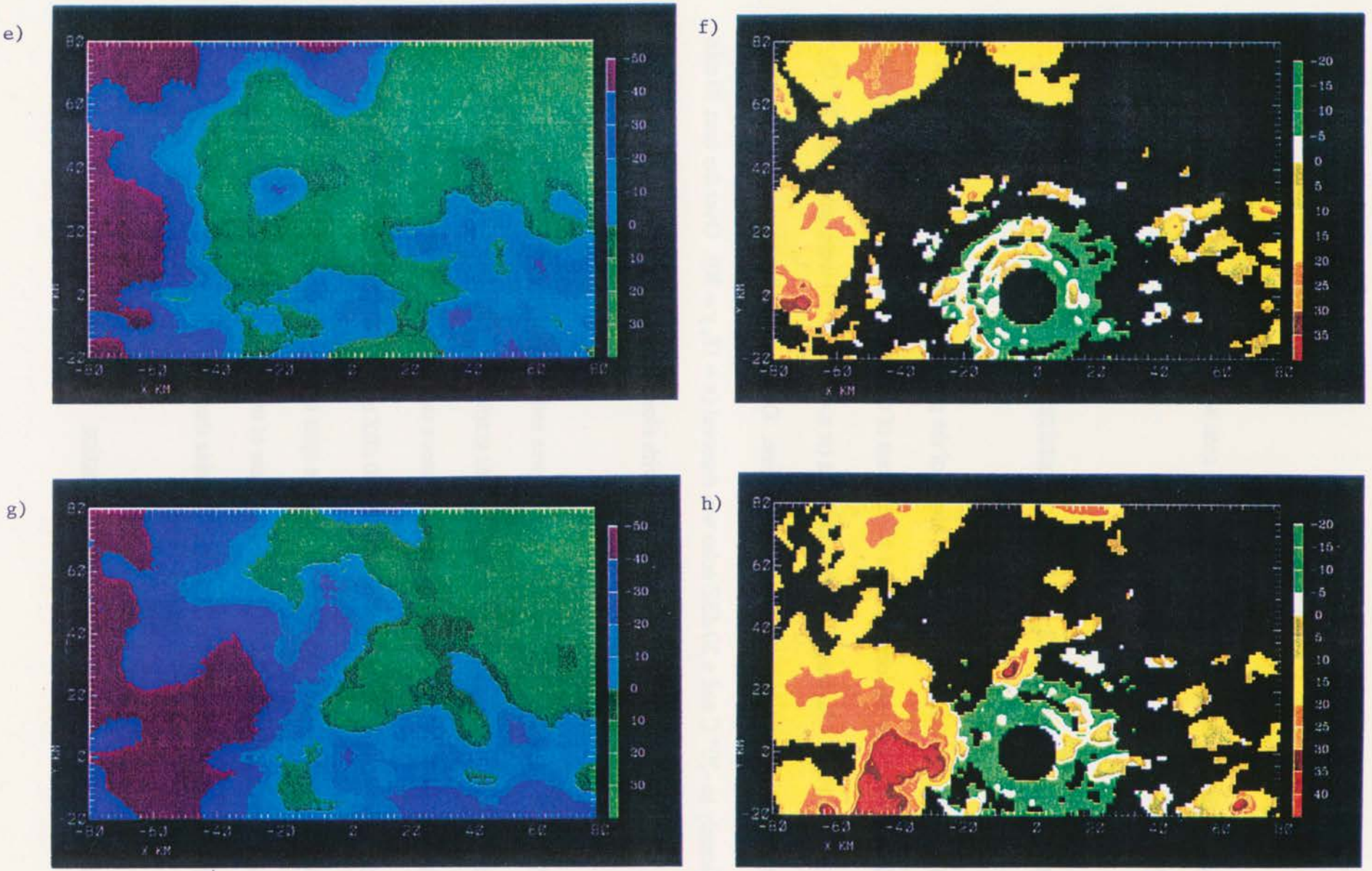

Figure 4.45. e) Temperatures at 2000 UTC, f) reflectivity at 2000 UTC, g) temperatures at 2030 UTC, and h) reflectivity at 2030 UTC.

echoes associated with gust front passage can be seen west and southwest of the radar in Figs. 4.45 f,h.

i. Cloud growth associated with gust front/horizontal roll interaction

The storm that formed within box 1, ahead of the gust front, originated from a group of cumulus clouds that were located about 10 km west of the boxed area and advected into it (see Fig. 4.43). In Fig. 4.45a, temperatures in that area (at x = -40, y = 30) were quite high (28° C), but no Rayleigh scattered echo was apparent at this time. Over the next hour, temperatures decreased significantly to -20° C and a 20 dBZ echo was detected (x = 18, y = 30). Over the next 30 min (Figs. 4.45g,h) the storm intensified to 45 dBZ with cloud top temperatures of -30° C.

This trend in decreasing cloud top temperatures and subsequent storm intensification is summarized in the time series graph in Fig. 4.46. This graph is very similar to those in Fig. 4.40 for a gust front interacting with rolls. The main difference on 21 July is that temperatures fall below 0° C only 15 min prior to the appearance of the 20 dBZ echo and 30 min prior to the 35 dBZ echo. The 24 August cases showed a much longer time span between the onset of subfreezing temperatures and first Rayleigh backscatter echo. The rate of temperature drops are by far the largest values observed with any of the cases presented in this thesis.

ii. Cloud growth above less organized roll convection

Time series graphs for data from boxes 2, 3, and 4 are shown in Fig. 4.47. Sub-freezing cloud

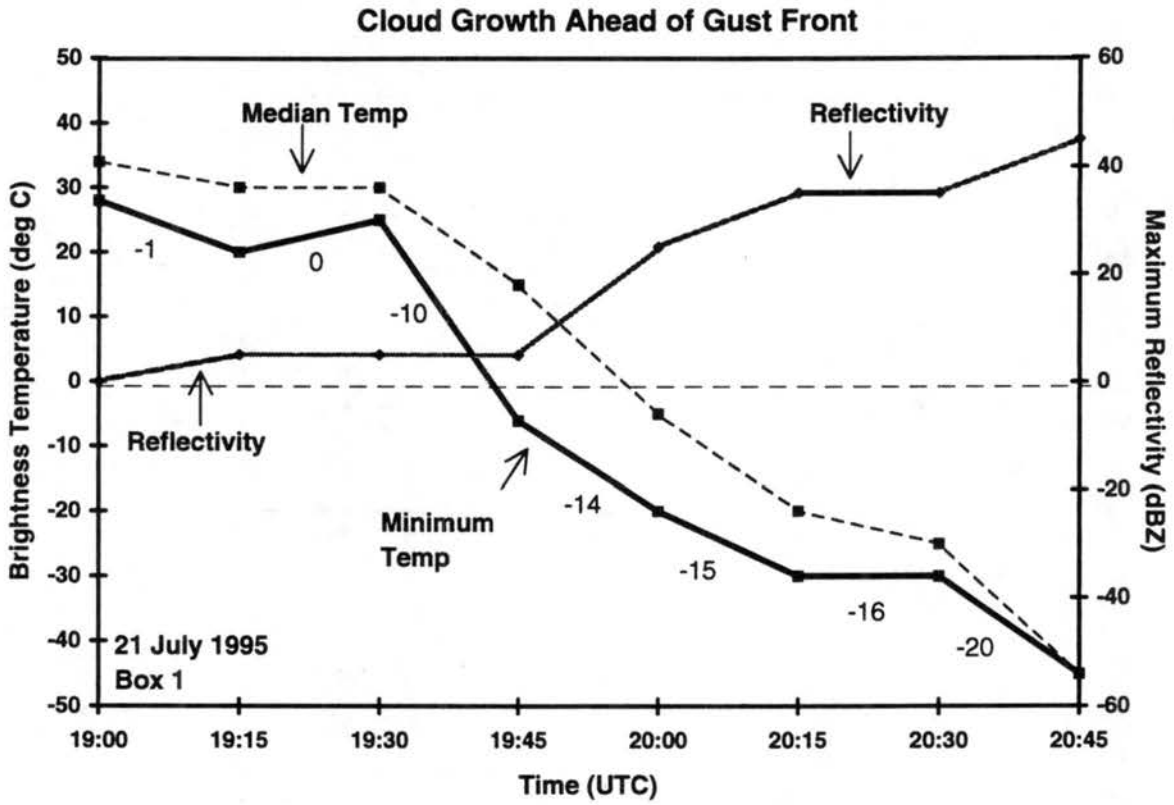

Figure 4.46. Time series plots of IR temperatures and maximum reflectivity associated with cloud growth ahead of a gust front on 21 July 1995. Median (dashed) and minimum temperature (black) curves and reflectivity (gray line) are shown for box 1.

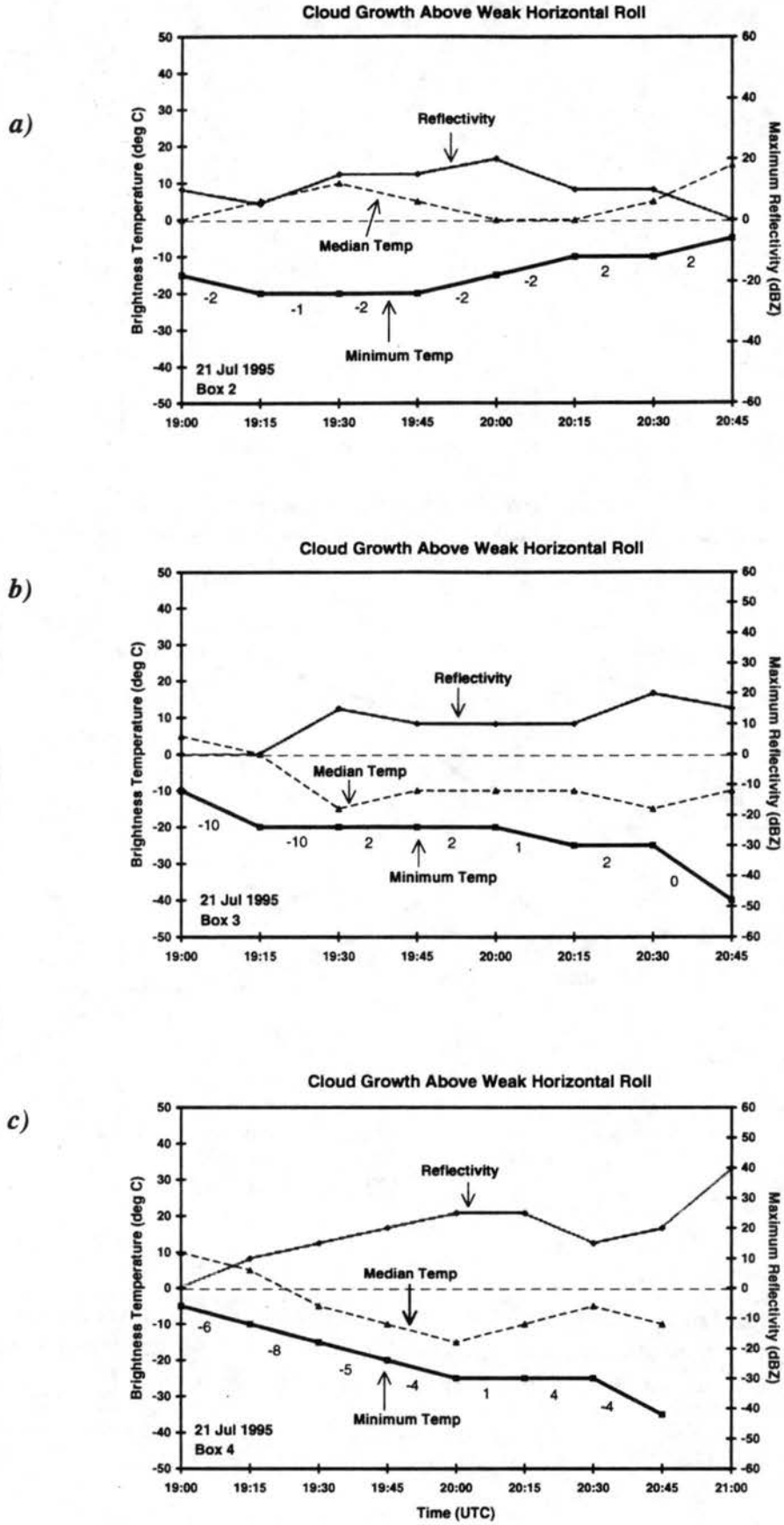

Figure 4.47. Same as Fig. 4.46, except for cloud growth above weak horizontal rolls within a) box 2, b) box 3, and c) box 4.

top temperatures already existed in all three boxed regions. This is also evident in the brightness temperature panels in Fig. 4.45 in the region east of the radar. Weak 10-20 dBZ reflectivity echo was associated with these clouds, with the reflectivity curves showing very little change over the duration of these storms. The temperature curves similarly exhibit a flat trend with time, with cloud top temperatures failing to drop much below -20° C, except in the area of box 4. In box 4 the storm did manage to reach 20 and 40 dBZ coincident with cloud top temperatures of -25 to -35 deg C and temperature rate of change values of < -4 deg C prior to 2000 and 2045. The top of the mid-level moisture on the sounding (Fig. 4.41) coincided with the environmental temperature of -30° C. In the classic dry microburst events documented by Wakimoto et al. (1994), environments were characterized by soundings similar to Fig. 4.41 and typically produced 20-25 dBZ storms of ~3 km in depth.

Without the presence of a gust front or organized surface convergence to encourage vigorous convection along these rolls, low reflectivity storms such as characterized in Fig. 4.46 are all that the environment was able to support. The low magnitude of temperature rates in Figs. 4.46a,b also reflect the lack of growth and from a forecasting perspective, a lowered expectation of vigorous growth. Looking at these rates and those presented from 23 and 24 August, there is a definite correlation between the magnitude and sign of temperature rate values and the type of convection that ensues. Monitoring the changes in cloud top temperature is equally as important as monitoring when cloud top temperatures drop below freezing.

4.4 24 July 1995

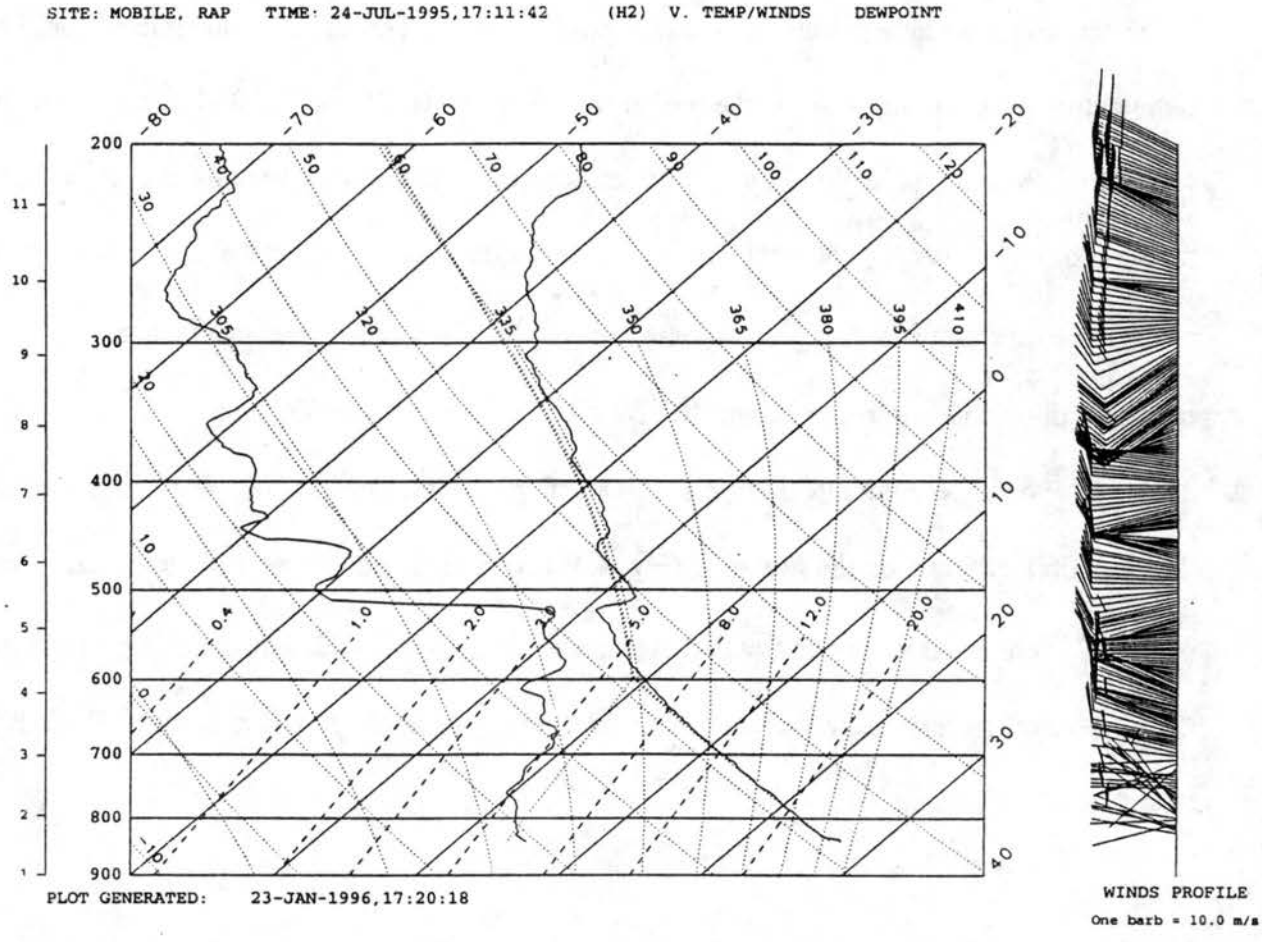

Figure 4.48. CLASS sounding taken at 1700 UTC on 24 July 1995 at the Denver NWS.

4.4.1 Environmental Conditions

The DEN sounding at 1200 UTC was not available on 24 July. The CLASS 1700 UTC sounding is shown in Fig. 4.48 instead. The major difference between this sounding and the 21 July sounding is the temperature (subsidence) inversion near 500 mb (5.6 km MSL or ~ 4 km AGL). This inversion, with a mean temperature of -8 deg C, reflects the presence of a pressure ridge that was located over the SW United States during the afternoon and the warm, dry air associated with it. Dewpoint temperatures ranged from the upper 30's to lower 40, evidence of a fairly dry boundary layer. As will be seen in the following subsections, the subsidence inversion capped the vertical extent of convection throughout the entire afternoon on this day. And with a LI of 1.25 and a low CAPE of 30 J/kg, the chance for intense convection was marginal.

4.4.2 Relationship of clouds to boundary layer features

As was seen on 21 July, the intensity of the clear air reflectivity in the boundary layer was quite low. With the enhanced color table scale, 4-6 dBZ thin lines can be seen at 1957 in Fig. 4.49 with a WNW-ESE orientation. East of the radar no obvious linear structure existed. The radar radial winds were on the order of 6-9 m/s from the WNW. Bands of higher velocities were embedded in the flow, parallel the thin lines located north of the radar. No gust fronts moved across the eastern Plains during the afternoon.

At 1815 UTC (Fig. 4.50a) the cumulus and cumulus congestus clouds seemed to parallel the WNW-ESE rolls observed in the data. However at 1932 (Fig. 4.50b), it could be argued that the

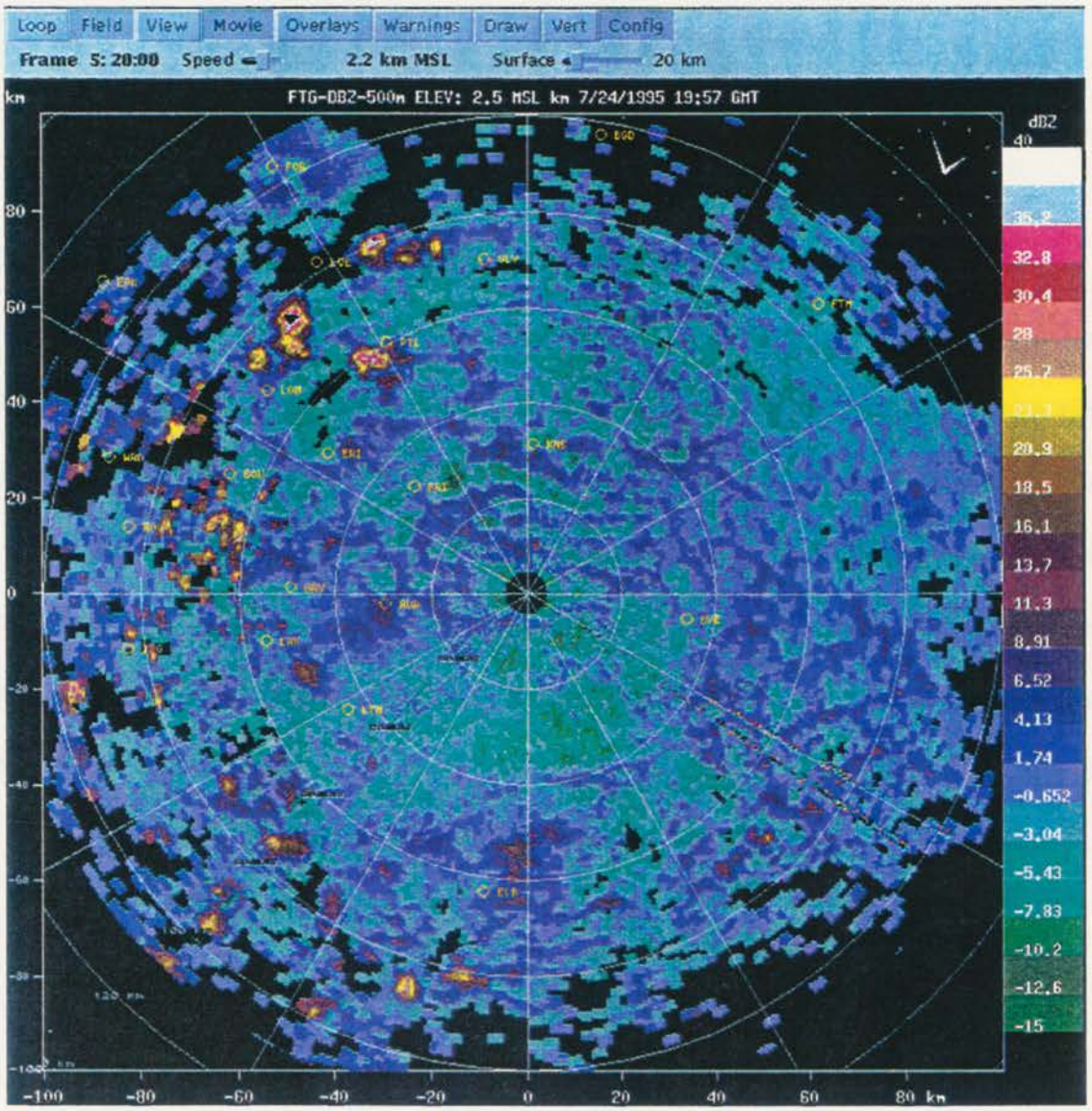

Figure 4.49. Cartesian reflectivity plot at 0.5 km AGL from 24 July 1995 at 1957 UTC. A finer colorscale increment has been used to show the low intensity, horizontal rolls.

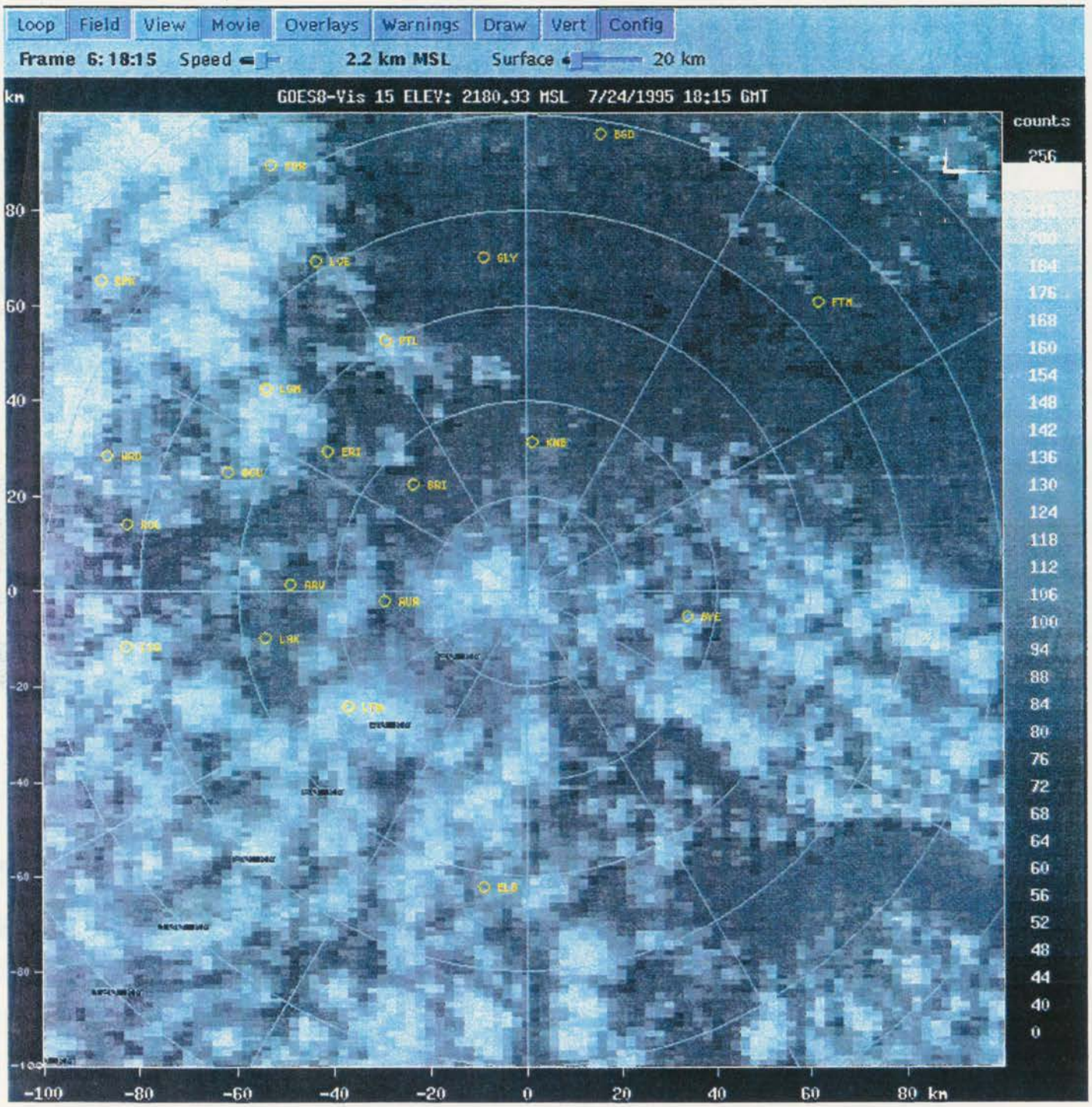

Figure 4.50. GOES-8 Visible data from 24 July 1995. Units are in radiance counts. a) Image at 1815 UTC.

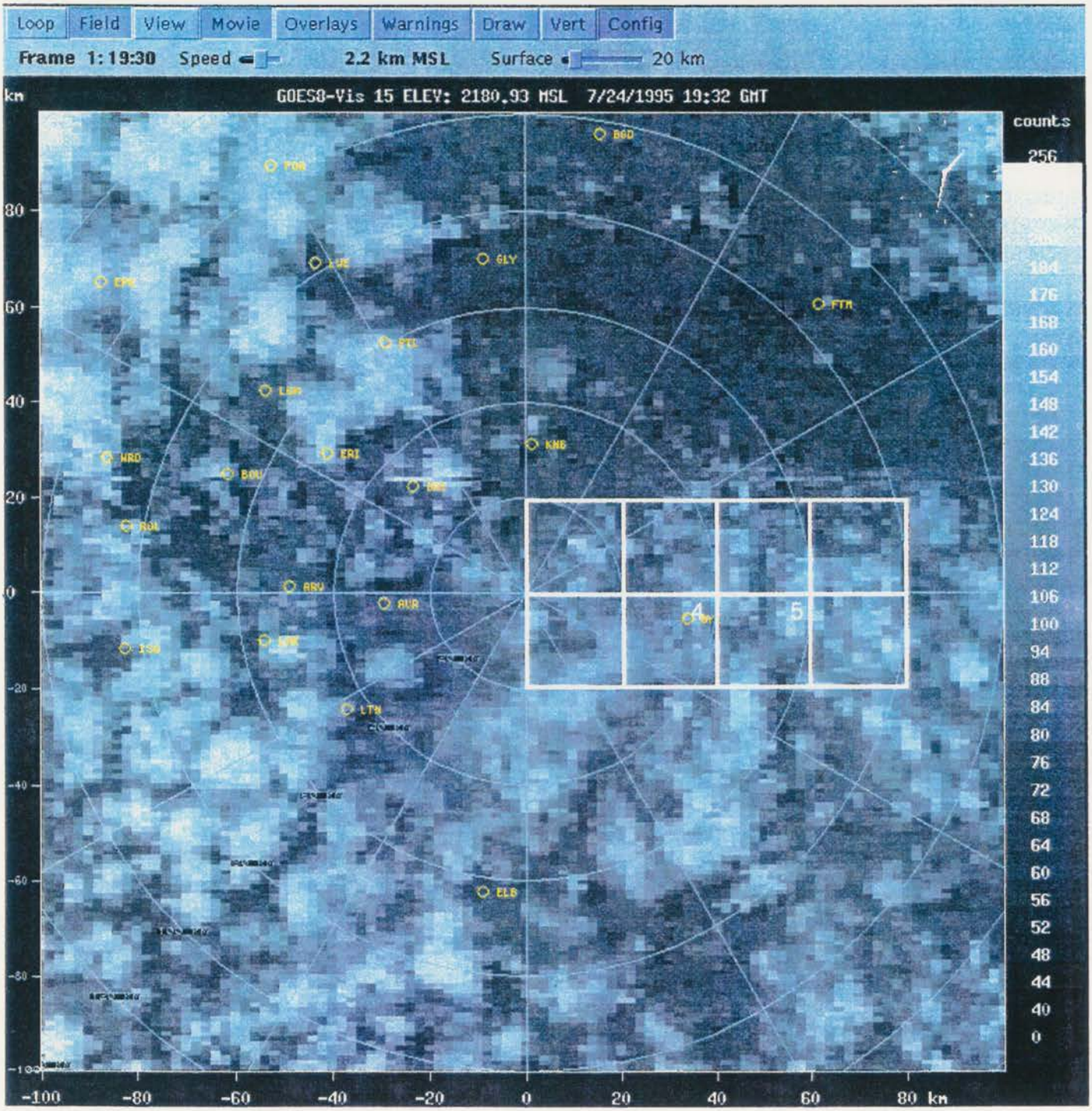

Figure 4.50. b) Image at 1932 UTC. The gridded region on the image represents the 20 x 20 km regions analyzed from this day. The numbered boxes represent those regions discussed in the text.

clouds are now oriented SW-NE. It is unlikely that the change in cloud orientation had anything to do with the boundary layer convergence patterns, since there is no noticeable change in the surface features. There is a possibility that the capping inversion provided a favorable environment for gravity wave ducting, originating from thunderstorms over the mountains, such as Kelvin-Helmholtz waves oriented perpendicular to the horizontal rolls. The upward lift provided by these waves might account for clouds that are located transverse to the cloud lines produced by the rolls. However, this would be difficult to prove without additional, substantiating data, so our reasoning remains speculative.

The lack of good correspondence between the radar boundary layer features and the clouds by 1902 is apparent in Fig. 4.51. Unfortunately, no radar data existed prior to 1902. As with 21 July, the boundary layer rolls were weak and shallow and it was difficult to pick out any preferred linear orientation, especially at 1.5 km AGL.

4.4.3 Growth of cumulus clouds

This day was chosen for analysis partially because the satellite Visible imagery showed an extensive field of cumulus congestus clouds that looked to be on the verge of developing into cumulonimbus clouds. It was also chosen to explore the effect of a stable layer on forecasting storm growth. It is expected that the trends in brightness temperature and radar reflectivity observed here would differ from what was observed in the previous sections (in the absence of stable layers). The boxes shown in Fig. 4.50b were not selected for analysis based on any a priori knowledge of cloud evolution nor for any special distinction in boundary layer features.

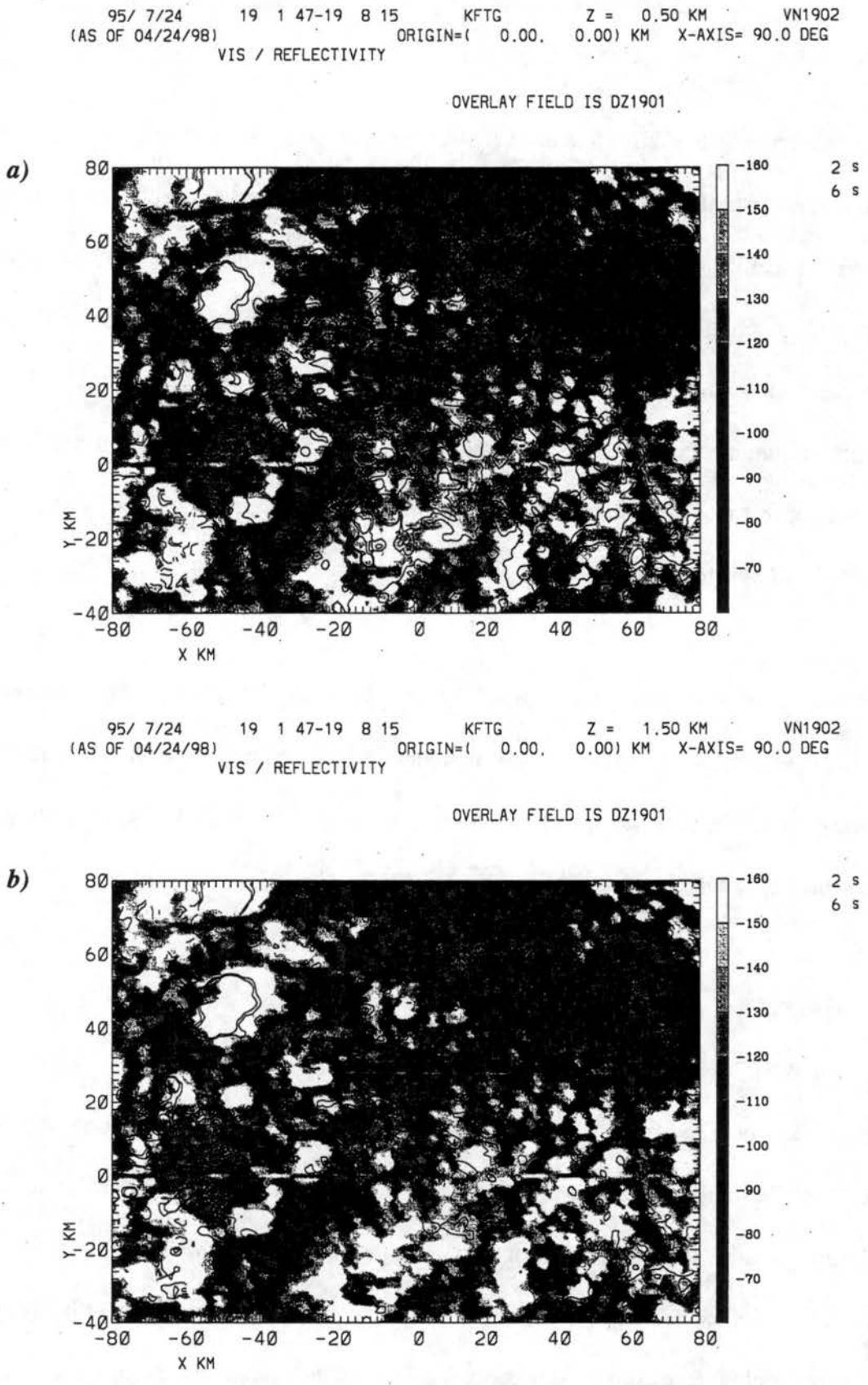

Figure 4.51. Visible data at 1902 UTC on 24 July 1995 with reflectivity contours overlaid. Contours are in increments of 2 and 6 dBZ. The Visible data is in radiance counts; values are negative for plotting purposes only. Reflectivity at a) 0.5 km AGL and b) 1.5 km AGL.

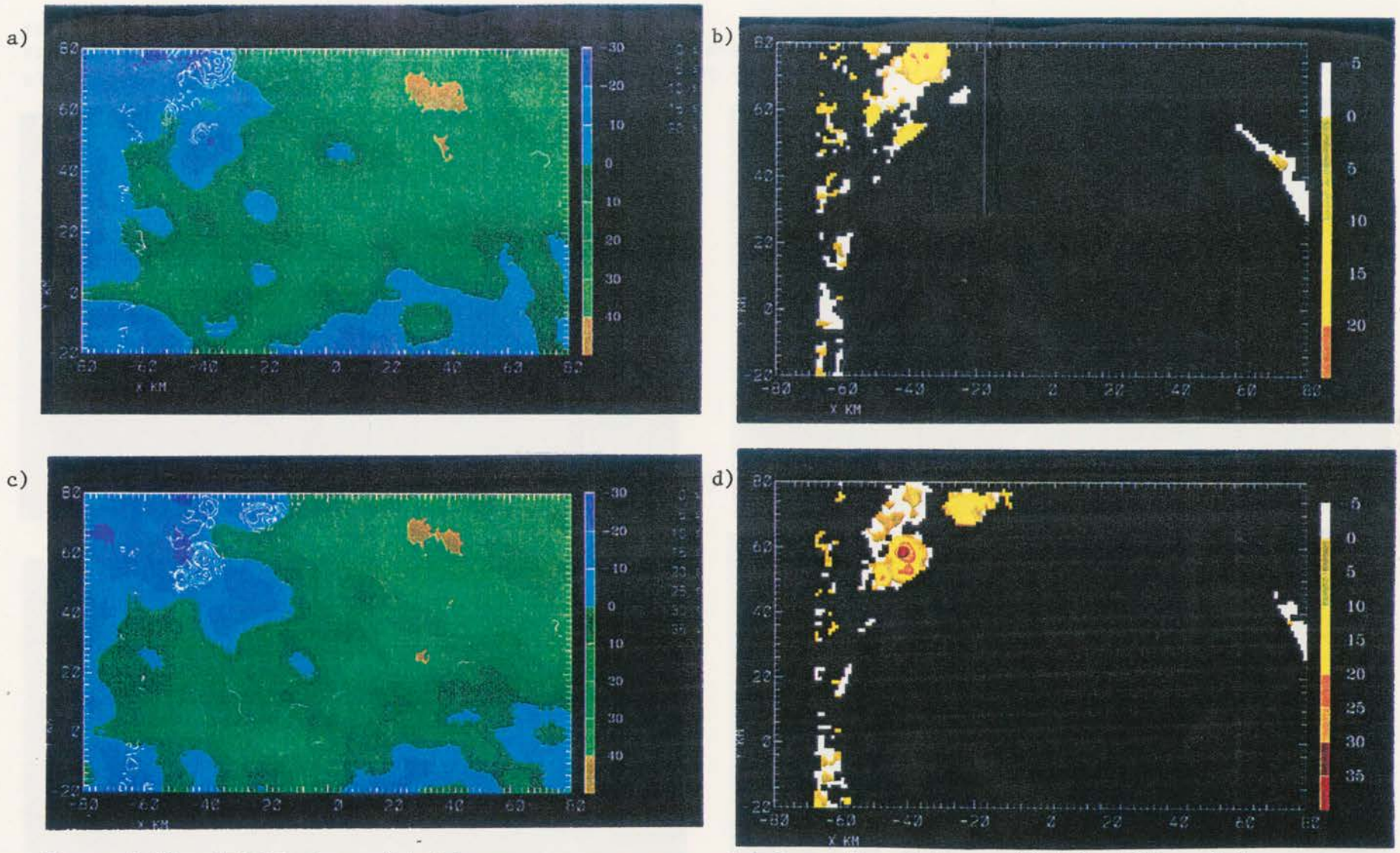

Figure 4.52. CEDRIC plots of brightness temperatures and radar reflectivity on 24 July 1995. a) Temperature at 1902 UTC with contours of reflectivity overlaid. b) Reflectivity at 4.5 km AGL. c), d) Same as a), b) except at 1932 UTC.

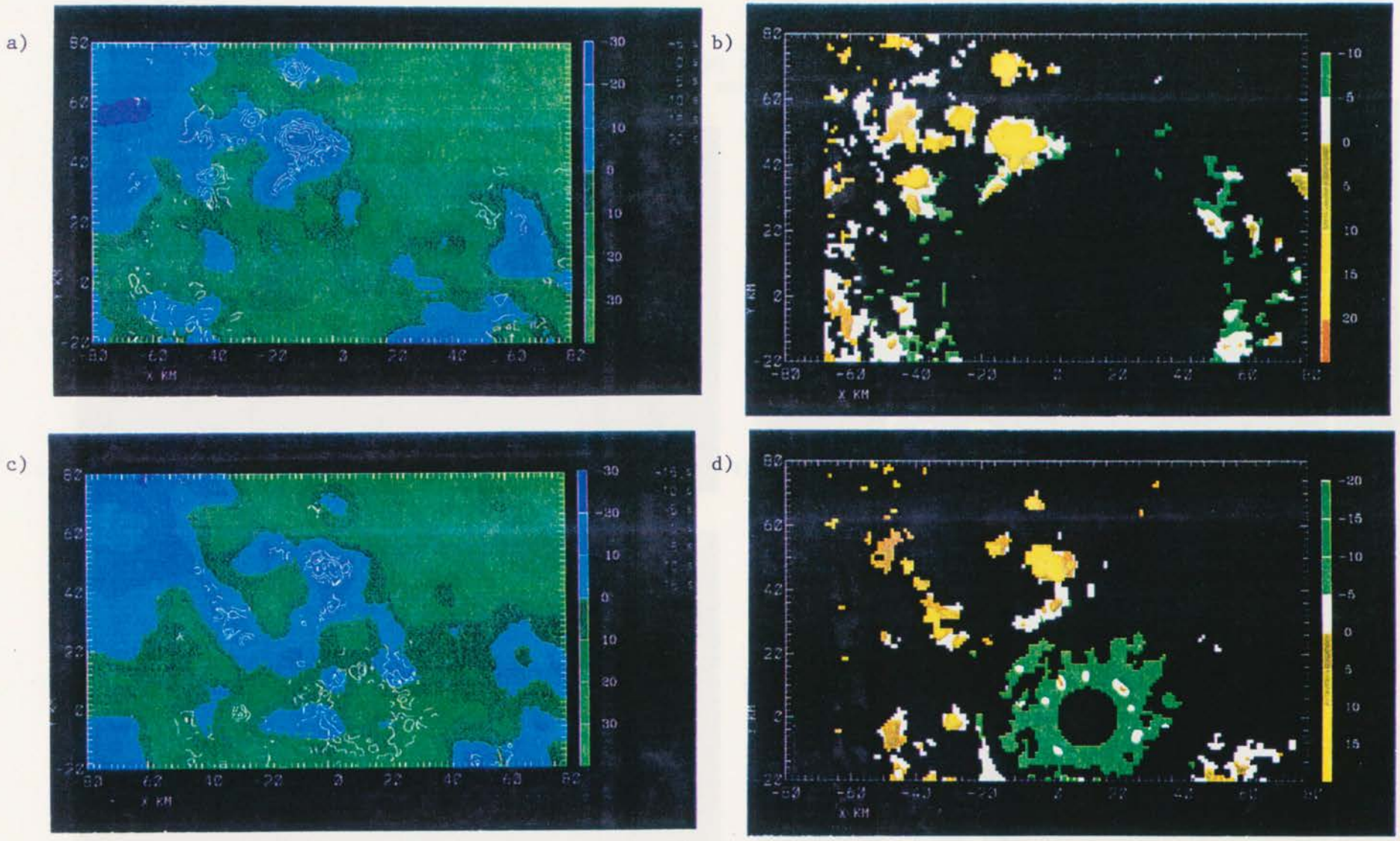

Figure 4.53. CEDRIC plots of brightness temperatures and radar reflectivity on 24 July 1995. a) Temperatures at 2002 UTC with contours of reflectivity overlaid. b) Reflectivity at 4.5 km AGL. c), d) Same as a), b) except at 2032 UTC.

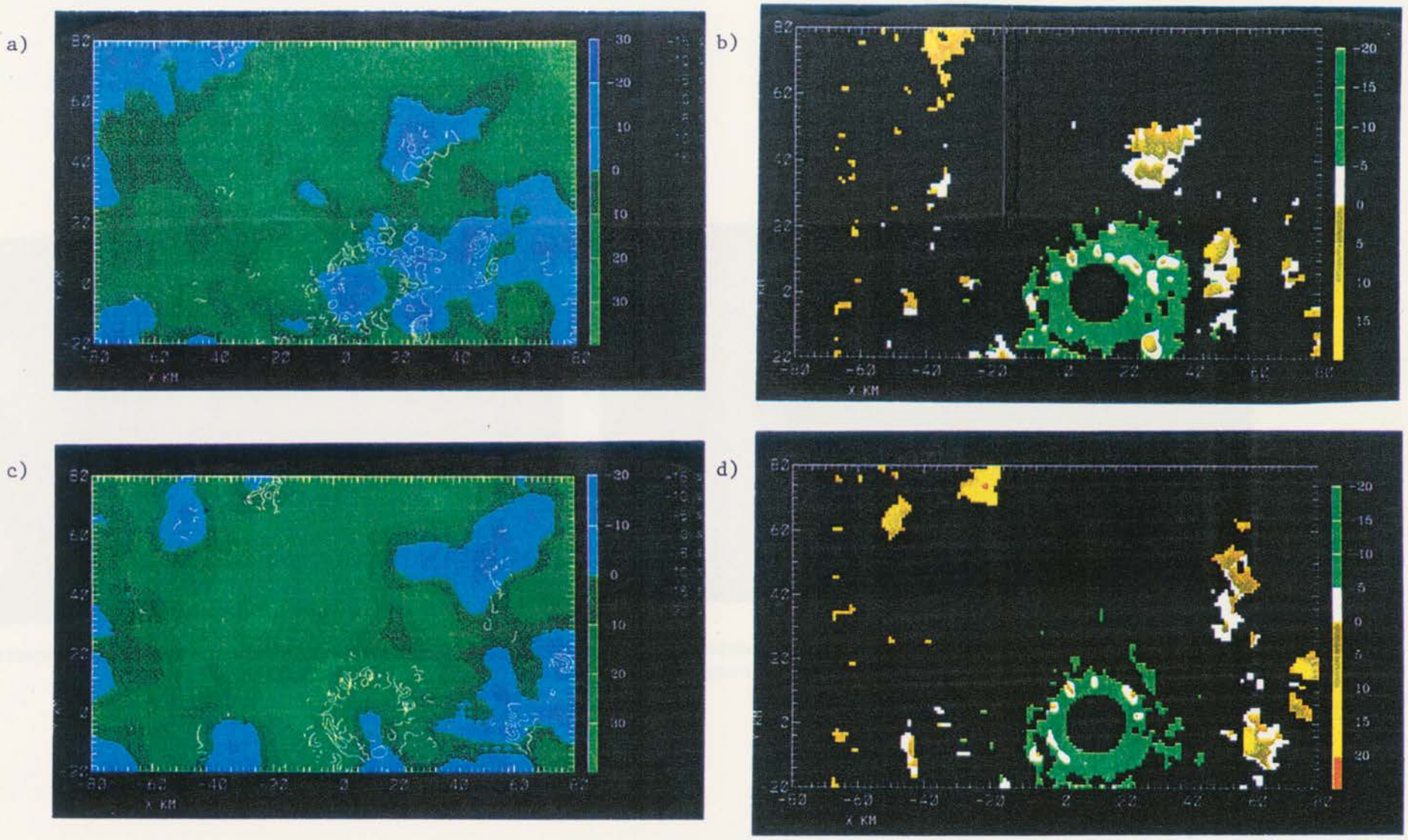

Figure 4.54. CEDRIC plots of brightness temperatures and radar reflectivity on 24 July 1995. a) Temperatures at 2115 UTC with contours of reflectivity overlaid. b) Reflectivity at 4.5 km AGL. c), d) Same as a), b) except at 2202 UTC.

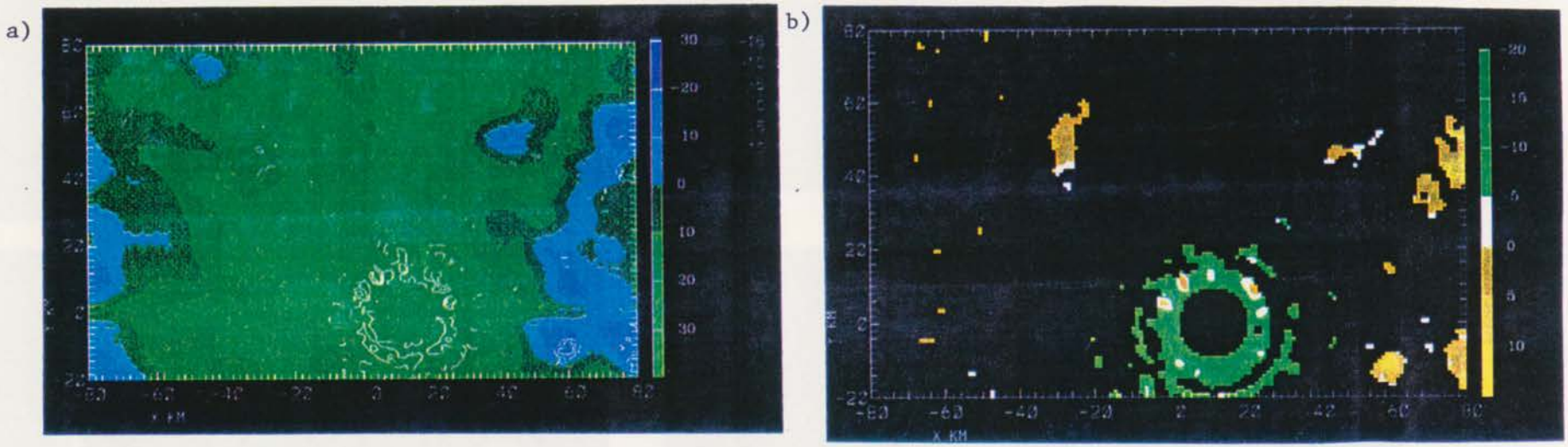

Figure 4.55. CEDRIC plots of brightness temperatures and radar reflectivity on 24 July 1995. a) Temperatures at 2232 UTC with contours of reflectivity overlaid. b) Reflectivity at 4.5 km AGL.

What is most striking about the weather on this day, given how promising the clouds looked on the Visible imagery, is that most of the storms produced failed to obtain cloud top temperatures below -15° C. This can be seen in all the brightness temperature panels in Figs. 4.52-4.55. These temperatures are actually colder than the -8° C environmental temperature associated with the strong stable layer. The fact that the cloud tops are colder suggests that the clouds were able to penetrate above the stable layer at 520 mb, but were not able to penetrate above the second, weaker stable layer (-15 deg C) at 450 mb in Fig. 4.48.

The reflectivity contours overlaid on the temperature plots do show that all echoes detected had sub-freezing cloud top temperatures. No echoes were observed in regions of > 0° C temperatures. This is consistent with all of the other cases presented in this thesis. The echoes that did form were weak, typically < 20 dBZ, with the exception of a few echoes near the mountains, to the NW of the radar. Several of the cumulus congestus clouds barely managed to have precipitation echoes of 5-10 dBZ intensity, as can be seen east of the radar in Figs. 4.54-4.55.

The time series graphs in Fig. 4.56 show the oscillating growth of the clouds as they attempted to penetrate the stable layers. These graphs show the same trends and weak pulsating growth as was observed within the other boxed regions that are not shown from this day. Cloud top temperatures were already subfreezing at -15° C very early in the afternoon. Rates of temperature change are either positive, indicating warm trends, or very small negative values indicating cooling trends. Within box 4, substantial warming of the clouds to 0° C was observed between 2000 and 2030. There was a signifcant decrease in the density of cumulus clouds during this time period. Fifteen minutes later temperatures fell again (at a greater rate) to -20° C, overshooting the

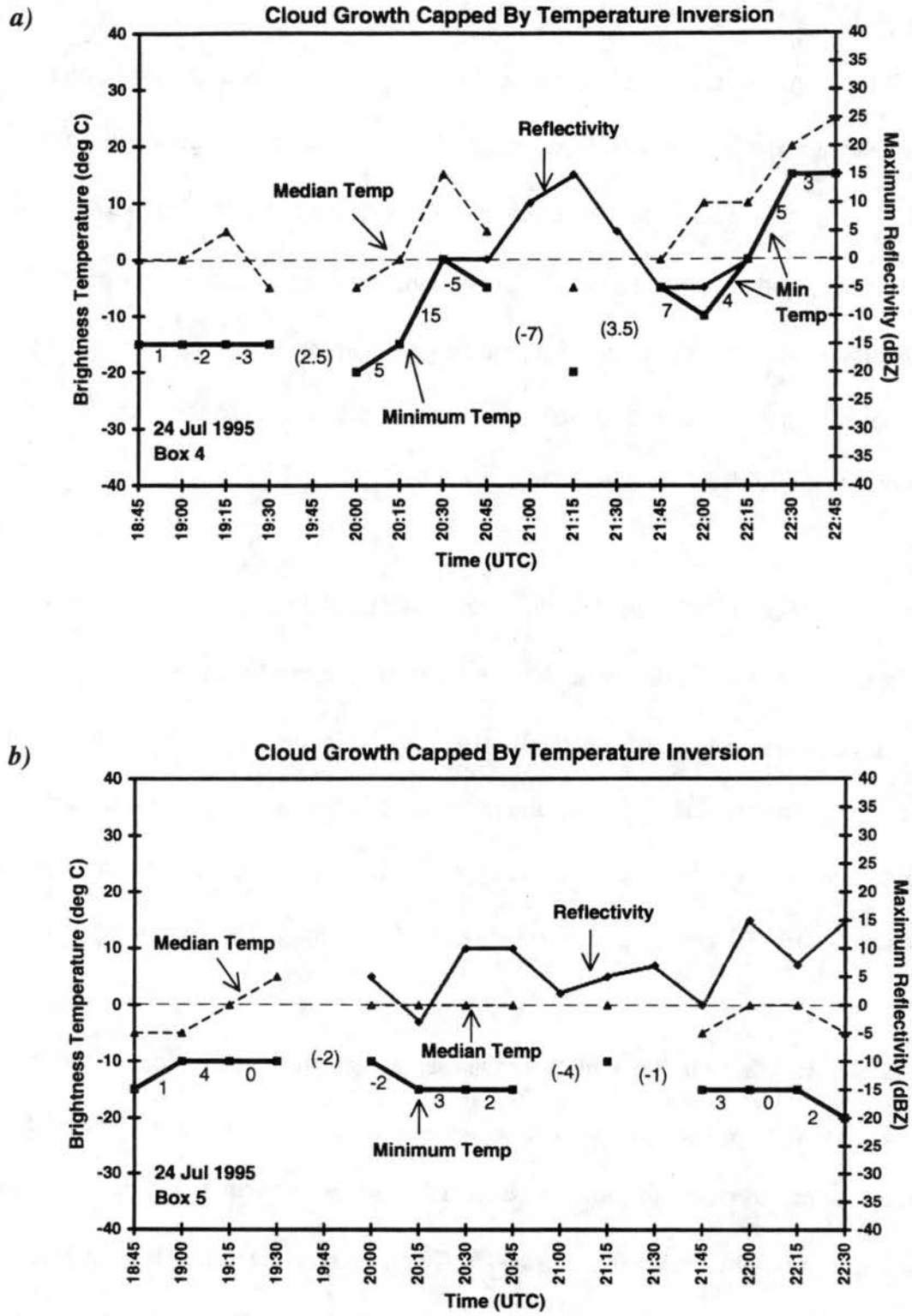

Figure 4.56. Time series plots of IR temperatures and maximum reflectivity associated with cloud growth capped by temperature inversions on 24 July 1995. Median (dashed) and minimum (black) temperature curves and reflectivity (gray curve) are shown for the regions defined by a) box 4 and b) box 5.

secondary stable layer. A weakly precipitating, 15 dBZ storm was produced but rapidly decays. Cloud top warming to above freezing temperatures ensued.

Within box 5, cloud growth was characterized by pulsating growth and decay. The minimum temperature curve remained relatively flat near -15° C and temperature change values were mostly positive. The median temperatures within the box were generally in the range of -5 to 0° C, another indication of the limited potential for cloud growth when warm, stable layers exist in the environment. In the time periods immediately prior to the brief surges of growth, the median rate of temperature change values do turn negative, in an otherwise constant series of positive rate values. Thus, even in unfavorable environments, the same trend of temperature falls before detection of significant echo was still observed.

Chapter 5

CONCLUSIONS

The focus of this thesis has been to show how operational WSR-88D radar data and GOES-8 satellite imagery can be used together to provide information on the growth of cumulus clouds into thunderstorms, and to increase the lead time in issuing forecasts of thunderstorm initiation. With the advent of the GOES-8 satellite 15 min update rate and higher data resolution, it is now possible to detect and track cumulus cloud growth more closely. The limitations of the satellite data for forecasting applications includes the occasional presence of early afternoon thunderstorm anvils that obscure cumulus clouds at lower altitudes, the lack of data at 2100 UTC, and the registration errors that can occur in the data in day-to-day operations. The WSR-88D radar has been shown to be very capable of detecting boundary layer, clear air convergence features, such as reflectivity thin lines associated with gust fronts and horizontal roll convection. The main limitation of the WSR-88D is the 1 km gate spacing that prevents better detection and resolution of Bragg backscatter return.

From the data presented here, it is clear that growth of cumulus clouds into thunderstorms is dependent not only on the characteristics of the environment, but is intimately tied to the type of boundary layer convergence features initiating and enhancing convection. The presence of strong, organized, surface convergence concentrating the available boundary layer moisture has been shown by several studies to produce deeper and long-lived convection. On 23 and 24 August,

cumulus cloud locations were well correlated with the convergence portions (i.e., reflectivity thin lines) of the horizontal rolls. On 24 July, cumulus cloud lines were initially aligned with the E-W horizontal rolls (at 1815 UTC). Later, when the clouds became more cellular in orientation, it was difficult to correlate the cloud locations with the shallow, convergence lines on this day. This was complicated too, by the widespread, cumulus congestus clouds that possibly could have been initiated by gravity wave currents trapped underneath the stable layers.

Cloud growth under a spectrum of boundary layer regimes have been presented. The most intense storms with reflectivity echoes > 40 dBZ occurred above gust fronts alone and when gust fronts intersected horizontal rolls, as on 24 August. Vigorous growth was also observed above the stationary boundary (DCVZ) on 23 August. Storm formation above horizontal rolls was variable and the intensity of the storms produced was clearly dictated by the environmental conditions. On 21 July, cloud growth above weak horizontal rolls was marginal, producing 10-15 dBZ, shallow echoes that persisted for up to 2 hrs. This was not surprising, given the morning sounding profile that was representative of environments characterized by low intensity, micoburst-producing storms. On 24 July, stable layers capped cloud growth, with cloud top temperatures rarely falling much below the environmental temperature within the stable layer. On 23 August, growth of clouds above the horizontal rolls, primarily where the rolls intersected the stationary DCVZ, was more vigorous, likely due to the additional convergence that resulted at the intersection points. Cloud growth was examined above horizontal rolls located in regions 60-80 km apart on 24 August. Storms formed above the rolls in the southern region, but not in the northern region where the density of cumulus clouds was larger. The difference in the abilty of storms to form in one region and not the other was attributed to the variability in the boundary layer moisture in the

two regions.

In all cases presented, cloud growth was evident in the satellite data in the form of decreasing cloud top temperatures, prior to first detection of 10-20 dBZ radar echoes. Even in the less favorable environments such as the microburst type environment of 21 July and 24 July, with the elevated stable layers, temperature falls were observed prior to the growth of reflectivity echoes. While temperature falls below 0° C may not have the same signifcance in warmer climates such as in the southeastern United States, for Colorado, subfreezing cloud top temperatures are precursors to the start of the precipitation phase in clouds. Cloud top temperatures below 0° C typically occurred 15 min prior to the detection of 20 dBZ echoes, and 30 min prior to the detection of 30 dBZ echoes. In one case of convection above a horizontal roll, the temperature falls preceded echo development by 45 min. Clouds above horizontal roll convection that did not have the benefit of extra convergence and extra lift as would be provided by a gust front, pulsated (growing and decaying) for a 2.5 hr period until cloud tops were finally able to penetrate to freezing temperature heights.

It is recognized that cloud top temperatures below 0° C may not always signify the start of the precipitation phase in clouds, or the start of enhanced cloud growth arising from increased thermal buoyancy due to release of latent heat. The data presented in sections 4c-d illustrated this point. However, in Colorado, first precipitation echo usually occurs at subfreezing temperatures. For forecasting thunderstorm initiation, both cloud top temperatures and the time rate of change of the cloud top temperature should be monitored. Subfreezing cloud top temperatures are important for growth as long as there is not a warming of cloud top temperatures with time (i.e., positive

rate of change values). Similarly, negative cloud top temperature changes are not as meaningful for storm growth until the actual cloud top temperatures fall below freezing and the latent heat released as precipitation starts to form, thus aiding storm updrafts. In addition, temperature change information and median temperature trends can be used to mark the change from slow growth of storms (that may have subfreezing tops) to rapid storm growth, such as on 21 July (Fig. 4.52, box 4). This information could also be used to mark transitions from decaying to new storm growth above gust fronts (see boxes 3 and 4 on 24 August).

Results from this study show that both satellite and radar data can be exploited to provide up to 30 min additional lead time in issuing forecasts of thunderstorm initiation, by monitoring the data in an automated way. The radar data can be used to detect surface convergence features and focus the forecaster specifically on those areas. In the absence of organized surface convergence, as on 24 August (box 11), vertical cloud development would be expected to be small. Growth of clouds above or ahead of these convergence features can then be tracked, by monitoring the satellite IR field for sub-freezing, cloud top temperatures and cooling temperature trends. Additional information about stable layers in the atmosphere, stability indices, and other pertinent environmental information would also need to be considered in forecasting storm initiation.

In the very near future, we plan to test out these forecasting concepts at the Sterling, Virginia National Weather Service office that provides forecasts for the Washington, D. C. metropolitain area. Satellite, radar, surface mesonet, TREC winds, soundings, and numerical model data will be combined in an automated thunderstorm nowcasting algorithm using functional templates and fuzzy logic to produce 30 and 60 min, site-specific forecasts of thunderstorms. Figure 5.1 shows

some of the input fields to the automated forecast algorithm that will be available to the forecaster for viewing. In addition to the radar and satellite imagery, the forecaster will be able to view 1) output from an automated cloud classification algorithm that identifies the prominent cumulus cloud lines (pink shaded areas) along with other cloud types, such as cumulus congestus (light blue areas) and clear sky (gray regions) and 2) an areal plot of the rate of temperature change over the last 15 min. Green shaded areas on the latter plot indicate regions of cooling cloud top temperatures and inferred growth (if cloud tops from the IR field are already below freezing). Forecasters will be able to use these products as guidance when issuing their storm term forecasts and ammendments.

However, until we have a more spatially extensive measurement of the moisture in the boundary layer (and not just at the surface), there will continue to be missed forecasts and false alarms. Systems such as DIAL (dual wavelength absorption LIDAR) may, in the future, provide the means for high resolution mapping of the moisture field over a larger domain.

In the future, we plan to examine the reflectance of clouds using the near-infrared (3.9 μm; channel 2) GOES-8 data in conjunction with the 10.5 μm IR channel, especially using rapid scan (5 min update) and super rapid scan (1 min update) data. Examinination of this data will further our understanding of cloud growth by monitoring the transition of the clouds from being composed primarly of water to being composed of both water and ice. It will be our objective to compare this transition on satellite with the appearance of the first radar precipitation echo and with any Bragg scatter echo present. A multiparameter radar with high spatial resolution, such as the CHILL radar, would be ideal for this kind of study. A second radar (3 or 5 cm) would be useful

Sterling, Virginia
28 August 1997
1900 UTC

Visible Satellite

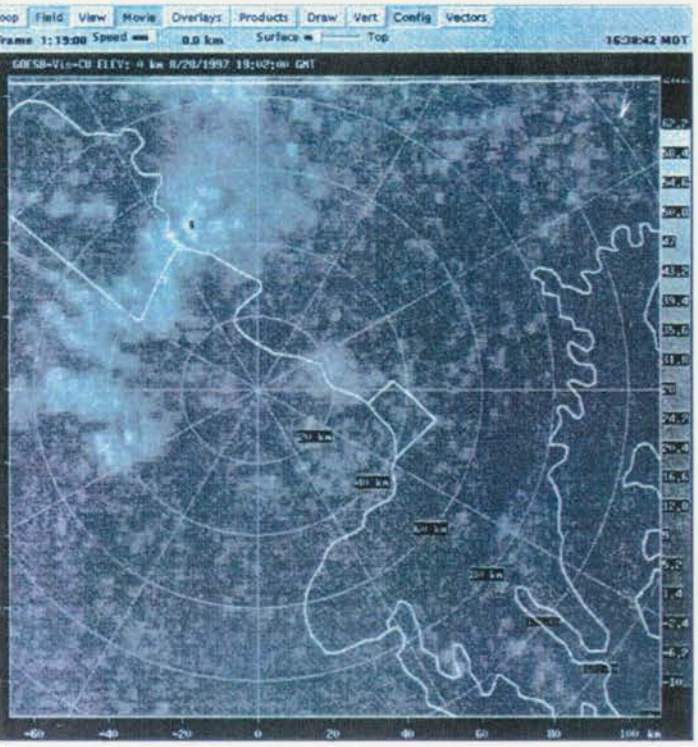

Radar Reflectivity

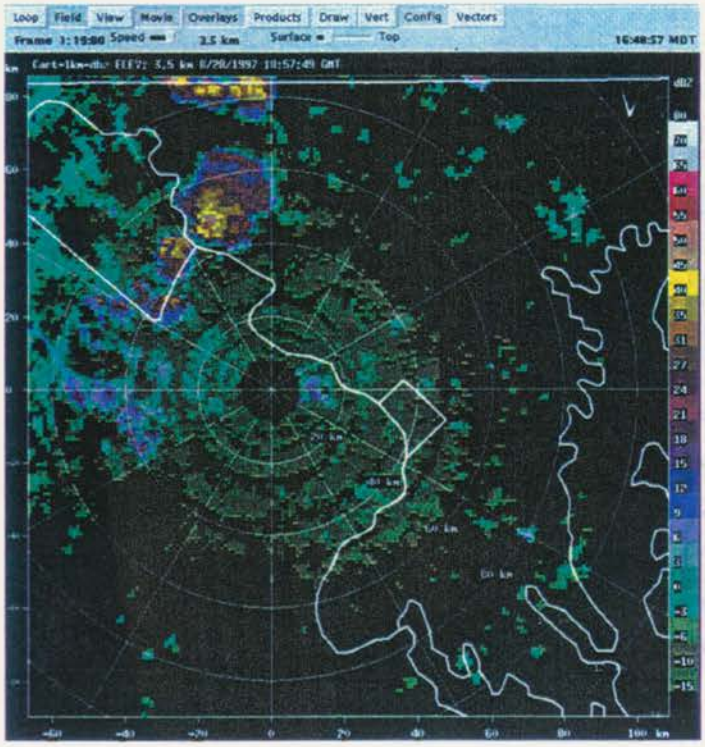

Cloud Type

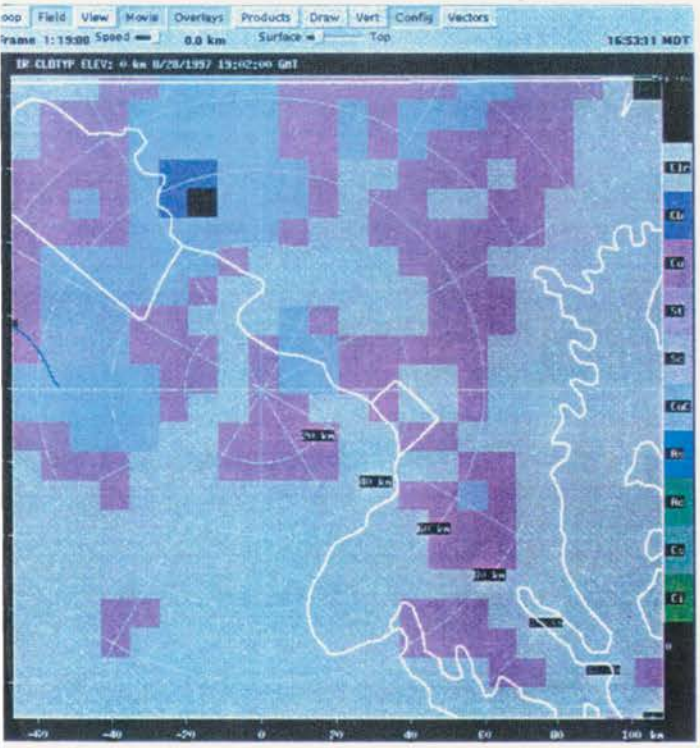

IR Temperature Change

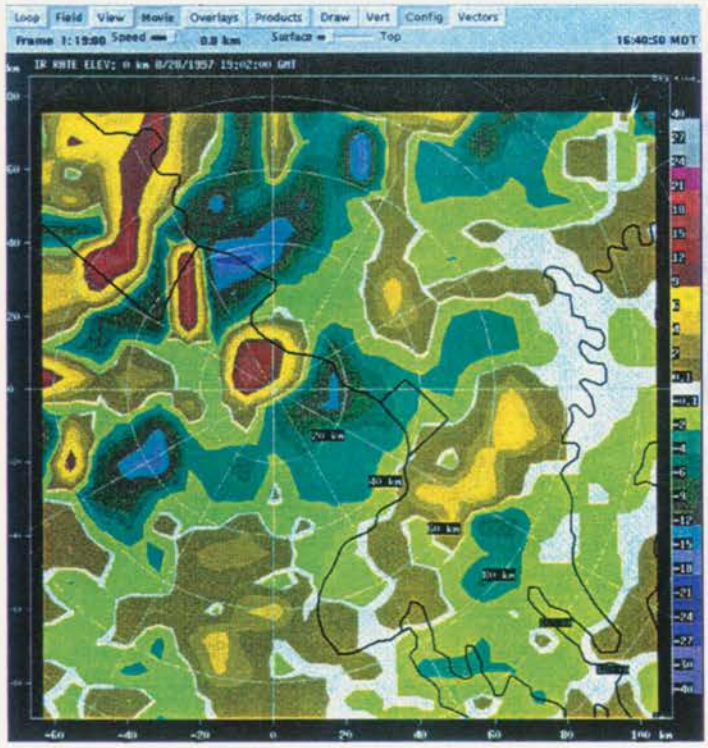

igure 5.1. Visible satellite, radar, and derived satellite products that forecasters can se as guidance in issuing short term, thunderstorm forecasts. See text for discussion.

for conclusively identifying the Bragg backscatter.

REFERENCES

Atkins, N. T., R. M. Wakimoto, and C. L. Ziegler, 1998: Observations of the fine-scale structure a dryline during VORTEX 95. *Mon. Wea. Rev.*, **126**, 525-550.

Atkins, N. T., R. M. Wakimoto, and T. M. Weckwerth, 1995: Observations of the sea-breeze front during CaPE. Part II: Dual-Doppler and aircraft analysis. *Mon. Wea. Rev.*, **123**, 944-969.

Atlas, D., K. R. Hardy, and K. Naito, 1966: Optimizing the radar detection of clear air turbulence. *J. Appl. Meteor.*, **5**, 450-460.

Battan, L. J., 1973: *Radar Observation of the Atmosphere*. University of Chicago Press, 323 pp.

Bean, B. R., and E. J. Dutton, 1968: *Radio Meteorology*. Dover Publications, Inc., New York, 435 pp.

Boyd, J. G., 1965: Observation of two intersecting radar fine lines. *Mon. Wea. Rev.*, **93**, 188.

Browning, K. A., and C. G. Collier, 1982: An integrated radar-satellite nowcasting system in the UK. *Nowcasting*. K. A. Browning, Ed., Academic Press, 47-61.

Byers, H. R., and R. R. Braham, Jr., 1949: *The Thunderstorm*. U.S. Govt. Printing Office, 287 pp.

Christian, T. W., and R. M. Wakimoto, 1989: The relationship between radar reflectivities and clouds associated with horizontal roll convection on 8 August 1982. Mon. Wea. Rev., 117, 1530-1544.

Cockbain, A. J., 1961: Low temperature thresholds for flight in *aphis fabae* Scop. *Entomol.. Exp. Appl.*, **4**, 211-219.

Cox, S. K., 1981: Radiation characteristics of clouds in the solar spectrum. *Clouds, Their Formation, Optical Properties, and Effects*. Hobbs and Deepak, Eds., Academic Press, Inc., 241-280.

Crook, N. A., T. L. Clark, and M. W. Moncrieff, 1991: The Denver cyclone. Part II. Interaction with the convective boundary layer. *J. Atmos. Sci.*, **48**, 2109-2126.

Crook, N. A., 1996: Sensitivity of moist convection forced by boundary layer processes to low-level thermodynamic fields. *Mon. Wea. Rev.*, **124**, 1767-1785.

Crook, N. A., J. B. Klemp, and R. Rotunno, 1996: Depth of lifting at a convergence line. *Preprints, 15th Conf. on Wea. Analysis and Forecasting*, Norfolk, Amer. Meteor. Soc., 276-279.

Crum, T. D., R. L. Alberty, and D. W. Burgess, 1993: Recording, archiving and using WSR-88D data. *Bull. Amer. Meteor. Soc.*, **74**, 645-653.

Estoque, M. A., 1962: The sea breeze as a function of the prevailing synoptic situation. *J. Atmos. Sci.*, **19**, 244-250.

Fankhauser, J. C., and C. Wade, 1982: The environment of the storms. *Hailstorms of the Central High Plains. Vol. 1*. C. Knight and P. Squires, Eds., Colorado Associated University Press, 5-33.

Fankhauser, J. C., N. A. Crook, J. Tuttle, L. J. Miller, and C. G. Wade, 1995: Initiation of deep convection along boundary layer convergence lines in a semitropical environment. *Mon. Wea. Rev.*, **123**, 291-313.

Foote, G.B., 1984: Influence of gust fronts on the propagation of storms. *Proc. Ninth Int. Cloud Physics Conf.*, Tallinn-Estonia, USSR, Academy of Sciences of the USSR, 419-422.

Gossard, E. E., and R. G. Strauch, 1983: *Radar Observation of Clear Air and Clouds*. Elsevier Science Publishing Co., Inc. New York, 280 pp.

Gossard, E. E., 1990: Radar research on the atmospheric boundary layer. *Radar in Meteorology*. D. Atlas, Ed., Amer. Meteor. Soc., 477-527.

Hardy, K. R., and H. Ottersten, 1968: Two scales of convection in the clear atmosphere. *Proc. Int. Conf. on Cloud Physics*, Toronto, Amer. Meteor. Soc., 534-538,

Hardy, K. R., and H. Ottersten, 1969: Radar investigations of convective patterns in the clear air. *J. Atmos. Sci.*, **26**, 666-672.

Henry, S. G., and J. W. Wilson, 1993: Developing thunderstorm forecast rules utilizing first detectable cloud radar-echoes. *Preprints, 5th Int'l Conf. on Aviation Weather Systems*, Vienna, Amer. Meteor. Soc.

Holle, R. L., and M. W. Maier, 1980: Tornado formation from downdraft interactions in the FACE mesonetwork. *Mon. Wea. Rev.*, **108**, 1010-1028.

Kelly, R. D., 1982: A single Doppler radar study of horizontal-roll convection in a lake-effect snow storm. *J. Atmos. Sci.*, **39**, 1521-1531.

Kessinger, C. J., and C. K. Mueller, 1991: Backround studies and nowcasting Florida thunderstorm activity in preparation for the CaPOW forecast experiment. *Preprints, 25th Conf. on Radar Meteor.*, Paris, Amer. Meteor. Soc, 416-419.

Kidder, S. Q., and T. H. Vonder Haar, 1995: *Satellite Meteorology, An Introduction*. Academic Press, Inc., 466 pp.

Knight, C. A. and L. J. Miller, 1993: First radar echoes from cumulus clouds. *Bull. Amer. Meteor. Soc.*, **74,** 179-188.

Konrad, T. G., 1968: The alignment of clear-air convective cells. *Proc. Int. Conf. Cloud Physics*, Toronto, Amer. Meteor. Soc., 539-543.

Kropfli, R. A., I. Katz, T. G. Konrad, and E. B. Dobson, 1968: Simultaneous radar reflectivity measurements and refractive index spectra in the clear atmosphere. *Radio Sci.*, **19**, 991-994.

Lee, B. D., R. D. Farley, and M. R. Hjelmfelt, 1991: A numerical case study of convection initiation along colliding convergence boundaries in northeast Colorado. *J. Atmos. Sci.*, **48,** 2350-2366.

LeMone, M. A., 1973: The structure and dynamics of horizontal roll vortices in the planetary boundary layer. *J. Atmos. Sci.*, **30,** 1077-1091.

Liou, K. N., 1980: *An Introduction to Atmospheric Radiation.* Academic Press, New York.

Menzel, W. P. and J. F. Purdom, 1994: Introducing GOES-I: The first of a new generation of geostationary operational environmental satellites. *Bull. Amer. Meteor. Soc.*, **75**, 757-781.

Mie, G., 1908: Beitrage zur optik truber Median, speziell kolloidaler Metallosungen, Ann. *Physik* **25**, 377-445.

Mohr, C. G., L. J. Miller, R. L. Vaughan, and H. W. Frank, 1986: The merger of mesoscale datasets into a common Cartesian format for efficient and systematic analyses. *J. Atmos. Oceanic Technol.*, **3,** 143-161.

Mueller, C. K., J. W. Wilson, and N. A. Crook, 1993: The utility of sounding and mesonet data to nowcast thunderstorm initiation. *Wea. Forecasting*, **8**, 132-146.

Pekeris, C. L., 1947: Note on the scattering of radiation in an inhomogeneous medium. *Phys Rev.*, **71,** 268-269.

Pielke, R., 1974: A three-dimensional numerical model of the sea breezes over south Florida. *Mon. Wea. Rev.*, **102,** 115-139.

Pielke, R. A., and M. Segal, 1986: *Mesoscale Meteorology and Forecasting*. Chap. 22: Mesoscale circulations forced by differential terrain heating. Amer. Meteor. Soc., p516-548.

Plank, V. G., 1960: Cumulus convection over Florida - a preliminary report. *Cumulus Dynamics, Proceedings of the First Conf. on Cumulus Convection.* C. E. Anderson, Ed. Pergamon Press, 211 pp.

Purdom, J. F. W., 1976: Some uses of high-resolution GOES imagery in the mesoscale forecasting of convection and its behavior. *Mon. Wea. Rev.*, **104,** 1474-1483.

Purdom, J. F. W., and K. Marcus, 1982: Thunderstorm trigger mechanisms over the southeast United States. *Preprints, 12th Conf. on Severe Local Storms,* San Antonio, Amer. Meteor. Soc., 487-488.

Roberts, R. D., and J. W. Wilson, 1995: The genesis of three nonsupercell tornadoes observed with dual-Doppler radar. *Mon. Wea. Rev.*, **123**, 3408-3438.

Rotunno, R., J.B. Klemp, and M. L. Weisman, 1988: A theory for strong, long-lived squall lines. *J. Atmos. Sci.*, **45,** 463-485.

Segal, M., W. E. Schreiber, G. Kallos, J. R. Garratt, A. Rodi, J. Weaver, and R. A. Pielke, 1989: The impact of crop areas in northeast Colorado on midsummer mesoscale thermal circulations. *Mon. Wea. Rev.*, **117**, 809-825.

Stephens, G. L., 1994: *Remote Sensing of the Lower Atmosphere.* Oxford University Press, 523 pp.

Stull, R. B., 1988: *An Introduction to Boundary Layer Meteorology.* Kluwer Academic Publishers, 666 pp.

Szoke, E. J., M. L. Weisman, J. M. Brown, F. Caracena, and T. W. Schlatter, 1984: A subsynoptic analysis of the Denver tornadoes of 3 June 1981. *Mon. Wea. Rev.*, **112**, 790-808.

Tatarski, V. I., 1961: *Wave Propagation in a Turbulent Medium.* Translated by R. A. Silverman, McGraw-Hill, New York, 285 pp.

Taylor, L. R., 1963: Analysis of the effect of temperature on insects in flight. *J. Anim. Ecol.*, **32**, 99-117.

Thorpe, A. M., M. J. Miller, and M. W. Moncrieff, 1982: Two-dimensional convection in non-constant shear. A model of mid-latitude squall lines. *Quart. J. Roy. Meteor. Soc.*, **108**, 739-762.

Tuttle, J. D., and G. B. Foote, 1990: Determination of the boundary layer airflow froma single Doppler radar. *J. Atmos. Oceanic Technol.*, **7**, 218-232.

Wade, C. G., and G. B. Foote, 1982: The 22 July 1976 case study: Low-level outflow and mesoscale influences. *Hailstorms of the Central High Plains*, Vol. 2, C. Knight and A. Squires, Eds., Colorado Associated University Press, 115-130.

Wakimoto, R. M., and N. T. Atkins, 1994: Observations of the sea-breeze front during CaPE. Part I: Single-Doppler, satellite, and cloud photogrammetry. *Mon. Wea. Rev.*, **122**, 1092-1114.

Wakimoto, R. M., C. J. Kessinger, and D. E. Kingsmill, 1994: Kinematic, thermodynamic, and visual structure of low-reflectivity microbursts. *Mon. Wea. Rev.*, **122**, 72-92.

Wallace, J. M., and P. V. Hobbs, 1977: *Atmospheric Science, An Introductory Survey.* Academic Press, Inc., 467 pp.

Walters, K. F. A., and A. F. G. Dixon, 1984: The effect of temperature and wind on the flight activity of cereal aphids. *Ann. Appl. Biol.*, **104**, 17-26.

Weckwerth, T. M., J. W. Wilson, and R. M. Wakimoto, 1996: Thermodynamic variability within the convective boundary layer due to horizontal convective rolls. *Mon. Wea. Rev.*, **124**, 769-784.

Weckwerth, T. M., J. W. Wilson, R. M. Wakimoto, and N. A. Crook, 1997: Horizontal convective rolls: Determining the environmental conditions supporting their existence and characteristics. *Mon. Wea. Rev.*, **125**, 505-526.

Wilson, J. W., and W. E. Schreiber, 1986: Initiation of convective storms at radar-observed boundary-layer convergence lines. *Mon. Wea. Rev.*, **114**, 2516-2536.

Wilson, J. W., G. B. Foote, N. A. Crook, J. C. Fankhauser, C. G. Wade, J. D. Tuttle, C. K. Mueller, and S. K. Krueger, 1992: The role of boundary-layer convergence zones and horizontal rolls in the initiation of thunderstorms: A case study. *Mon. Wea. Rev.*, **120**, 1785-1815.

Wilson, J. W., and C. K. Mueller, 1993: Nowcasts of thunderstorm initiation and evolution. *Wea. Forecasting*, **8**, 113-131.

Wilson, J. W., T. M. Weckwerth, J. Vivekanandan, R. M. Wakimoto, and R. W. Russell, 1994: Boundary layer clear-air radar echoes: Origin of echoes and accuracy of derived winds. *J. Atmos. and Oceanic Tech.*, **11**, 1184-1206.

Wilson, J. W., and D. L. Megenhardt, 1997: Thunderstorm initiation, organization and lifetime associated with Florida boundary layer convergence lines. Accepted for publication by *Mon. Wea. Rev.*

Wilson, J. W., A. Crook, C. Mueller, and M. Dixon, 1997: State-of-the-art of nowcasting thunderstorms. Invited paper for the Convective Weather Forecasting Workshop, *7th Conf. on Aviation, Range and Aerospace Meteor.*, Long Beach, CA, Amer. Meteor. Soc.

Zhong, S., and E. S. Takle, 1992: An observational study of sea- and land-breeze circulation in an area of complex heating. *J. Appl. Meteor.*, **31**, 1426-1438.